Ifremer
Direction de la Technologie Marine et des Systèmes d'Information
Cellule Océano-Météo
Michel Olagnon, Marc Prevosto, Sylvie Van Iseghem

Shell International Exploration and Production, B.V.
Kevin Ewans, George Z. Forristall

May 2004

Shell International
Exploration and Production, BV

WASP

West Africa Swell Project

Final report

WASP

Final report

Kevin Ewans**
George Z. Forristall**
Michel Olagnon*
Marc Prevosto*
Sylvie Van Iseghem*

* Ifremer - Centre de Brest
** Shell International Exploration and Production, B.V.

WASP

Final report

Contents of the CD

- **WASP.pdf** Final Report
- **Appendix_Wasp.pdf** Appendices
- **Animations directory** Five animation AVI files
- **Chapters directory** Final Report split by chapter
- **Appendices directory** Appendices split by appendix

Contents

CHAPTER 1

Introduction

The OGP Workshop on the Metocean and Engineering Aspects of Floating Systems which was held at St. Albans in April 2001 identified better discrimination of the low frequency end of the wave spectrum as one of the most pressing problems for the design and analysis of floating systems. The responses of many floating systems have proven to be very sensitive not only to the amplitude and frequency of the swell, but also to the details of the shape of the swell peak in the spectrum. There has been relatively little serious study of the low frequency end of the wave spectrum compared to the effort that has gone into the study of the high frequency tail of the spectrum.

Much of the present interest in swell comes from the active deep water developments taking place off West Africa. The West African environment is generally mild, but swell from storms in the Southern Ocean is persistent and can reach fairly high amplitudes with very low periods. Enough data is now available so that a serious study of the characteristics of swell off West Africa can be made.

In response to this need and opportunity, Shell Global Solutions, in association with Ifremer and Oceanweather, formed a Joint Industry Project to analyze and compare the available data on swell off West Africa. This report describes the results of that West Africa Swell Project (WASP).

In-situ measurements were contributed by Shell, Ifremer, ChevronTexaco and Marathon. Hindcast directional wave spectra were provided for 10 sites off the West African coast by Oceanweather. Details of the data used in the project are given in Chapter 2.

In Chapter 3 we examine some typical examples of swell generation and propagation using fields of wave height and period obtained from the NOAA Wavewatch III model. A simple theoretical model of swell generation indicates that a triangular or log-normal spectral shape could be appropriate for swell a long distance from its origin.

Models of spectral shape are considered in more detail in Chapter 4. For the frequency spectrum, the models considered were a modification of the Jonswap form, a triangle, a Gaussian function and a log-normal function. The directional spread was described by a wrapped normal distribution.

Further considerations on spectral shape are given in Chapter 5. Calculations with synthetic data show that because of sampling variability, it is difficult to distinguish between models of spectral shape for narrow spectra.

Measured or hindcast wave spectra off West Africa are generally multi-modal. In addition to a wind sea peak, more than one swell system is often present. The first step in parameterizing a spectrum is thus to partition it into its components. The partitioning and paramaterization algorithms are described in Chapter 6. The accuracy of the various parameterizations is measured by calculating the rms difference between the original and fitted spectra. Differences in the response of single degree of freedom oscillators to the original and fitted spectra give another measure of the goodness of fit that is closely related to engineering applications.

The response of single degree of freedom oscillators is further explored in Chapter 7. The system responses of oscillators with a range of parameters are calculated for each spectrum in the data set. The response spectrum is then a plot of the maximum response over a range of natural periods and damping factors. Extreme values of the response can be calculated, and the spectrum which gives the maximum response can be scaled up to give a design spectrum for a system with similar characteristics.

Scatter plots of wave height and period are given in Chapter 8. Environmental contours for wave height and period are calculated using kernel density estimators to smooth the sample distributions.

Chapter 9 shows comparisons of the hindcast and measured swell. Plot of the evolution of the peak period, height and direction of the swell systems are particularly instructive.

In Chapter 10 we test whether the measured swell spectrum is stationary over relatively short time periods. The question is whether the swell comes in gusts, with more energy during some times and less in others. Statistical test are performed for both synthetic data and the Ekoundou measurements, which consist of long continuous time series.

Chapter 11 gives our conclusions about the best parametric description of the swell partitions in wave spectra. The log-normal distribution is selected as the best functional form for the frequency spectrum, and fits are given for the standard deviation of the distribution as a function of peak frequency. Fits are also given for the standard deviation of the wrapped normal distribution for wave spreading as a function of peak frequency.

Our work on infragravity waves is described in Chapter 12, which includes a large annotated bibliography. The spectra at low frequencies for the Ekoundou and Malabo measurements are calculated and compared to calculations of second order bound waves.

Finally, our conclusions are summarized in Chapter 13.

The main part of the appendices is published in a separate document "WASP-West Africa Swell Project, *Appendices*".

CHAPTER 2

WASP Data Base

Kevin Ewans
George Z. Forristall
Michel Olagnon
Marc Prevosto

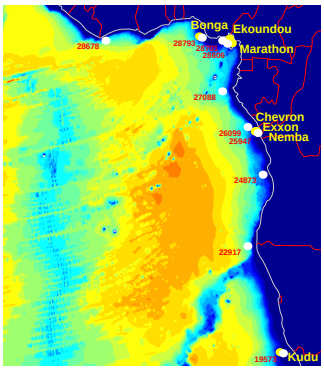

WASP was planned to analyze and compared existing data on swell off West Africa. In-situ measurements of swell at several sites were contributed to the project by participants. Those data sets are briefly described in the next section. Spectra from 10 hindcast grid points in the WANE study were also obtained from Oceanweather for comparison with the measurements. The hindcast grid points span the West African coast from Côte d'Ivoire to Namibia. Details of the hindcast data set follow the section on in-situ measurements. The location of the measurements and hindcast points are illustrated in Figure 2.1.

In-situ measurements

Participants in the project contributed measurements made at several sites along the West African coast. The locations of these measurements are listed in Table 2.1, and other details of the measurements are described below.

TABLE 2.1 : In-situ measurement locations

Site	Location		Instrument	Dates
Bonga	4° 33’ N	4° 36’ E	Directional Waverider	4 Jul 1998 – 23 Sep 1998
Bonga	4° 33’ N	4° 36’ E	Directional Waverider	6 Feb 1999 – 3 Aug 1999
Bonga	4° 33’ N	4° 36’ E	Wavescan	1 Nov 2001 –19 Dec 2002
Kudu	28º 38’ S	14º 35’ E	Directional Waverider	27 Jun 1998 – 13 Apr 1999
Ekoundou	4° 17’ N	8° 23’ E	Wavestaff	7 Jun 1982 – 18 Jul 1982
Cabinda 1	5º 22’ S	12º 10’ E	Wavestaff	8 Mar 1990 – 15 Mar 1991
Cabinda 2	5º 30’ S	11º 45’ E	Wavestaff	8 Mar 1990 – 15 Mar 1991
Malabo	3º 47’ N	8º 42’ E	Pressure	6 Oct 2002 –1 Apr 2003

Bonga Directional Waverider. Shell collected wave measurements from 1997 through 1999 in the Bonga field offshore Nigeria using a directional Waverider buoy. The water depth was approximately 1000 m. There was a long gap between the two deployments, which were made with different instruments. Parameters of the directional spectrum were calculated on board and saved every 30 minutes.

Bonga Wavescan. In 2001 and 2002, an Oceanor Wavescan buoy was used to collect data at the Bonga site. The buoy calculates the directional spectrum from the heave, pitch and roll of the buoy as measured by a SEATEX MRU-4. Wind and current were also measured but not used in this study. Time series of wave elevations were recorded as well as the spectra.

Kudu. A directional Waverider was used for wave measurements in the Kudu field off Namibia. The water depth at the site was approximately 180 m.

Ekoundou. Ifremer collected wave data in 1982 on a free-standing conductor pipe monitoring program at Ekoundou (Rio del Rey area, Cameroon) in 18 m water depth. Only 70 records are available, but the data are of high quality, 40 minutes with 20 Hz sampling frequency, from a VEGA wavestaff. During the experiment (June 7-17 and July 3-18), significant wave height varied from 1 to 2.5 m. The data are particularly interesting because time series were recorded and data collection from a wavestaff avoids the problem of measuring very low frequency waves from an accelerometer buoy. Details are given in Appendix 2.1.

Cabinda 1 and 2. These measurements were made by ChevronTexaco near the ALP platform in Takula field off Cabinda. The Cabinda 1 measurements were in 8 m of water and the Cabinda 2 measurements were in 85 m water depth.

Malabo. These measurements were made by ASL Environmental Services for Marathon. The sites were on the north side of Bioko Island near Punta Europa. Waves were measured using both pressure transducers and ADCPs configured to calculate directional wave spectra. The site is mostly sheltered from the southerly swell, but the measurements are potentially interesting for the study of infragravity waves since the pressure transducers are accurate at low frequencies.

Bonga and Kudu Buoy Data QC Checks

Routine QC checks revealed a number of problems with the wave buoy data recorded at the Bonga and Kudu locations. Further checks and analyses were undertaken to identify the extent of the problem data and to select a good quality subset for analysis. The QC analyses for each of the data sets are given in the following sections.

The Check Ratio. The check ratio, $k(f)$, is defined as follows

$$k(f) = \left\{ \frac{C_{xx}(f) + C_{yy}(f)}{C_{zz}(f)} \right\}^{1/2} \qquad \textbf{(EQ 2.1)}$$

where for example $C_{xx}(f)$ is the variance density of the horizontal motion along the x-axis.

Thus, $k(f)$ essentially gives the ratio of the horizontal to vertical motions at frequency, f, and in deep-water it should be unity. A deviation from unity may indicate shallow-water effects, the presence of strong currents, or noise. Accordingly, it is an indicator of the quality of the data, particularly the signals required to make estimates of the directional distribution.

When $k(f)$ is greater than 2.5, it is set equal to 2.5, for plotting convenience – a value greater than two already indicates a problem.

FIGURE 2.1 : Data base locations

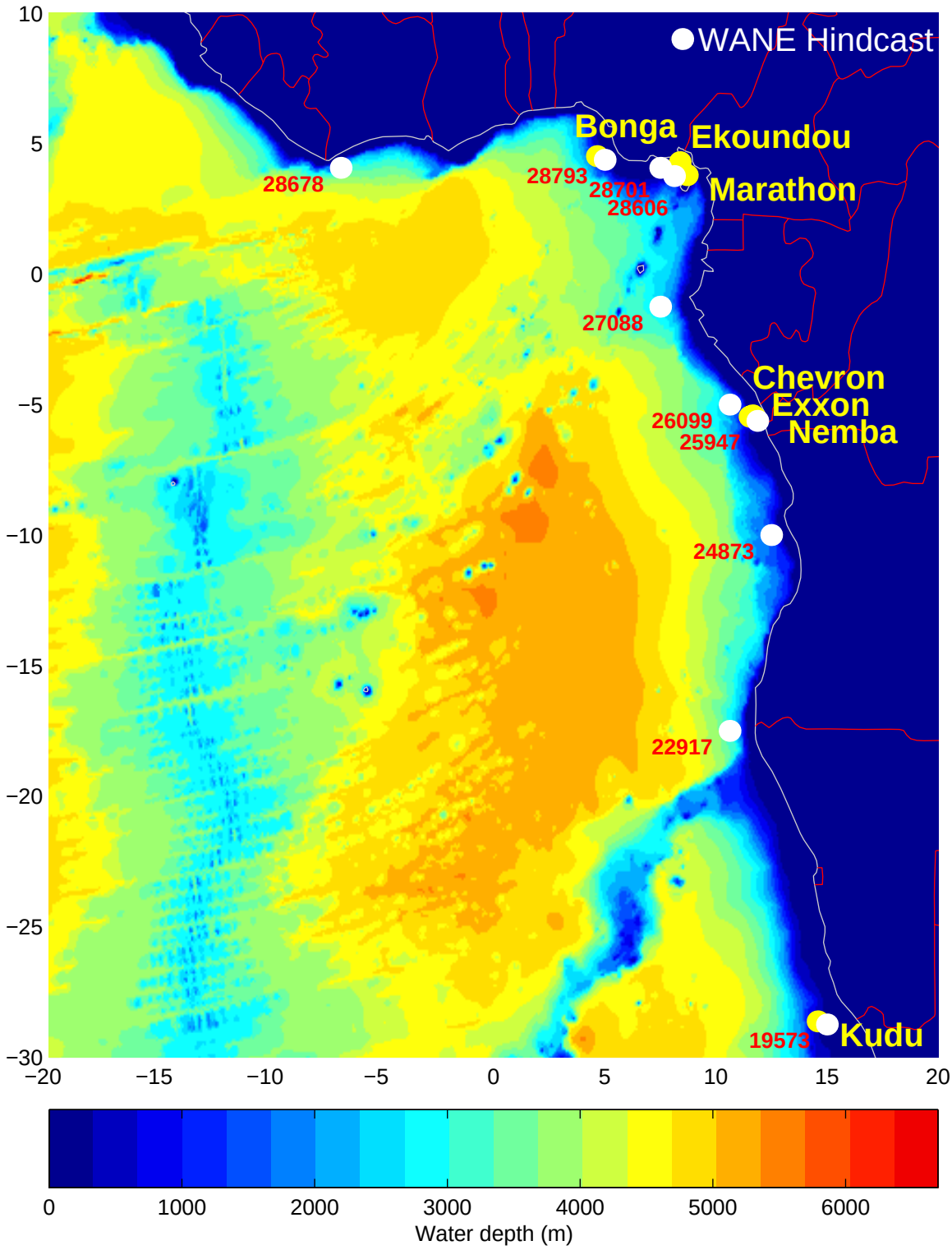

Bonga Directional Waverider Buoy. The entire set of wave variance density spectra derived from the Bonga Directional Waverider buoy is plotted in figure 2.2. The plot shows that the measured spectra tend to have peaks at around 0.025 Hz, 0.07 Hz, and 0.15 Hz. The peak at 0.025 Hz is spurious, indicating a likely unstable platform.

FIGURE 2.2 : Bonga DWR variance density frequency spectra

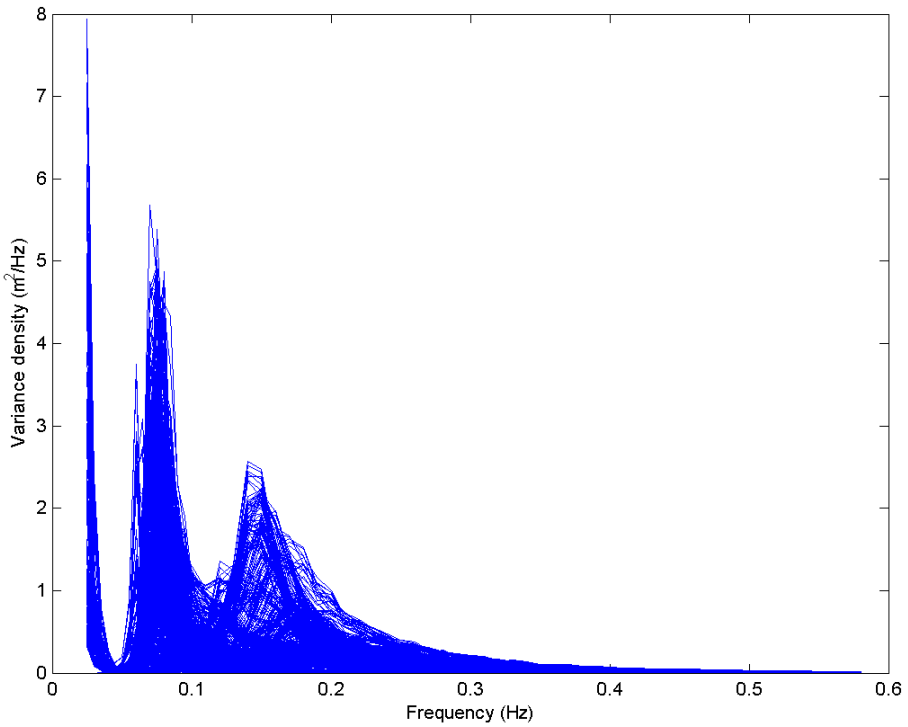

Figure 2.3, which gives time series of the significant wave height and peak frequency, shows that the 2nd deployment period has many spectra with peak frequencies less than 0.03 Hz, while none occur in the 1st deployment. Further, a spurious peak in the Hs time series during the 2nd period corresponds to the occurrences of the low frequency peak. Figure 2.4 shows these problems are eliminated from the data set when the bandwidth over which Hs and fp are calculated is simply constrained to the frequency range $f \geq 0.04$ Hz .

FIGURE 2.3 : Time series plot of the significant wave height, Hs, and peak frequency, fp, for the Bonga DWR data set.

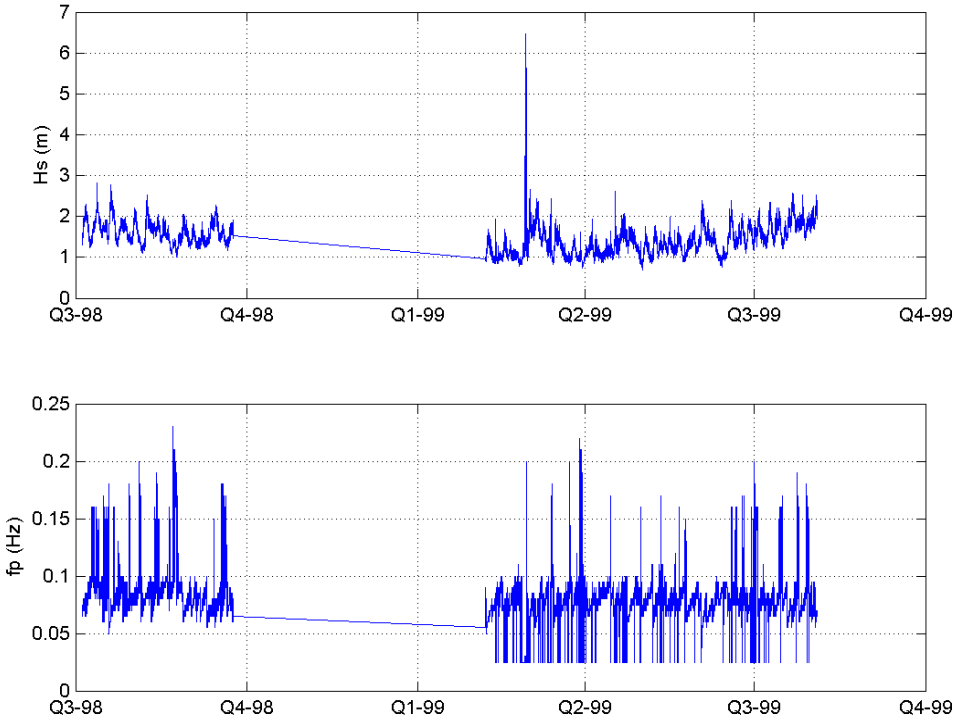

FIGURE 2.4 : Time series plot of the significant wave height, Hs, and peak frequency, fp, computed for $f \geq 0.04$ Hz , for the Bonga DWR data set.

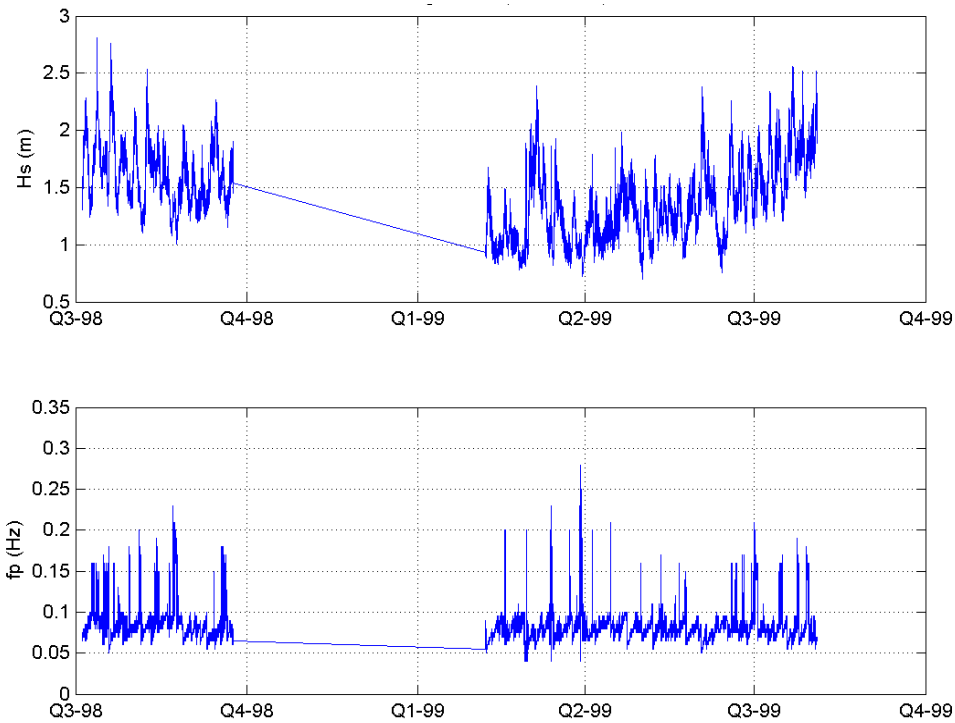

Azimuths from the Bonga location to some key land features are shown in figure 2.5. In particular, low frequency swell is not expected to arrive from the sector 268° through north to 163°. It is possible for swell to arrive from within the sector 143° to 163°.

FIGURE 2.5 : Azimuths from the Bonga location to key land features

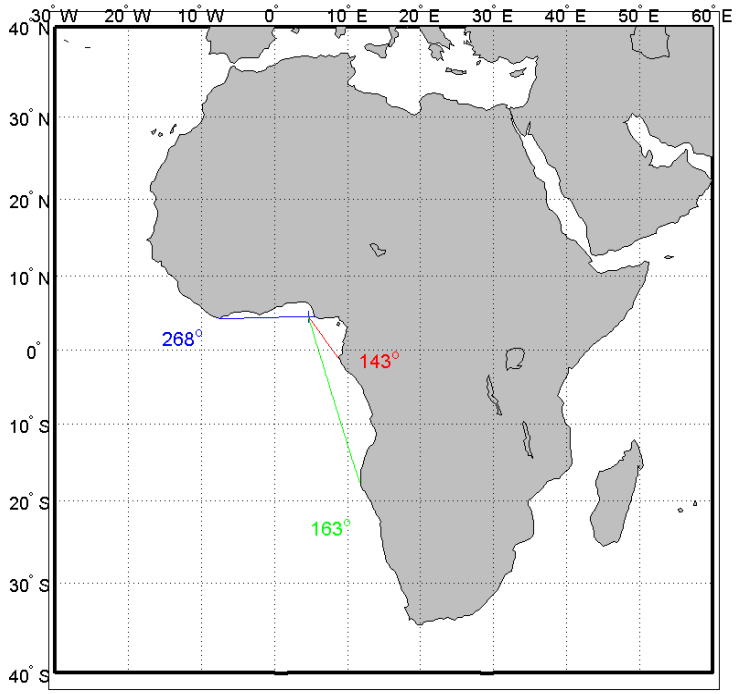

Figure 2.6 shows the distribution of the peak frequency against the peak direction for the Bonga data set, with the frequency constrained to $f \geq 0.04$ Hz . The plot shows a large number of recordings for which the low-frequency swell arrival direction is within the sector 268° through north to 163°. Data for these occurrences are plotted in red on the time series of Hs and fp in figure 2.7. The plot shows that nearly all of these events occurred during the 2nd deployment, indicating a problem with the measurements during this period.

Figures 2.8 and 2.9 are example spectra from the 1st and 2nd deployments. While both variance density spectra are similar and appear to be good, the low frequency peak in the variance density spectrum of figure 2.9 has an associated mean direction from the Northeast. The check ratio plot (bottom) shows that this peak is associated with values $k \geq 2.5$, and accordingly in error [the site is deepwater and does not have particularly strong currents]. Figure 2.10, which plots the time series of the check ratio computed over three frequency bands, shows that the check ratio is too high for the low-frequency band for most of the 2nd deployment. Accordingly, the directional data in the 2nd deployment were invalidated.

FIGURE 2.6 : Polar plot of peak frequency, f_p, against peak direction, θ_p, for $f \geq 0.04$ Hz, for the Bonga DWR data set.

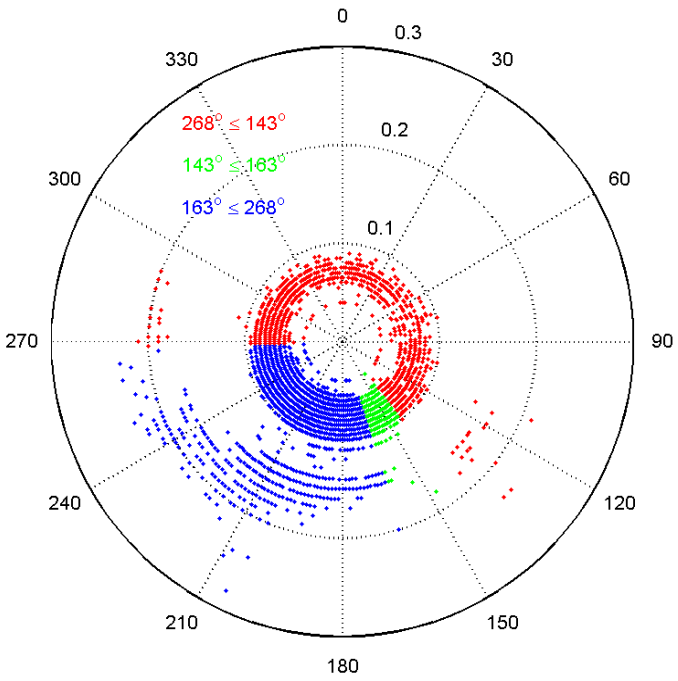

FIGURE 2.7 : Time series plot of the significant wave height, Hs, and peak frequency, fp, computed for $f \geq 0.04$ Hz, for the Bonga DWR data set. The points plotted in red have $290° < \theta_p < 140°$

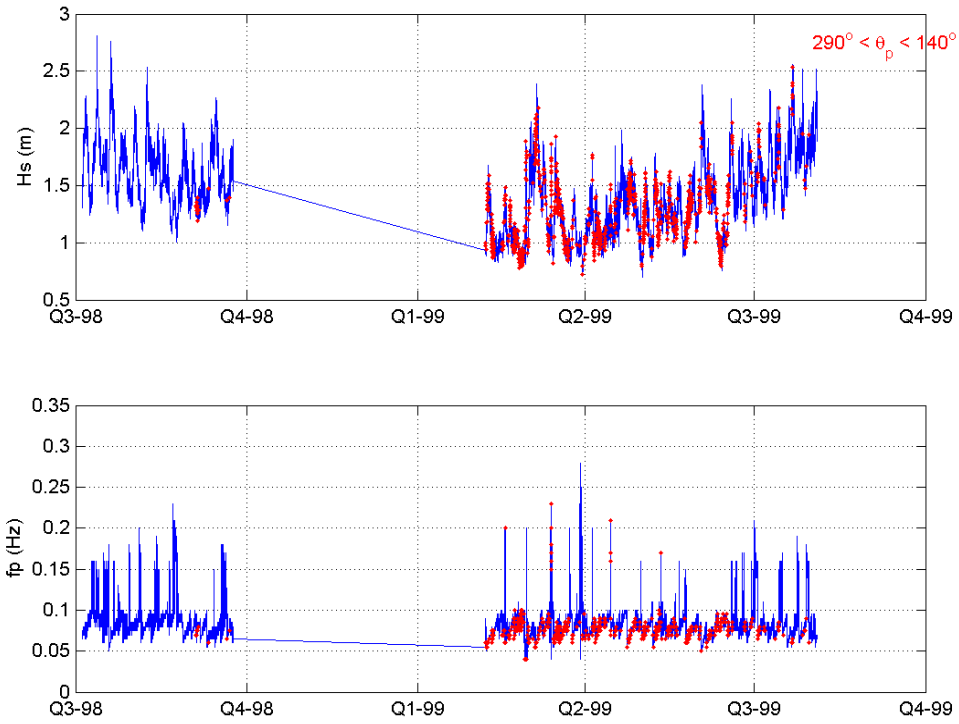

FIGURE 2.8 : Spectra for a record from the 1st deployment of the Bonga DWR. From top to bottom are the variance density spectrum, the mean direction spectrum, the circular rms spreading spectrum, and the check ratio spectrum.

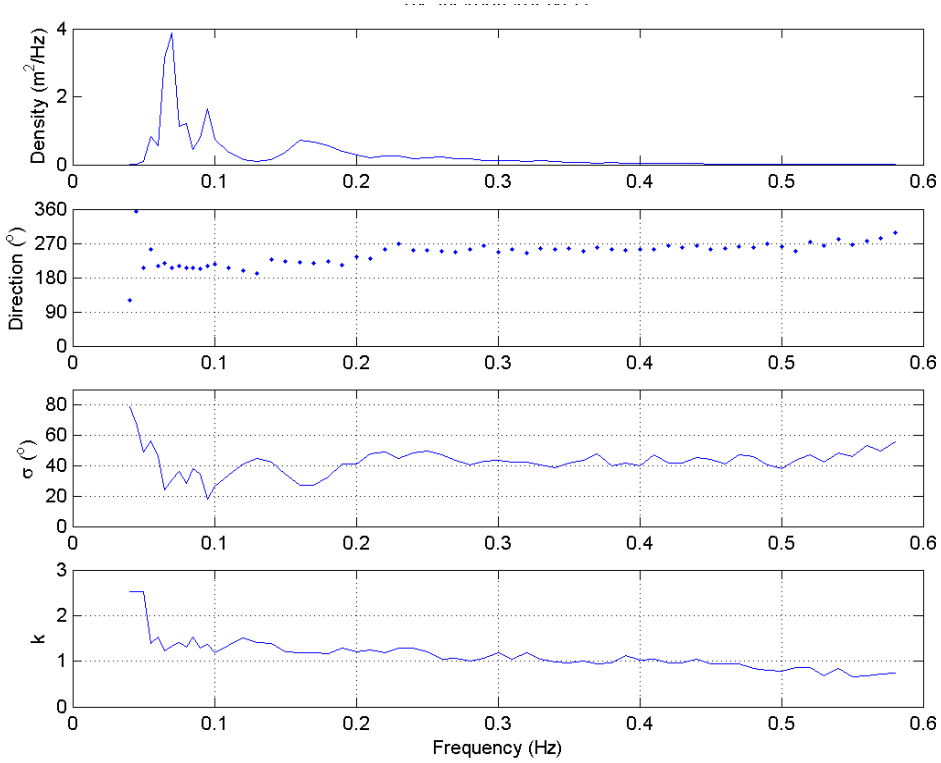

FIGURE 2.9 : Spectra for a record from the 2nd deployment of the Bonga DWR. From top to bottom are the variance density spectrum, the mean direction spectrum, the circular rms spreading spectrum, and the check ratio spectrum.

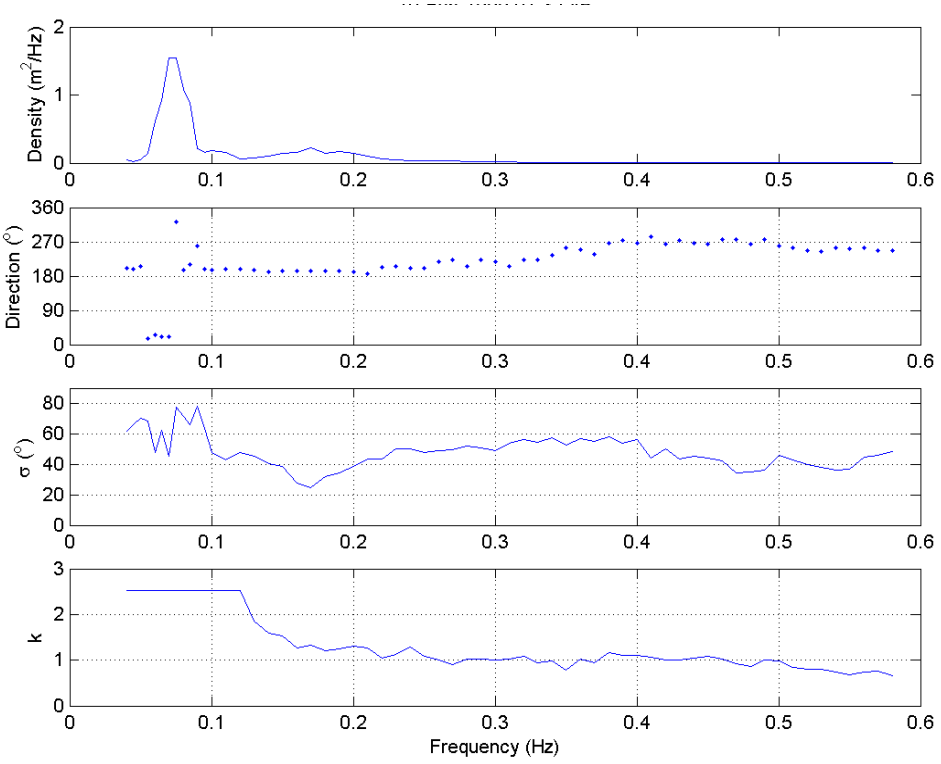

FIGURE 2.10 : Time series plot of the check ratio averaged over the bands 0.04-0.12 Hz (blue), 0.12-0.30 Hz (green), and 0.30-0.58 Hz (red).

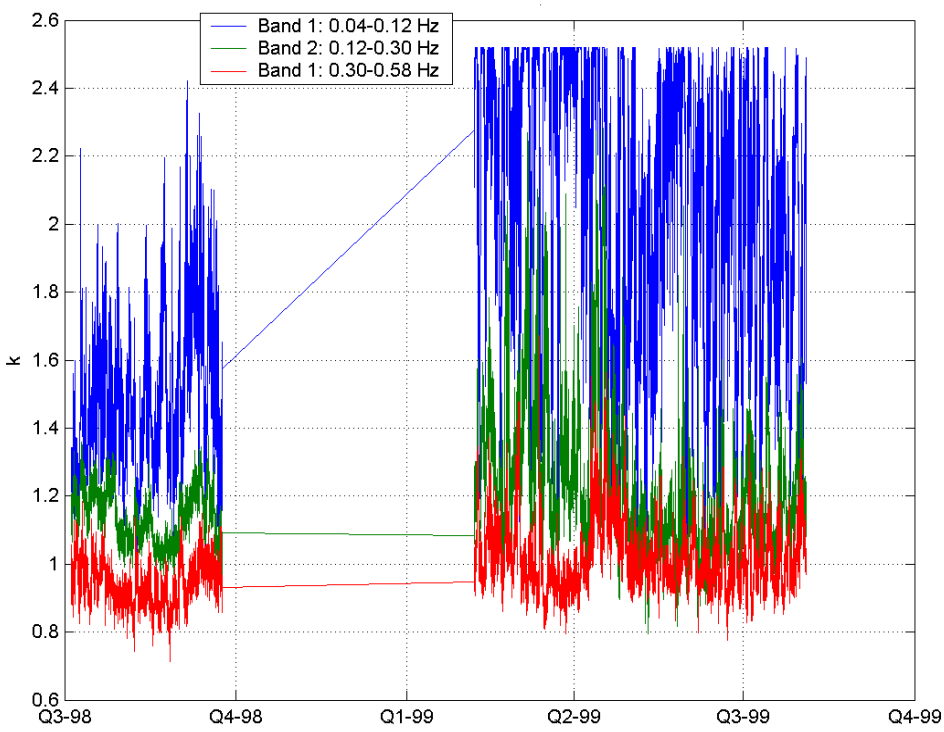

Bonga Wavescan Buoy. The variance density spectra for the entire Bonga Wavescan data set are plotted in figure 2.11. There are no peaks with frequencies less than 0.04 Hz, as was observed in the Bonga DWR data set. The spectra correspond to 3-hour averages, and although they appear rather noisy for 3-hourly averaged spectra, they are considered good.

Figure 2.12 is a polar plot of the peak frequency against the peak direction. Cursory examination of this plot would suggest the distribution of points appear reasonable. For example, none indicate landward directions. However, a distinct lack of points from the southeast is apparent when compared with figure 2.6 and with expectation.

The plot of the check ratio spectrum (figure 2.12) shows a large number of spectral estimates with $k \geq 2.5$. In addition, the scatter plot of the check ratio against variance density for spectral estimates at the spectral peak (figure 2.14) shows a large number of estimates with low values of k. In fact, these data are clustered around $k = 0.5$, some distance from the optimum value of $k = 1$.

Two typical examples of spectra from this data set are given in figures 2.15 and 2.16. The plots show the low check ratios across the spectrum, the directional spreading values are high and noisy by comparison with for example figure 2.8. These were typical of all the spectra from this data set. Consequently, it was decided to invalidate the Bonga Wavescan directional data.

FIGURE 2.11 : Bonga Wavescan variance density frequency spectra

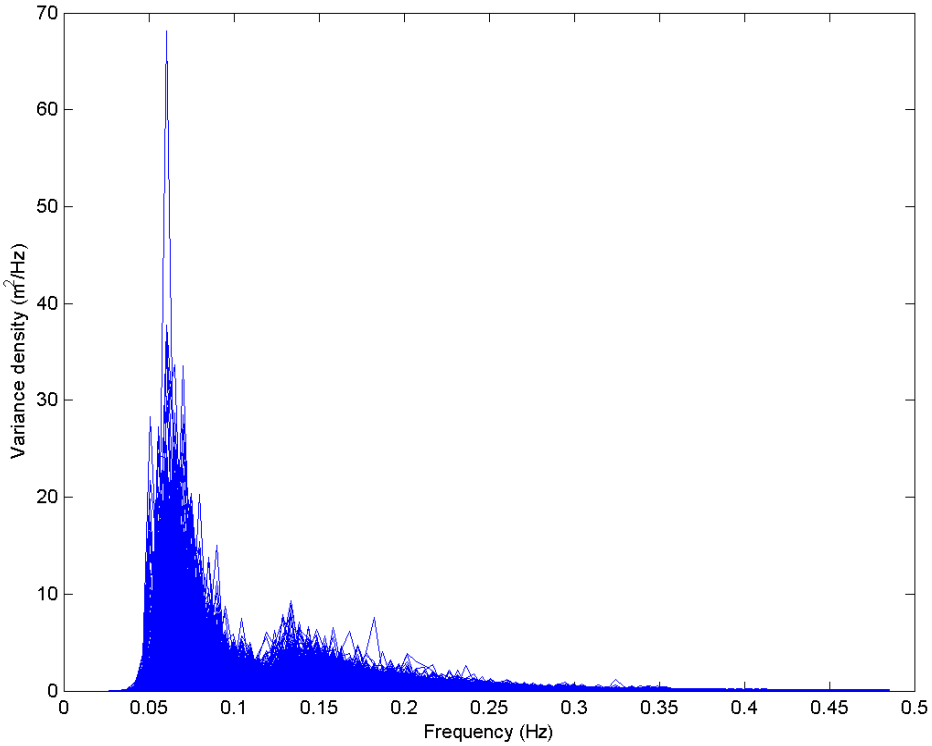

FIGURE 2.12 : Polar plot of peak frequency, f_p, against peak direction, θ_p, for the Bonga Wavescan data set.

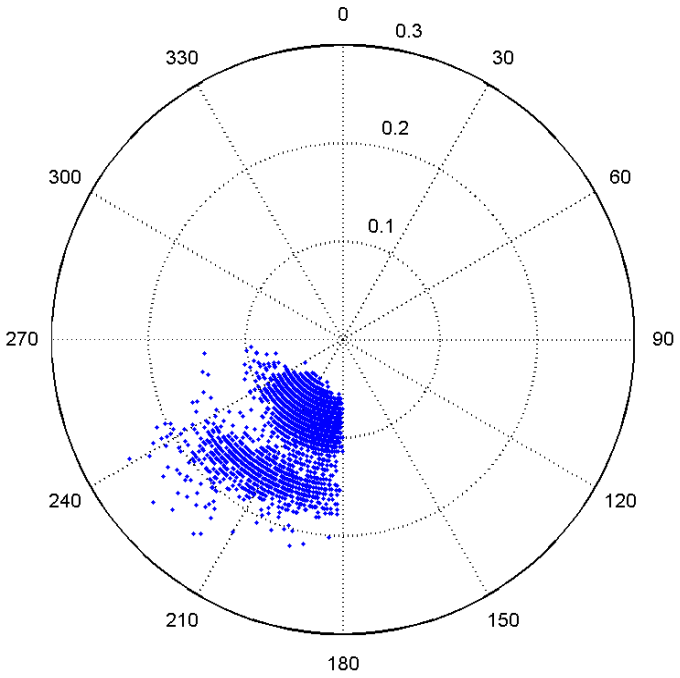

FIGURE 2.13 : Check ratio spectra for the Bonga Wavescan dataset.

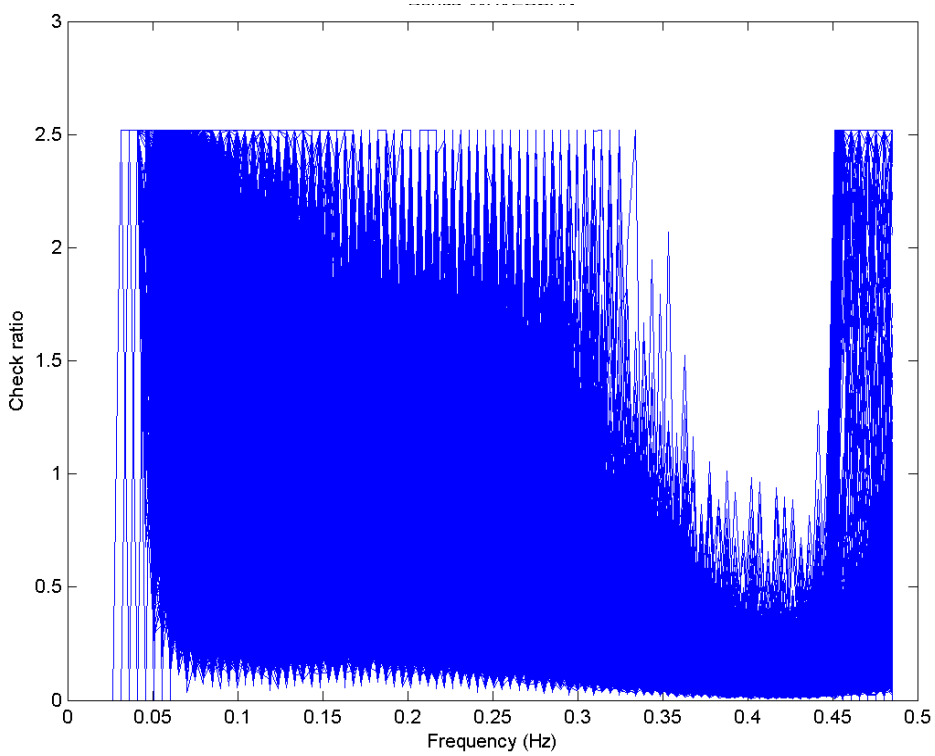

FIGURE 2.14 : Scatter plot of the check ratio versus the variance density of spectral estimates at the peak frequency.

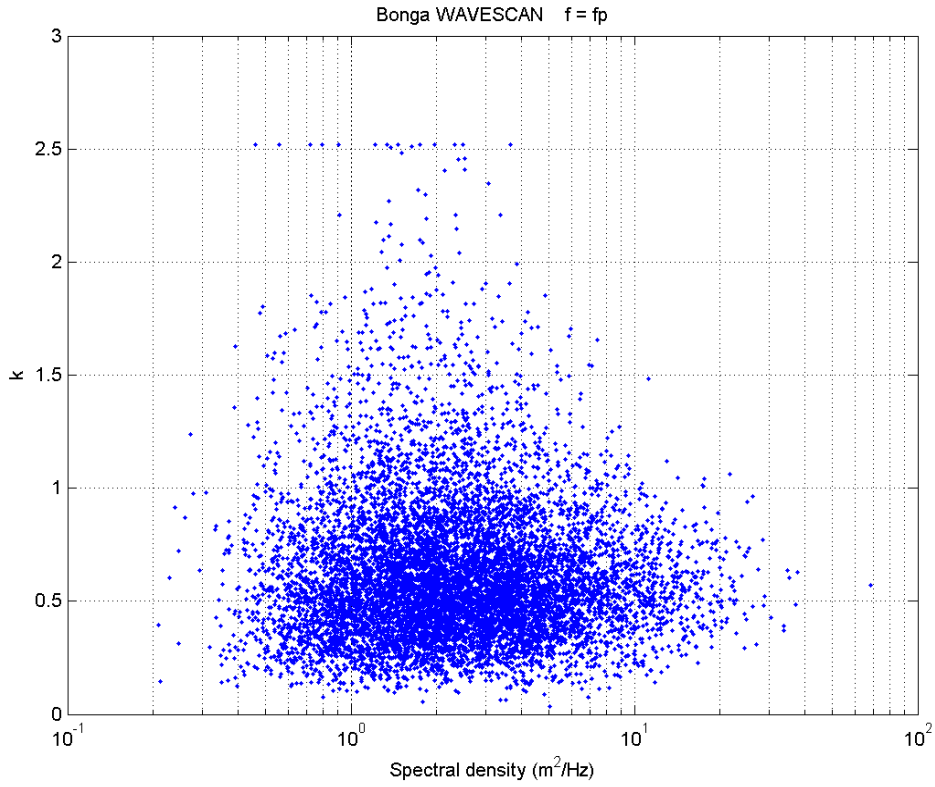

FIGURE 2.15 : Spectra for 2-Feb-2002 from Bonga Wavescan data set. From top to bottom are the variance density spectrum, the mean direction spectrum, the circular rms spreading spectrum, and the check ratio spectrum.

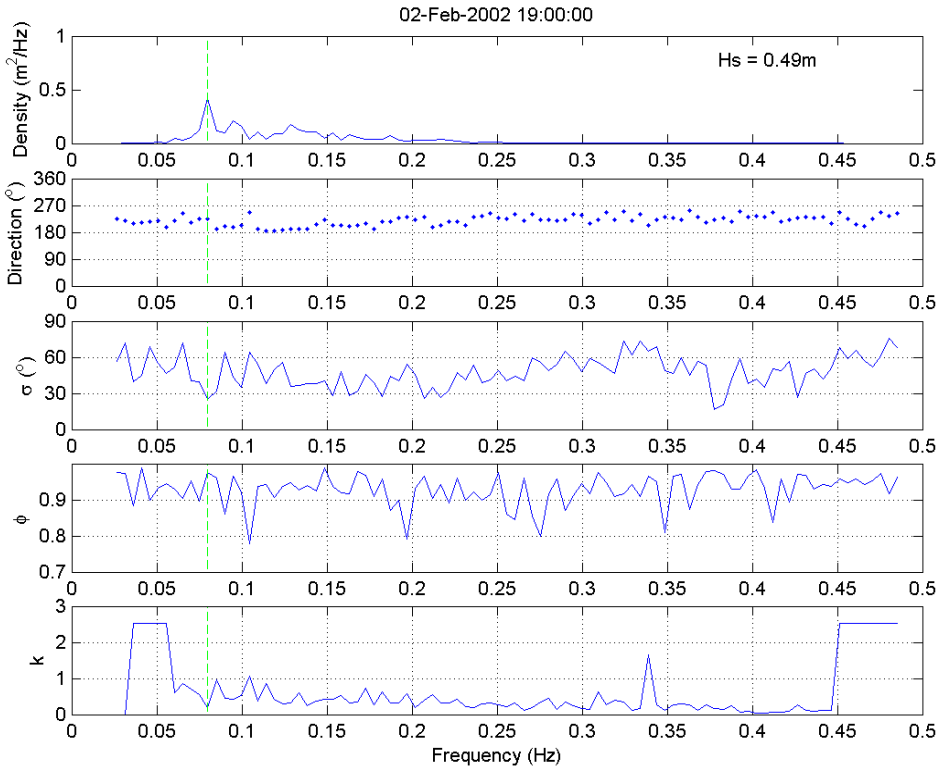

FIGURE 2.16 : Spectra for 21-Jun-2002 from Bonga Wavescan data set. From top to bottom are the variance density spectrum, the mean direction spectrum, the circular rms spreading spectrum, and the check ratio spectrum.

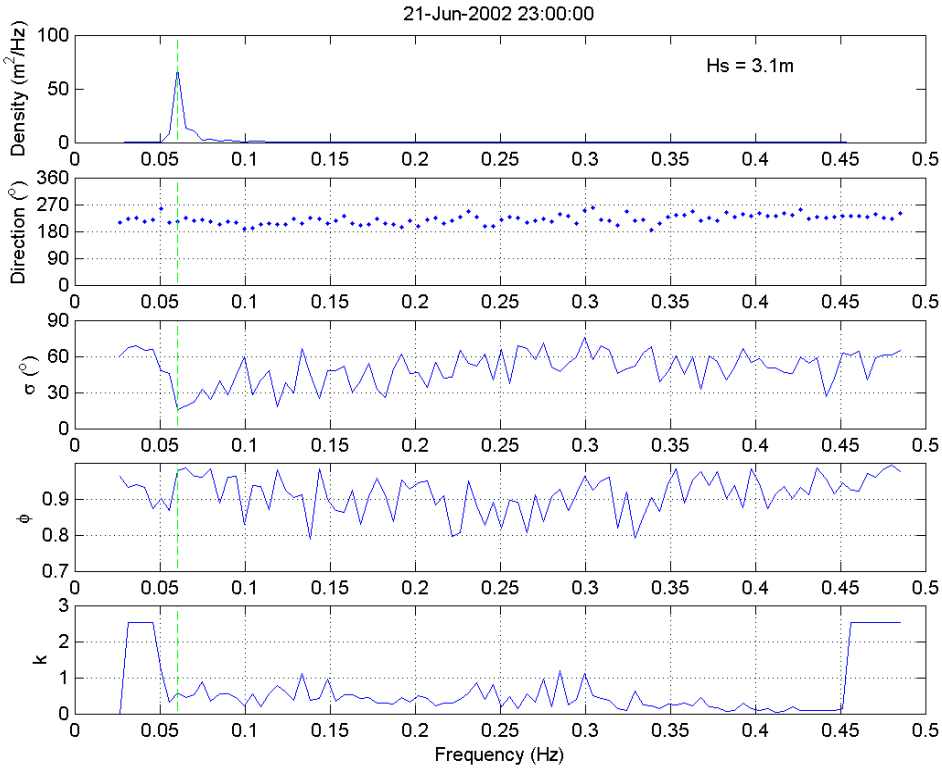

Kudu Directional Waverider Buoy. QC plots for the Kudu Directional Waverider Buoy data are given in figure 2.17 through to figure 2.21. The plots indicate the Kudu data are of good quality. There are no spectra with spurious low frequency peaks (figure 2.17), the polar distribution of peak frequency (figure 2.18) does not contain any unrealistic directions (i.e. there are no landward directions), and the check ratio spectra (figure 2.19) indicate that most spectral estimates are associated with values of $k \approx 1$.

Figure 2.19 shows that a number of spectra have values of $k \geq 2.5$ at low frequency, but inspection of individual spectra (e.g. figures 2.20 and 2.21) revealed that these occurred for low frequency estimates, below the peak frequency.

Accordingly, it was concluded that the Kudu data in their entirety are good quality data.

FIGURE 2.17 : Kudu Directional Waverider variance density frequency spectra.

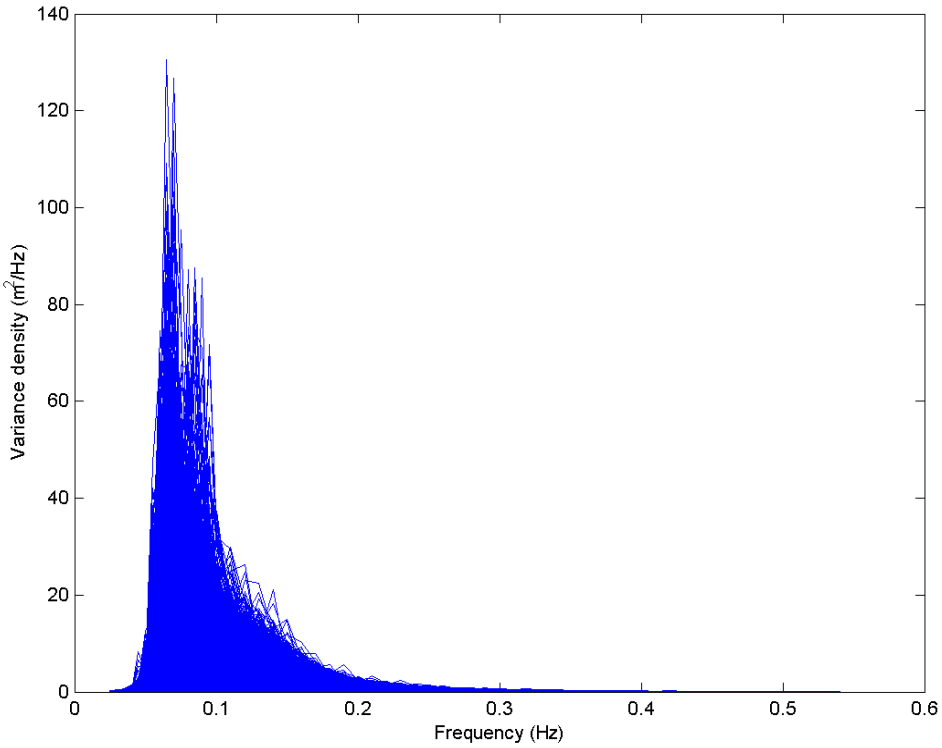

FIGURE 2.18 : Polar plot of peak frequency, f_p, against peak direction, θ_p, for the Kudu Directional Waverider data set.

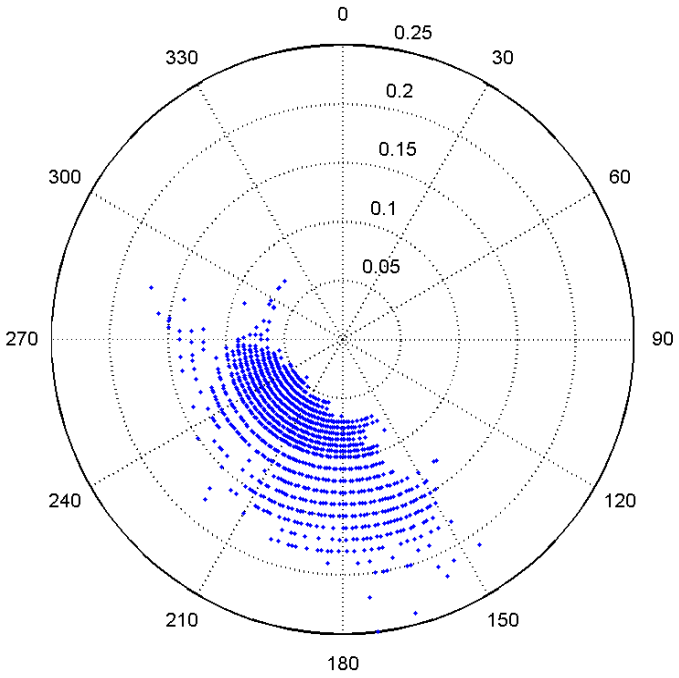

FIGURE 2.19 : Check ratio spectra for the Kudu Directional Waverider dataset.

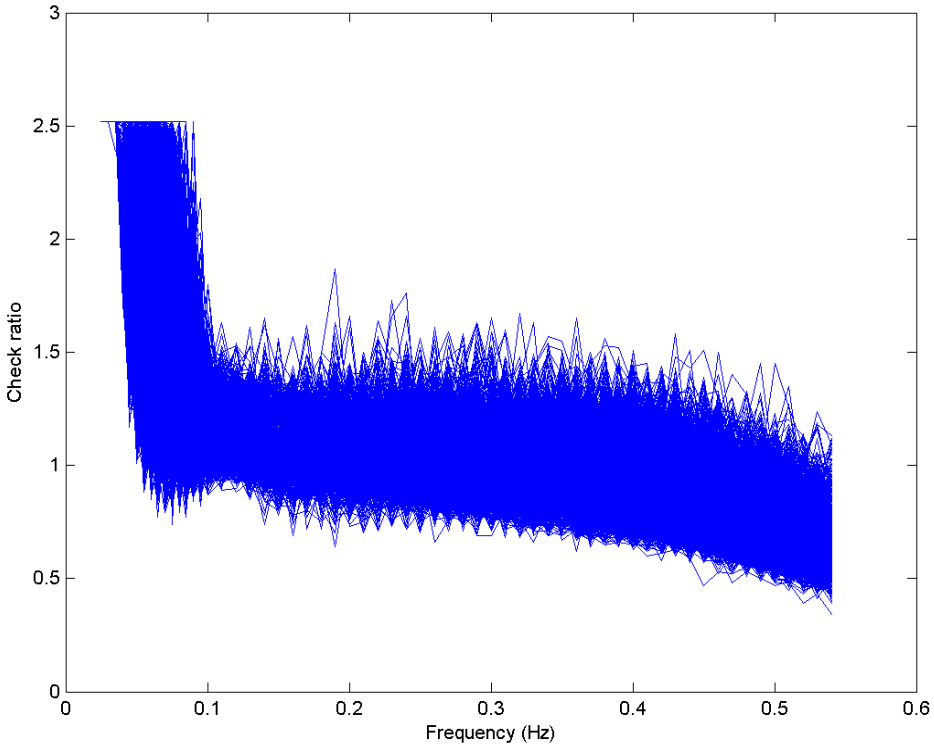

FIGURE 2.20 : Spectra for 30-Jun-1998 from Kudu DWR data set. From top to bottom are the variance density spectrum, the mean direction spectrum, the circular rms spreading spectrum, and the check ratio spectrum.

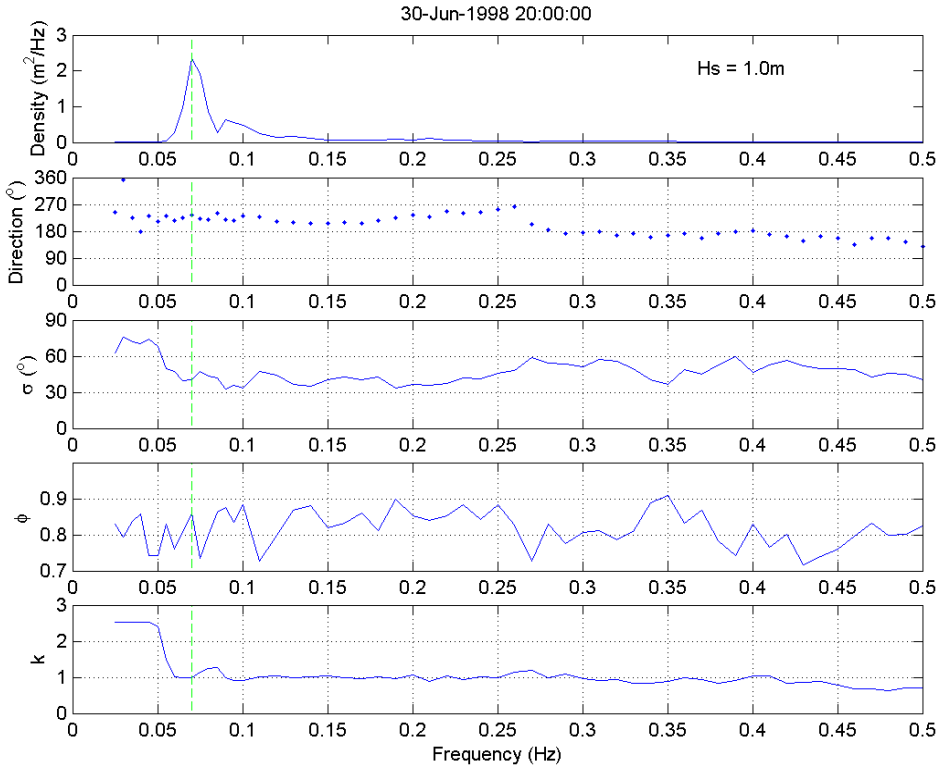

FIGURE 2.21 : Spectra for 11-Sep-1998 from Kudu DWR data set. From top to bottom are the variance density spectrum, the mean direction spectrum, the circular rms spreading spectrum, and the check ratio spectrum.

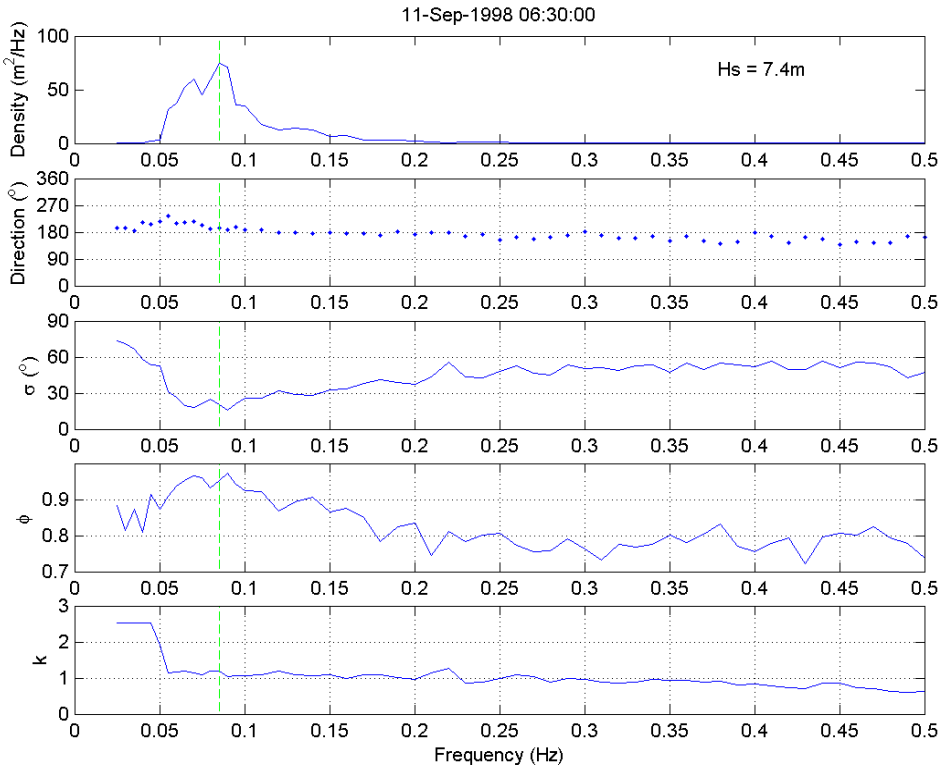

Hindcast data base

Hindcast WANE

WANE is a follow-on study to Oceanweather's original WAX (West Africa Extremes) JIP (Joint Industry Project) for the West Coast of Africa. WANE provides a comprehensive database of wind, wave and ocean currents and is sold on a per-point basis.

A 15-year continuous period, each three hours, and 80 individual storms were hindcast using Oceanweather's wave model on a 0.325 by 0.625 degree grid covering the entire South Atlantic. Wave spectra from the GROW global hindcast were used at the WANE boundaries. All the calculations are made in infinite depth.

Ten points have been used in the WASP project, the location of which are given in table 2.2 and plotted in fig. 2.1.:

TABLE 2.2 : WANE points

WANE points #	Latitude	Longitude
28678	4.0625	-6.875
28793	4.3750	5.000
28701	4.0625	7.500
28606	3.7500	8.125
27088	-1.2500	7.500
26099	-5.0000	10.625
25947	-5.6250	11.875
24873	-10.0000	12.500
22917	-17.5000	10.625
19573	-28.7500	15.000

Data set. Three types of data sets have been used:

- "WANE Storm". These are storm spectra time series for the 82 storms that were hindcast in WANE. The time step for the storm spectra is hourly.
- "WANE OPR". These are the operational time series for the fifteen years hindcast in WANE. The time step for the operational spectra is 3 hourly.
- "WANE Qscat". These are the Quikscat wind hindcasts which was done for a two year period. The time step for the QuikScat period is 3 hourly.

Explanation of spectra: For each date the synthetic parameters and directional spectra are given

- *Synthetic parameters*: wind speed, wind direction, peak period, sea and swell partitions as well as significant wave height. See the details of the parameters in Appendix 2.2.
- *Directional spectrum discretization*: The spectra are discretized in 23 frequencies and 24 directions. The 24 directional bins are each 15 degrees wide; the first bin, with a nominal direction 7.5 degrees, extends from 0 to 15 degrees. Frequency bins are spaced in geometric progression (see Appendix 2.3 for details). The 23rd frequency band is an integrated band comprising what would be bins 23 through 44 (continuing the geometric progression) of a fully discrete bin system.
- *Spectrum tail*: To model the cascade of wave energy from high to low frequencies endorsed by non-linear interactions, interactions are computed involving bins out to 44. This requires a parametric assumption about the spectral density

between 0.30652 and 2.52741 Hz; and the customary assumption is that density is proportional to ω^{-x}, where x is a disposable parameter. Here x = 4.5 is used for the following reasons:

- There are quasi-physical arguments supporting the exponents 4 & 5. The exponent 5 is germane to a Pierson-Moskowitz spectrum.

- A crude energy balance computation in the tail, with wind input scaled as ω^2 and interactions scaled as ω^{11}, shows that 4.5 is the only exponent capable of yielding an equilibrium spectrum in the tail.

To compute a "density" at 0.32157 Hz, we compute what fraction of the integrated band belongs to the bin from 0.30652 to 0.33737 Hz. Sparing a few details, the result is:

dens = (variance component)*rbw

where rbw is a function of the exponent as follows:

x	rbw (s)
4.0	8.11849
4.5	9.24794
5.0	10.32933

Hindcast NOAA

For some purposes in the project (swell genesis, hindcast vs measurements) the hindcast data base "NOAA WAVEWATCH III" has been used. This data base was obtained free from the NOAA ftp site.

Model Description. WAVEWATCH III [2.2] is a third generation wave model developed at NOAA/NCEP in the spirit of the WAM model. It is a further development of the model WAVEWATCH I, as developed at Delft University of Technology and WAVEWATCH II, developed at NASA, Goddard Space Flight Center. It nevertheless differs from its predecessors on all important points; the governing equations, the models structure, numerical methods and physical parameterizations.

WAVEWATCH III solves the spectral action density balance equation for wavenumber-direction spectra. The implicit assumption of these equations is that the medium (depth and current) as well as the wave field vary on time and space scales that are much larger than the corresponding scales of a single wave. Furthermore, the physics included in the model do not cover conditions where the waves are severely depth-limited. This implies that the model can generally by applied on spatial scales (grid increments) larger than 1 to 10 km, and outside the surf zone.

Model characteristics. We have used the global model which covers all the longitudes from 77°S to 77°N. The resolution is 1.25° (lon) x 1.° (lat). The minimum water depth considered is 25 meters. Each three hours five parameters are given for each point of the grid (Peak period, Significant wave height, Wave direction at the peak period, 10 meter wind speed, 10 meter wind direction).

The time period used in the project was the eight years 1995-2002.

Appendix 2.1: Ekoundou - Free standing conductor pipe

Position. 8 Deg 23' E - 4 Deg 17' N, Cameroon - immediate vicinity of the Nigerian border.

Water depth. Approximately 18 m (between 17 and 18.9 depending on source). The interface between water and mud is poorly defined and when the 101 m outer casing for the pipe was installed, it dropped for 29 m under its mere weight, and was driven for 47 additional m, thus giving 76 m in soil, 8 m in air, and 17 m in water.

Recording. 47616 samples at 20 Hz (about 40 min.), every 6 hours. Due to a software bug, recordings were in fact made at T, T+1h, T+6h, T=7h, T+12h, etc. The measurements were made between June 7th and July 18th, 1982. A serious breakdown occurred between June 17th and July 3rd, with no data for that period.

General conditions. The period was the "bad season", with significant wave heights up to nearly 2 meters. Most of the time, combinations of several swell components could be observed, from the SouthWest and South directions. Current was mostly tidal current, but local observers reported frequent sheared profiles, with waste rejected near the mudline surfacing upstream and coming back to the quarters platform.

Sensors.

- VEGA capacitive wave staff.

  A wave staff was installed between an outrigger at level -6 m and the small platform on top of the pipe. The outrigger is approximately in direction 195, and thus waves should not significantly be affected by the wake of the pipe since they come from the S to W directions. Measurement range: 0-10m; Nominal precision: 2% full scale; Operating frequency: 400Hz.

- Marsh Mc Birney 524M currentmeter.

  A currentmeter measuring horizontal wave particle velocities was installed on the same outrigger supporting the wavestaff, a small distance upstream. Its x-channel was heading towards the pipe ("Pipe North", 15 deg.) and the y-channel to the "Pipe West", 285 deg. direction. Measurement range: ± 3 m/s; Nominal precision: 2% full scale.

- SUNDSTRAND QA 1300 KA horizontal Linear accelerometers

  At the platform level (+8m) and in a box slightly above the mudline (-15.3 m). Directions opposite to the currentmeter: x towards 195, y towards 105.

- SYSTRON DONNER 4590 F angular accelerometers

  At the platform level (+8m) only.

- MAIHAK MDS 16 vibrating string strain-gauges

  At the same level as the "mudline" accelerometers (-15.3 m), every 90 degrees around the tube.

Appendix 2.2: WANE synthetic parameters

- Wind Direction (WD): From which the wind is blowing, clockwise from true north in degrees (meteorological convention). Winds are 1-hour averages of the effective neutral wind at a height of 10.0 meters.

- Wind Speed (WS): 1-hour average of the effective neutral wind at a height of 10.0 meters, units in meters/second.
- Total Variance of Total Spectrum (ETOT): The sum of the variance components of the hindcast spectrum, over the 552 bins of the 3G wave model, in meters squared.
- Peak Spectral Period of Total Spectrum (TP): Peak period is the reciprocal of peak frequency, in seconds. Peak frequency is computed by taking the spectral density in each frequency bin, and fitting a parabola to the highest density and one neighbour on each side. If highest density is in the 0.32157 Hz bin, the peak period reported is the peak period of a Pierson-Moskowitz spectrum having the same total variance as the hindcast spectrum.
- Vector Mean Direction of Total Spectrum (VMD): To which waves are travelling, clockwise from north in degrees (oceanographic convention).
- Total Variance of Primary Partition (ETOT1): The sum of the variance components of the hindcast spectrum, over the 552 bins of the 3G model, in meters squared. To partition sea (primary) and swell (secondary) we compute a P-M (Pierson-Moskowitz) spectrum, with a $\cos^3$ spreading, from the adopted wind speed and direction. For each of the 552 bins, the lesser of the hindcast variance component and P-M variance component is thrown into the sea partition; the excess, if any, of hindcast over P-M is thrown into the swell partition.
- Peak Spectral Period of Primary Partition (TP1): Peak period is the reciprocal of peak frequency, in seconds. Peak frequency is computed by taking the spectral density in each frequency bin, and fitting a parabola to the highest density and one neighbour on each side. If highest density is in the 0.32157 Hz bin, the peak period reported is the peak period of a Pierson- Moskowitz spectrum having the same total variance as the hindcast spectrum.
- Vector Mean Direction of Primary Partition (VMD1): To which waves are travelling, clockwise from north in degrees (oceanographic convention).
- Total Variance of Secondary Partition (ETOT2): The sum of the variance components of the hindcast spectrum, over the 552 bins of the 3G model, in meters squared.
- Peak Spectral Period of Secondary Partition (TP2): Peak period is the reciprocal of peak frequency, in seconds. Peak frequency is computed by taking the spectral density in each frequency bin, and fitting a parabola to the highest density and one neighbour on each side. If highest density is in the 0.32157 Hz bin, the peak period reported is the peak period of a Pierson-Moskowitz spectrum having the same total variance as the hindcast spectrum.
- Vector Mean Direction of Secondary Partition (VMD2): To which waves are travelling, clockwise from north in degrees (oceanographic convention).
- First and Second Spectral Moment of Total Spectrum (MO1, MO2): Following Haring and Heideman [2.1] the first and second moments contain powers of $\omega = 2\pi f$; thus:

$$M01 = \iint 2\pi f dS \qquad \textbf{(EQ 2.2)}$$

$$M02 = \iint (2\pi f)^2 dS \qquad \textbf{(EQ 2.3)}$$

  where dS is a variance component and the double sum extend over 360 bins.
- Significant Wave Height (HSIG): 4.000 times the square root of the total variance, in meters.

- Dominant Direction (DOMDIR): Following Haring and Heideman [2.1], the dominant direction ψ is the solution of the equations

$$A\cos(2\psi) = \iint \cos(2\theta\pi)\,dS \qquad \textbf{(EQ 2.4)}$$

$$A\sin(2\psi) = \iint \sin(2\theta\pi)\,dS \qquad \textbf{(EQ 2.5)}$$

  The angle ψ is determined only to within 180 degrees. Haring and Heideman choose from the pair (ψ,ψ+180) the value closer to the peak direction.

- Angular Spreading Function (ANGSPR): The angular spreading function (see Gumbel, Greenwood & Durand [2.3]) is the mean value, over the 552 bins, of cos(θ-VMD), weighted by the variance component in each bin. If the angular spectrum is uniformly distributed over 360 degrees, this statistic is zero; if uniformly distributed over 180 degrees, 2/π; if all variance is concentrated at the VMD, 1. For the use of this statistic in fitting an exponential distribution to the angular spectrum, see Pearson & Hartley [2.4].
- In-Line Variance Ratio (INLINE): called directional spreading by Haring and Heideman, [2.1], p 1542. Computed as:

$$r = \frac{\iint \cos^2(\theta - \psi)\,dS}{\iint dS} \qquad \textbf{(EQ 2.6)}$$

  If spectral variance is uniformly distributed over the entire compass, or over a semicircle, r = 0.5; if variance is confined to one angular band, or to two band 180 degrees apart, r = 1.00 . According to Haring and Heideman, $\cos^2$ spreading corresponds to r = 0.75 .

Appendix 2.3: WANE frequency bands

Frequency bins are spaced in geometric progression to facilitate the computation of interactions. The nominal frequency is the geometric mean of the two ends (see Table 2.3 below). The frequency ratio is $0.75^{-1/3}$, i.e. 1.100642416; this ratio was chosen in preference to the 1.1000 of official WAM to simplify interaction formulas. The first 22 bins are straightforward; the last requires explanation. The 23rd frequency band is an integrated band comprising what would be bins 23 through 44 (continuing the geometric progression) of a fully discrete bin system.

TABLE 2.3 : Frequency bands

#	nom. freq	left end	right end	bandwidth
1	0.0390000	0.0371742	0.0409155	0.0037413
2	0.0429251	0.0409155	0.0450333	0.0041178
3	0.0472451	0.0450333	0.0495656	0.0045323
4	0.0520000	0.0495656	0.0545540	0.0049884
5	0.0572334	0.0545540	0.0600444	0.0054904
6	0.0629935	0.0600444	0.0660874	0.0060430
7	0.0693333	0.0660874	0.0727386	0.0066512
8	0.0763112	0.0727386	0.0800592	0.0073206
9	0.0839914	0.0800592	0.0881166	0.0080574
10	0.0924444	0.0881166	0.0969849	0.0088683
11	0.1017483	0.0969849	0.1067457	0.0097608
12	0.1119885	0.1067457	0.1174888	0.0107431
13	0.1232593	0.1174888	0.1293131	0.0118244
14	0.1356644	0.1293132	0.1423275	0.0130144
15	0.1493180	0.1423275	0.1566517	0.0143242
16	0.1643457	0.1566517	0.1724175	0.0157658
17	0.1808858	0.1724175	0.1897700	0.0173525
18	0.1990906	0.1897700	0.2088690	0.0190989
19	0.2191276	0.2088690	0.2298900	0.0210211
20	0.2411811	0.2298900	0.2530267	0.0231367
21	0.2654541	0.2530267	0.2784919	0.0254652
22	0.2921701	0.2784919	0.3065200	0.0280281
23	0.3215748	0.3065200	2.5274134	

References

[2.1] Haring, R.E., Heideman, J.C., 1978, "Gulf of Mexico rare wave return periods", *Proc. 10th Offshore Tech. Conf.*, OTC 3230, pp. 1537-1550.

[2.2] Tolman, H.L., 1999, "User manual and system documentation of WAVEWATCH-III version 1.18", *NOAA/NWS/NCEP/OMB Technical Note 166*, p. 110.

[2.3] Gumbel, E.G., Greenwood, J.A., Durand, D., 1953, "The circular normal distribution: Theory and tables", *American Statistical Society Journal*, vol. 48, pp. 131-152.

[2.4] Pearson, E.S., Hartley, H.O., "Biometrika Tables for Statisticians", Cambridge University Press.

CHAPTER 3

Swell Genesis

Michel Olagnon
Marc Prevosto

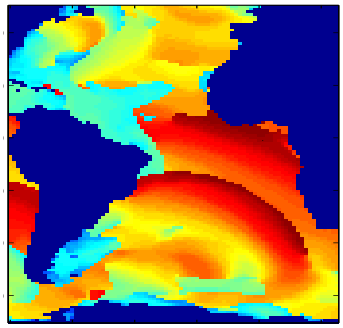

South swells: During the months of May through October, swells generally approach West African coast from the south to south-westerly direction. These swells are generated by storms in the South Atlantic mainly between 40°S and 60°S. South Atlantic swells, travel sometimes thousands of miles across the ocean before breaking along the West African coast and can produce sea-states up to 7 meters in the South (Namibia) to 4 meters in Angola and 3 meters close to the equator.

Northwest swells: During the months of October through April, swells approach West African coast from the north-westerly directions. These swells are generated by big storms that blow off North America and travel first across the North Atlantic Ocean and secondly across the South Atlantic. The wave heights of these swells are obviously lower than for the south swells, with significant wave up to 0.5 meters. The locations far north, from Côte d'Ivoire to Cameroon are sheltered for these swells.

Statistics of monthly significant wave height of the sea-states calculated from the 15 years of WANE hindcast is given in figure 3.1 for a point close to Congo. The other plots are given in Appendix 3.1.

FIGURE 3.1 : Sea-state Hs, WANE hindcast 26099

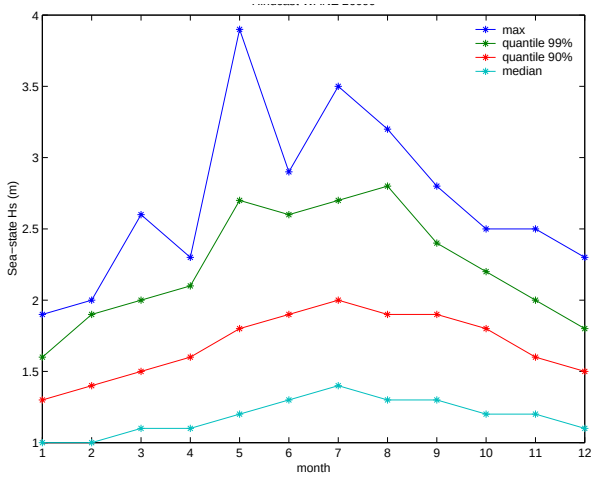

The presence of the North-West swells is very clear on the plotting of joint occurrences T01-Direction of the wave systems. See for example the case of the Angola location (Figure 3.2). Obviously, the number of sea-states with N-W swell systems is very low (several hundreds during 15 years) and if we look at the joint occurrences Hs-Direction (Figure 3.3), we observe that they correspond to very low Hs. The same plots for the other locations are given in Appendix 3.2.

FIGURE 3.2 : Joint occurrence T01-Direction

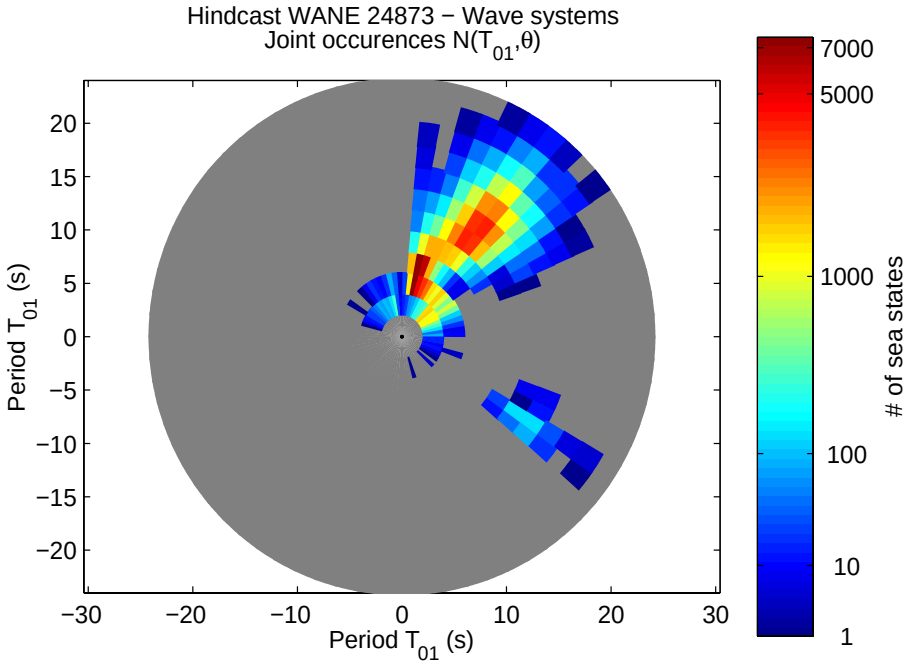

FIGURE 3.3 : Joint occurrence Hs-Direction

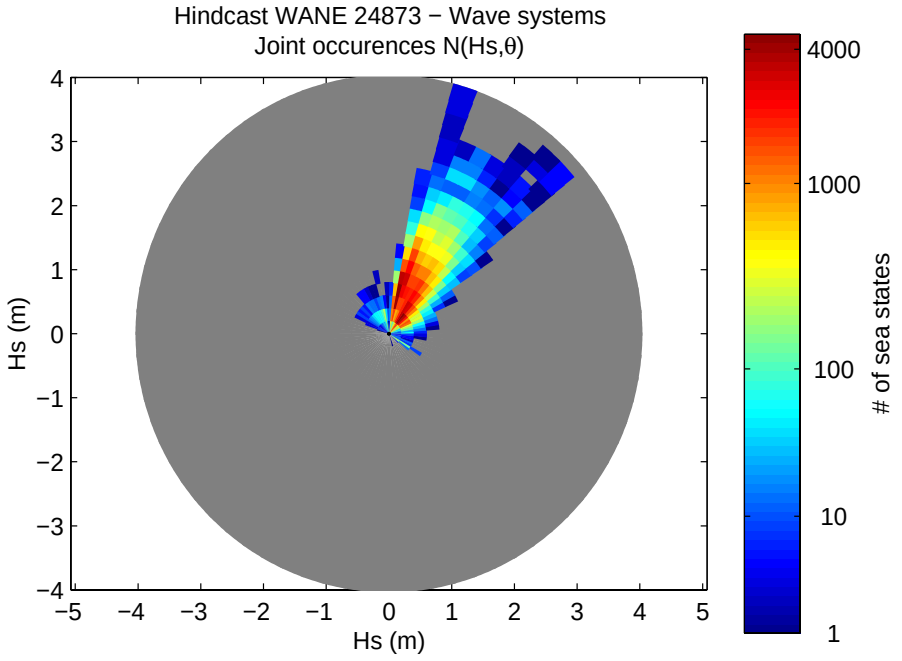

In the sequel of this chapter we first analyse more precisely some typical situations of swell. In a second part we study the process of generation and propagation of the swell what permits to give a model for the shape of the swell spectra.

Typical situations of swell

Three typical situations have been extracted from the NOAA hindcast data base, focusing on the Angola point.

- the biggest South-South-West swell system (Hs=4 meters), completed with a South-West example;
- the biggest 3 wave systems (2 examples are given);
- the biggest North-West swell system (Hs=0.3 meters).

For each of these situations an animation has been constructed which shows dynamically the process of generation and propagation of the swell thanks to the movie of the time evolution of the sea-state field of the Atlantic. These movie are furnished as AVI files on a CD-ROM which accompanied this report.

Illustrations

Some static information about these typical situations are given hereafter.
First the sea-state field of the Atlantic at a date of interest (call afterwards "date of analysis") is given (Figures 3.4, 3.7, 3.10 and 3.13). They show on the left, the Hs, focusing on the highest values, and on the right the peak period, focusing on the long waves. As it is a peak period, when we observe a front of swell at 15s as in Fig. 3.4, it is obvious that before this front arrived longer waves corresponding to the same swell propagation, but with a spectral peak amplitude lower than the global peak of the sea-state spectrum corresponding to a swell that have already arrived.

Secondly, the time evolution of the triplet (Hs, Tp, Direction) for each wave system of the sea-states at a chosen location (here the Angola point) is plotted, from several days before the "date of analysis" of the sea-state field to just after (Figures 3.5, 3.8, 3.11 and 3.14, black arrows). The wave systems come from the partitioning of the directional spectra of WANE Operational hindcast (see Chapter 6). The "date of analysis" is indicated by two blue dash-dotted lines. The peak period, in ordinate, is given by the dot of the arrows, the Hs by the length of the arrows (the scale is given top-left by the maximum Hs of the figure), the direction by the direction of the arrows. Moreover, a theoretical wind-sea calculated from the local wind used in the WANE Operational hindcast is given by red arrows (Eqs. 3.1-3.2). The model comes from Carter [3.1] and corresponds to a duration-limited sea.

$$Hs = 0.0146 D^{5/7} U^{9/7} \qquad \textbf{(EQ 3.1)}$$

$$T_m = 0.54 D^{3/7} U^{4/7} \qquad \textbf{(EQ 3.2)}$$

with U the wind speed in m/s, and D the duration of the wind in hours. Here an empirical choice of 18 hours has been made for D. The direction of the wind-sea is put to the direction of the wind.

Finely the point and directional spectra corresponding to the "date of analysis" are given in Figs. 3.6, 3.9, 3.12 and 3.14.

South-South-West swell. The biggest Swell (in Hs) encountered during the 8 years of the NOAA data base is a south-south-west swell. It has not been generated by the biggest storms of the South Atlantic, but by a "moderate" storm (Hs~8m) closer to the West coast of Africa. It is a very pure swell (see Fig. 3.6) with a mild slope in high frequencies, due to the vicinity of the storm. It could be called a "young swell". See the animation HsTP_SSO.avi.

South-West swell. This is an example of a South-West swell generated by a very severe storm. A storm travelling from West to East between 40° and 50° West latitudes, is now South of Africa. All along its travel, with first a Hs of 13m close to South America which decreased to 8m South of Africa. The first waves of this swell begin to appear at the end of the historic (Fig. 3.5), with very long periods (25s). Meanwhile this swell did not generate later Hs higher than 2.2m. The process of generation is very clear on the animation. See the animation HsTP_SO.avi.

Mutiple swells. We have selected two examples of multiple wave systems. The first sea-state (figs. 3.7-3.9) is composed of very long waves (Tp=22s), the first waves of the last South Pacific storm, a second swell system (Tp=15s), and a last one (Tp=6s) which seems to be a wind sea when considering its time evolution and comparing to a theoretical wind sea coming from model (Eqs. 3.1-3.2). See the animation HsTP_3S1997.avi.
The second situation (figs. 3.10-3.12) is also clearly with three wave systems, but here, the one with the shortest waves (Tp=7s) seems, looking at the time history of the peak period, to be the tail of one of the swells propagating from South-West. Perhaps mixed with a wind sea. See the animation HsTP_3S1998.avi.

North-West swell. During winter, some North Atlantic storms generate swell sufficiently powerful to travel until the West African coast (see Fig. 3.13). Some locations are sheltered from this swell (see the diagrams of appendix 3.2 for details). During the 8 years of the NOAA data base, the biggest Hs corresponding to these swells was 0.3m. Of course these swell are much less severe than the South swell, but they arrive abeam to floating systems oriented to the main swell directions. We have here again an example of superposition of three to four wave systems. See the animation HsTP_NO.avi.

These five examples illustrate the diversity of the situations (type and number of wave systems, Hs, period, direction) and show the difficulty of a fine statistical description of the swell climatology in West Africa.

List of appendices: WANE Operational Data

Appendix 3.1: Monthly Sea-state Significant Wave Height

Appendix 3.2: Wave systems, Hs-Dir & T01-Dir joint occurrence

FIGURE 3.4 : South-South-West swell system, oceanic wave field.

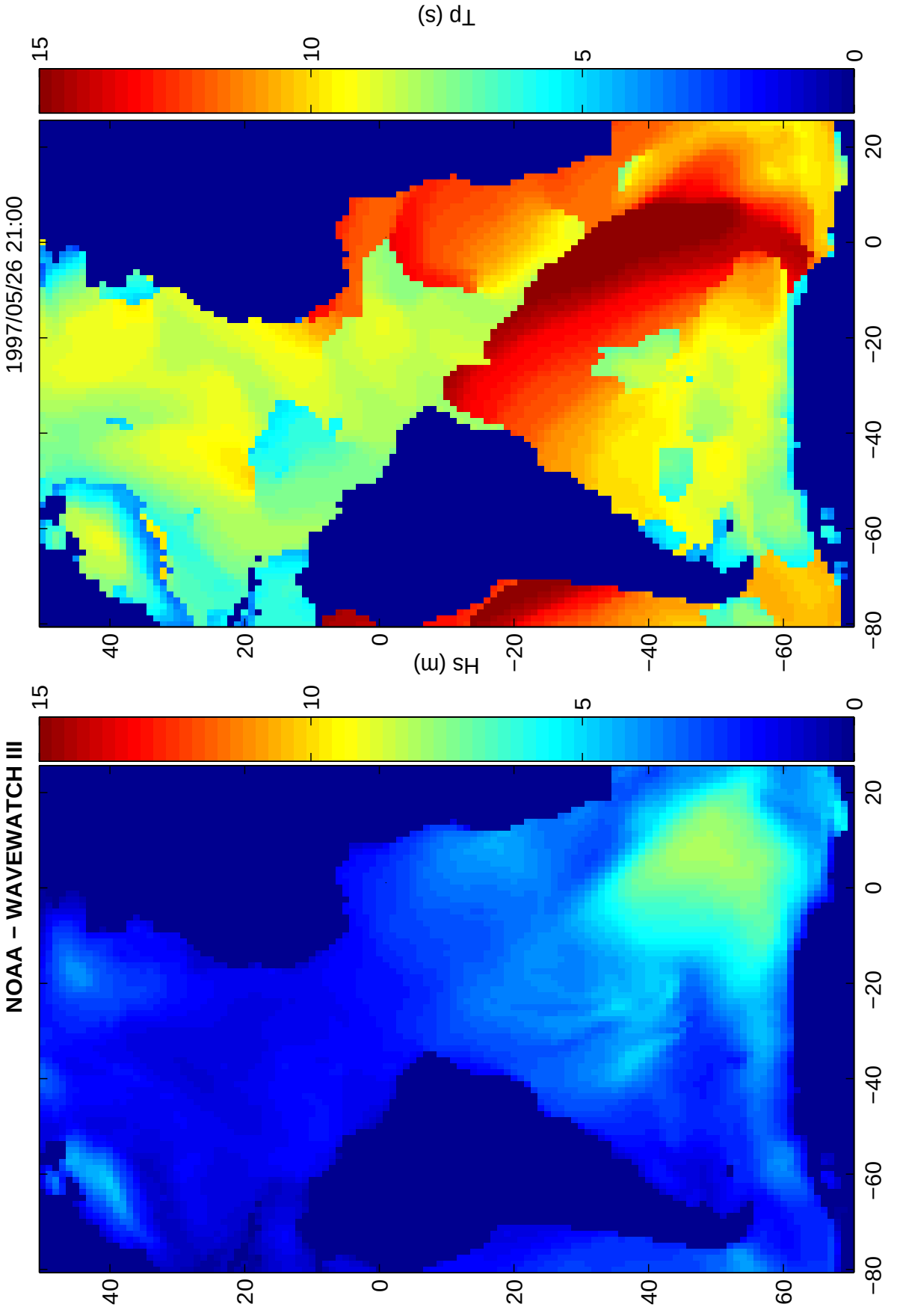

FIGURE 3.5 : South-South-West swell system, history of wave systems.

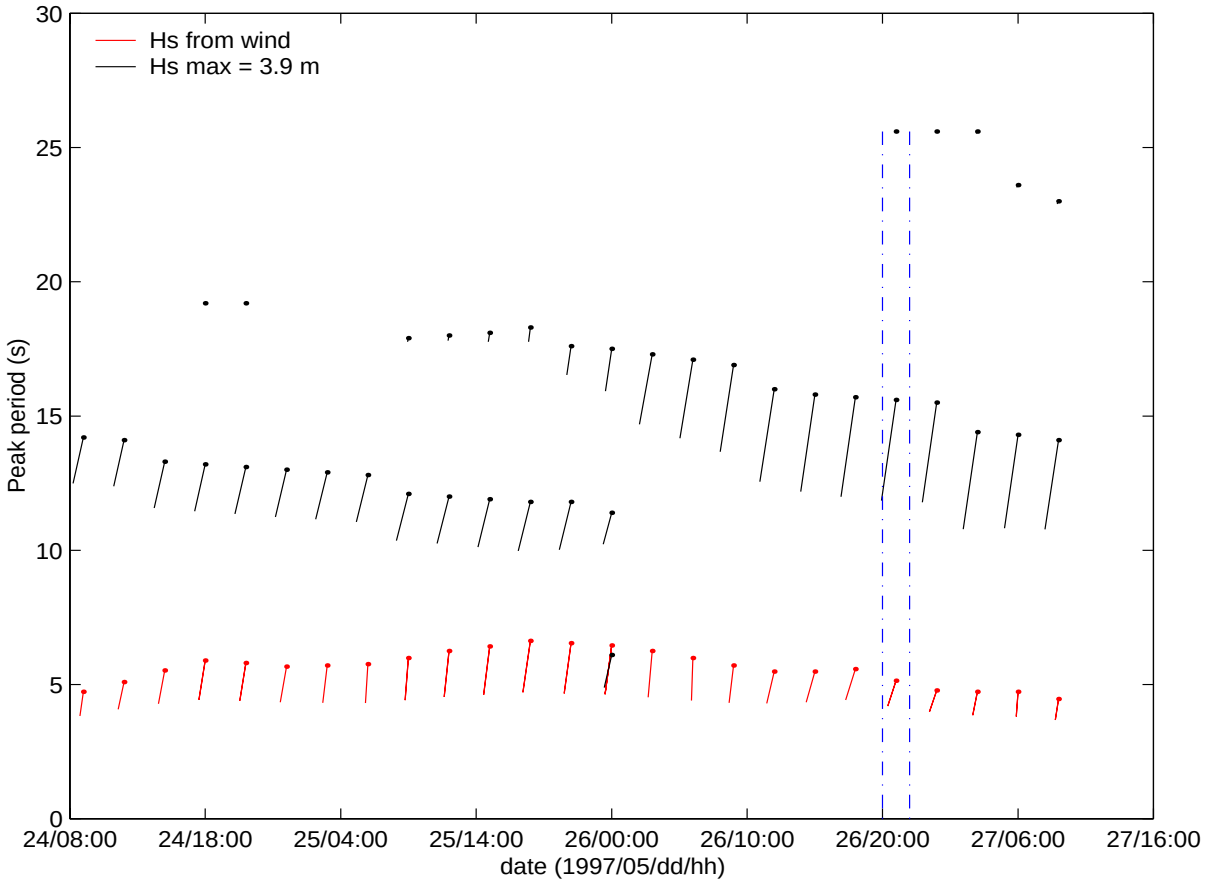

FIGURE 3.6 : South-South-West swell system, directional and point spectra.

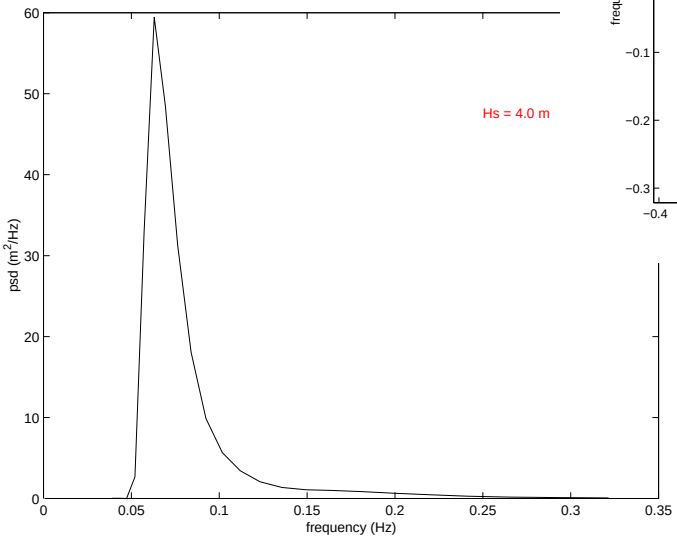

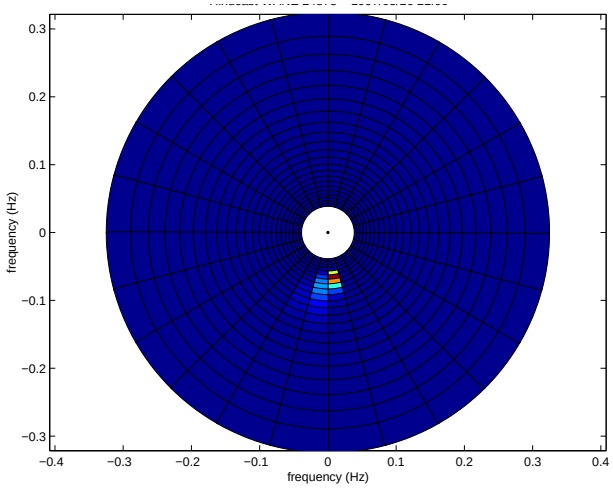

FIGURE 3.7 : **Multiple swell system, 1997, oceanic wave field.**

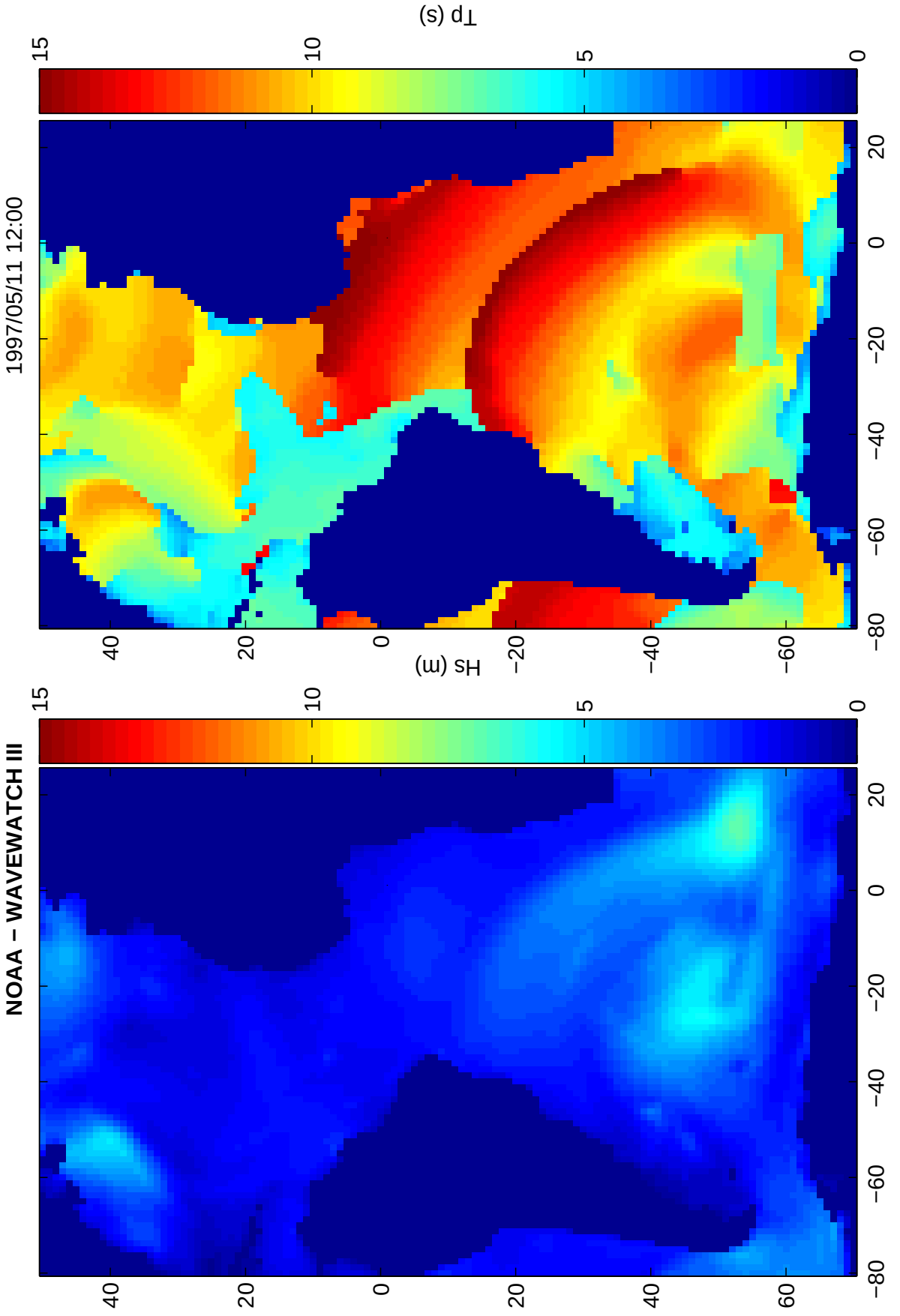

FIGURE 3.8 : Multiple swell system, 1997, history of wave systems.

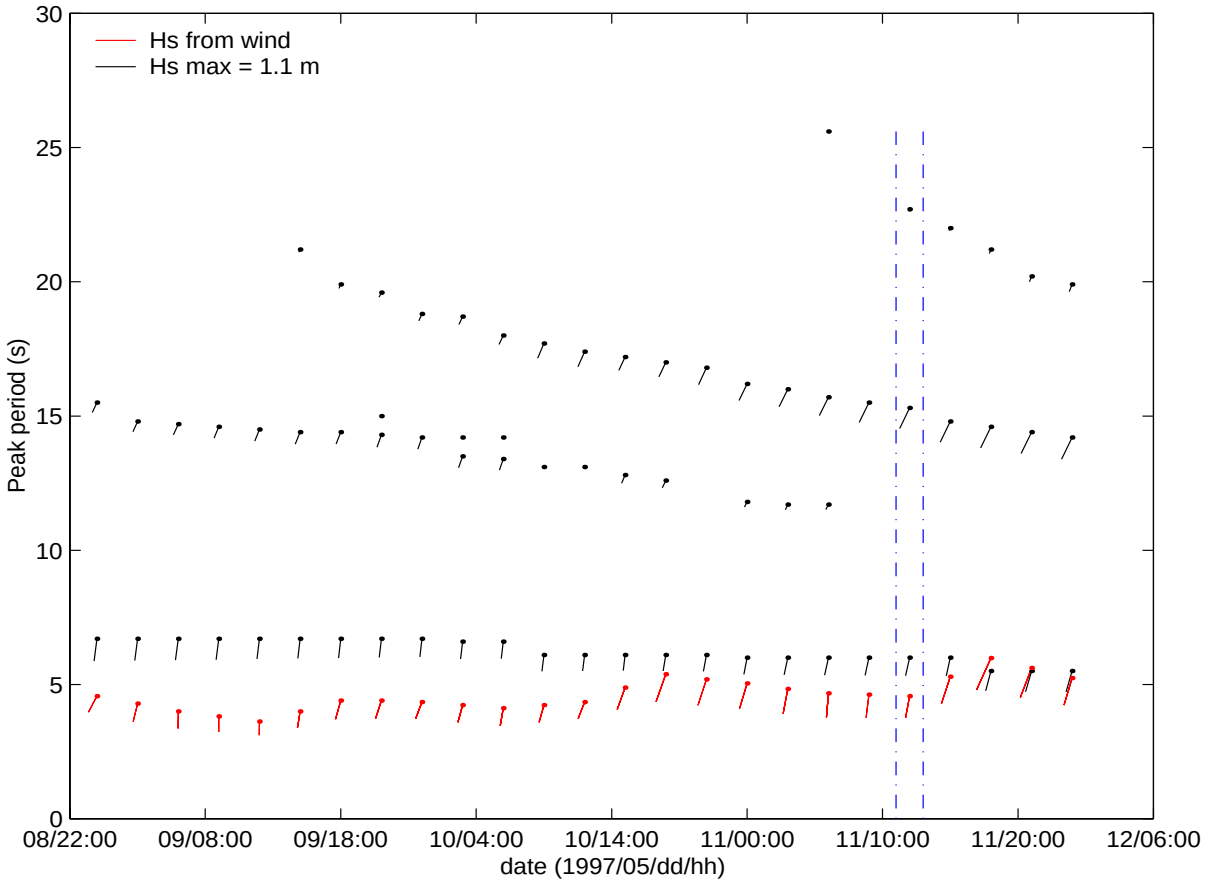

FIGURE 3.9 : Multiple swell system, 1997, directional and point spectra.

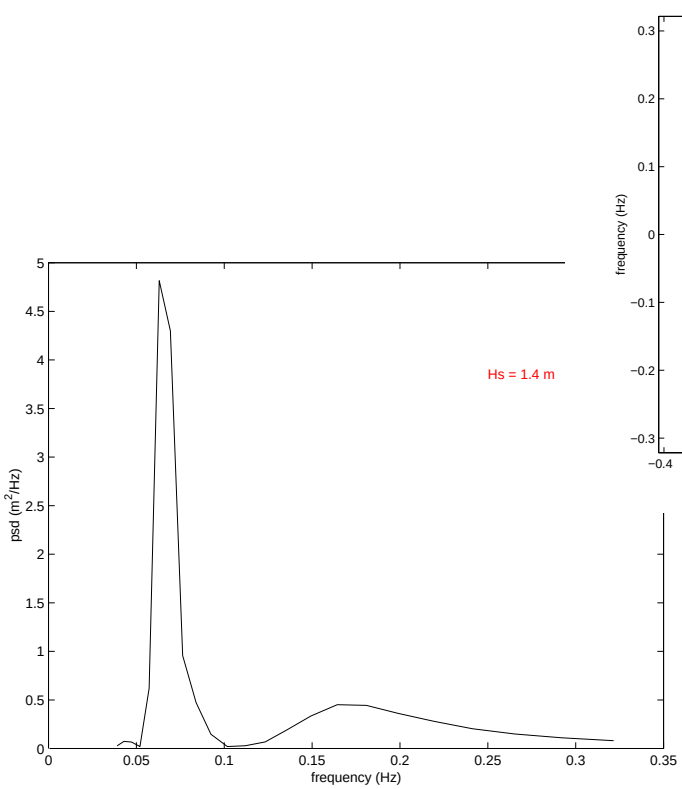

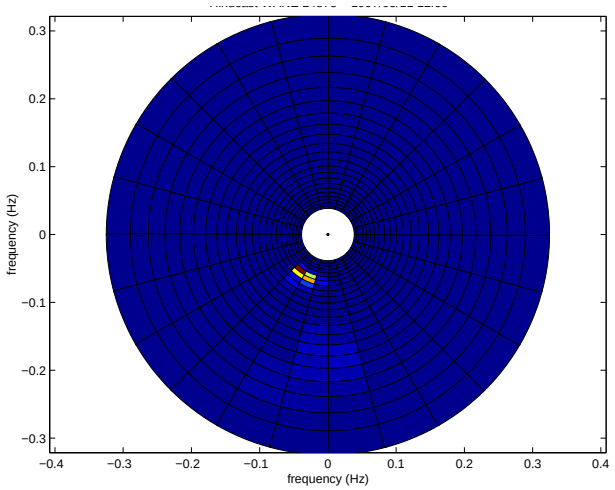

FIGURE 3.10 : **Multiple swell system, 1998, oceanic wave field.**

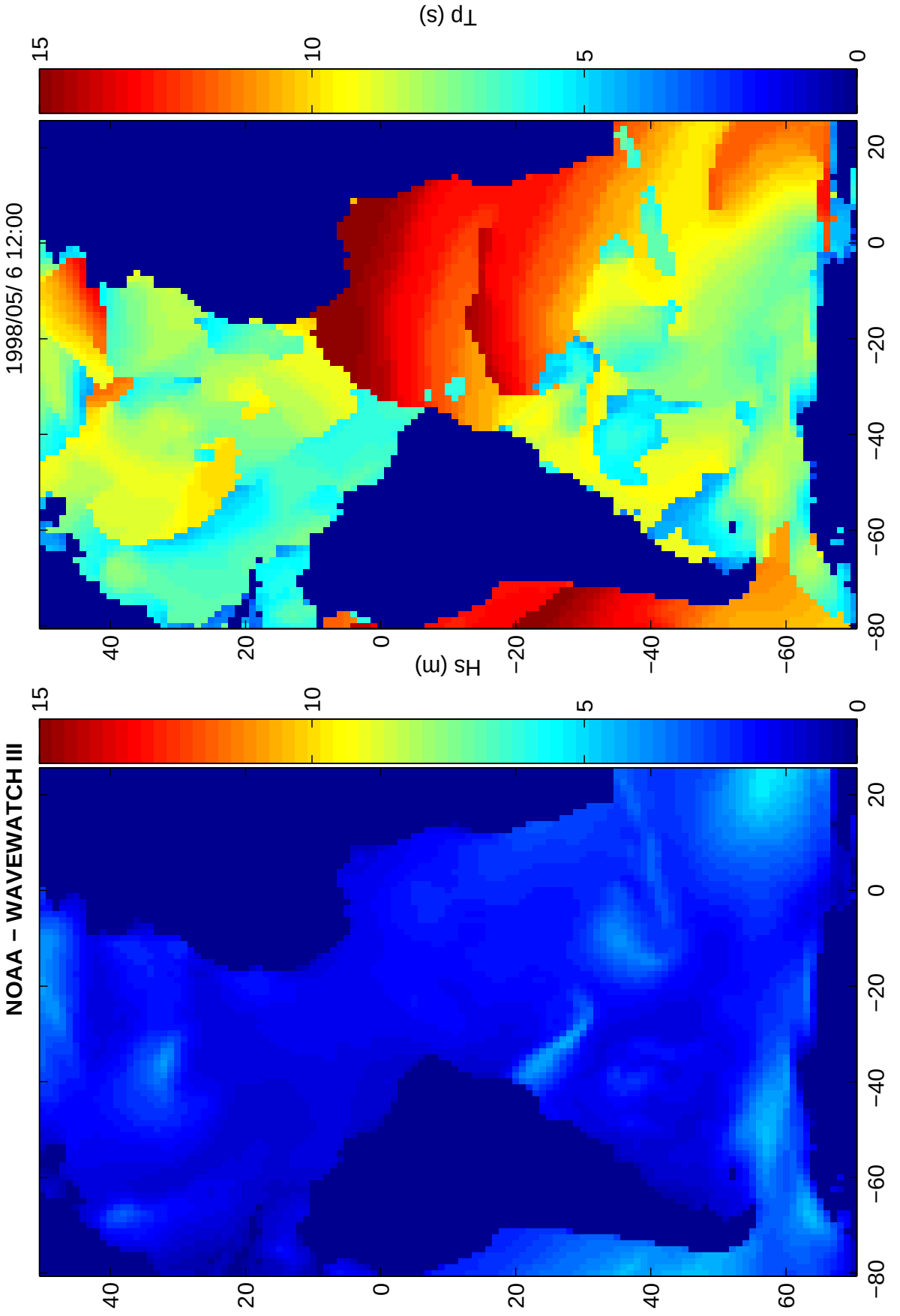

FIGURE 3.11 : Multiple swell system, 1998, history of wave systems.

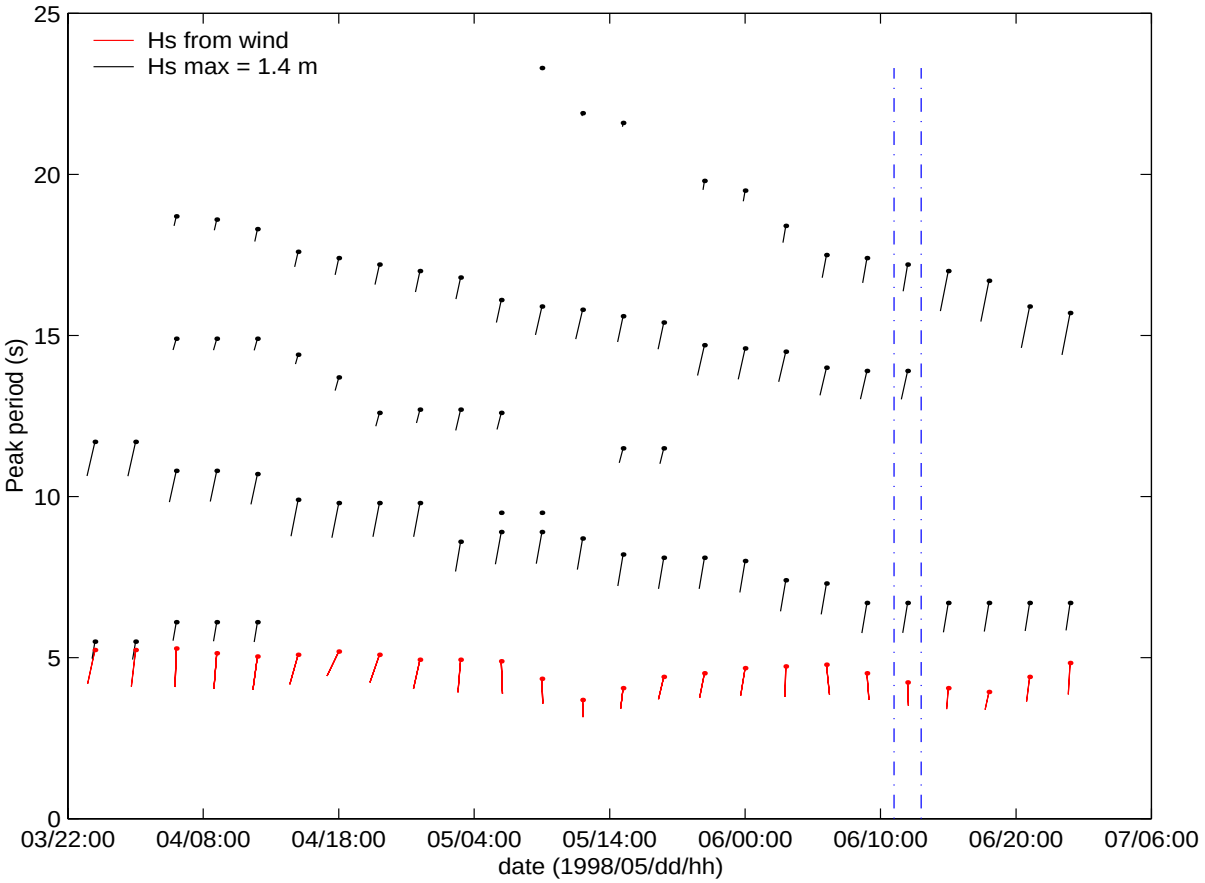

FIGURE 3.12 : Multiple swell system, 1998, directional and point spectra.

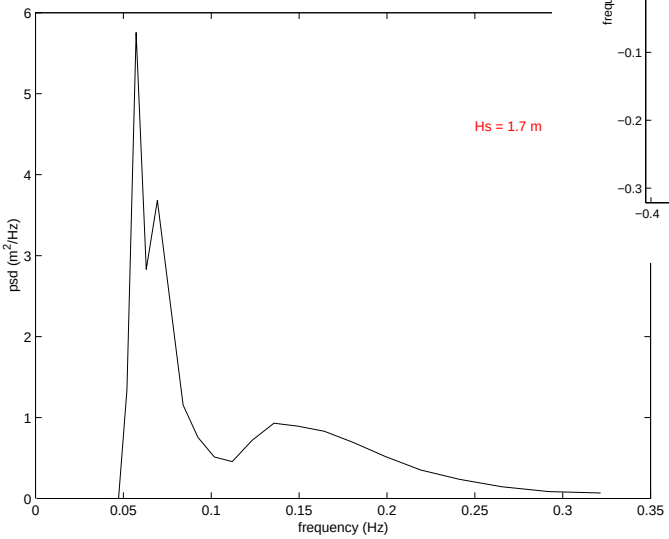

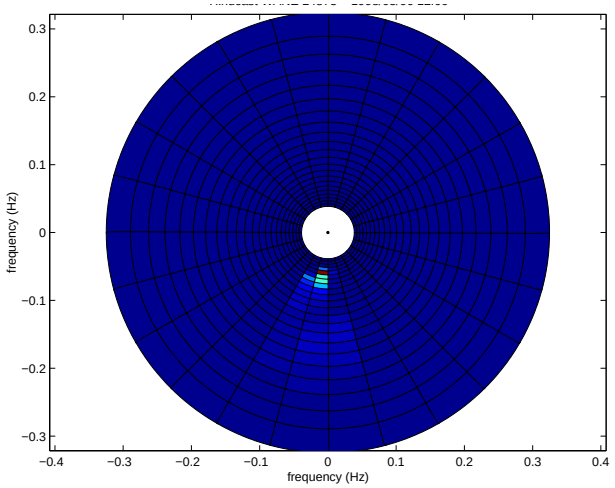

FIGURE 3.13 : North-West swell system, oceanic wave field.

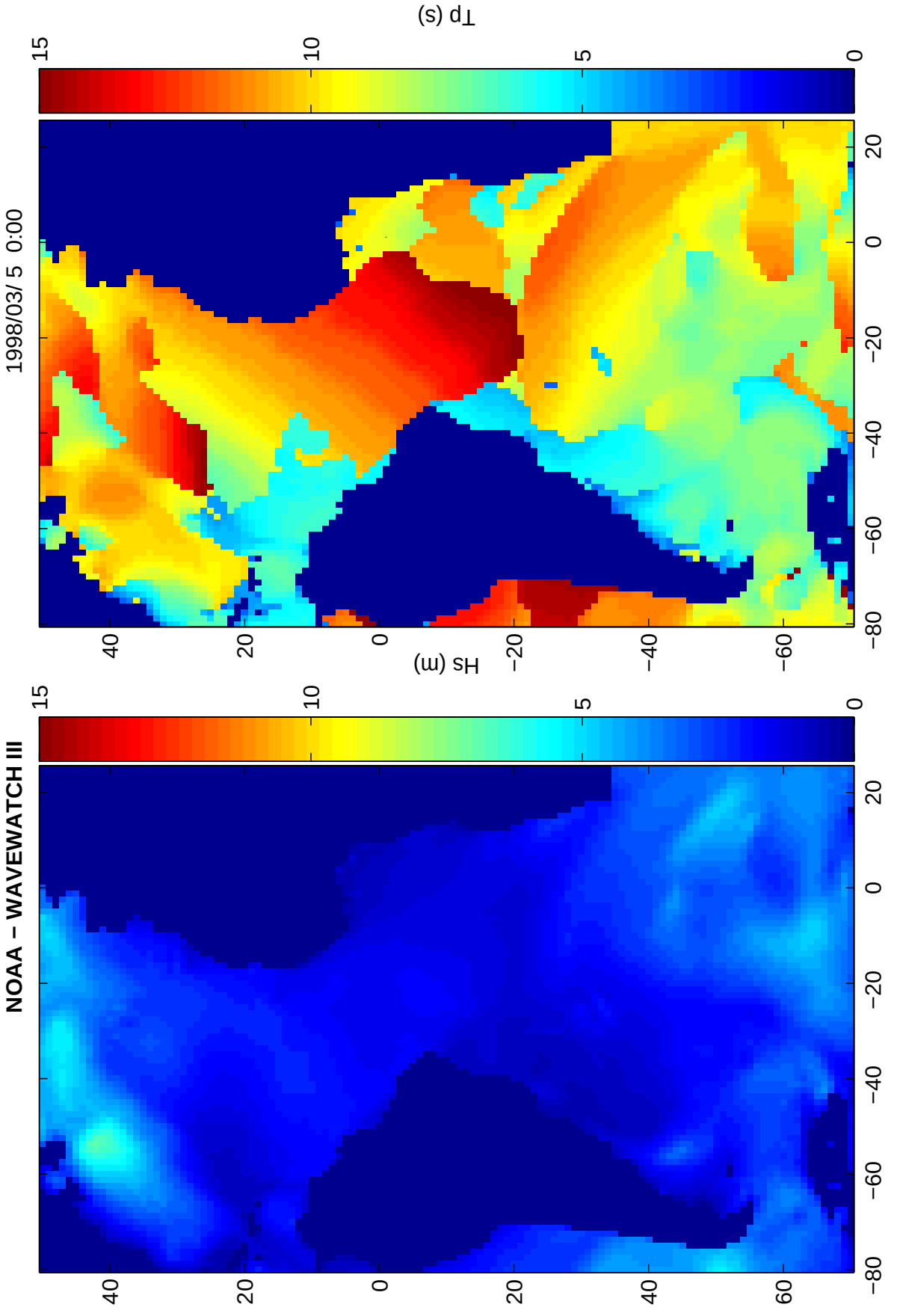

FIGURE 3.14 : North-West swell system, history of wave systems.

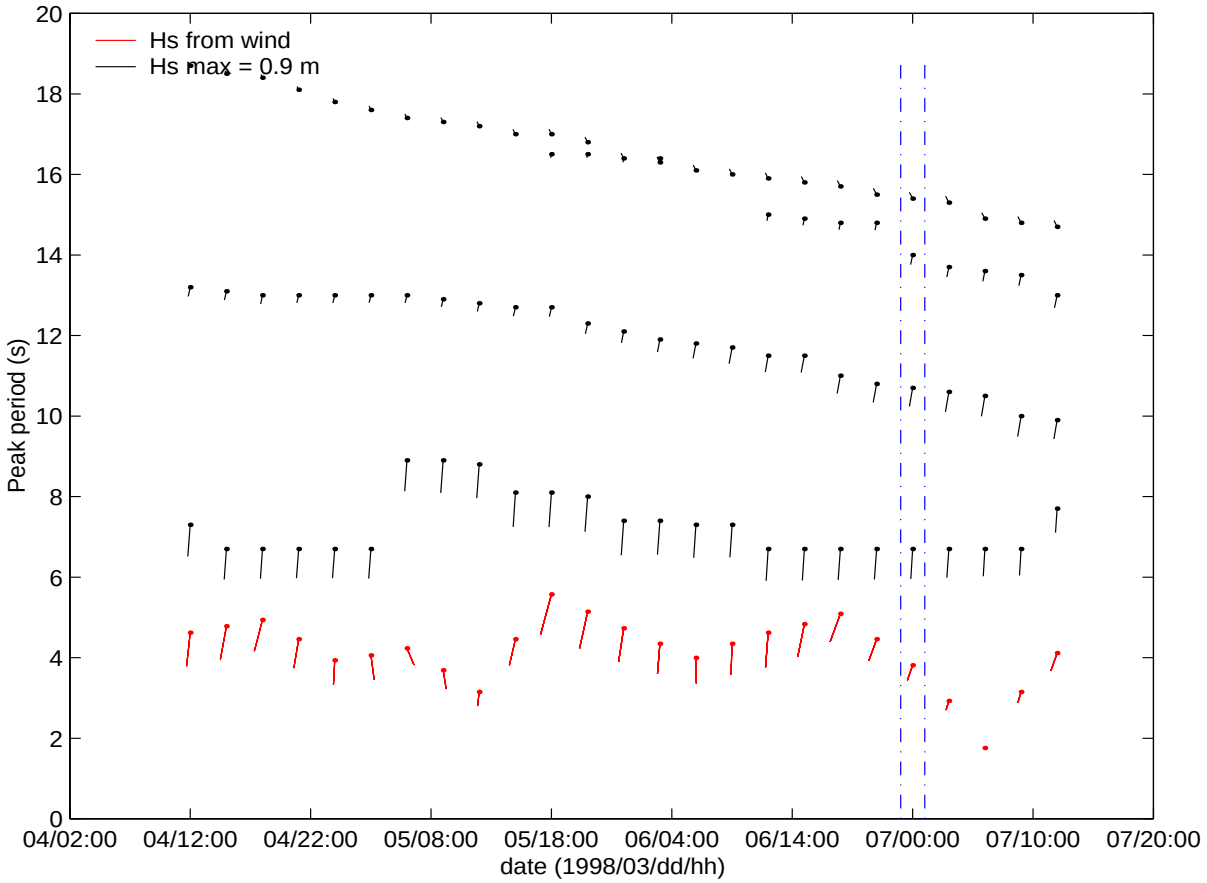

FIGURE 3.15 : North-West swell system, directional and point spectra.

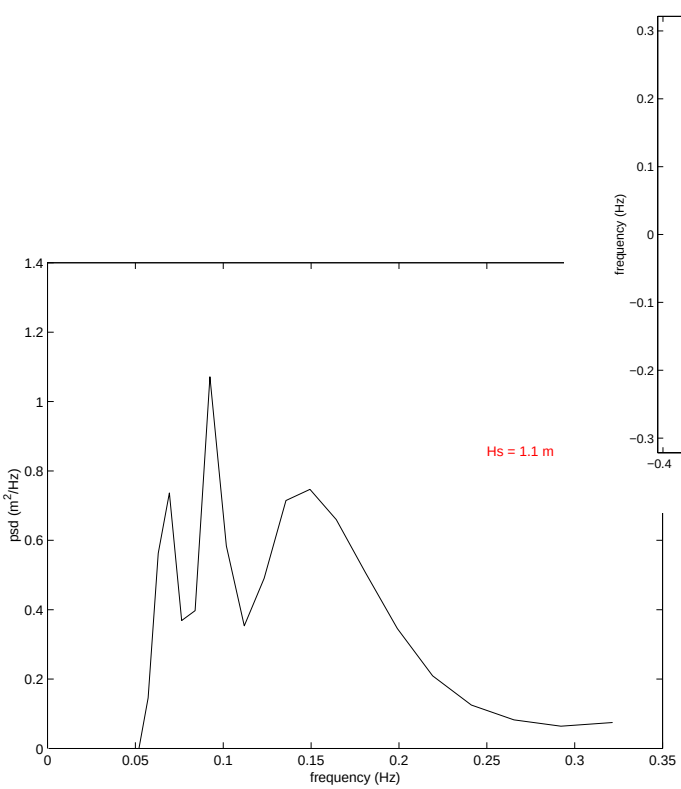

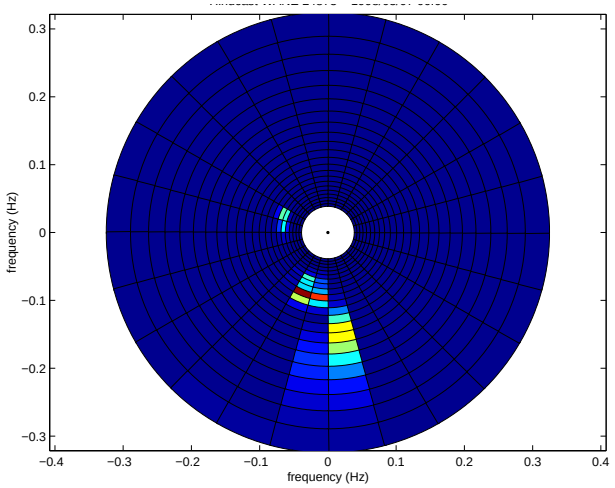

Swell spectrum shape generation

Swell of a given (large) period is generated in some area within a storm where the fetch and storm duration have been sufficiently large, and then propagates onto the observation point.

FIGURE 3.16 : Generating area at a given instant versus distance

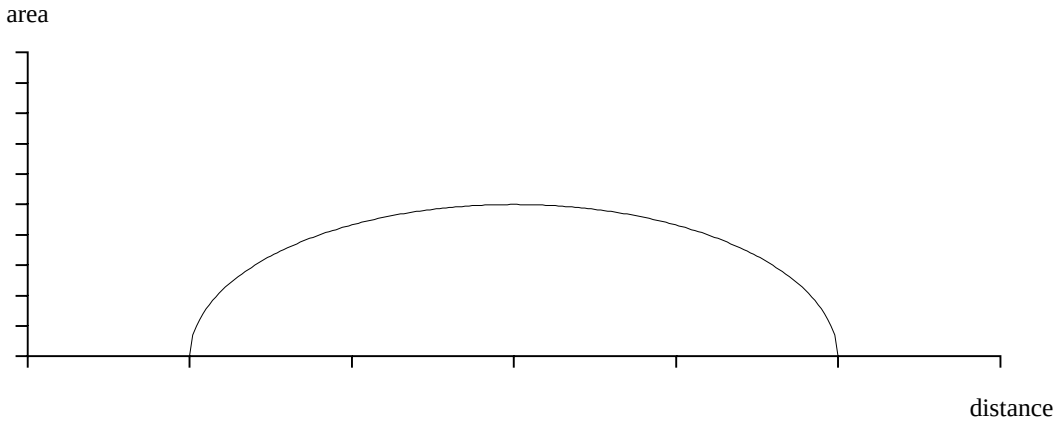

If one examines the significant wave height maps that can be found in forecasts or in observations, wave height as a function of location exhibits conical "hills" at storms. The same "triangle" shape is used by several authors to model the time-history of storms, for instance Y.Tomita or C.Cooper.

Since it is realistic to assume that for a given large period, swell builds up when the overall significant wave height has reached a sufficient threshold, *i.e.* for the top part of the conical hill, the area where swell is generated will have an approximately circular shape. Assuming that circular shape for the generation area at any given instant, its size will be distributed with distance to a far away observation point according to the nearly elliptical shape of figure 3.16.

Let us try to figure out the time histories of the far and near boundaries of generation for swell with periods close to T_0 that will be reaching the observation point at a given instant, in the case of a storm the centre of which is staying at a constant distance of the observation point while it grows, lives and decays.

Wave celerity is proportional to the wave period. Swell with periods around T_0 originating from the storm and reaching the observation at time τ=0 will thus have been generated at an earlier time $\tau_d(T_0) = -\frac{4\pi D}{gT_0}$ where D is the distance from the storm to the observation point.

Waves generated when the storm starts to build up at $\tau=-\tau_s$ can only reach the observation point at time τ=0 if their period is about $T_t(\tau_s, D) = \frac{4\pi D}{-g\tau_s}$. At first, waves have a very short period so that $T_t(\tau_s,D)$ is not reached for waves at any location within the storm. At some point in time, the storm growth will be sufficient for the period of the longest waves to catch up with the threshold period (that is increasing also with time).

From that time on, the far away limit for the generation area will be driven by two opposing factors: on one hand, waves will be generated with longer periods over a larger area, due to the increase in the duration of wind effect, so the limit should move away from the observation point, but on the other hand, moving the limit

windwards reduces the fetch length for waves at that limit. For some time, the limit will be able to accommodate the increase of the threshold period $T_t(\tau,D)$ with τ even though some fetch reduction occurs as the distance D to observation point grows moderately. Then, at some time, saturation will be reached given the fetch and the wind speed and duration, and it will not be possible to have any further increase in periods. In addition, the storm will start to decay and the wind speed will no longer be sufficient to generate periods even only as large as previously. The far away limit will thus move swiftly closer to the observation point, so as to increase fetch and to reduce the threshold period $T_t(\tau,D)$.

FIGURE 3.17 : Generating area limits over time for swell propagating to the origin

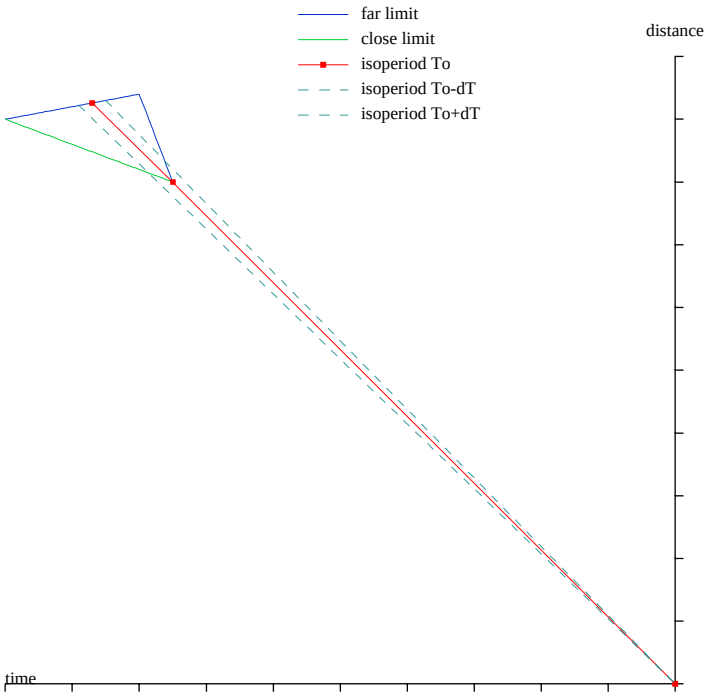

The evolution of the closest limit will be governed by the storm geographical extent in the direction of the observation point. Increased fetch and duration of wind effect will join to help match the threshold period $T_t(\tau,D)$, until one is sufficiently on the border of the storm for the wind to decrease. The limit will thus complete the triangle of figure 3.17. It should be noted that if the distance of the storm to the observation point were to vary, the triangle should be skewed accordingly.

Energy observed at the origin at a given individual period will have been collected along an isoperiod line (see figure 3.17) such that the time spent since generation corresponds to the distance travelled by a wave of that period.

Using the above simplified model, a calculated spectral shape for swell is given on figure 3.18. That shape is not available as a closed form formula, and may vary according to the original assumptions. Yet, it is noteworthy that it takes non-zero values only within a bounded frequency interval.

Also, a simple triangle, slightly asymmetrical, represents a realistic approximation to that shape. In the same way, a Log-normal shape might be used, and preferred to a Gaussian, symmetrical, one.

FIGURE 3.18 : Calculated spectral shape for swell

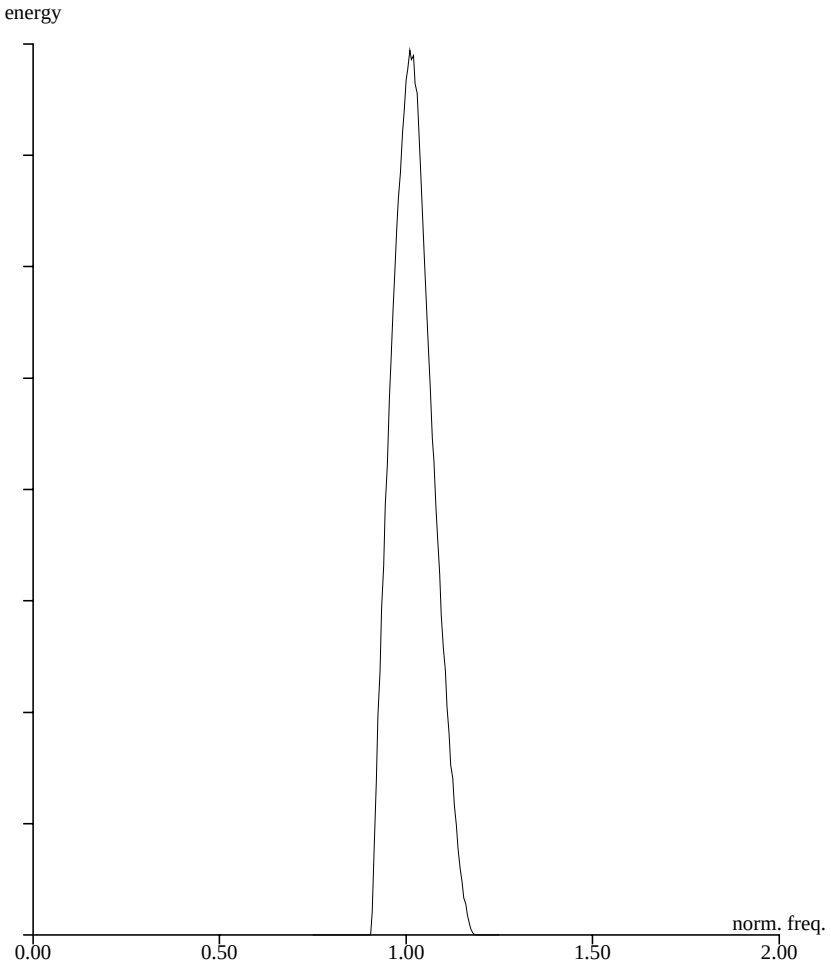

References

[3.1] Carter, D.J.T., 1982, "Prediction of wave height and period for a constant wind velocity using the Jonswap results", *Ocean Engineering*, vol. 9, pp. 17-33.

CHAPTER 4

Models of spectral shapes

Kevin Ewans
Michel Olagnon

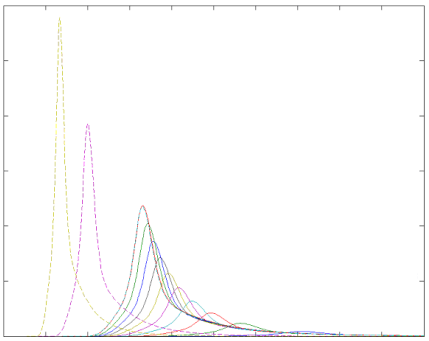

This chapter deals with item 3. of the WASP scope of work: *Shape of the Swell Peak in the Power Spectrum*. The idea is to characterize spectra by a small number of parameters from which the whole spectral shape can be precisely reconstructed, and to carry out climate statistics on those parameters, so as to enable the fatigue and extreme design analyses of structures sensitive to swell.

Several studies have shown the limitations of conventional spectral shapes when it comes to swell.

General

A sea-state can be described in terms of its frequency-direction spectrum, $S(f, \theta)$, by the following model.

$$S(f, \theta) = G(f)H(f, \theta) \qquad \textbf{(EQ 4.1)}$$

where

$$G(f) = \int_0^{2\pi} S(f, \theta)d\theta \qquad \textbf{(EQ 4.2)}$$

is the power or variance density spectrum, and $H(f, \theta)$ is the directional distribution, which has the properties.

$$H(f, \theta) \geq 0$$

$$\int_0^{2\pi} H(f, \theta)d\theta = 1 \qquad \textbf{(EQ 4.3)}$$

We can further define the directional distribution, $D(\theta)$, as

$$D(\theta) = \int_0^{\infty} S(f, \theta) df \qquad \text{(EQ 4.4)}$$

The frequency-direction spectrum can be written in terms of the components

$$S(f, \theta) = \sum_i^n S_{swell_i}(f, \theta) + S_{sea}(f, \theta) \qquad \text{(EQ 4.5)}$$

In turn, the frequency-direction spectrum of the i^{th} swell component can be written (dropping the subscript i for convenience as:

$$S_{swell}(f, \theta) = G_{swell}(f) H_{swell}(f, \theta) \qquad \text{(EQ 4.6)}$$

with the following definitions

$$G_{swell}(f) = \int_0^{2\pi} S_{swell}(f, \theta) d\theta$$

$$D_{swell}(\theta) = \int_0^{\infty} S_{swell}(f, \theta) df \qquad \text{(EQ 4.7)}$$

Spectral models

Conventional models

The most common spectral models used for engineering are essentially the Pierson-Moskowitz one:

$$\alpha \frac{g^2}{(2\pi)^5} f^{-5} e^{-\frac{5}{4}\left(\frac{f}{f_p}\right)^{-4}} \qquad \text{(EQ 4.8)}$$

that is often found more convenient under the form recommended by the ISSC:

$$0.11087 \frac{H_s^2}{T_z^4} f^{-5} e^{-0.44336 \frac{f^{-4}}{T_z^4}} \qquad \text{(EQ 4.9)}$$

and the one that was obtained by modifying it to represent the more narrow-banded sea-states of the North Sea in the JONSWAP project after which it was named:

$$\alpha \frac{g^2}{(2\pi)^5} f^{-5} e^{-\frac{5}{4}\left(\frac{f}{f_p}\right)^{-4}} \gamma \; exp\left(-\frac{\left(1 - \frac{f}{f_p}\right)^2}{2\sigma^2} \right) \qquad \text{(EQ 4.10)}$$

with σ set to 0.07 for the ascending part of the spectrum ($f \le f_p$) and 0.09 for the descending part ($f \ge f_p$).

Another generalized form of the Pierson-Moskowitz spectrum, or of the Wallops spectrum, is:

$$C\frac{H_s^2}{f_p}\left(\frac{f}{f_p}\right)^{-p} e^{-\frac{p}{q}\left(\frac{f}{f_p}\right)^{-q}} \qquad \text{(EQ 4.11)}$$

This last formulation allows, by choosing high values for q, to come close to the maximum steepness, triangular spectrum described in Olagnon & Krogstad (1998) [4.11]. When q is set to 4, it is the Wallops spectrum.

The need for models for spectra with two peaks has been recognized for many years, and several authors have suggested two-peaked models: Ochi & Hubble (1976) [4.10], Guedes Soares (1984, 1992) [4.3,4.4] or Torsethaugen (1993, 1996) [4.16,4.17] for instance. Those two-peaked models are usually built as the combination of two of the previous spectra, sometimes using some sensible constraints on the parameters in order to reduce their number.

Applicability to West Africa

The above models are sometimes believed to be universal, yet one can but advise caution against such generalizations, since they were almost exclusively validated in moderate or high latitudes such as the North Atlantic, the North Sea or in semi-closed regions such as the Gulf of Mexico, and never in regions where swell would be predominant. In those regions, significant differences have been reported between responses to the actual measured spectra and simplified models, see for instance van Iseghem *et al* (2001) [4.18].

FIGURE 4.1 : A spectrum with 2 swell components and its Jonswap model

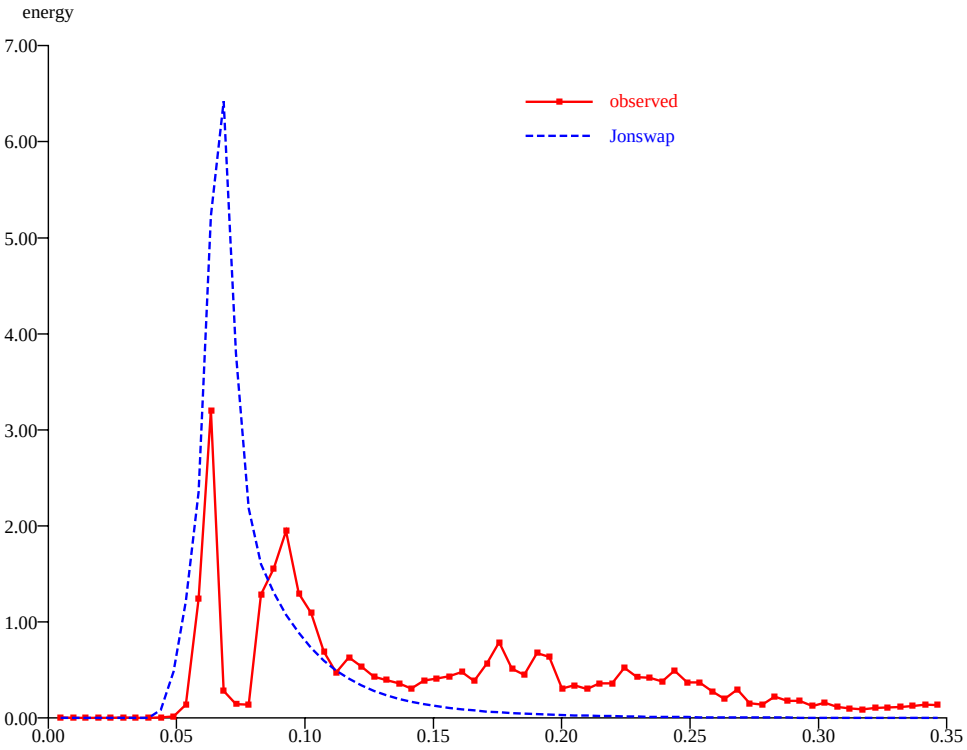

The single-peak models that they derive from take the energy distribution as results from interaction between wind shear on the sea surface and the water. Swell, however, corresponds to waves generated in a remote area, far from the observation point, and the energy distribution will thus have been modified from the original

one by the propagation process and should not be expected to have kept full similarity with that in the generation area. Especially, the physical constraints of a propagation delay from the generation area to the observation location, at celerities that depend strongly on frequency, will “carve” into the original spectrum and allow only a limited number of frequency bands to reach the observation point at a given time. Those considerations are detailed in "Swell spectrum shape generation", chapter 3.

Figure 4.1 shows how inadequate the Jonswap shape may be for a West Africa spectrum with two swell components. On first examination, it appears clearly that a model for such a spectrum must be able to take into account two peaks or more. However, when considering the previously mentioned two-peaked models, it appears that those models are still not suitable for many observed spectra since they are limited to 2 peaks. Even if one were ready to neglect the energy in the range 7-3 seconds, it is easy to find cases with a third swell component, as shown on figure 4.2. In addition, models commonly assume that one of the components is wind sea and only the other swell. Moreover, even that swell component is often modelled by pushing the parameters of a wind sea spectrum beyond the range of wind seas, and swell is thus not very well modelled.

FIGURE 4.2 : A spectrum with 3 swell components and its conventional model as the sum of two Jonswap

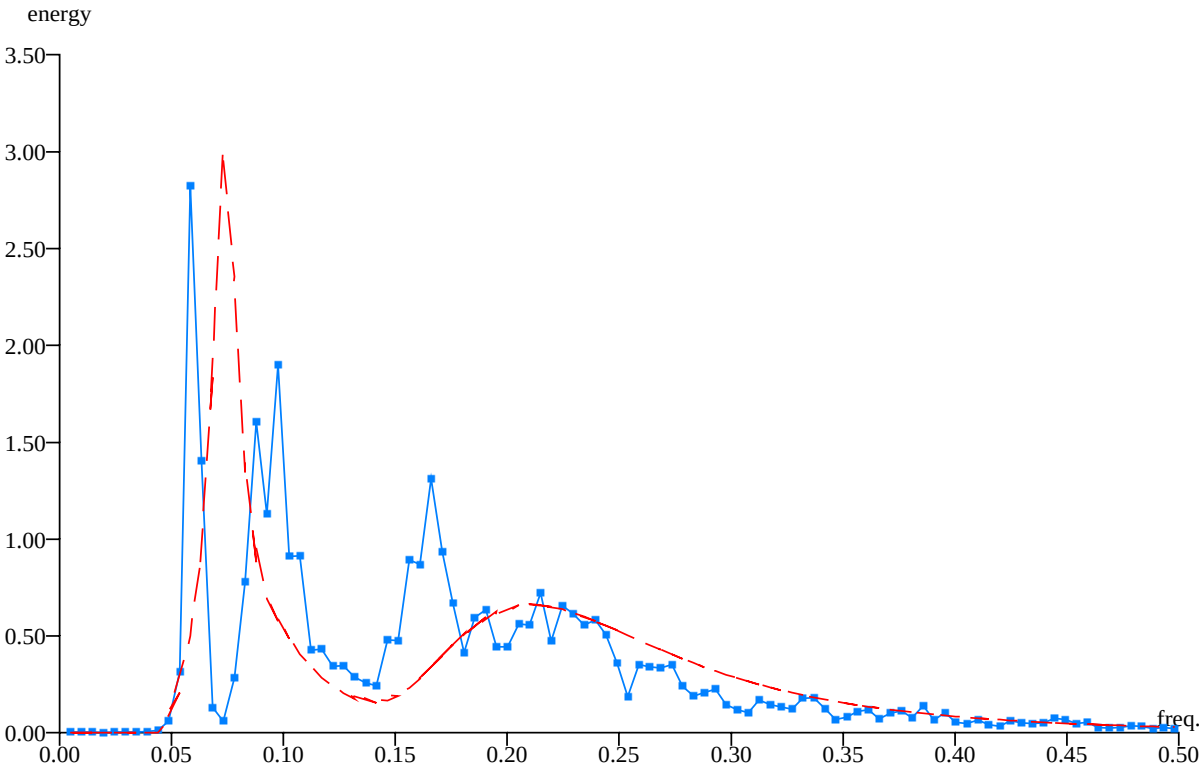

A pragmatic consequence is that each peak of the spectrum should be modelled separately, allowing for a relatively large number of independent spectral peaks (for instance, three different swells and one wind sea).

The impact of this conclusion is that partitioning the spectra into several wave components can significantly improve the accuracy of the computed responses (see for instance Quiniou-Ramus *et al* (2003) [4.14]). However, the climate statistics and the choice of design sea-states become much more complex, and the choice of

spectral shapes, now for identified wave systems, solves only part of the design conditions problem.

Spectral shapes for individual swell wave systems

Swell peaks are much narrower than the wind sea peaks that may be observed in the North Sea. In average, they will be all the more narrow as the swell generation occurs very remotely. Modelling such narrow peaks by a Jonswap implies to have γ take much higher values than those in the commonly used range of 1 to 7. Very high values of γ for swell are somewhat in contradiction with the construction of the Jonswap shape, where that parameter is used to reflect the non-saturation of a fetch-limited wind sea, and they lead to a risk of unnoticed numerical accuracies in the practical computations.

Following the considerations in "Swell spectrum shape generation", chapter 3, and in order to keep the complexity of the fitting and reconstruction processes within reasonable limits, simpler formulations than the Jonswap one were thus also sought for, via the method described in Olagnon (2001) [4.12] and recalled hereafter

Methodology . It is not easy to validate or define a spectral shape, even restricted to a given location or area. Measurements that one has access to are of too short duration, or too short stationary duration, to provide significant parameters from the fit on a single measured estimate. Conventionally, one chooses a parametric model, fits it to the available spectra, and studies the residual. The main problem is: "*How does one build the parametric model ?"*

In order to get rid of this problem, the assumption is made of a **unique underlying spectral model, valid for all sea-states**, but undefined at this stage, of the form:

$$S(f) = m_0 F\left(\frac{f}{f_c}\right) \qquad \textbf{(EQ 4.12)}$$

where f_c is a frequency characteristic of the sea-state, for instance f_{02} or modal frequency f_p, and F is normalized in such a way that:

$$\int_0^\infty F(u)\mathrm{du} = 1 \qquad \textbf{(EQ 4.13)}$$

The validation of the assumption that no other parameter is necessary to describe the spectra is only performed in retrospect at the end of the study.

In order to simplify the analysis and to give more chances of validity to the assumption, only single-peaked spectra should be used. In cases such as West Africa, where most spectra exhibit several peaks, only the largest peak in the range of interest (swell or sea) will be considered, and the characteristic frequency is set to the corresponding modal frequency f_p.

For all measured spectra, the frequency scale is normalized with that peak frequency f_p, once in the swell range, once in the wind sea range, and the spectra are then normalized by their value at f_p.

From the above unicity assumption and spectral estimation theory, it stems out that for each normalised frequency $\tilde{f} = f/f_p$, the observed spectral density is a random variable with a χ^2 distribution with ν degrees of freedom of average value $F(\tilde{f})$.

ν is fixed, since we use the same smoothing/averaging scheme for each spectral estimate, and as the χ^2 distribution is fully defined by its parameter, all parameters of the distribution of the spectral densities (mean, mode, percentiles) should be in constant ratios with respect to each other and can be expressed as $C \times F(\tilde{f})$, if the above assumption that all have the same normalized shape is verified.

Figure 4.3 shows the averages and percentiles for synthetic data deriving from a single given spectrum (red line).

FIGURE 4.3 : Triangular shape, linear scale - green: median, 30%, 70% percentiles, dotted blue: 10% and 90% percentiles, black: average, red: reference spectrum

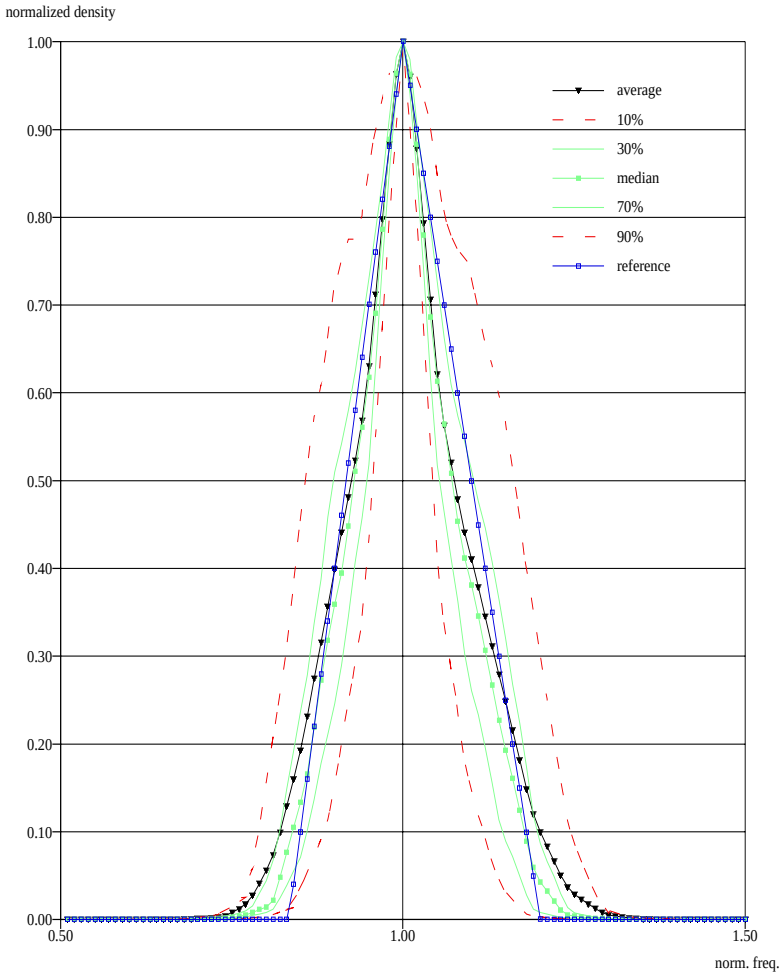

JONSWAP-Glenn

A variation of the JONSWAP function, given in terms of three parameters – significant wave height, H_s, peak frequency, f_p, and the peak enhancement factor, γ, is given by

$$G(f) = c\left(\frac{f}{f_p}\right)^{-5} e^{-\frac{5}{4}\left(\frac{f}{f_p}\right)^{-4}} \gamma^{exp\left(-\frac{\left(1-\frac{f}{f_p}\right)^2}{2\sigma^2}\right)} \quad \textbf{(EQ 4.14)}$$

where

$$\sigma = 0.07 \quad \text{for} \quad f \le f_p$$
$$\sigma = 0.09 \quad \text{for} \quad f > f_p \qquad \text{(EQ 4.15)}$$

and

$$c = \frac{5H_s^2}{16 f_p}\left(1.15 + 0.1688\,\gamma - \frac{0.925}{(1.909 + \gamma)}\right)^{-1} \qquad \text{(EQ 4.16)}$$

FIGURE 4.4 : Comparative JONSWAP-Glenn and JONSWAP spectral plots. JONSWAP spectra (continuous lines) are plotted for a range of fetches for a fixed wind-speed of 10 m/s. The parameters of the three JONSWAP-Glenn spectra (dashed lines) are specified next to each.

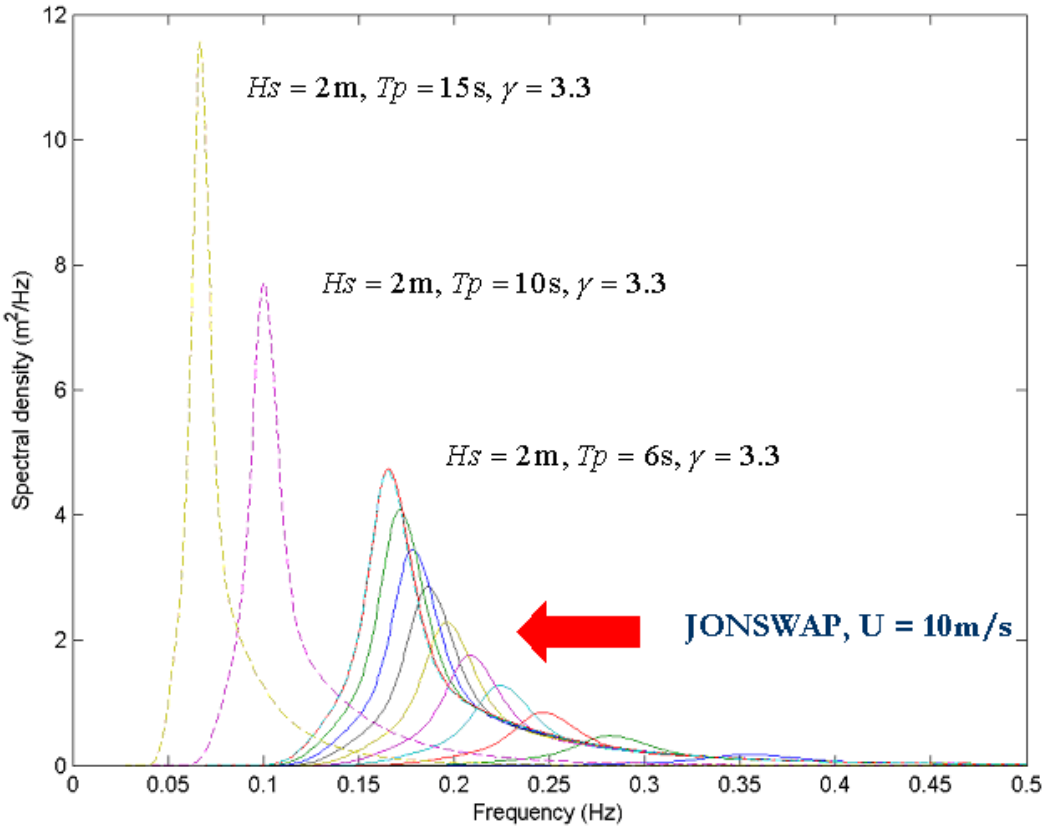

The function is plotted in Figure 4.4 for H_s = 2m, γ = 3.3, and T_p = 6s, 10s, 16s, together with a number of JONSWAP spectra specified at different distances along a fetch for a wind speed of 10 m/s.

Figure 4.4 shows the differences between the standard JONSWAP and the JONSWAP-Glenn spectra. In particular, the JONSWAP spectrum has a one-to-one relationship between the peak frequency and the variance or H_s, which is not the case for the JONSWAP-Glenn spectra.

Triangle

The triangle spectrum is defined, in terms of three parameters, – significant wave height, H_s, peak frequency, f_p, and a third parameter, m, as follows

$$
\begin{aligned}
G(f) &= \frac{2m(m\text{-}1)}{2m\text{-}1}\frac{H_s^2}{16f_p}\left(m\frac{f}{f_p}-(m-1)\right) && \frac{m\text{-}1}{m}f_p < f < f_p \\
G(f) &= \frac{2m(m-1)}{2m-1}\frac{H_s^2}{16f_p}\left(m-(m-1)\frac{f}{f_p}\right) && f_p \le f < \frac{m}{m\text{-}1}f_p \\
G(f) &= 0 && \text{elsewhere}
\end{aligned}
\qquad \text{(EQ 4.17)}
$$

Examples of this spectral form are given in Figure 4.5.

FIGURE 4.5 : Triangle spectra for H_s = 4m, f_p = 0.10 Hz, and various values of m.

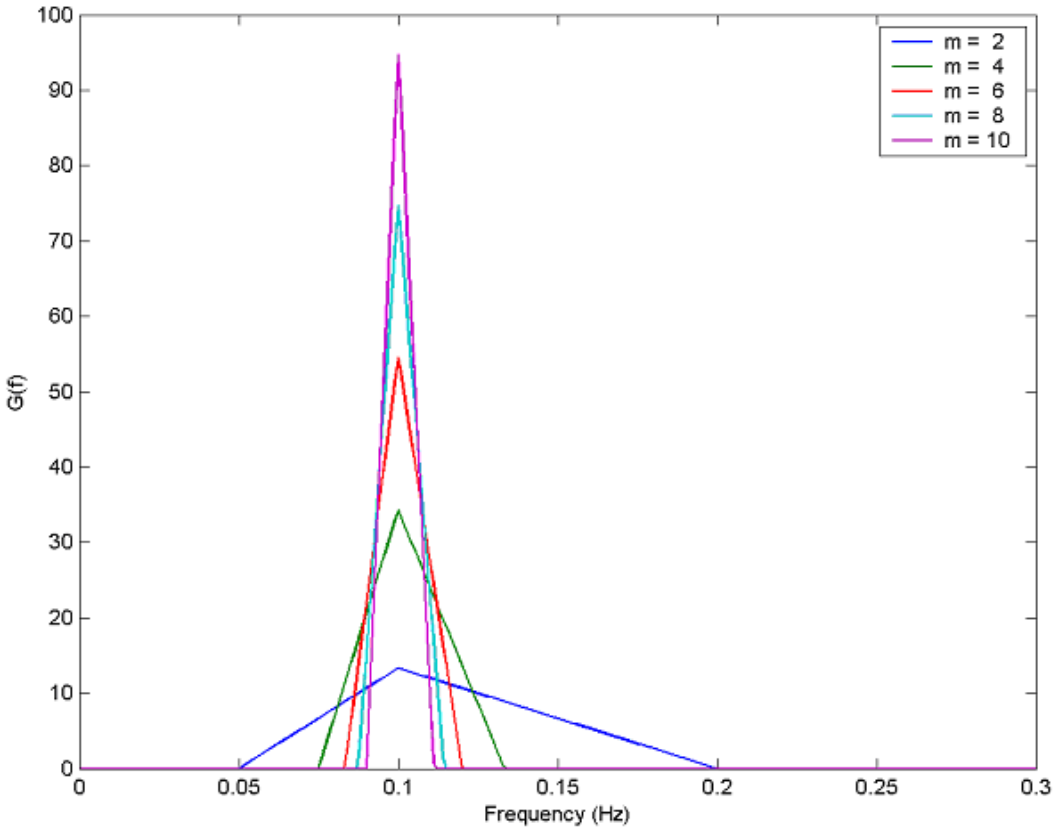

Gaussian

The Gaussian spectral form is also expressed as a function of three parameters - – significant wave height, H_s, peak frequency, f_p, and a standard deviation, σ, as follows.

$$
G(f) = \frac{m_0}{\sigma\sqrt{2\pi}}\exp\left(\frac{-(f-f_p)^2}{2\sigma^2}\right) \qquad \text{(EQ 4.18)}
$$

where σ is the standard deviation.
Examples of this spectral form are given in Figure 4.6.

FIGURE 4.6 : Gaussian spectra for H_s = 4m, f_p = 0.10 Hz, and various values of σ.

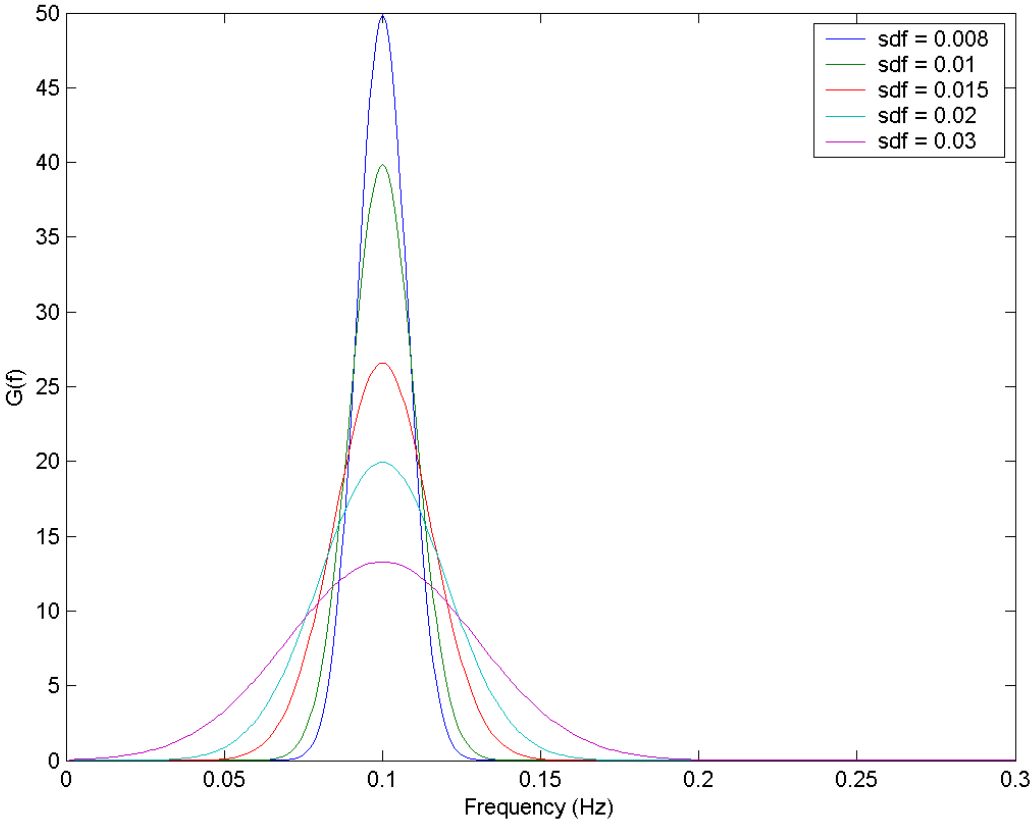

Lognormal

A variation of the Gaussian spectral form is the lognormal. It allows for some asymmetry in the shape. It is given by

$$G(f) = \frac{m_0}{f\sigma\sqrt{2\pi}} \exp\left(\frac{-(\ln(f)-\mu)^2}{2\sigma^2}\right) \quad \textbf{(EQ 4.19)}$$

where the lognormal parameters μ and σ can be expressed in terms of f_p and a parameter s corresponding to the standard deviation of the normal distribution as follows

$$\sigma = \sqrt{\ln\left(\frac{s^2}{f_p^2}+1\right)} \quad \textbf{(EQ 4.20)}$$

$$\mu = \ln(f_p) + \sigma^2 \quad \textbf{(EQ 4.21)}$$

Examples of this spectral form are given in Figure 4.7.

Spectral Fitting

The four spectral functions were each fitted to the spectral partitions derived from the wind-sea and swell partitioning approach. Accordingly, the parameters were varied in order to achieve the best-fit functions by the method of least squares. The fits to the components are then summed to obtain a description of a particular spectrum. In all cases the wind-sea component is assumed to have a JONSWAP-Glenn spectrum. Thus, four descriptions of each spectrum are obtained, one for each spectral type. An example of fitting the four spectral functions to a spectral partition is given in Figure 4.8.

FIGURE 4.7 : Lognormal spectra for H_s = 4m, f_p = 0.10 Hz, and various values of σ.

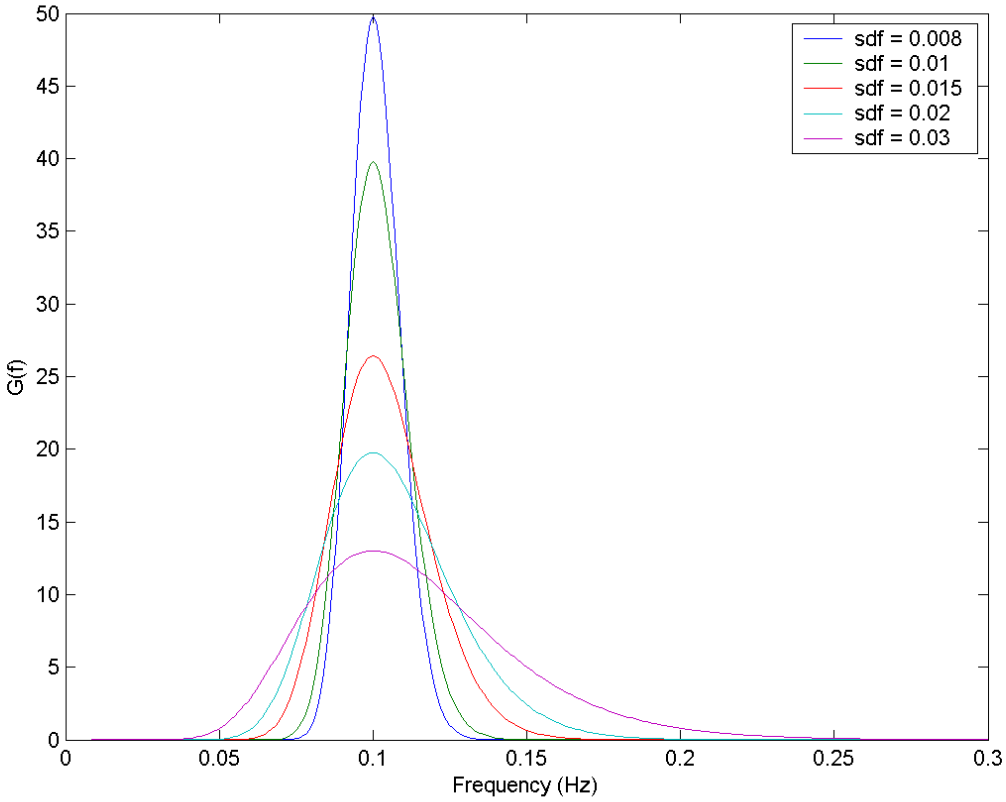

Wrapped-Normal Distribution

A convenient description of the directional distribution for a unimodal swell component is given by the so-called Wrapped-Normal distribution, defined as follows.

$$D(\theta) = \frac{1}{\sqrt{2\pi}\sigma_{wn}} \sum_{k=-\infty}^{\infty} \exp\left(-\frac{1}{2}\left(\frac{\theta - \theta_0 - 2\pi k}{\sigma_{wn}}\right)^2\right) \qquad \textbf{(EQ 4.22)}$$

where θ_0 is the mean wave direction, σ_{wn} is the standard deviation or angular width and gives a measure of the spreading. The summation over k ensures the distribution is continuous through 360. In practice it is sufficient to limit the summation to $k = -5,...,5$.

References

[4.1] Borgman, L., "A technique for computer simulation of ocean waves.", *Probabilistic Mechanics and Structural Reliability Specialty Conference*, ASCE, Jan. 1979.

[4.2] Gonella, J., "A rotary component method for analysing meteorological and oceanographic vector time series.", *Deep Sea Research*, Vol.19, 1972.

[4.3] Guedes Soares, C., "Representation of double peak spectra.", *Ocean Engineering*, Vol.11, 1984, pp. 185–207.

FIGURE 4.8 : An example of fitting the spectral functions to total spectrum.

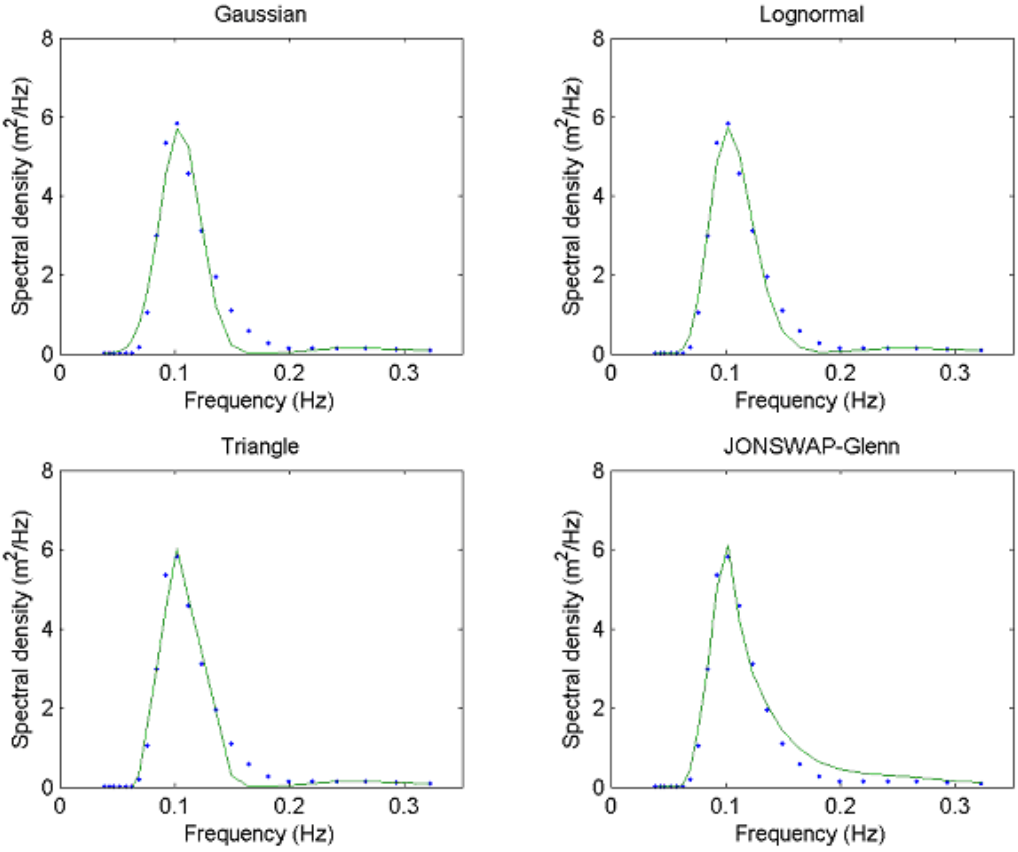

[4.4] Guedes Soares, C., "Spectral Modeling of Sea States With Multiple Wave Systems", *Journal of Offshore Mechanics and Arctics Engineering*, vol.114 1992.

[4.5] Hasselmann, K., Ross, D.B., Müller, P. & Sell, W. "A parametric wave prediction model", *J. Phys. Oceanogr.*, vol. 6, no. 2, pp. 200–228.

[4.6] Hasselmann, K, *et al.* "Measurements of wind-wave growth and swell decay during the Joint North Sea Wave Project", *Deutsche Hydrographische Zeitschrift*, Reihe A **8** (12), 1973, 95 pp.

[4.7] International Association for Hydraulic Research, 1986, "List of Sea State Parameters" *Supplement to bulletin* No 52.

[4.8] Massel, S.R. *Ocean Surface Waves, their Physics and Prediction*, World Scientific 1996.

[4.9] Mooers, C.N.K., "A technique for cross-spectrum analysis of complex valued time series.", *Deep Sea Research*, Vol.20, 1973.

[4.10]Ochi, M.K. & Hubble, E.N., “Six-parameter wave spectra.”, *Coastal Engineering*, 1976.

[4.11]Olagnon, M. & Krogstad, H.E. “Observed short- and long-term distributions of wave steepness”, *Proc. Int. Offshore and Polar Engineering Conf.*, Vol. 3, Montréal (1998), pp. 63–70.

[4.12]Olagnon, M. "Representativity of some standard spectral models for waves”, *Proc. Int. Offshore and Polar Engineering Conf.*, ISOPE Vol. 3, Stavanger (2001), pp. 92-99.

[4.13]Pierson, W.J. & Moskowitz, L. “A proposed spectral form for fully developed wind seas based on the similarity of S.A. Kitaigorodskii”, *J. Geophys. Res.*, vol. 69, no. 24, pp. 5181–5190.

[4.14]Quiniou-Ramus, V., Hoche, M.-A., François, M., Nerzic, R., Ledoux, A., Orsero, M. (2003) “Recent Breakthroughs in the Analysis of Total E&P Angola Block 17 wind/wave/current records and their impact on floating structures design” *Proc. XVth Deep Offshore Technology Conf.*, DOT, Marseilles, Nov. 19-21 2003.

[4.15]Rychlik, I., 1996, “A note on significant wave height” *J. Ocean Engineering* vol 23 No.6, pp. 447-454.

[4.16]Torsethaugen, K. “A two Peak wave spectrum model” *Proc. Int. OMAE Conf.*, Vol.2, (1993), pp. 175–180.

[4.17]Torsethaugen, K. “Model for a double peak wave spectrum” *Report SINTEF SFT22 A96204*, (1996).

[4.18]van Iseghem, S., Deleuil, G. & Guérin, P. “Improved characterizations for design waves” *Proc. Int. Offshore and Polar Engineering Conf.*, ISOPE Vol.3, Stavanger (2001).

CHAPTER 5

Bias, variability and dispersion on spectral shapes

Michel Olagnon
Marc Prevosto

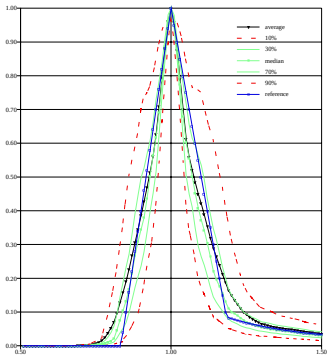

This chapter deals with item 3. of the WASP scope of work: Shape of the Swell Peak in the Power Spectrum.

Spectral estimation is a complex problem, and some of the implications of the difficulties induced by the necessary finite length of stationary field records and of the random variability between actual instances deriving from the same spectrum are often overlooked.

This chapter is an attempt to provide some assessment of the significance and accuracy of results obtained regarding swell spectral shapes in the previous chapter.

General

The spectrum of a sea-state is a stochastic description that can theoretically only be exactly computed if the sea-state extends to infinity in time and in space.

In practice, sea-states are only stationary for durations of the order of magnitude of a few hours and measurements are often even shorter. The properties of the spectrum must thus be estimated from a short segment of time-history that appears as an instance within the set of all the possible sea-states that may derive from that theoretical spectrum.

Variability within that set (leading to random uncertainty) is large, and processing techniques are used to improve the quality of the estimate of the spectrum. Those techniques, smoothing and averaging, lead to biases and other epistemic uncertainties, and though engineers are usually well aware of the existence of the problem, they may sometimes satisfy themselves with the fact that they use a reputable processing method and omit to consider the actual range of uncertainties and its consequences on the significance of results.

Assessment of the significance of the differences between spectral shapes, either within the range of theoretical models investigated, or with field observations, is carried out in the present chapter.

Sensitivity study . The analysis was carried out by simulating 1000 random instances from each given spectral density, with H_S=0.636 m and T_p=12.2 s. Each instance was 1024 seconds at 2 Hz, randomly extracted from the centre 80% (to avoid any side-effects from the generation) of 16384 seconds simulated at 4 Hz. The spectra are then estimated by Walsh averaging of 256 second time-windows, tapered by a 50% Tukey (cosine) window, and overlapping by 75%.

FIGURE 5.1 : Gaussian shape, linear scale - green: median, 30%, 70% percentiles, dotted blue: 10% and 90% percentiles, black: average, red: reference spectrum

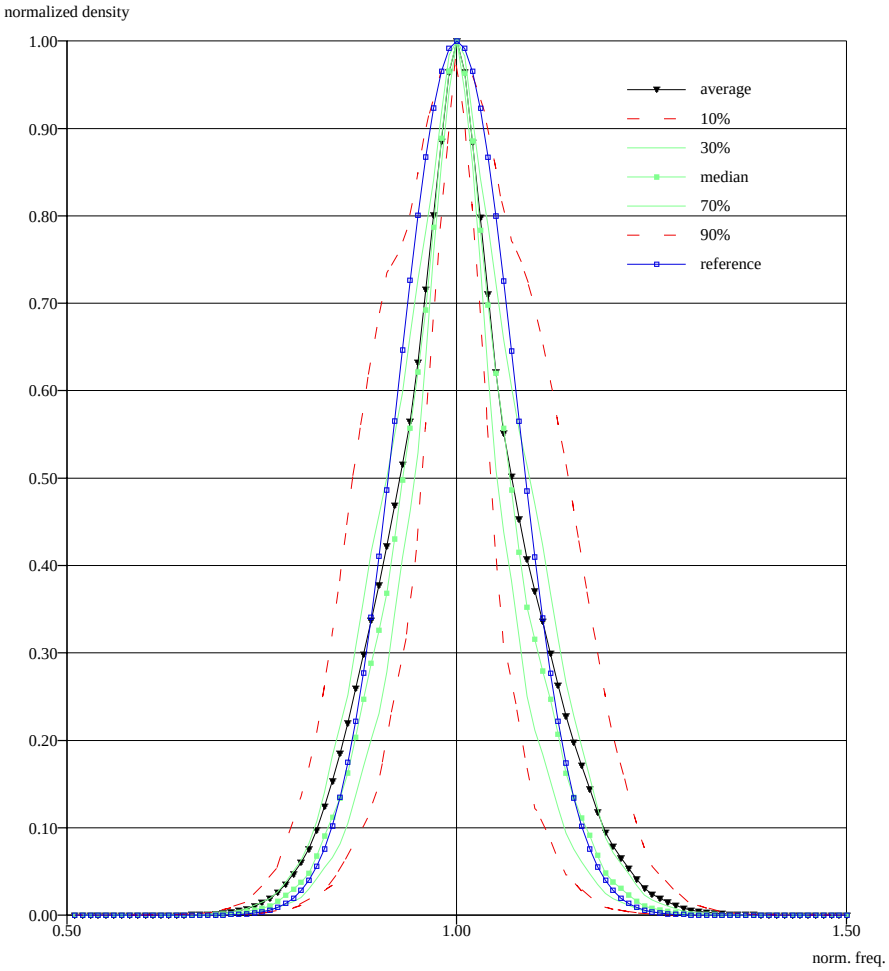

Several simple shapes were considered for the spectrum of each partition or identified wave system. The four spectral shapes examined are a triangular density (Figure 4.3), a Gaussian density (Figure 5.1), a Log-normal density (Figure 5.2) and a Jonswap density (Figure 5.3).

The widths of the spectra are chosen with m=6 (Goda parameter Q_p=7.3) for the triangles, standard deviation 0.00614 (so as to be as similar as possible to the previous width) for the normal and log-normal shapes, and γ=19 for the Jonswap.

As can be seen from Figures 4.3,5.1-5.3, the median shapes are relatively close to the reference ones, although the method and the computations tend to sharpen the peak and to spread the base.

FIGURE 5.2 : Log-normal shape, linear scale - green: median, 30%, 70% percentiles, dotted blue: 10% and 90% percentiles, black: average, red: reference spectrum

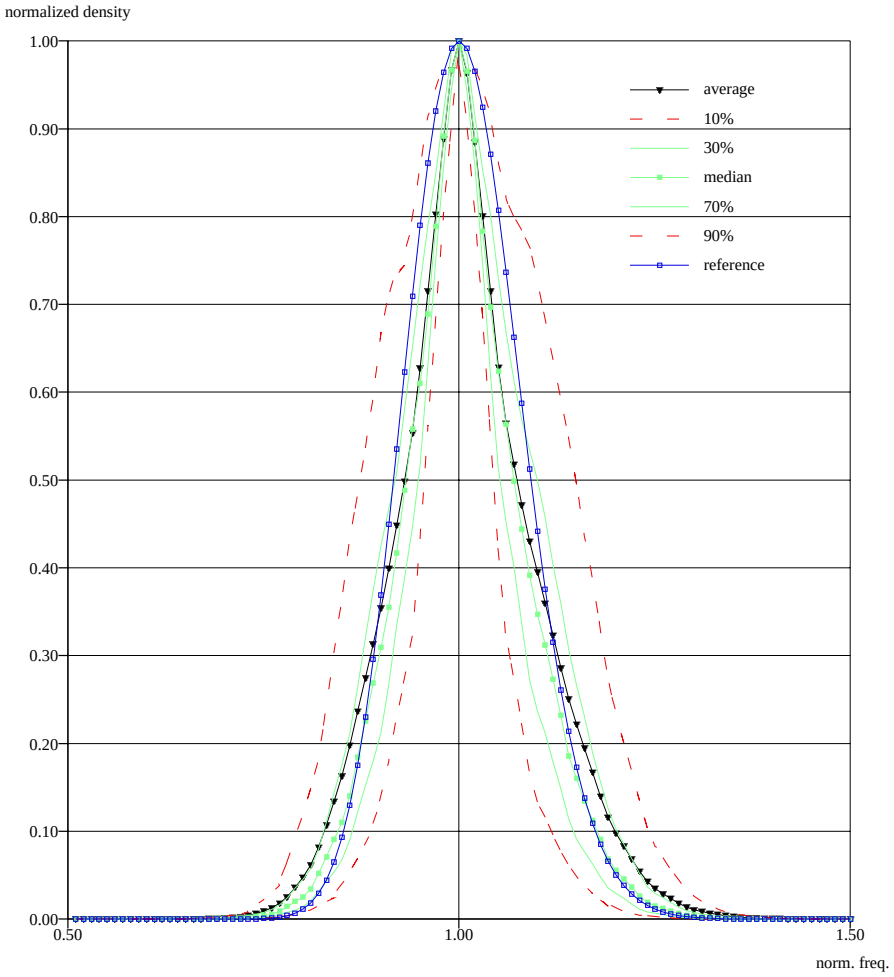

One may assume that the sharpness is mainly due to lack of resolution and to normalization by the frequency of the observed maximum of each instance rather than by a constant frequency, and that the widening of the base of the peak is more the effect of spectral leakage despite the window.

It is also noteworthy that the differences between the various shapes that were investigated are small with respect to those estimation uncertainties, as can be observed on figure 5.8.

Table 5.1 shows the natural variability of the characteristic parameters over the 1000 instances of simulated histories. Here again, the differences between the shapes are very small with respect to natural variability. In addition, one may observe that some parameters, such as the Jonswap overshooting factor γ, exhibit a very large natural variability and may thus be difficult to use in practice.

TABLE 5.1 : Natural (sample) variability of spectral parameters for the 4 shapes investigated

Parameter	Triangle	Gaussian	Log-normal	Jonswap
H_S	0.636	0.636	0.636	0.636
$E(H_S)$	0.632	0.631	0.629	0.632
$\sigma(H_S)$	0.072	0.073	0.071	0.073
T_p	12.20	12.20	12.20	12.20
$E(T_p)$	12.14	12.23	12.19	12.13
$\sigma(T_p)$	0.49	0.45	0.46	0.30
Λ_{01}	227	232	229	200
$E(\Lambda_{01})$	228	233	228	199
$\sigma(\Lambda_{01})$	6	6	6	7
Q_p	7.33	7.53	7.56	7.47
$E(Q_p)$	7.63	7.85	7.82	7.33
$\sigma(Q_p)$	0.96	1.11	1.08	1.43
γ	18.1	19.4	19.6	19.
$E(\gamma)$	21.3	23.4	23.0	19.6
$\sigma(\gamma)$	8.6	11.3	10.4	11.9
m	6	6.15	6.17	6.1
$E(m)$	6.2	6.39	6.37	5.9
$\sigma(m)$	0.72	0.83	0.8	1.07
σ_f	$6.1\ 10^{-3}$	$6.1\ 10^{-3}$	$6.1\ 10^{-3}$	$2.4\ 10^{-3}$
$E(\sigma_f)$	$6.5\ 10^{-3}$	$6.5\ 10^{-3}$	$6.6\ 10^{-3}$	$3.0\ 10^{-3}$
$\sigma(\sigma_f)$	$0.6\ 10^{-3}$	$0.6\ 10^{-3}$	$0.6\ 10^{-3}$	$0.3\ 10^{-3}$
δ_f	$3.0\ 10^{-2}$	$2.9\ 10^{-2}$	$2.9\ 10^{-2}$	$2.9\ 10^{-2}$
$E(\delta_f)$	$2.9\ 10^{-2}$	$2.9\ 10^{-2}$	$2.9\ 10^{-2}$	$3.2\ 10^{-2}$
$\sigma(\delta_f)$	$0.36\ 10^{-2}$	$0.38\ 10^{-2}$	$0.37\ 10^{-2}$	$0.65\ 10^{-2}$

FIGURE 5.3 : Jonswap shape, linear scale - green: median, 30%, 70% percentiles, dotted blue: 10% and 90% percentiles, black: average, red: reference spectrum

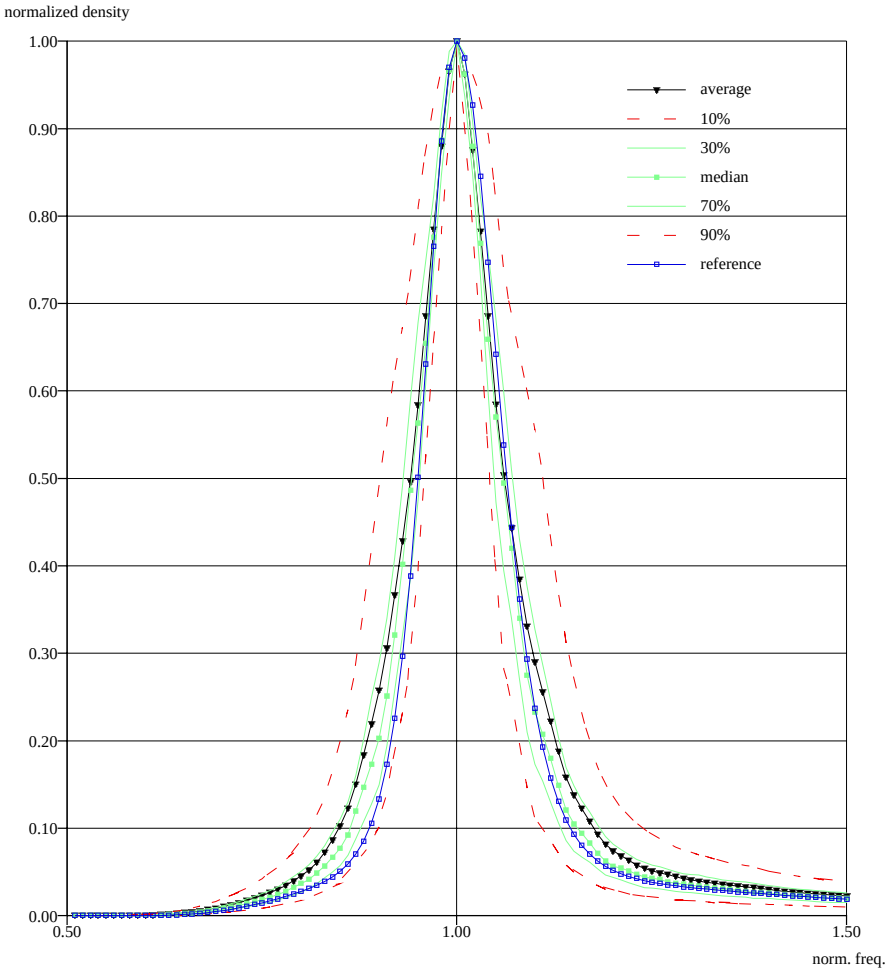

Theoretical biases in spectral estimation

In the estimation of the spectral density from measurements, a bias is introduced on the spectral shape due to two reasons. First the effect of windowing and secondly the non stationarity of the sea-states coming to the time evolution of the frequency of the swells.

Windowing

To increase the number of degree of freedom in the spectral estimator or in other words to decrease the variance of the estimator, the time series is split in pieces, with or without overlapping, and the spectral estimator is obtained in calculated the average of the individual spectral estimator. Making this, theoretically is equivalent to multiplying the theoretical infinitely long stationary time series with a window (rectangular or others), the length of the pieces. So the operation of windowing modify the spectral density of the time process in a way which can be calculated as the convolution between the "true" spectrum and the Fourier transform of the window (see for example Brillinger [5.1]). This effect is particularly crucial when the bandwidth of the spectral peaks is narrow and when the peaks are very close to each other. The choice of the optimal window is then a compromise between the bias on the peak bandwidth and the boundary effect of the neighbouring peaks. The properties of a great number of windows have been studied by Harris [5.2].

FIGURE 5.4 : Biases on the peak of the spectral shape - Tp=16s, m=6.

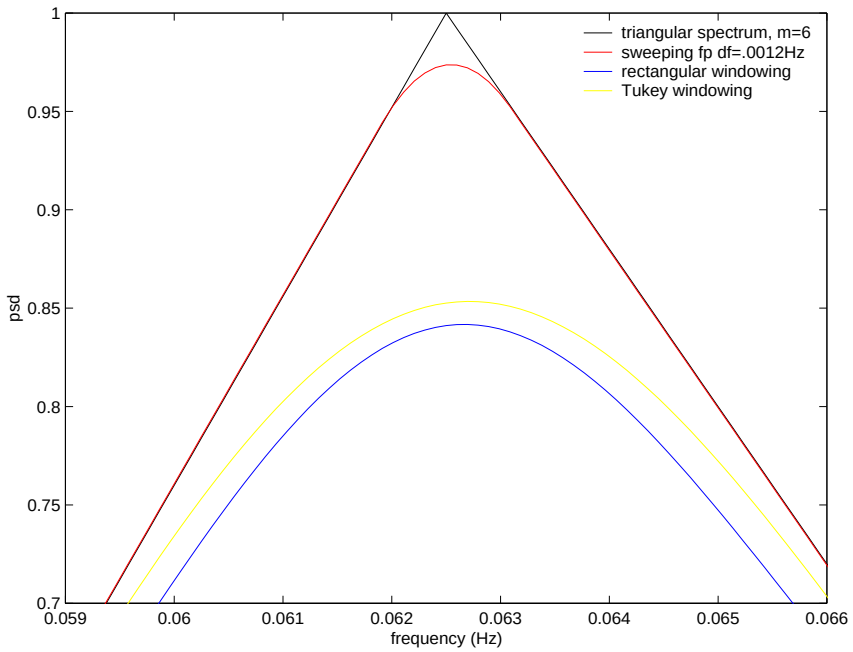

The bias introduced on the triangular spectral shape with two different m coefficient has been calculated for a rectangular and a Tukey (50-percent cosine taper) window (in blue and yellow Figs. 5.4 to 5.7). The effect is important on the amplitude of the peaks and on the flanks, transforming the triangular shape to a smoothed one.

Non stationarity

The duration of the time series used to estimate the spectral density must correspond to a stationary period of time of the process. Of course when measuring

waves, this hypothesis is never verified as the mean frequency and Hs are always moving (see for example the time evolution of the peak frequency of the wave systems in Fig. 3.11). In the case of a wind sea, the sweeping of the mean frequency is not really a problem as it is relatively small compared to the frequency bandwidth of the spectrum. In the case of swell, it could be different and so the effect of a sweeping frequency must be analysed. A maximum of the interval of sweeping frequency during 3 hours, df=.0012Hz, has been evaluated from the hindcast data base. It shows (in red figs. 5.4 to 5.7) that, for both the cases of triangular shapes, the bias that is introduced is very small and that it could be neglected compared to the effect of the windowing.

FIGURE 5.5 : Biases on the flank of the spectral shape - Tp=16s, m=6.

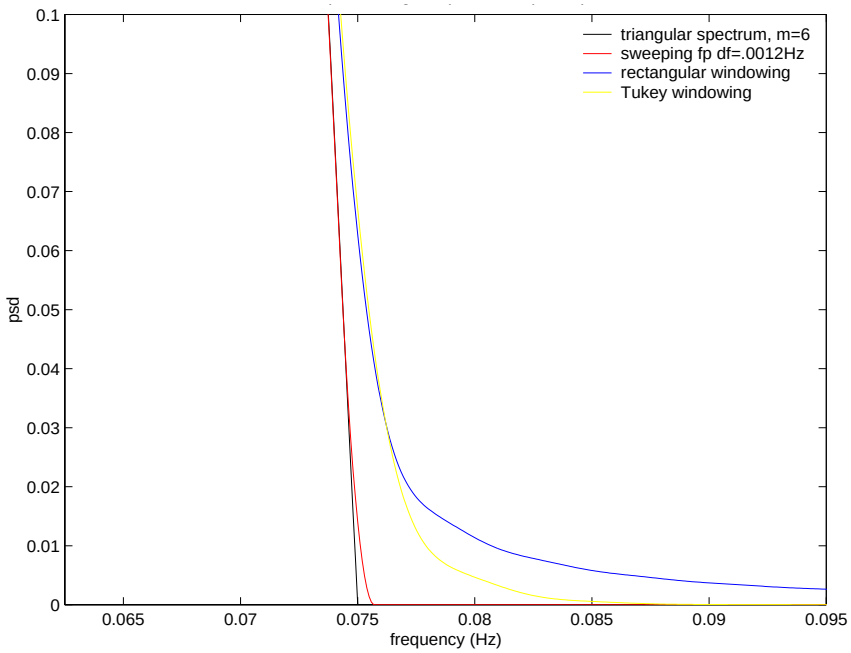

FIGURE 5.6 : Biases on the peak of the spectral shape - Tp=16s, m=10.

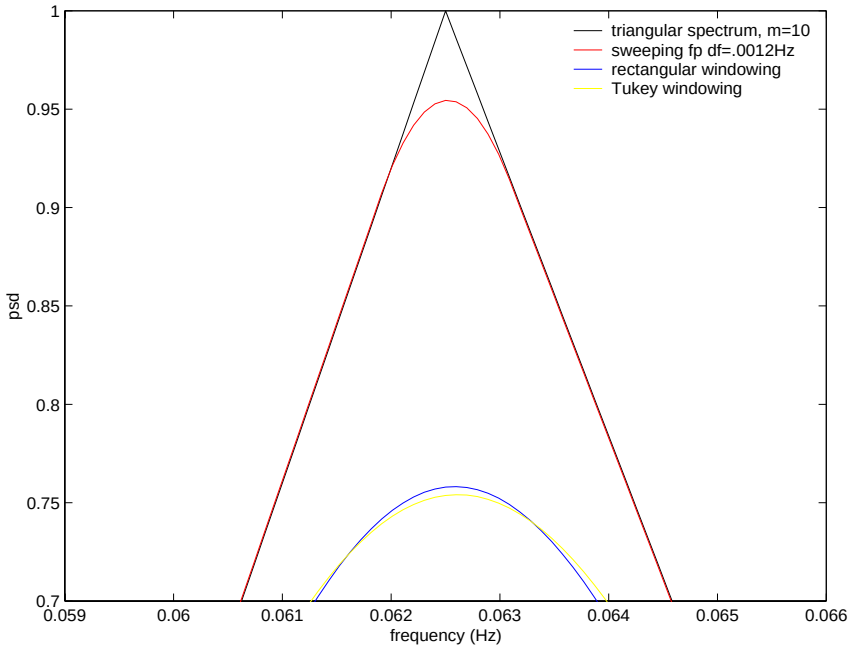

FIGURE 5.7 : Biases on the flank of the spectral shape - Tp=16s, m=10.

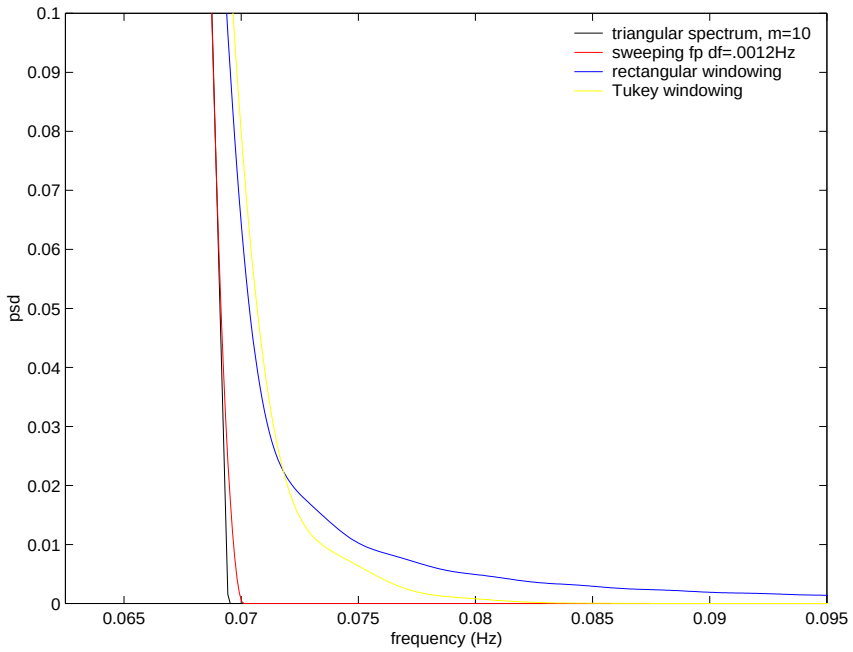

Choice of shapes fit to measurements

Ekoundou

Swell. In order to simplify the analysis and to give more chances of validity to the assumptions of section “Spectral shapes for individual swell wave systems”, Chapter 4, that the normalized shape would be the same for all sea-states, only single-peaked spectral ranges need to be used, and swell conditions should be separated from wind sea conditions. For the Ekoundou spectra, this can be done rather easily by taking only the largest peak in each of the intervals [0, 8s] and [8, 20s] for analysis of respectively wind sea and swell spectral shapes.

For all measured spectra, the frequency scale was adjusted so that would they end up with a common peak frequency f_p, once in the swell interval, once in the wind sea interval, and the spectra were then normalized by their value at f_p.

Figure 5.9 shows the resulting shapes for the swell (T_p>8s) peaks. Given that the influence of other neighbouring peaks cannot be rubbed out by the method, it was decided to use a triangular shape (displayed in green) to model the peak rather than some function that would follow more closely the black empirical one outside of the interval [0.9f_p, 1.1f_p].

FIGURE 5.8 : Spectral shapes are difficult to discriminate in practice

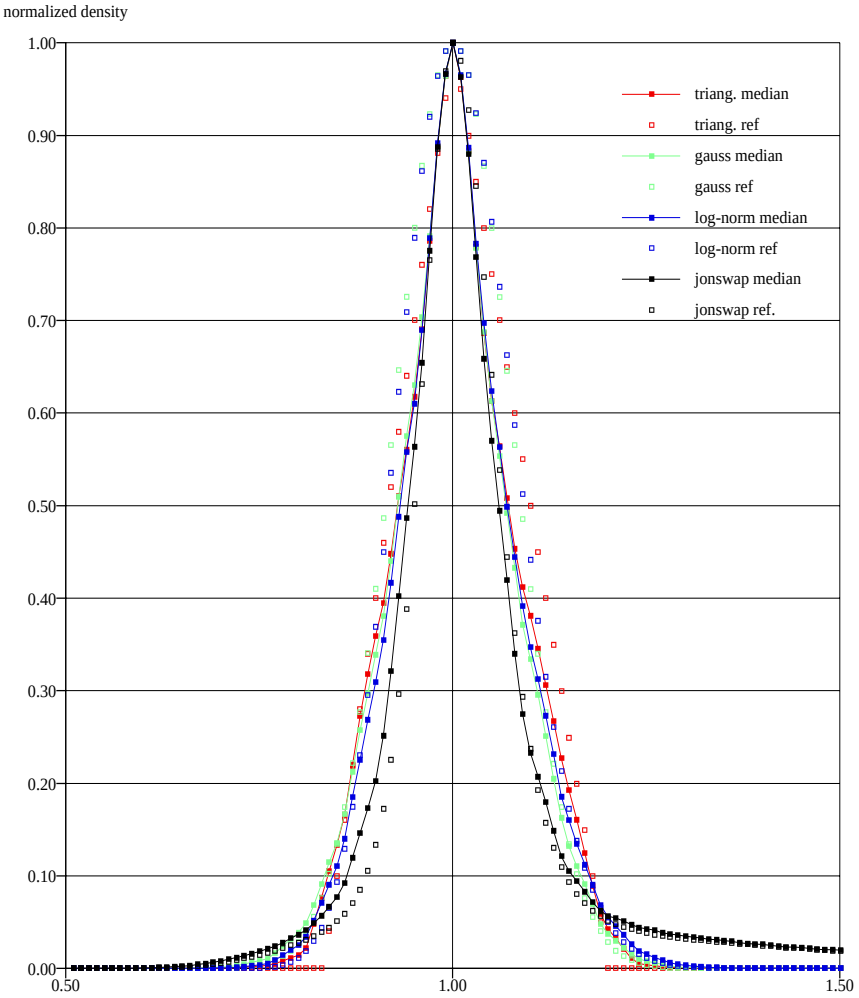

For the sake of simplicity, the triangle was chosen to start at $\frac{5f_p}{6}$ and to end at $\frac{6f_p}{5}$, thus providing the following formula:

$$
\begin{aligned}
S(f) &= \frac{60}{11}\frac{H_s^2}{16f_p}\left(6\frac{f}{f_p}-5\right) \qquad \frac{5f_p}{6} < f < f_p \\
S(f) &= \frac{60}{11}\frac{H_s^2}{16f_p}\left(6-5\frac{f}{f_p}\right) \qquad f_p < f < \frac{6f_p}{5} \\
S(f) &= 0 \qquad \textit{elsewhere}
\end{aligned}
\qquad \textbf{(EQ 5.1)}
$$

The same triangle was tried for hindcast spectra (figure 5.10), and gives a good agreement, which seems to confirm that the shape is determined by a propagation transfer function as discussed in "Swell spectrum shape generation", chapter 3.

FIGURE 5.9 : Spectral shape of swell peaks, linear scale - blue: median, 25%, 75% percentiles, dotted red: 10% and 90% percentiles, black: average, green: proposed shape

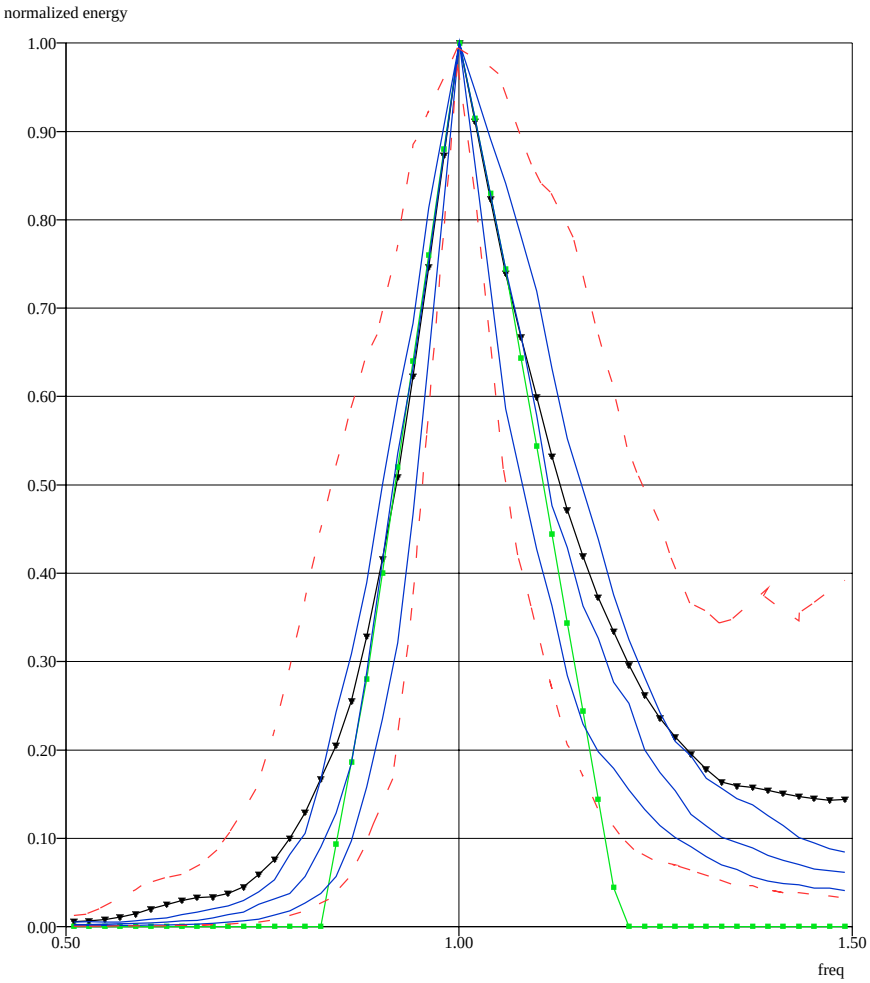

One may note that the empirical shapes exhibit a “thick tail” in the high frequency range. A possible interpretation is that some swells are not pure swells, but were generated in close enough areas to be mixed with a small proportion of wind sea. Although on first thought the wind sea was believed to be independent of the swell, some indications from other locations give raise to the possibility that swells in the 12-8 second period range may have a similar spectral tail as wind seas.

Wind sea. Wind sea peaks have a somewhat different shape, as can be seen on figure 5.11. The linear curves show that the range of frequencies below the peak frequency f_p suffers from significant leaking of the swell or other wind sea components. Instead of following the empirical average function in that part, the proposed model was thus chosen close to the 25% percentile, assuming that that curve would be more representative of the components not affected by any lower frequency ones.

FIGURE 5.10 : Normalized shapes for Wane spectra 28793, 10%, 25%, 50%, 75%, 90% fractiles and average

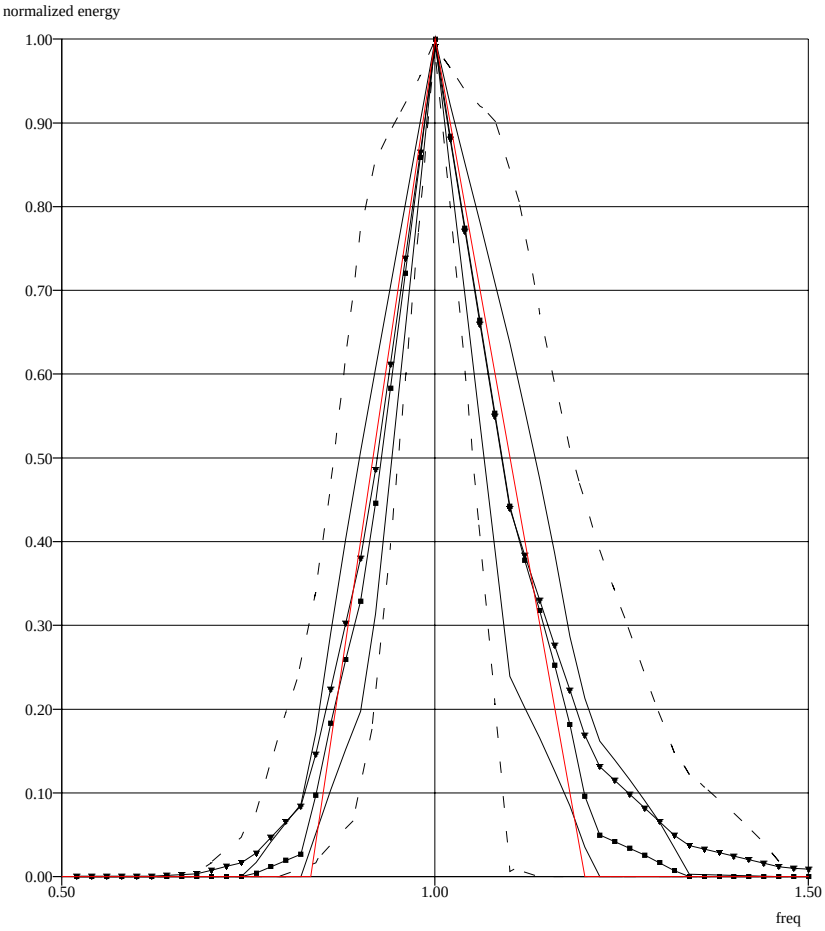

The high frequency part was split into a short, steep descent, making the peak's tip symmetrical in log scale onto $1.05f_p$, and an $f^{-4.5}$ tail. The transition point was chosen to bring the proposed shape below the median, in order again get free from the influence of higher frequency wave components that probably bias the average shape.

It was recognized in previous studies that the high frequency tail of the spectrum is influenced by the free-standing pipe's oscillations at its natural frequencies, and thus that the actual slope of the tail of the spectrum could not be precisely inferred from the measurements. A slope of $f^{-4.5}$ seemed a reasonable compromise between the often suggested values of f^{-4} and f^{-5}.

$$
\begin{aligned}
S(f) &= \frac{1}{0.2817}\frac{H_s^2}{16 f_p}\left(\frac{f}{f_p}\right)^{12} && f < f_p \\
S(f) &= \frac{1}{0.2817}\frac{H_s^2}{16 f_p}\left(\frac{f}{f_p}\right)^{-12} && f_p < f < 1.05 f_p \\
S(f) &= \frac{1}{0.2817}\frac{H_s^2}{16 f_p}\frac{1}{1.05^{7.5}}\left(\frac{f}{f_p}\right)^{-4.5} && 1.05\, f_p < f
\end{aligned}
\qquad \textbf{(EQ 5.2)}
$$

In both cases, the various estimates of $F(\tilde{f})$ fall within a small width, and the assumption of a unique spectral model for each type of waves is thus validated.

The partition of the higher part of the wind sea spectrum into a short steep descent followed by a $f^{-4.5}$ power law was also observed in other regions of the world, where it led to successful models.

It should be noted that with this model, each wave component can be described with three parameters: H_s, T_p, and a flag indicating whether it represents a swell or a wind sea component.

FIGURE 5.11 : Spectral shape of wind sea peaks, linear and log-log scales - blue: median, 25%, 75% percentiles, dotted red: 10% and 90% percentiles, black: average, green: proposed shape

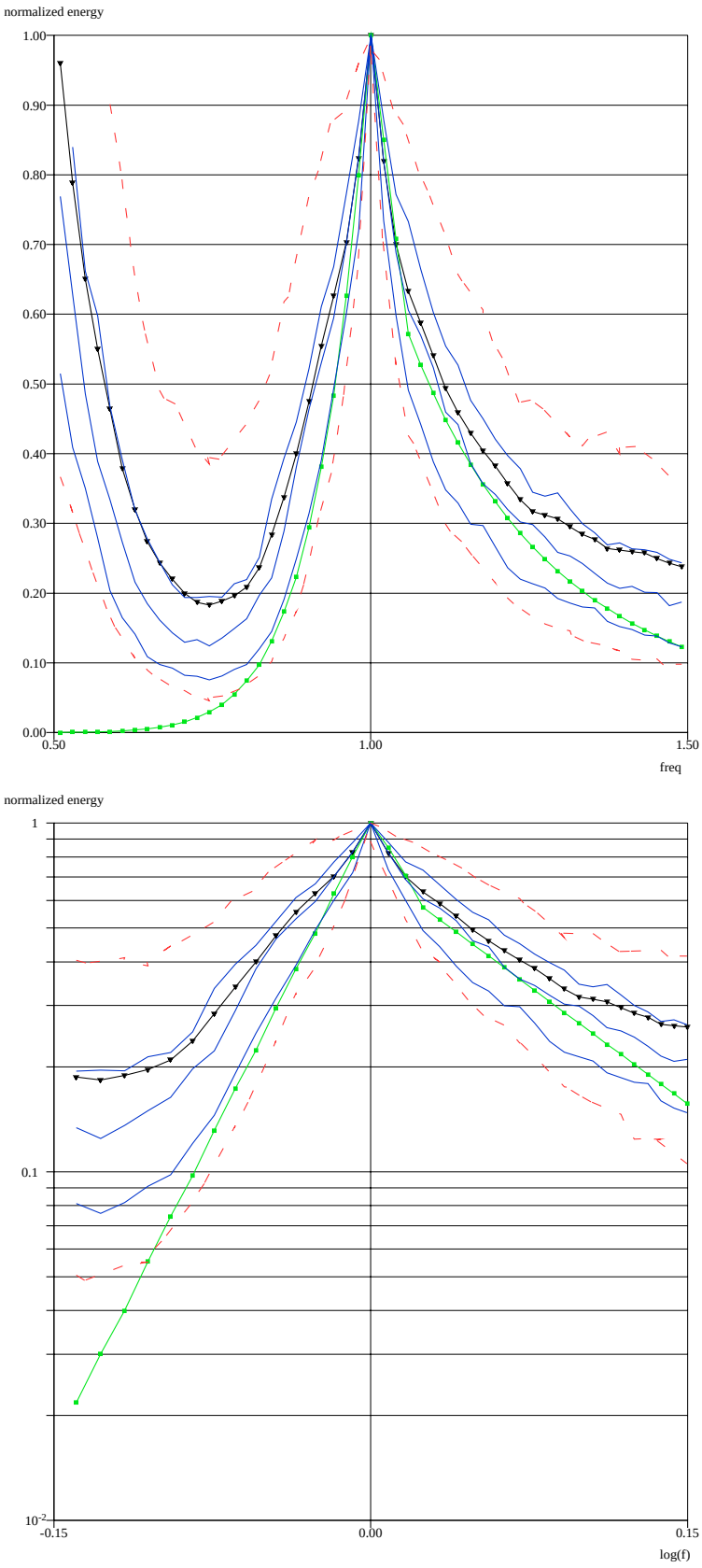

Spectrum reconstruction. Knowing models 5.1 and 5.2, the spectrum of figure 4.1 can then be described as a superposition of six wave systems:

TABLE 5.2 : Wave system parameters

Type	H_s	T_p
Swell	0.64	16.10
Swell	0.83	10.86
Swell	0.46	8.27
Wind Sea	0.67	4.13
Wind Sea	0.46	6.58
Wind Sea	0.79	5.67

FIGURE 5.12 : Component per component model of the spectrum of figure 4.1

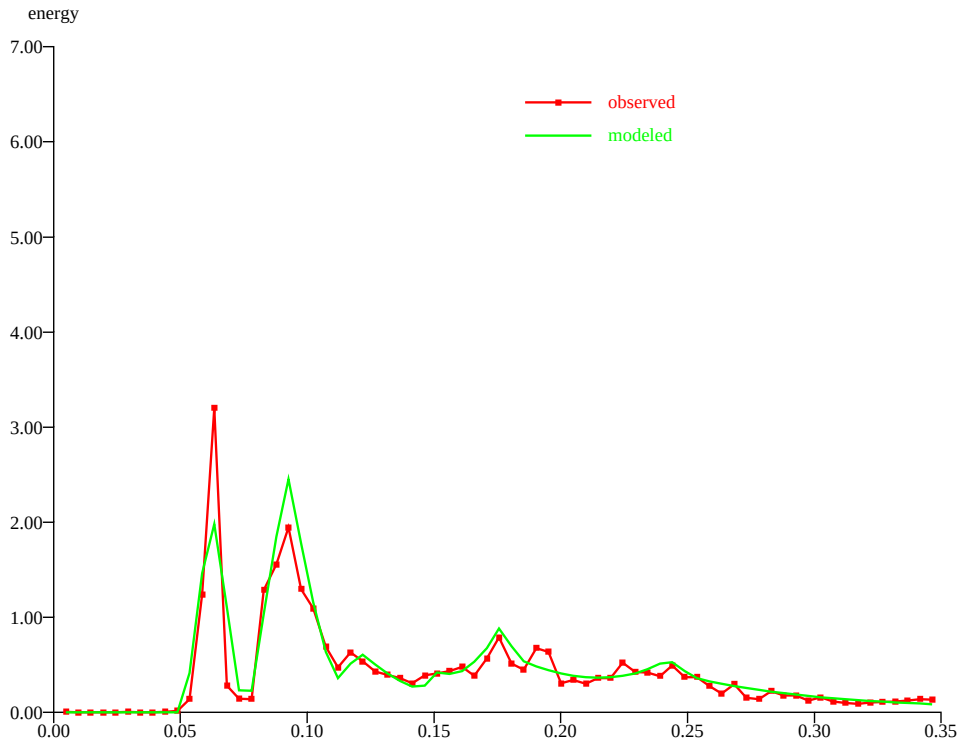

Bonga

For Bonga Wavescan measurements (figure 5.13), the above shape does not seem to be narrow enough. A triangle extending only from $\frac{8}{9}f_p$ to $\frac{9}{8}f_p$ gives a much better fit.

FIGURE 5.13 : Normalized shapes for Bonga Wavescan, 10%, 25%, 50%, 75%, 90% fractiles and average

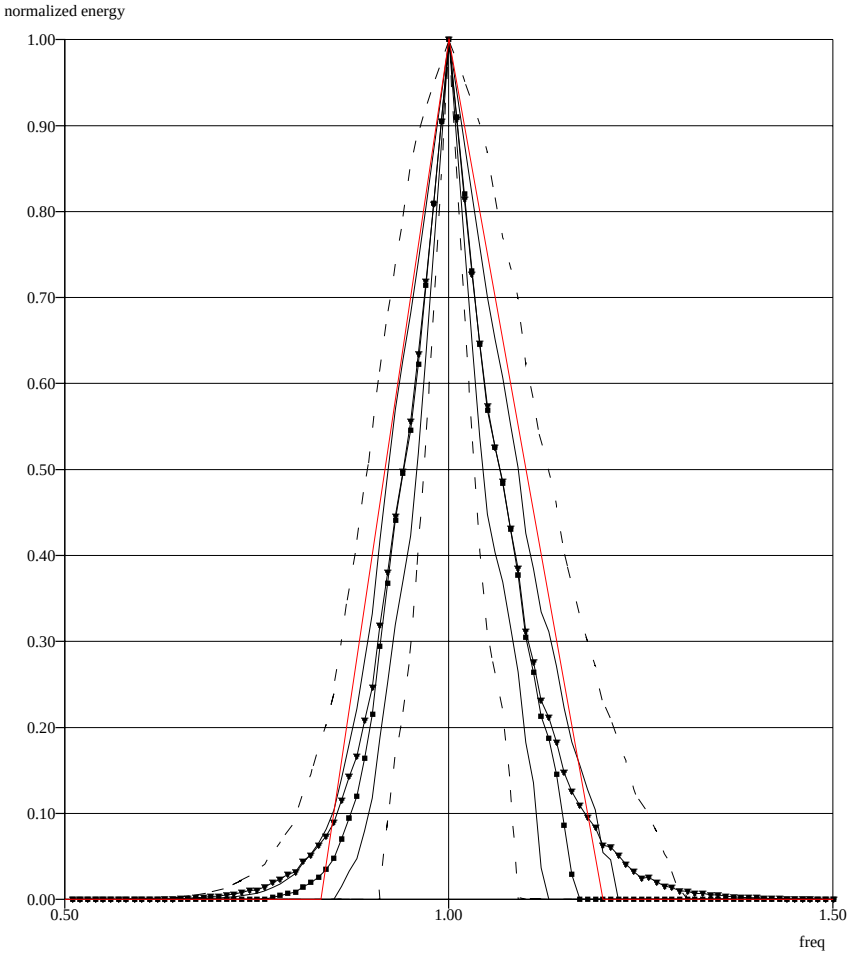

Chevron

For Chevron measurements (figure 5.14), on the opposite to Bonga, the width of the peaks seems much larger. However, the sampling frequency and recording durations are somewhat coarse, and may artificially widen the shape.

FIGURE 5.14 : Normalized shapes for Chevron data, 10%, 30%, 50%, 70%, 90% fractiles and average

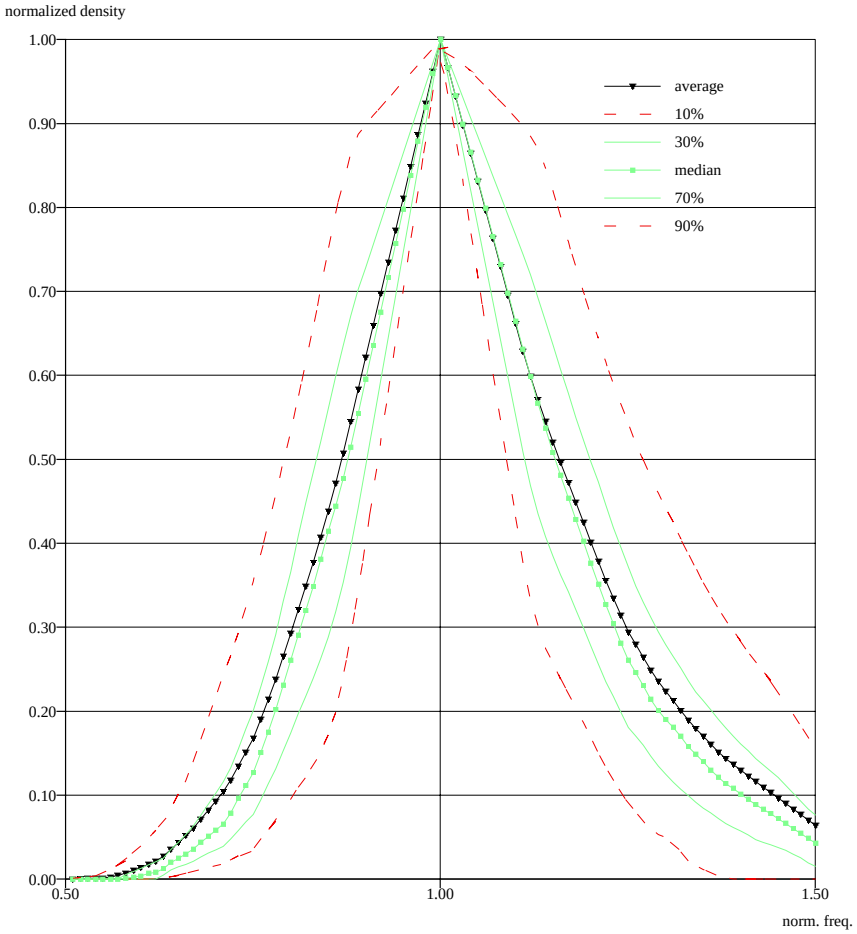

Recommended triangular shape

From those results, we suggest that an additional parameter should be used to control spectral width in addition to the normalizing ones H_S and T_p. The swell spectra can be chosen within the triangular family of triangles extending from $\frac{m-1}{m}\mathrm{f_p}$ to $\frac{m}{\mathrm{m-1}}f_\mathrm{p}$ and parameterized by the value m:

$$
\begin{aligned}
S(\mathrm{f}) &= \frac{2m(m\text{-}1)}{2m\text{-}1}\frac{H_\mathrm{s}^2}{16f_\mathrm{p}}\left(\mathrm{m}\frac{f}{f_p}-(\mathrm{m}-1)\right) && \frac{\mathrm{m\text{-}1}}{m}f_p<f<f_p \\
\mathrm{S(f)} &= \frac{2m(\mathrm{m}-1)}{2m-1}\frac{H_\mathrm{s}^2}{16f_\mathrm{p}}\left(\mathrm{m}-(\mathrm{m}-1)\frac{f}{f_p}\right) && f_p\le f<\frac{\mathrm{m}}{\mathrm{m\text{-}1}}f_p \\
\mathrm{S(f)} &= 0 && \textit{elsewhere}
\end{aligned}
\qquad \textbf{(EQ 5.3)}
$$

Spectral moments are given by:

$$M_p = \frac{H_s^2}{16} f_p^p \frac{2(m^{p+1} - (m-1)^{p+1})(m^{p+2} - (m-1)^{p+2})}{(p+1)(p+2)(2m-1)m^p(m-1)^p} \quad \text{(EQ 5.4)}$$

and thus

$$\begin{aligned} M_0 &= \frac{H_s^2}{16} \\ M_1 &= \frac{H_s^2}{16} f_p \left(1 + \frac{1}{3m(m-1)}\right) \\ M_2 &= \frac{H_s^2}{16} f_p^2 \left(1 + \frac{1}{3m(m-1)}\right)\left(1 + \frac{1}{2m(m-1)}\right) \\ M_4 &= \frac{H_s^2}{16} f_p^4 \left(1 + \frac{1}{m(m-1)} + \frac{1}{5m^2(m-1)^2}\right)\left(1 + \frac{1}{\frac{3}{4}m(m-1)} + \frac{1}{3m^2(m-1)^2}\right) \end{aligned} \quad \text{(EQ 5.5)}$$

Note that the peakedness factor Q_p is then $\frac{4m-2}{3}$ and thus m can be estimated as $\frac{3Q_p + 2}{4}$, with the usual definition of Q_p: (EQ 5.6)

$$Q_p = \frac{2}{M_0^2} \int_0^\infty f S^2(f) df \quad \text{(EQ 5.7)}$$

Also,

$$\varepsilon_2 = \frac{1}{\sqrt{6m(m-1)+2}} \quad \text{(EQ 5.8)}$$

References

[5.1] Brillinger, D.R., 2001, "Time Series: Data Analysis & Theory", *Soc. for Industrial & Applied Math*, p. 540.

[5.2] Harris, F.J., 1978, "On the Use of Windows for Harmonic Analysis with the Discrete Fourier Transform", *Proc. IEEE*, vol. 66, no. 1, pp. 51-84.

CHAPTER 6

Partitioning and parameterization of spectra

Kevin Ewans

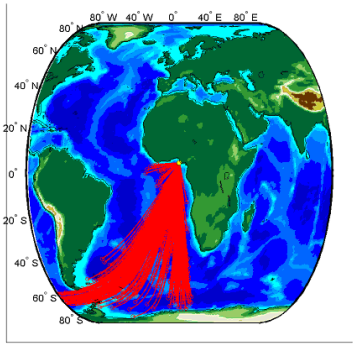

The objective of the swell parameterisation work is to obtain the most appropriate spectral description of the swell components in the West African sea-states. This involved partitioning each wave spectrum into wind-sea and swell components, and then fitting each individual swell partition with the frequency spectrum shapes – Normal, lognormal, triangle, and JONSWAP-Glenn. In addition, for those data for which a directional analysis was possible, a Wrapped-normal directional distribution was fitted to the directional distribution.

The partitioning is described in the next section, followed by the parameterisation of the spectra.

Partitioning

The partitioning of the spectra into wind-sea and swell partitions was performed using the program *APL Waves*, developed by the Applied Physics Department of Johns Hopkins University (Hanson and Phillips, 2000, [6.1]). The input to the program is a data file of wave frequency-direction spectra. The program then partitions the 3D spectrum into separate peaks as in the example of figure 6.1.

A number of parameters can be set within *APL Waves* to optimise the partitioning for a particular data set.

- **Wave height threshold setting**. The purpose of these is to reduce the "noise" resulting from small isolated peaks in the input directional wave spectra. Wave systems falling below these significant wave height thresholds are excluded in the output files. Separate thresholds for wind-sea and swell components are set.
- **Wind-sea multiplier**. This parameter is used to determine if a wave system is classified as wind-sea or swell. A wave system is grouped as wind-sea if it is forced by the local wind such that the mean phase speed of the waves, c_p, is less than or equal to the wind speed component in the direction of the waves ($U_{10}\cos\delta$) when multiplied by the wind-sea multiplier *wsmult*

  Hence, if $c_p \le wsmult\, U_{10}\cos\delta$, then the wave system is wind-sea.

- **No. Swells per Record**. This sets the number of swells allowed per observation. This value was set to 5 for analyses in WASP.
- **Spread Factor**. This sets the minimum polar distance between adjacent peaks in order for them to consider separate peaks.
- **Swell Separation Angle**. If the directions of adjacent wave spectrum peaks are within the swell separation angle, the peaks are combined.
- **Largest Record Gap**. This is the upper limit to consecutive missing records allowed in a swell group.
- **Minimum number of records**. This is the minimum number of records for a swell group to be considered valid.

FIGURE 6.1 : Schematic wave frequency-direction spectrum, showing different partitions.

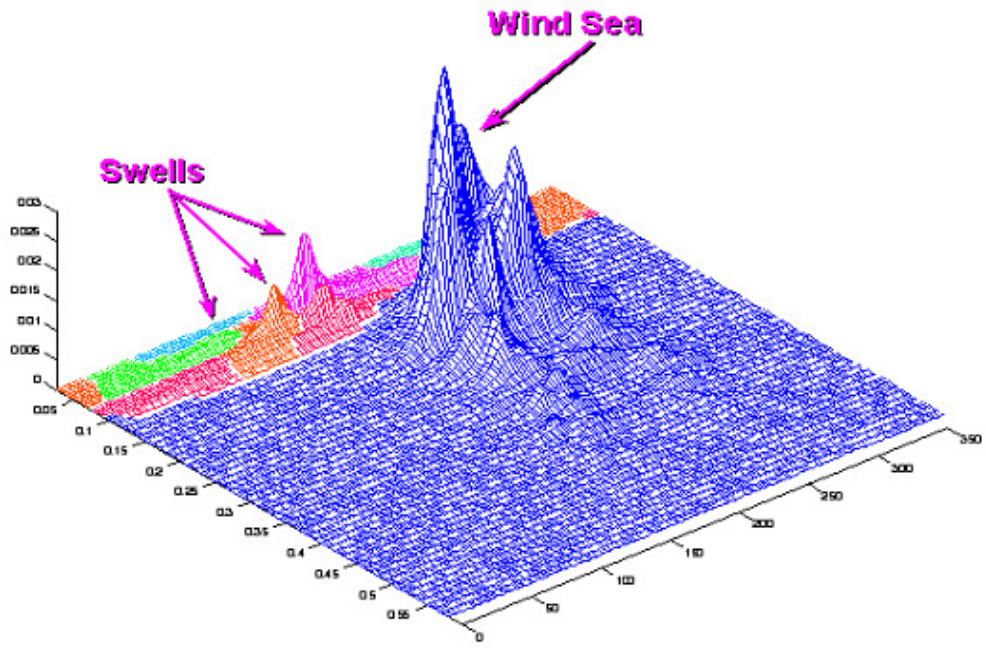

If wind data are not available to determine the wind sea component, the wind speed and direction is estimated from the spectrum by means of an iterative process based on the method of Wang and Hwang (2001)[6.3].

Frequency-direction spectra are required for input to the partitioning analysis. These are directly available in the case of the hindcast dataset, but they must be derived in the case of the measured data. The standard approach for doing this is to follow the technique proposed by Longuet-Higgins et al. (1963)[6.2], in which the directional distribution is expanded as Fourier series. Unfortunately, most directional wave measurement systems, including heave-pitch-roll buoys, provide a limited number of Fourier Coefficients, and the determination of the directional distribution is not accurate. As a result there has been a number of possible ways proposed to compute the directional distribution to try and optimize the estimate, and the choice of a particular method is somewhat arbitrary. Perhaps the most popular methods are the Maximum Likelihood Method (MLM) and the Maximum Entropy Method (MEM). These two were used to derive the frequency-direction spectra for some test data for comparison, but the MEM was found to provide swell sources estimates with better directional resolution than the corresponding MLM

estimates. Accordingly, the MEM estimates were used for the partitioning analyses.

Swell groups are constructed from swell partitions that are likely to originate from the same region and source winds. Swell events are identified from these groups and the generation time and location of the event is calculated.

Results

General

The wave spectrum partitioning was run on the operational and QSCAT hindcast data sets as well as the directional measured data sets. Figure 6.2 is an example of the spectral partitioning. The plot shows a spectrum with two swell partitions; the two partitions overlap in frequency, indicating that they also have different directions.

FIGURE 6.2 : One dimensional representation of spectral partitions. This example contains two swell partitions.

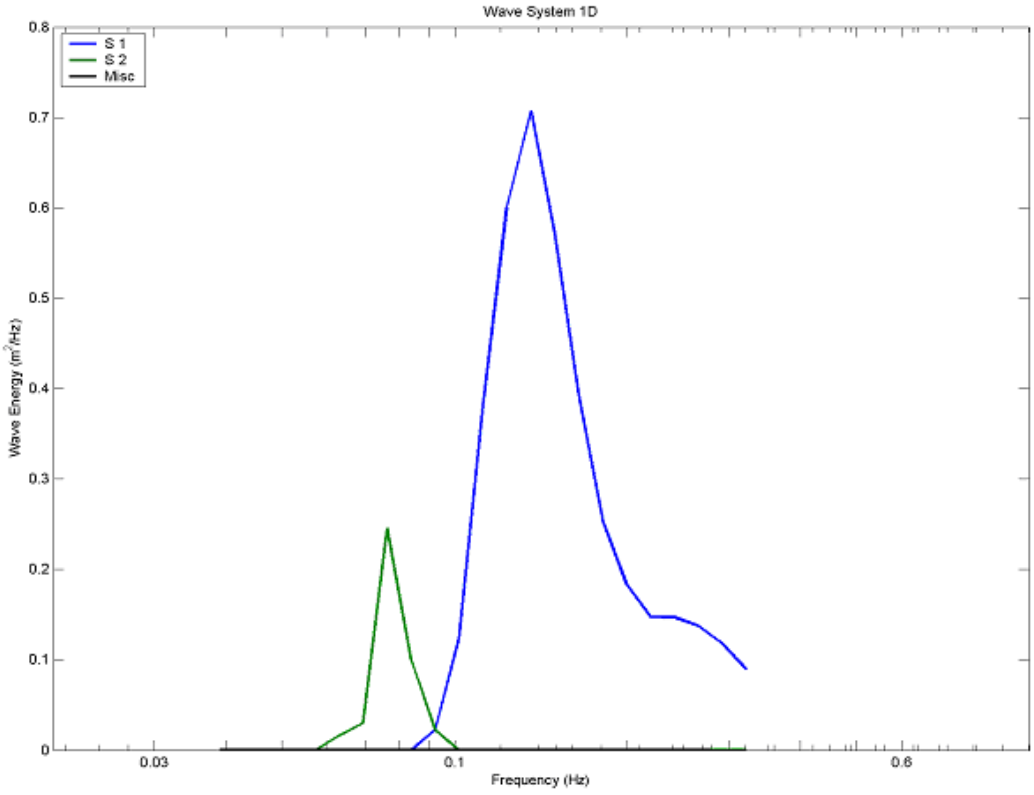

A plot of the great circle paths of swells from source to observation point, resulting from APL Waves analysis of QSCAT hindcast grid point 28793 is given in figure 6.3. The equivalent plots for all the data sets are given in Appendix 6.2.

A wave vector history diagram for a one month section of the QSCAT hindcast grid point 28793 is given in figure 6.4. The wave partition vectors are given in the upper plot; the wind vectors are given in the lower plot. The vectors in the upper plot are positioned at the mean frequency of the partitions, and the length and direction of

the vectors gives respectively the significant wave height and direction of the partition.

FIGURE 6.3 : Great circle paths of swells from source to observation point, resulting from APL Waves analysis of QSCAT hindcast grid point 28793.

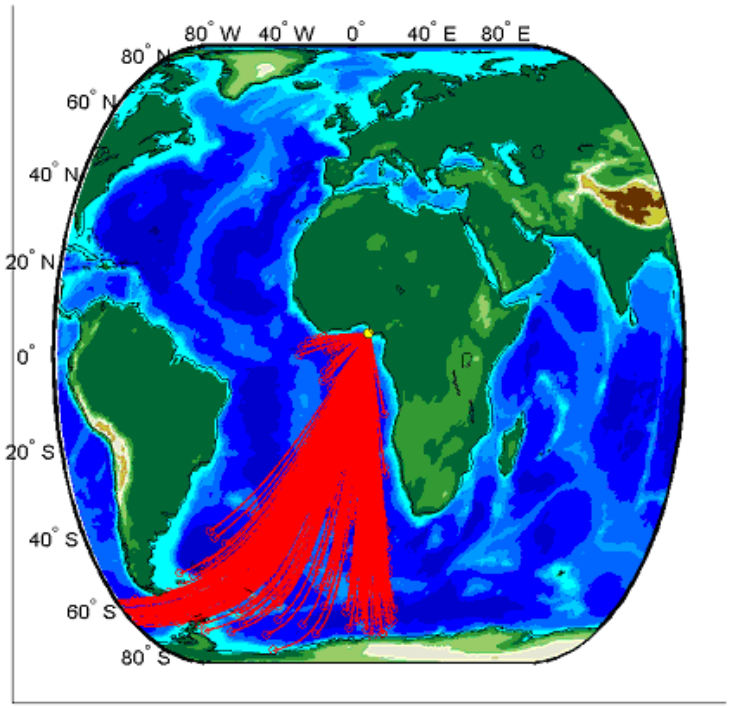

FIGURE 6.4 : System vector diagram of 1-month of partitions for the QSCAT 28793 (Bonga) data set

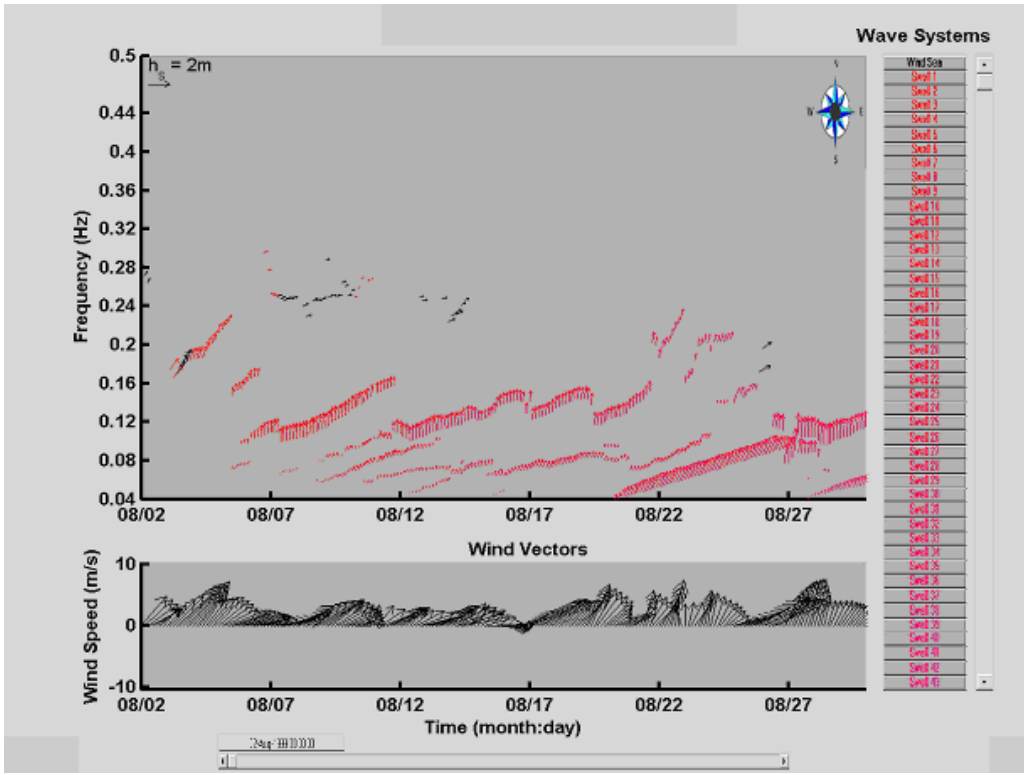

Comparison of QSCAT and Measured Data Partition Tracks

Figures 6.5 and 6.6 present swell system tracks for the Bonga and Kudu locations respectively. The upper and lower left plots give tracks for respectively MLM and MEM directional spectra, and lower right plot gives tracks for the QSCAT directional spectra. It is clear from the plots that the tracks of the MEM spectra are more similar to the QSCAT tracks than the MLM tracks are. It is also interesting to note the analysis of the measured data sets for the Kudu location indicates the existence of swell sources in the North Atlantic. The Bonga and Kudu locations were the only locations for which reliable measured directional wave data existed.

Spectral Parameterisation

Introduction

The objective of the spectral parameterisation work is to obtain a good spectral description of the swell frequency spectrum. Four spectral functions, as described in Chapter 4, were evaluated. This involved fitting spectral functions to the partitioned spectra, and then comparing the fits with the original spectrum.

Method

Following partitioning of the spectra, the frequency-direction spectrum is partitioned into separate regions – each partition corresponding to a swell or a wind-sea component, with of course a maximum of one wind-sea partition per spectrum. The frequency spectrum of each partition is calculated, by integrating over direction, and fit with each of the four spectral functions – Gaussian, lognormal, triangle, and JONSWAP-Glenn, as described in Chapter 4. The fit was performed by the method of least squares.

The fit spectral functions are summed over the partitions, resulting in four model estimates of the frequency spectrum of the total sea-state. In all cases the JONSWAP-Glenn spectrum is used to describe the wind-sea; the four models then consist of a JONSWAP-Glenn wind-sea added to a Gaussian, lognormal, triangle, or JONSWAP-Glenn fit to all the swell components.

The model spectra are then compared against the original spectra to deduce the best function for describing the swell.

The analysis was performed for the WANE OPR and QSCAT data sets and the measured spectral data, but for efficiency the evaluations were mostly restricted to the QSCAT data set on account of the better definition of wind-sea component possible with the QSCAT winds and for efficiency.

Results - Frequency spectrum comparisons

The frequency spectrum comparisons involve a comparison of the spectral amplitudes at each frequency. For example, figure 6.7 gives scatter plots of the model spectral amplitudes against the measured spectral amplitudes at 0.052 Hz for the QSCAT 28678 (Côte d'Ivoire) grid point. The correlation coefficient indicates that on average the lognormal spectral fits gives the best fit at this frequency for this data set.

FIGURE 6.5 : Swell system tracks for the Bonga location. Upper and lower left plots give tracks for respectively MLM and MEM directional spectra for the Bonga Directional Waverider data. Lower right plot gives tracks for the QSCAT 28793 location.

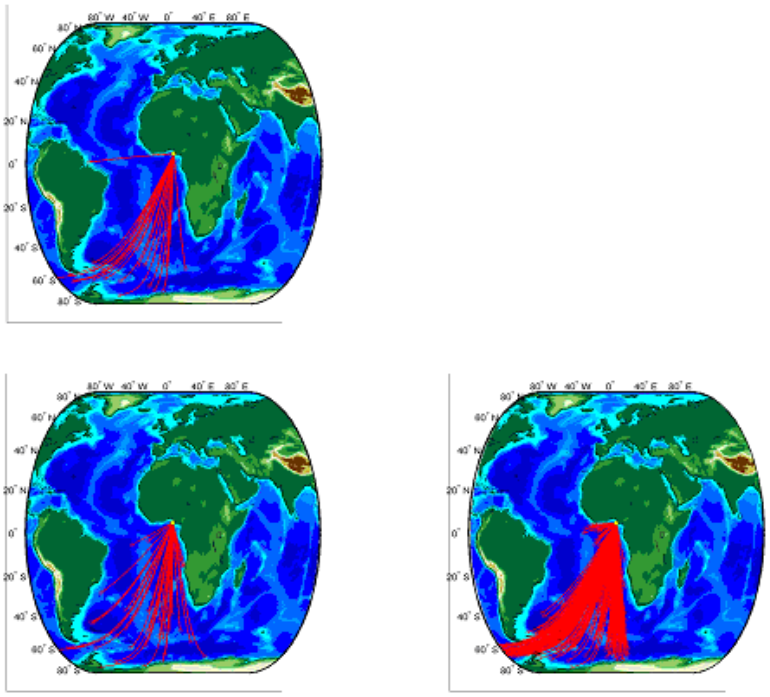

FIGURE 6.6 : Swell system tracks for the Kudu location. Upper and lower left plots give tracks for respectively MLM and MEM directional spectra for the Kudu Directional Waverider data. Lower right plot gives tracks for the QSCAT 19573 location.

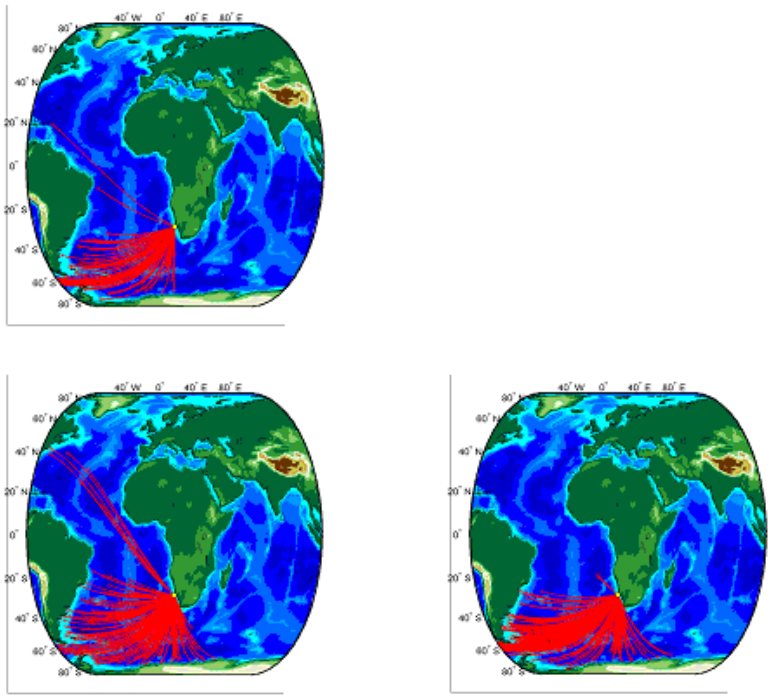

Figures 6.8, 6.9, and 6.10 give the corresponding scatter plots for spectral estimates at frequencies 0.063 Hz, 0.0763 Hz, and 0.0924 Hz respectively. In general, the lognormal model also gives the best fit to the spectra for these frequencies for this data set.

A more concise presentation of the goodness of fit for each frequency is given in figure 6.11. In this figure the rms spectrum, the rms error, and the scatter index is given as a function of frequency, for each model.

The rms spectrum, $G_{rms}(f)$, of N measured spectra, $G_i(f)$, is defined by

$$G_{rms}(f) = \sqrt{\frac{1}{N}\sum_{i=1}^{N} G_i^2(f)} \qquad \textbf{(EQ 6.1)}$$

The rms error is defined by

$$G_{error}(f) = \sqrt{\frac{1}{N}\sum_{i=1}^{N} (G_i(f) - G_i'(f))^2} \qquad \textbf{(EQ 6.2)}$$

where $G_i'(f)$ is the i^{th} model spectrum.

The spectral scatter index is given by

$$G_{SI}(f) = \frac{G_{error}(f)}{G_{rms}(f)} \qquad \textbf{(EQ 6.3)}$$

The rms spectrum in figure 6.11 is that of the measured spectrum and is therefore the same for each spectral model. It indicates that on average the most energetic part of the spectrum is at 0.10 Hz. The rms error is lowest for the lognormal and JONSWAP-Glenn functions over most of the bandwidth. However, the scatter index shows that at very low frequencies (around 0.050 Hz), the lognormal performs better than the JONSWAP-Glenn model. This is more easily seen in figure 6.12, although figure 6.12 also shows that the JONSWAP-Glenn model does give a slightly better description at frequencies around the spectral peak, for this data set.

FIGURE 6.7 : Scatter plot of the model spectral amplitude (fit) against the original spectral amplitude (measured) at 0.052 Hz for the QSCAT 28678 (Côte d'Ivoire) grid point. The upper left plot is that for the Gaussian swell model, the upper right is that for the Lognormal swell model, the lower left is that for the Triangle swell model, and the lower right is that for the JONSWAP-Glenn spectral model. The correlation coefficient is given in the lower right corner of each plot.

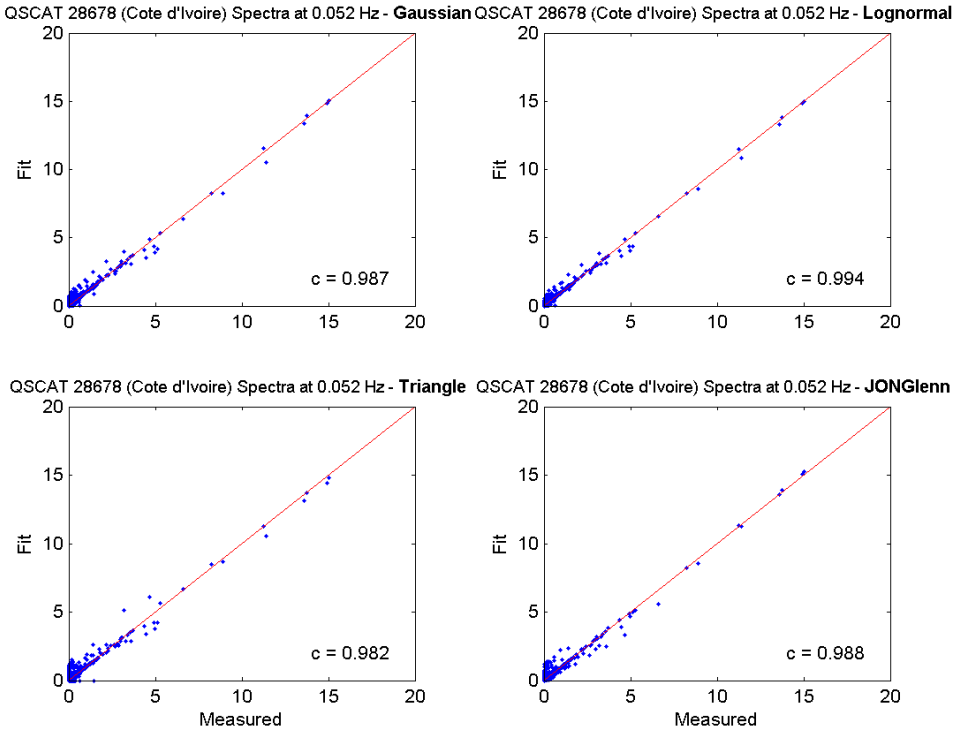

FIGURE 6.8 : Scatter plot as for figure 6.7 but for 0.063 Hz.

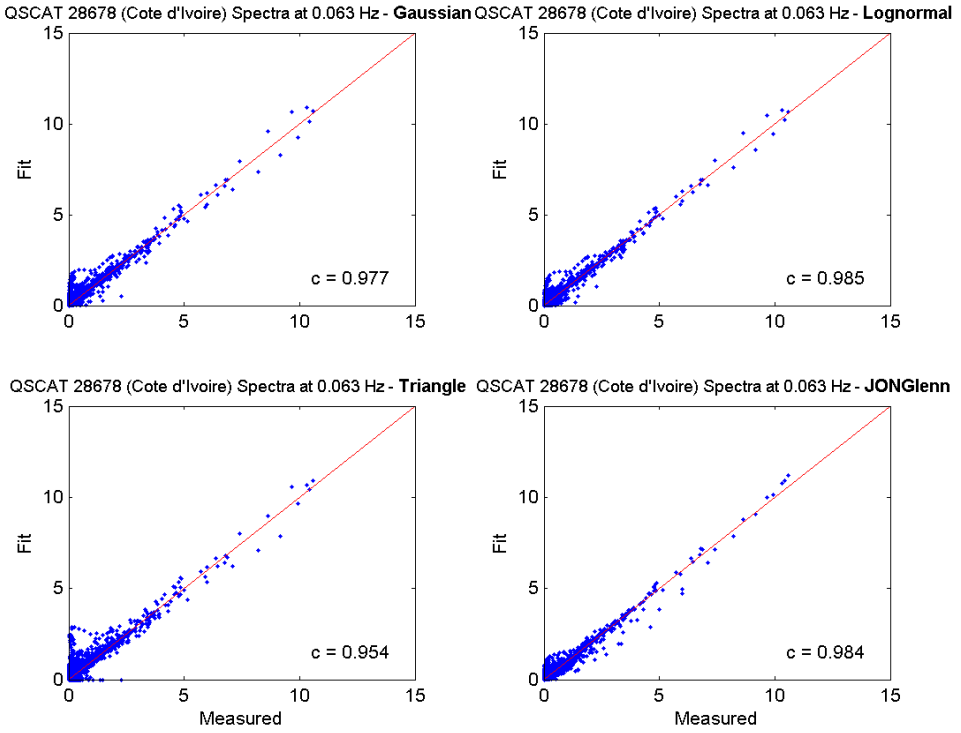

FIGURE 6.9 : Scatter plot as for figure 6.7 but for 0.0763 Hz.

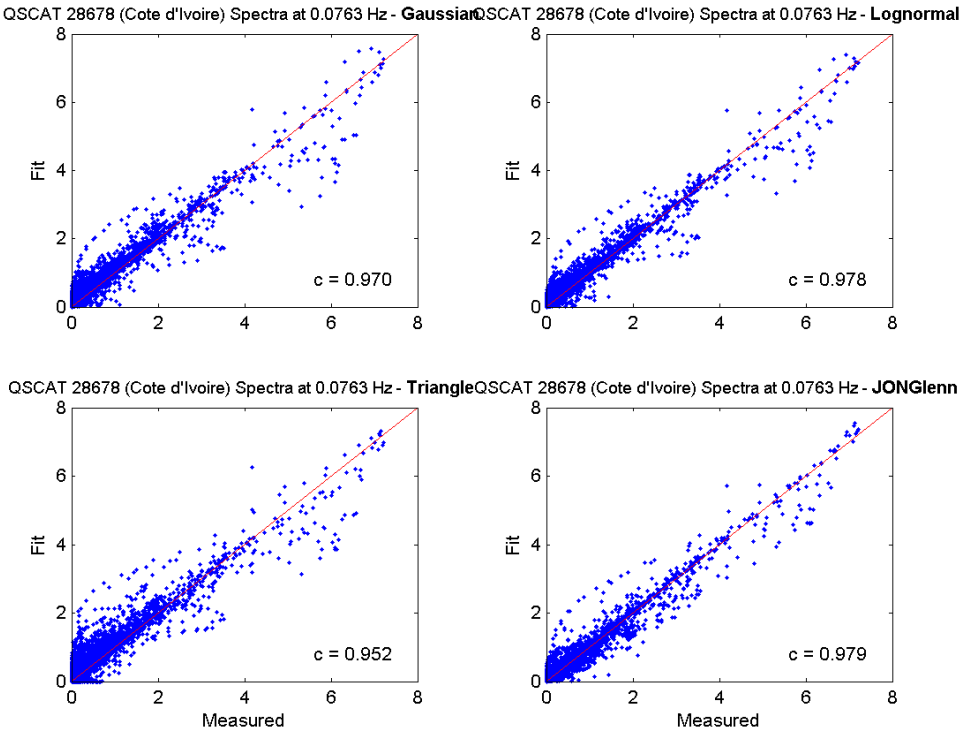

FIGURE 6.10 : Scatter plot as for figure 6.7 but for 0.0924 Hz.

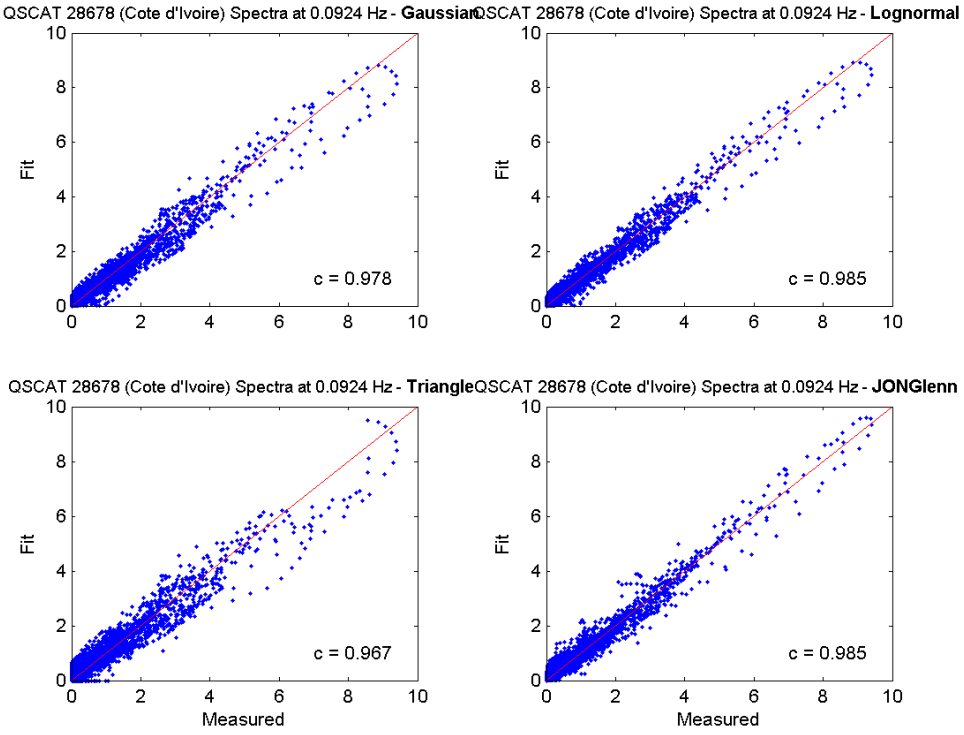

FIGURE 6.11 : RMS spectrum, rms error, and scatter index as a function of frequency for each spectral model, for the QSCAT 28678 (Côte d'Ivoire) grid point.

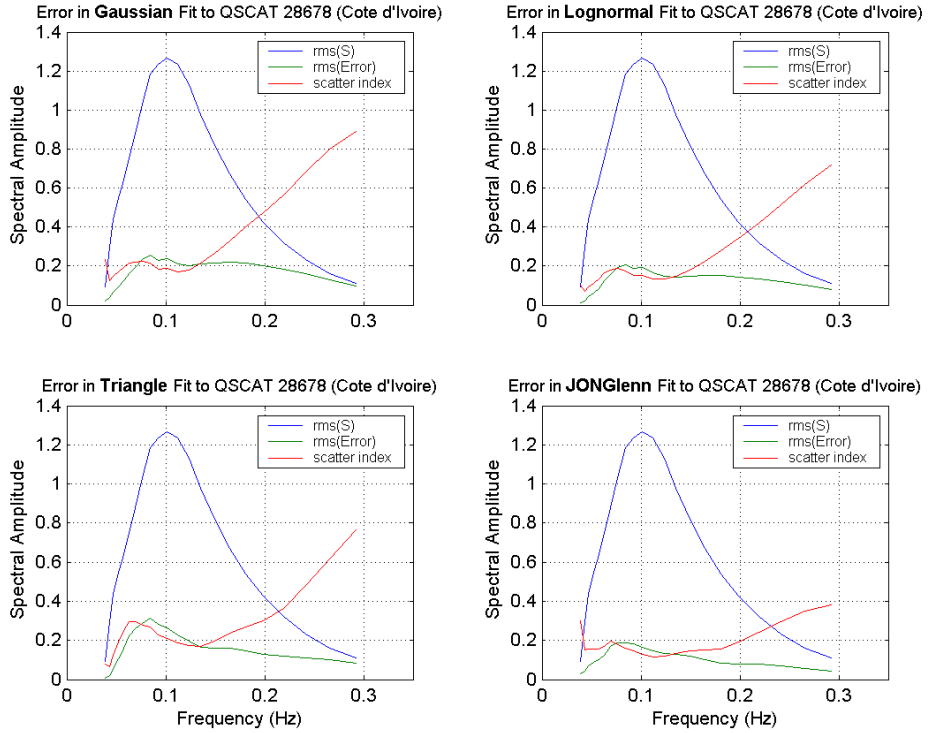

FIGURE 6.12 : RMS spectrum and scatter index as a function of frequency for each spectral model, for the QSCAT 28678 (Côte d'Ivoire) grid point.

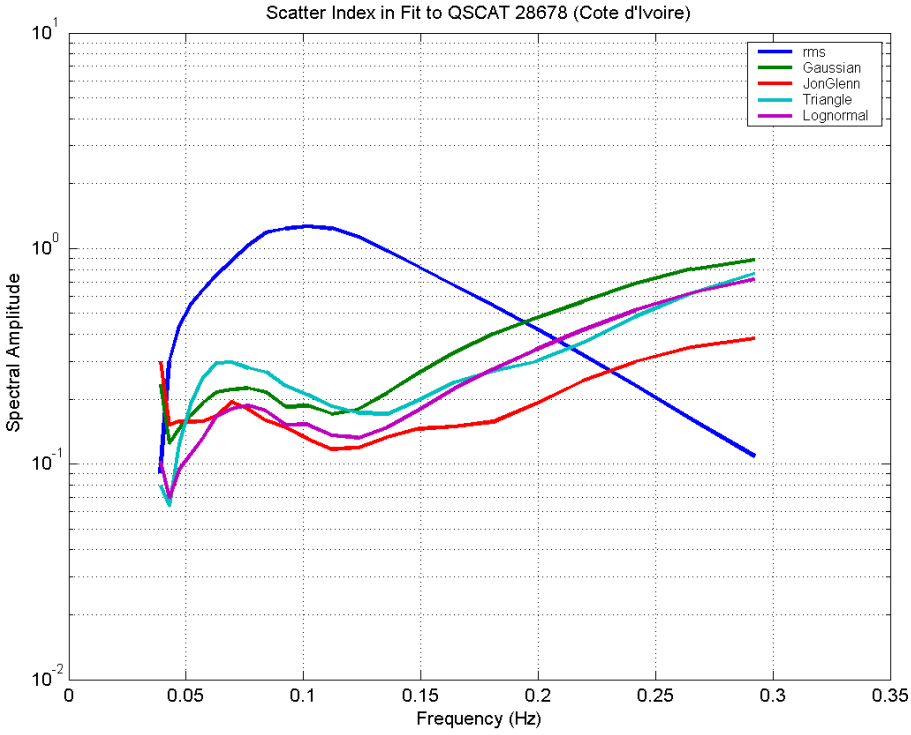

Equivalent figure for the QSCAT data sets at Bonga, Nemba, Namibia, and Kudu are given in figure 6.13, 6.14, 6.15, and 6.16 respectively. These sites are more or less equally spaced north to south along the West African coast. The plots show that the lognormal model has the lowest SI for frequencies less than 0.08 Hz, indicating the low frequency tail is best described with the lognormal spectrum on average. The JONSWAP-Glenn SI is approximately the same as that of the lognormal for frequencies between 0.08 Hz to say 0.13 Hz, for the Bonga, Nemba, and Namibia data, but has clearly the lowest SI for frequencies above 0.08 Hz at the Kudu site. This later observation is consistent with an increasing contribution of the local wind-sea to wave spectra the further south is the location, for which a JONSWAP-Glenn spectrum, with a high frequency f^{-5} tail, is expected to provide the best description. At the Kudu location, the wind-sea component dominates.

Comparable plots for the measured data are given in figures 6.17 to 6.22.

The scatter index spectra of the measured data (figures 6.17 to 6.22) also indicate that the lognormal model provides the best fit to the spectral shape at frequencies below 0.07 Hz, in general. However, the JONSWAP-Glenn spectrum appears to be a better model than lognormal for frequencies above 0.07 Hz in most cases. By comparison, this trend only appeared in the QSCAT data for frequencies greater than 0.13 Hz.

It is also of interest that the trend in the scatter indices in figure 6.17, in which the directional distributions are computed using MEM, is largely similar to that in figure 6.18, in which the directional distributions are computed assuming the directional distribution follows a cos2s distribution. This is important as the cos2s distribution needs to be assumed to allow partitioning of non-directional data using the Johns Hopkins program.

FIGURE 6.13 : RMS spectrum and scatter index as a function of frequency for each spectral model, for the QSCAT 28793 (Bonga) grid point.

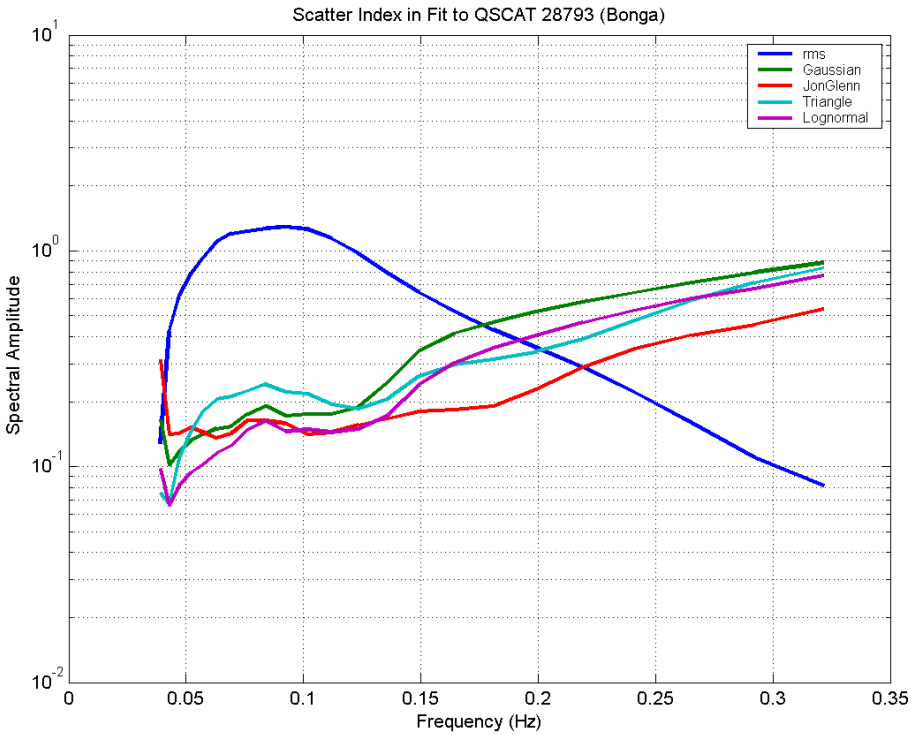

FIGURE 6.14 : RMS spectrum and scatter index as a function of frequency for each spectral model, for the QSCAT 26099 (Nemba) grid point.

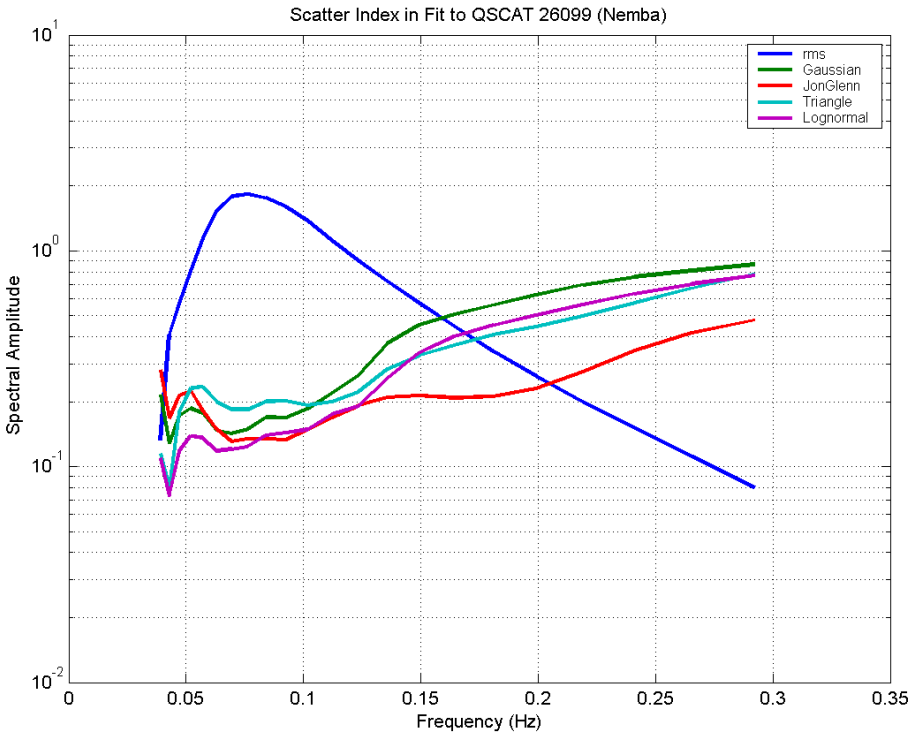

FIGURE 6.15 : RMS spectrum and scatter index as a function of frequency for each spectral model, for the QSCAT 22917 (Namibia) grid point.

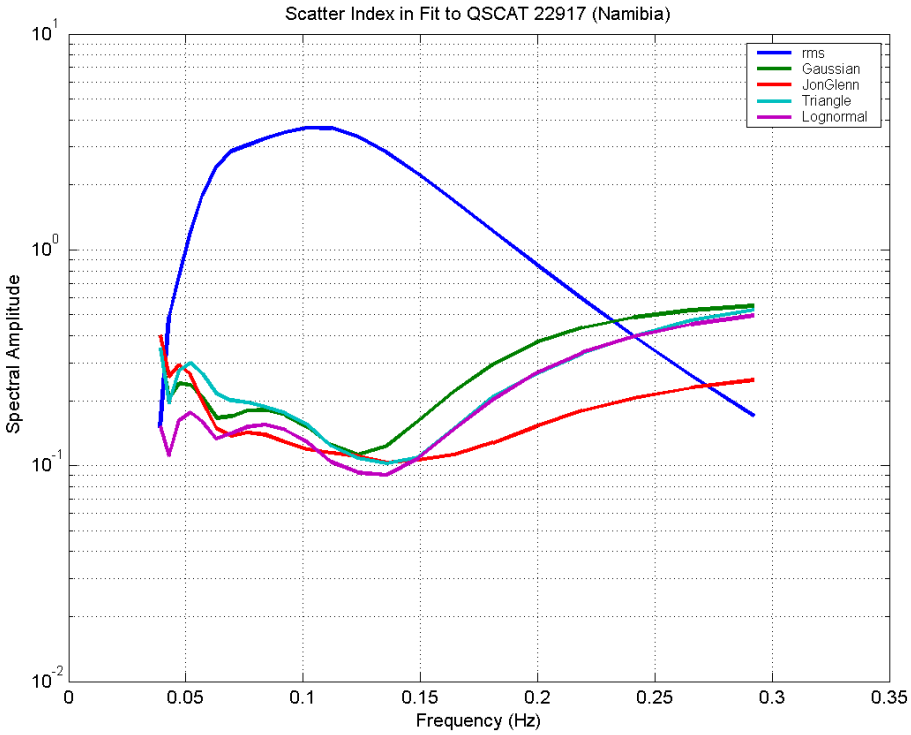

FIGURE 6.16 : RMS spectrum and scatter index as a function of frequency for each spectral model, for the QSCAT 19573 (Kudu) grid point.

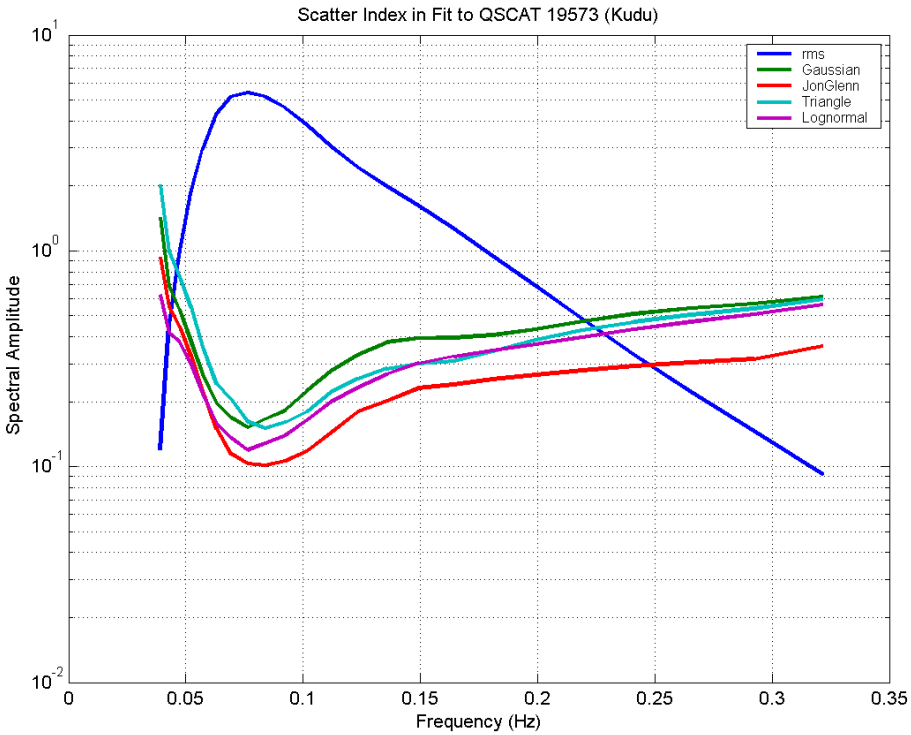

FIGURE 6.17 : RMS spectrum and scatter index as a function of frequency for each spectral model, for the Bonga DWR data set, with frequency-direction spectra computed by MEM.

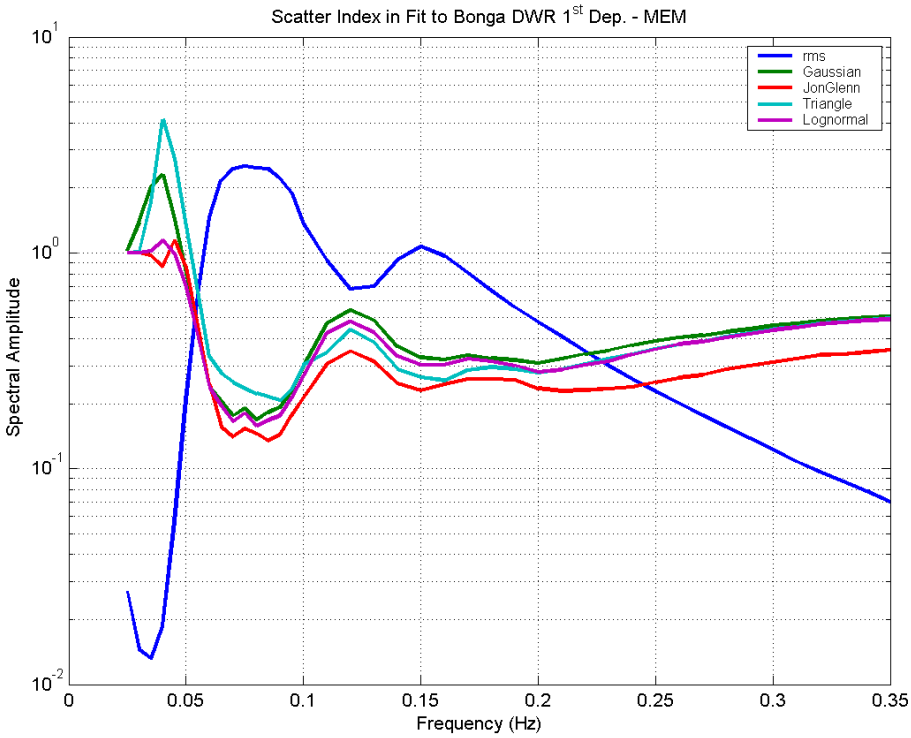

FIGURE 6.18 : RMS spectrum and scatter index as a function of frequency for each spectral model, for the Bonga DWR data set, with frequency-direction spectra computed by Cos2s

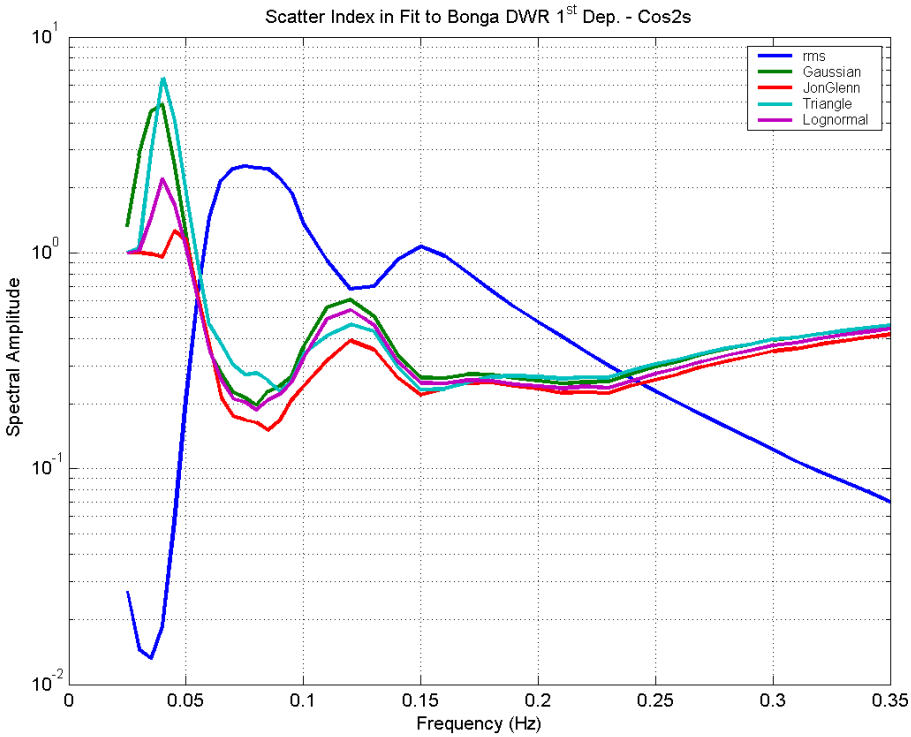

FIGURE 6.19 : RMS spectrum and scatter index as a function of frequency for each spectral model, for the Ekoundou data set

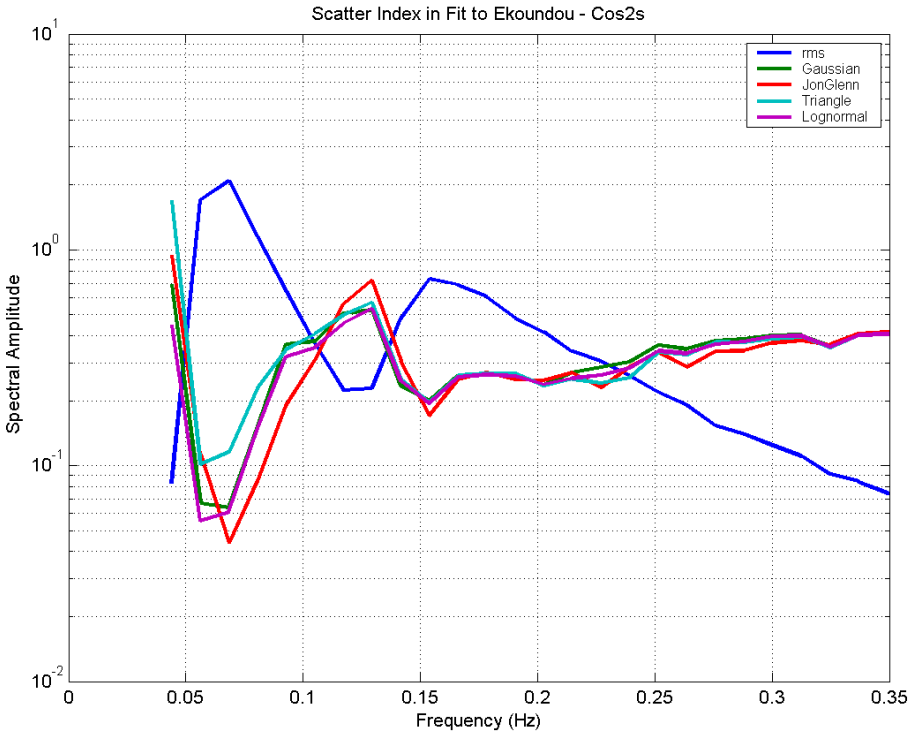

FIGURE 6.20 : RMS spectrum and scatter index as a function of frequency for each spectral model, for the Chevron 8m water depth data set

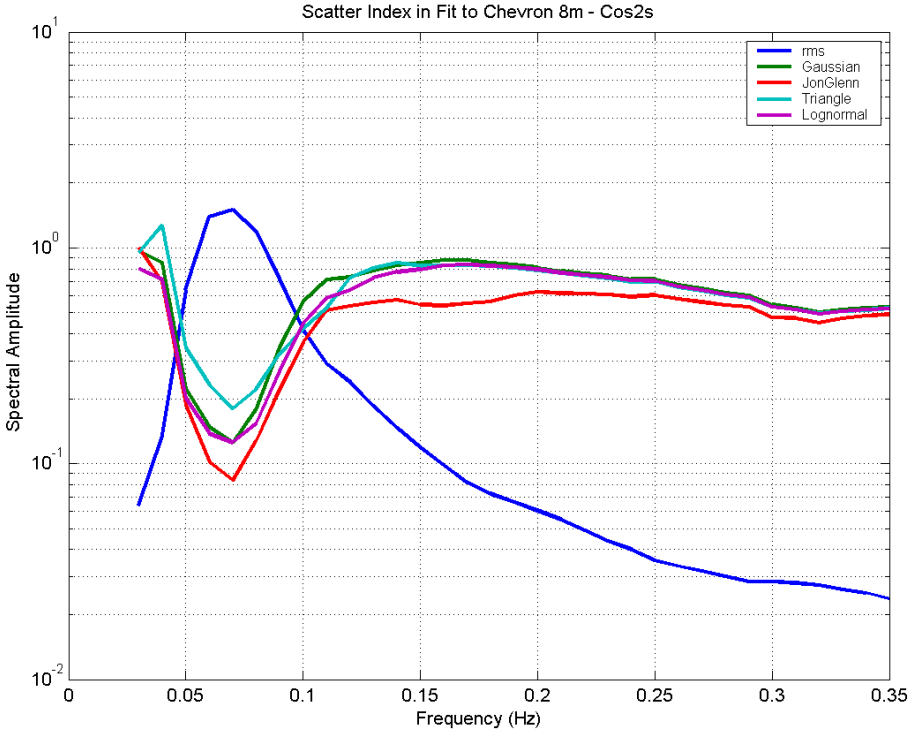

FIGURE 6.21 : RMS spectrum and scatter index as a function of frequency for each spectral model, for the Chevron 85m water depth data set

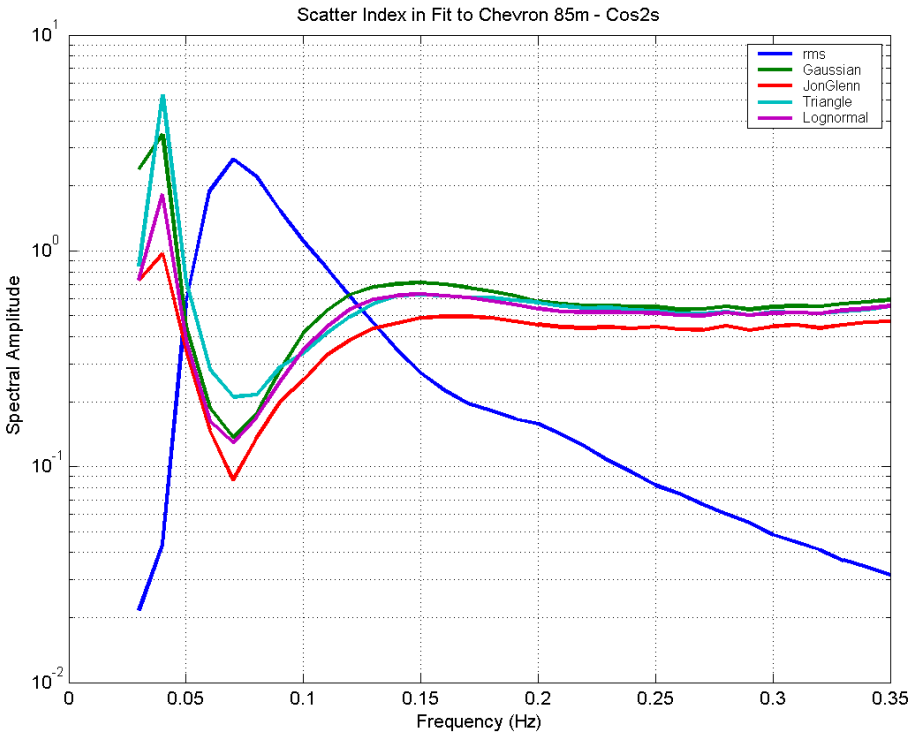

FIGURE 6.22 : RMS spectrum and scatter index as a function of frequency for each spectral model, for the Kudu DWR data set

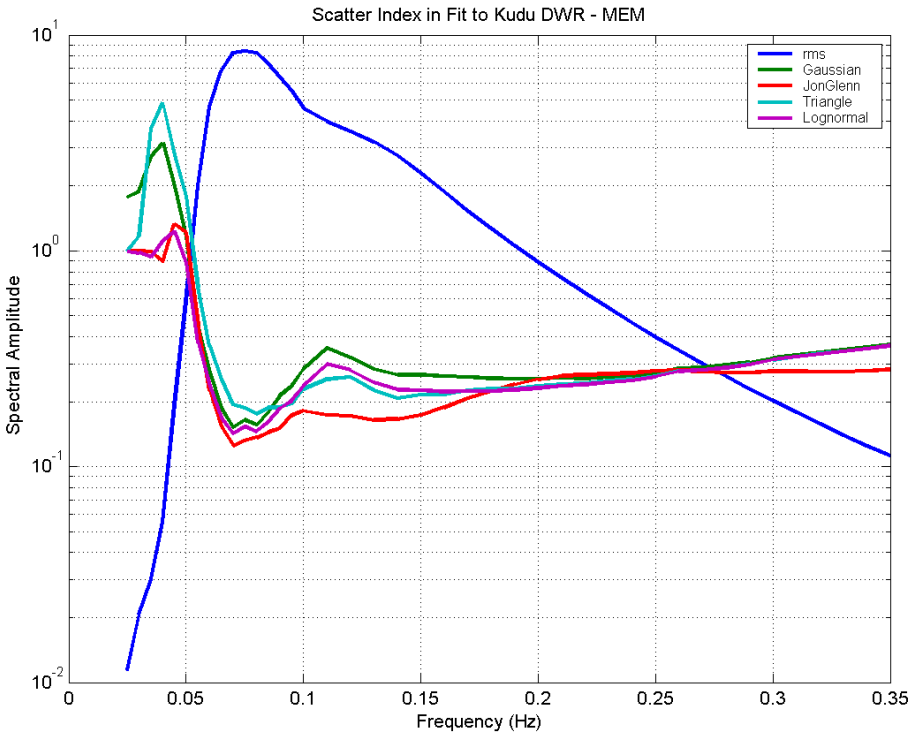

Results - Single Degree of Freedom Oscillator Comparisons

The single degree of freedom oscillator (SDF) comparisons involves a comparison of the SDF response derived from the measured spectrum with the modelled spectrum.

The SDF response, $R(f)$, is given by

$$R(f) = T^2(f)G(f) \quad \textbf{(EQ 6.4)}$$

where $T(f)$ is the SDF amplitude transfer function (see Chapter 7).

Now, $T(f) = T(f\,;\,T_p, \xi)$ **(EQ 6.5)**

where T_p is the natural or peak period and ξ is the damping of the SDF.

Accordingly, the responses were calculated for a number of SDF amplitude transfer functions over a range of T_p and ξ to capture the effects of different natural periods and damping. Thus, sixteen T_p values over the range 10 – 26s, and six ξ values over the range 0.05 – 0.30 were used, giving a total of 96 different response functions.

Comparisons were made from SDF rms response amplitude derived from the measured against that derived from the modelled spectrum. By way of example, figure 6.23 gives scatter plots of the SDF response rms amplitude from the model spectrum (fit) against that from the original spectrum (measured) for a SDF transfer function with parameters $T_p = 10\text{s}$, and $\xi = 0.05$, for the QSCAT 28678 (Côte d'Ivoire) grid point. The upper left plot is that for the Gaussian swell model, the upper right is that for the lognormal swell model, the lower left is that for the triangle swell model, and the lower right is that for the JONSWAP-Glenn spectral model. The correlation coefficient is given in the lower right corner of each plot. Each point in these plots represents the rms amplitude response corresponding to one spectrum.

Figure 6.23 shows that all four models give a reasonable description of the measured spectrum in terms of the rms amplitude response, but the spread of points about the straight line is lowest for the Lognormal and the JONSWAP-Glenn spectral models. Comparable plots for responses of SDFs with different transfer function parameters are given in figures 6.24, 6.25, and 6.26.

The transfer function for figure 6.24 has the same natural period as that for figure 6.23 but with substantially higher damping. This transfer function is therefore much less peaked and less sensitive to differences in the shape of the spectrum around T_p - in this case 10s. The lognormal model response provides the best agreement with the original spectrum response in this case, marginally better than that from the JONSWAP-Glenn spectrum.

The transfer function associated with the data in figure 6.25, with $T_p = 26\text{s}$, and $\xi = 0.05$, is highly sensitive to differences in spectral levels in a narrow-band of frequencies around 0.04 Hz. Figure 6.25 shows that the responses to the triangle and lognormal spectral models provide the best agreement with those of the measured spectra, with the lognormal spectrum showing marginally better skill.

When the damping of the transfer function associated with the data in figure 6.25 is increased to $\xi = 0.30$ (figure 6.26) the JONSWAP-Glenn spectrum that shows comparable skill to the lognormal spectrum.

FIGURE 6.23 : Scatter plot of the SDF response rms amplitude from the model spectrum (fit) against that from the original spectrum. (measured) for T_p = 10s, and ξ = 0.05 for the QSCAT 28678 (Côte d'Ivoire) grid point. The correlation coefficient is given in the lower right corner of each plot.

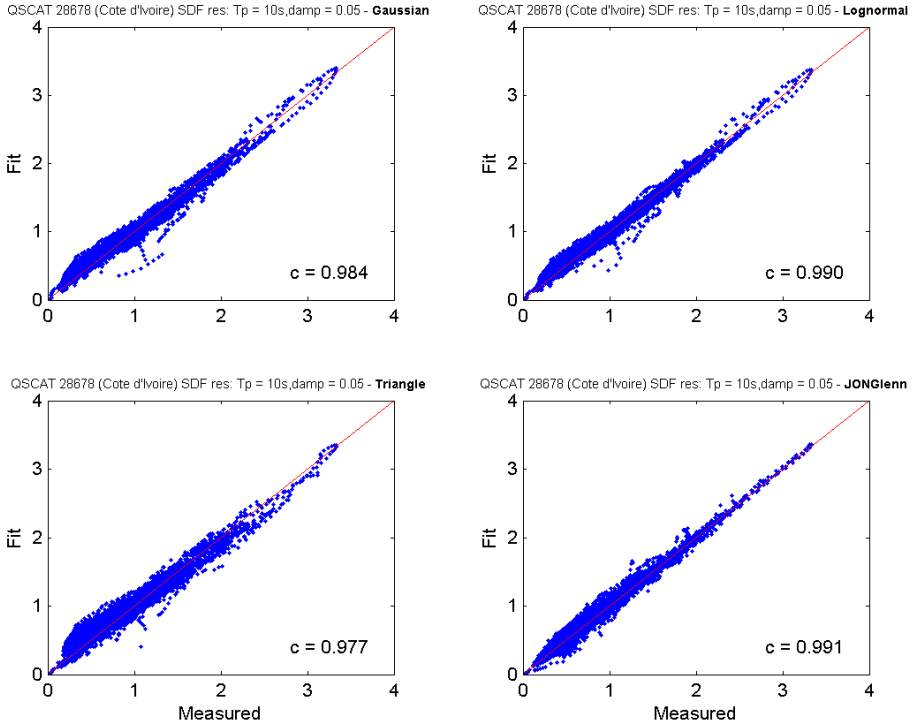

FIGURE 6.24 : Scatter plot as for figure 6.23 but for T_p = 10s, and ξ = 0.30 SDF transfer function parameters.

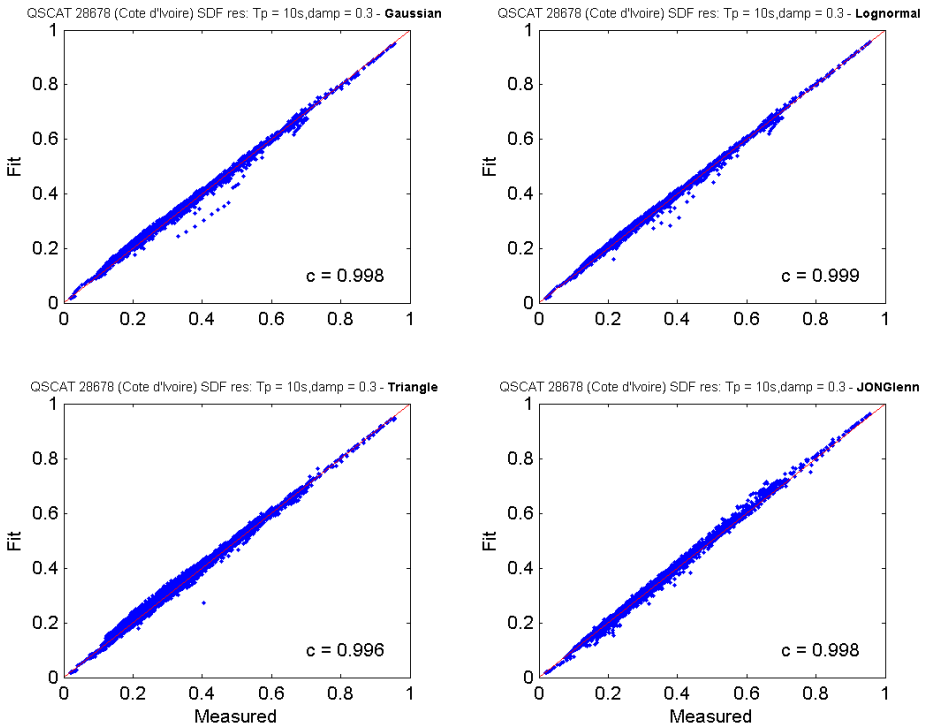

FIGURE 6.25 : Scatter plot as for figure 6.23 but for T_p = 26s, and ξ = 0.05 SDF transfer function parameters.

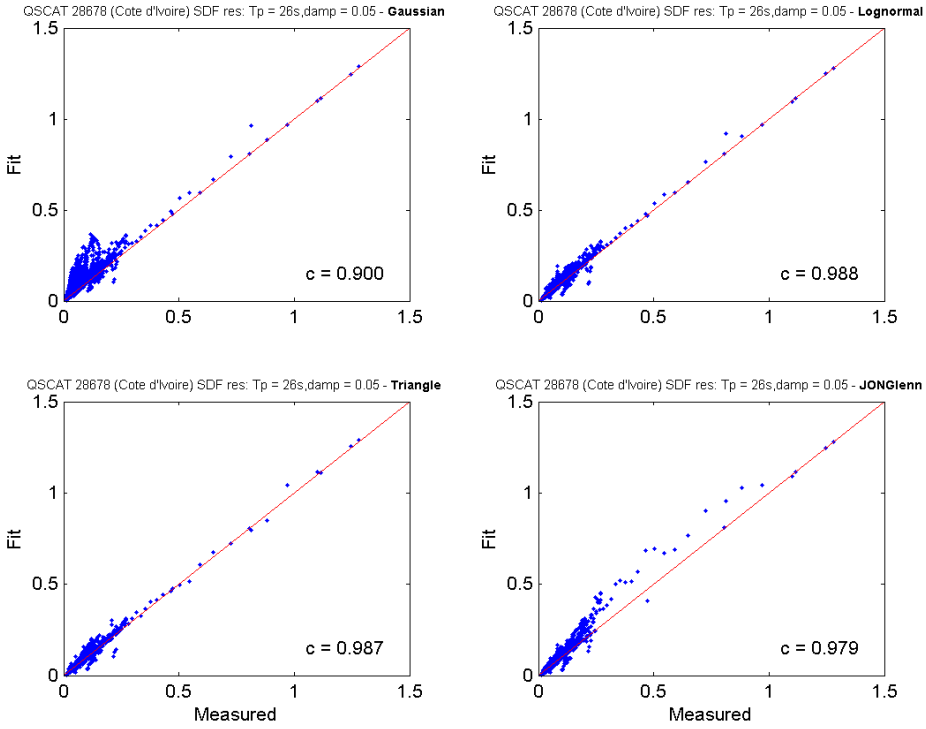

FIGURE 6.26 : Scatter plot as for figure 6.23 but for T_p = 26s, and ξ = 0.30 SDF transfer function parameters.

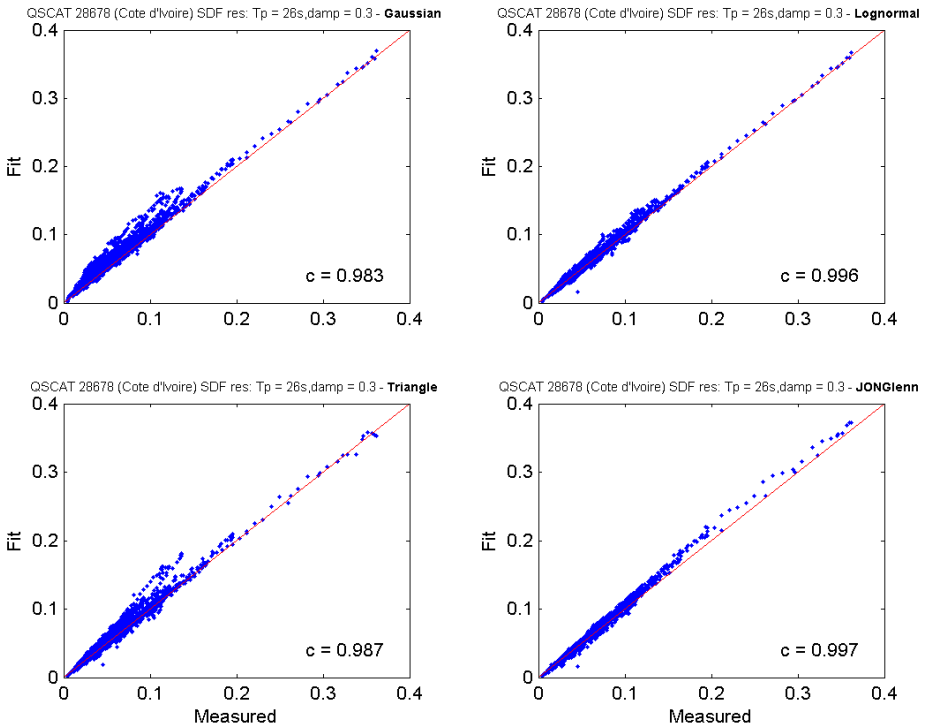

The observations of the agreement in SDF response to the measured and modelled spectra are better illustrated in figure 6.27. The plots show the scatter index of the comparisons of the responses to the modelled and measured spectra for the 96 SDF transfer functions and the four modelled spectral types. The plots show decreasing scatter indices for increasing damping, decreasing scatter indices for increasing T_p for the triangle and lognormal, and generally lower scatter indices for the lognormal responses by comparison with the other three models.

FIGURE 6.27 : Scatter index of the SDF response to the measured and modelled spectra. One plot for each spectral model.

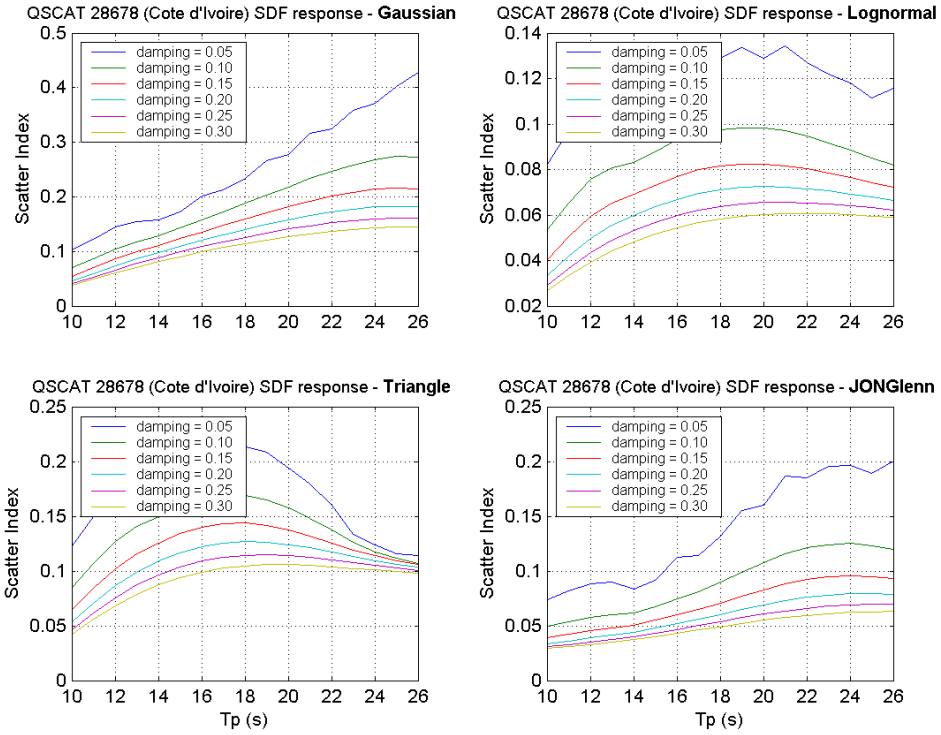

A direct comparison of the scatter indices of the response comparisons is given in figure 6.28 for the QSCAT 28678 (Côte d'Ivoire) data set. The plots show that the response from the JONSWAP-Glenn spectral model gives the best agreement with that of the measured spectra for SDF transfer functions with $T_p < 20\text{s}$, while the lognormal spectral model performs best for transfer functions with $T_p > 20\text{s}$. This is largely true for the Bonga location as well figure 6.29, but for the more southern locations, for example figures 6.30, 6.31, and 6.32, the lognormal provides the better model for most transfer functions and all for which Tp>18 seconds. This trend is also more or less true for the measured data sets - figures 6.33 to 6.38.

FIGURE 6.28 : Scatter index of the SDF response to the measured and modelled spectra, for the QSCAT 28678 (Côte d'Ivoire) data set. Each plot corresponds to a different value of ξ .

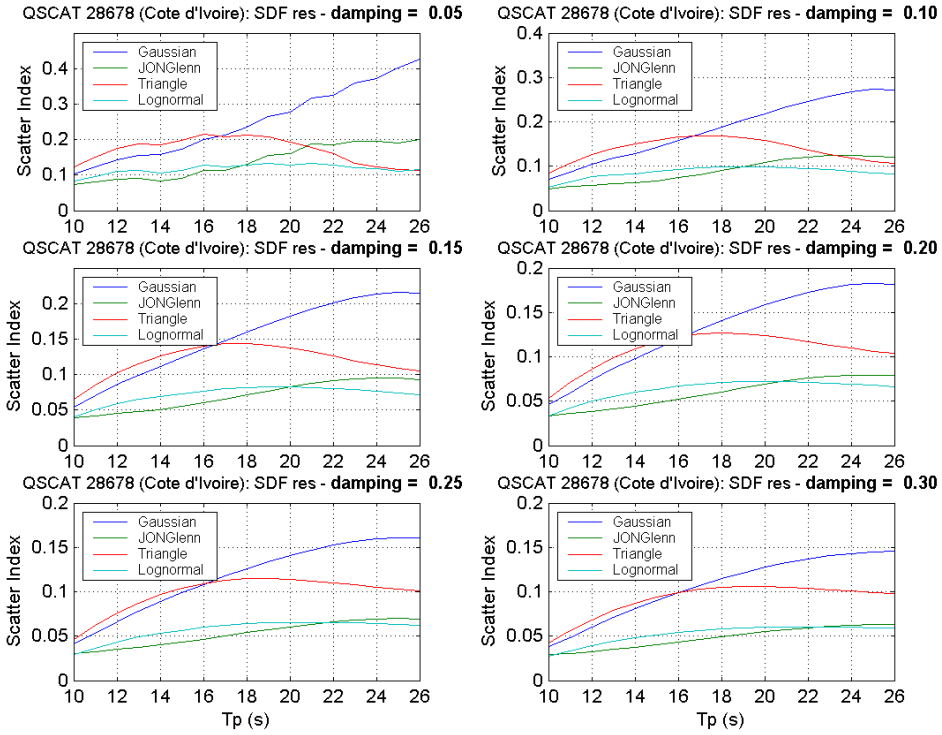

FIGURE 6.29 : Scatter index of the SDF response to the measured and modelled spectra, for the QSCAT 28793 (Bonga) data set. Each plot corresponds to a different value of ξ .

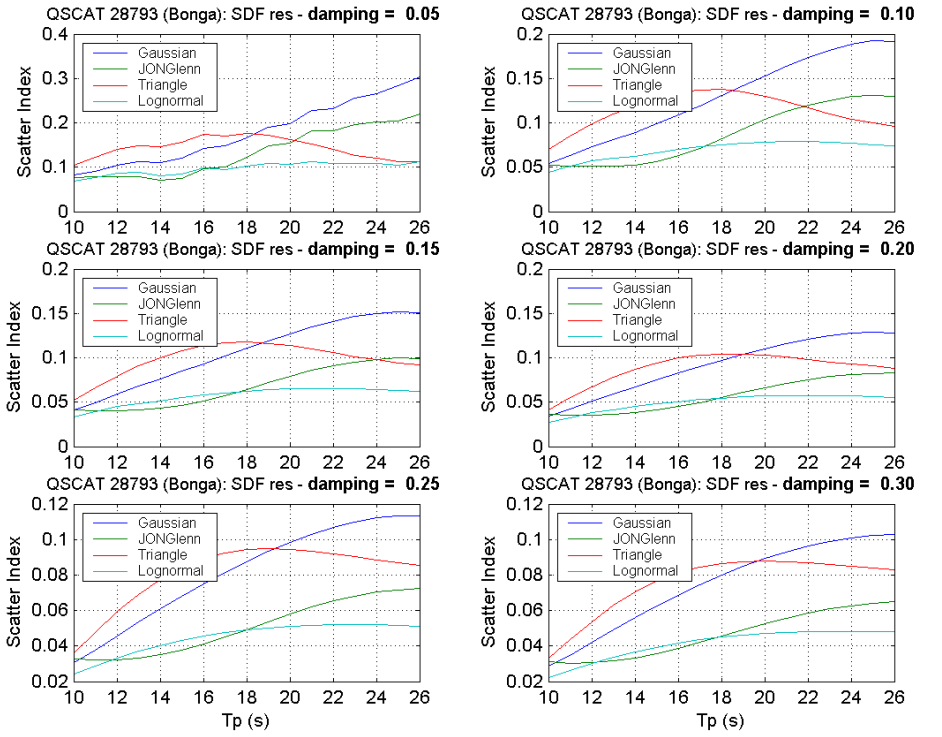

FIGURE 6.30 : Scatter index of the SDF response to the measured and modelled spectra, for the QSCAT 26099 (Nemba) data set. Each plot corresponds to a different value of ξ.

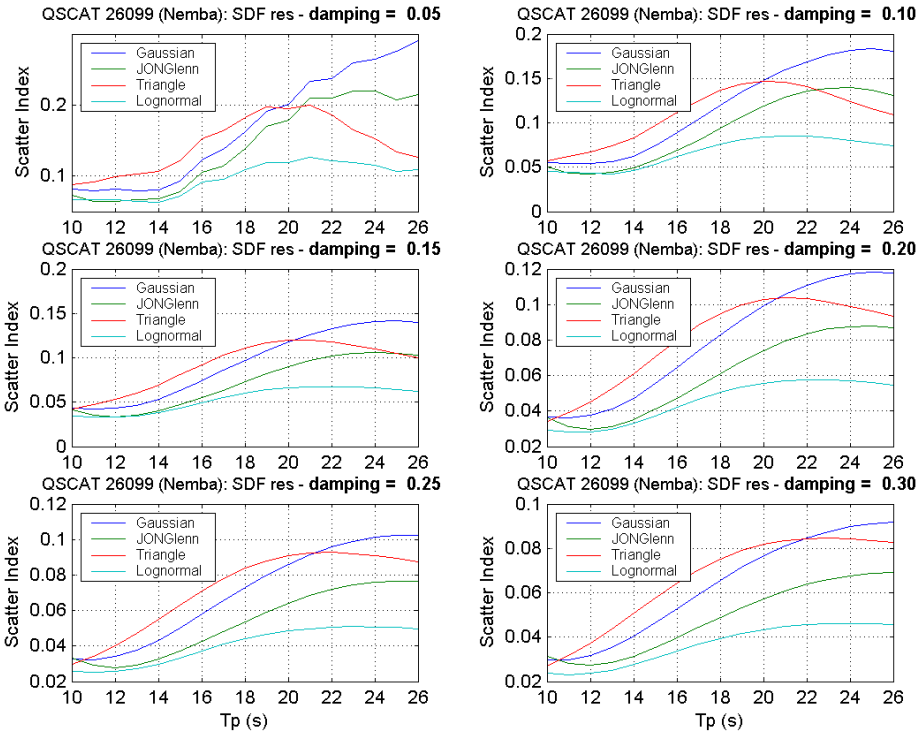

FIGURE 6.31 : Scatter index of the SDF response to the measured and modelled spectra, for the QSCAT 22917 (Namibia) data set. Each plot corresponds to a different value of ξ.

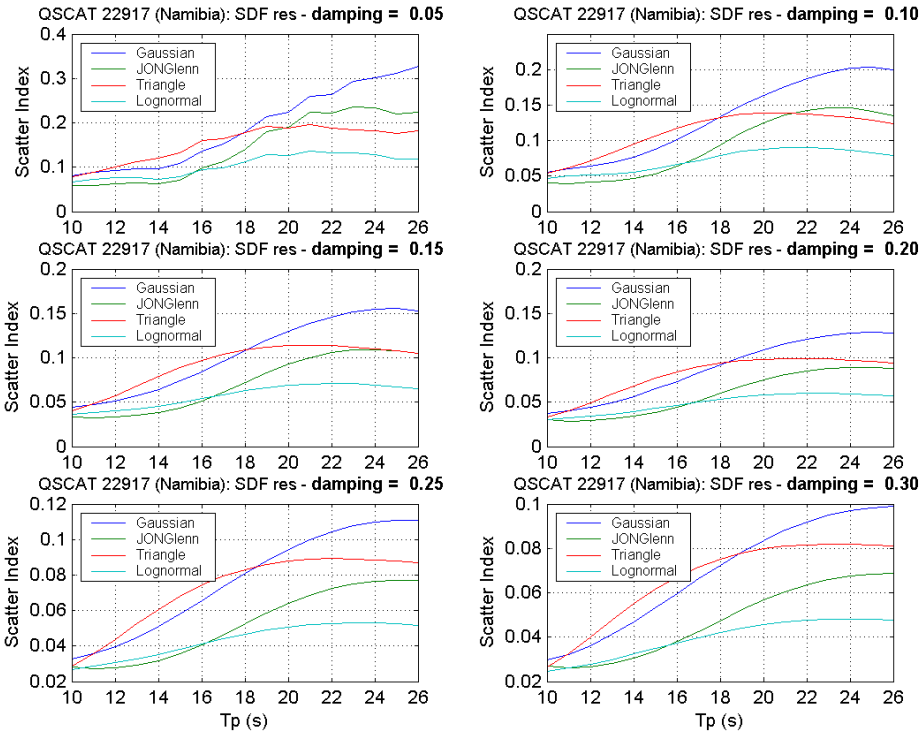

FIGURE 6.32 : Scatter index of the SDF response to the measured and modelled spectra, for the QSCAT 19573 (Kudu) data set. Each plot corresponds to a different value of ξ .

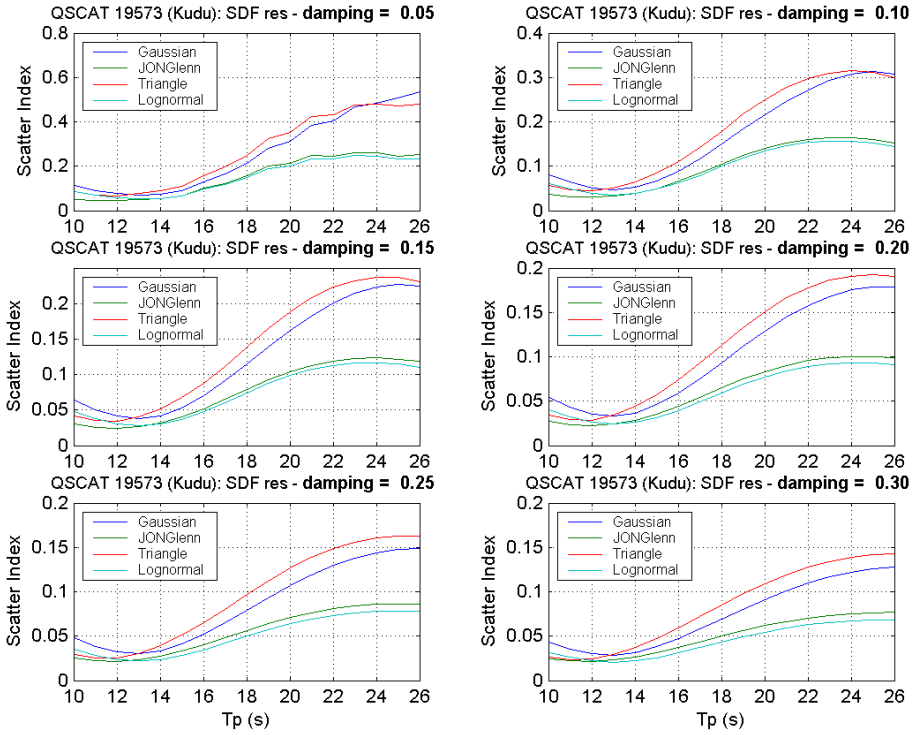

FIGURE 6.33 : Scatter index of the SDF response to the measured and modelled spectra, for the Bonga DWR MEM data set. Each plot corresponds to a different value of ξ .

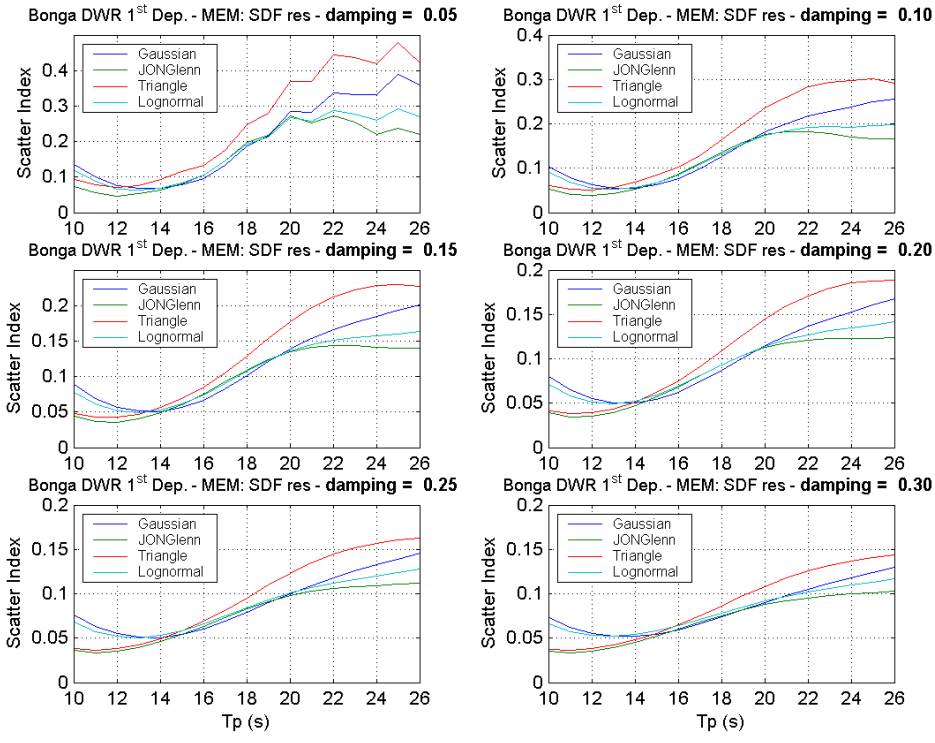

FIGURE 6.34 : Scatter index of the SDF response to the measured and modelled spectra, for the Bonga Wavescan Cos2s data set. Each plot corresponds to a different value of ξ.

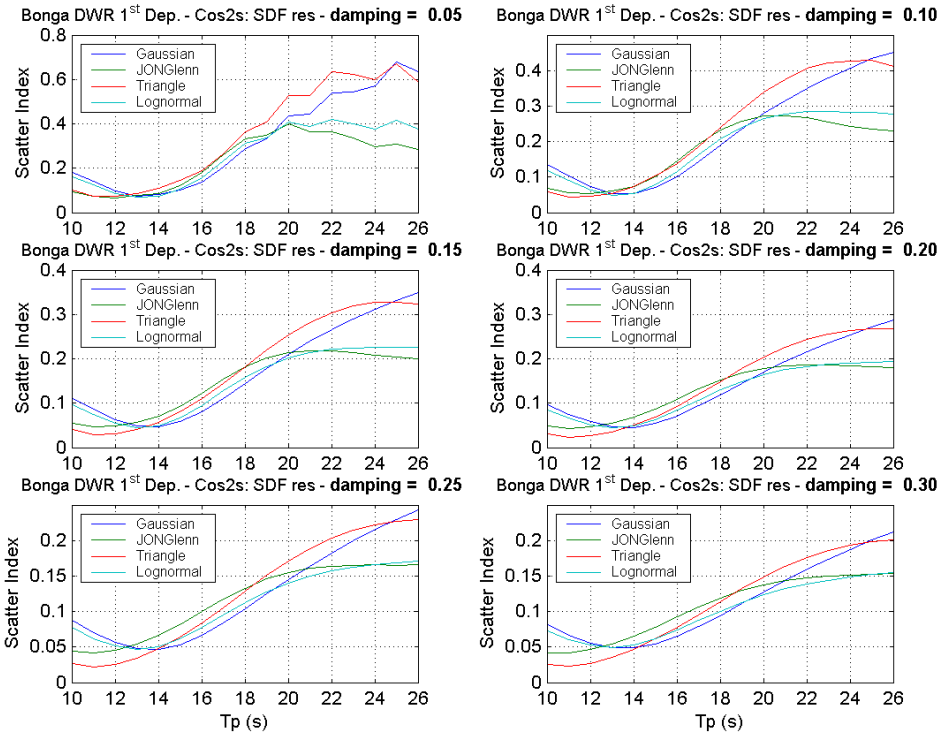

FIGURE 6.35 : Scatter index of the SDF response to the measured and modelled spectra, for the Bonga Ekoundou Cos2s data set. Each plot corresponds to a different value of ξ.

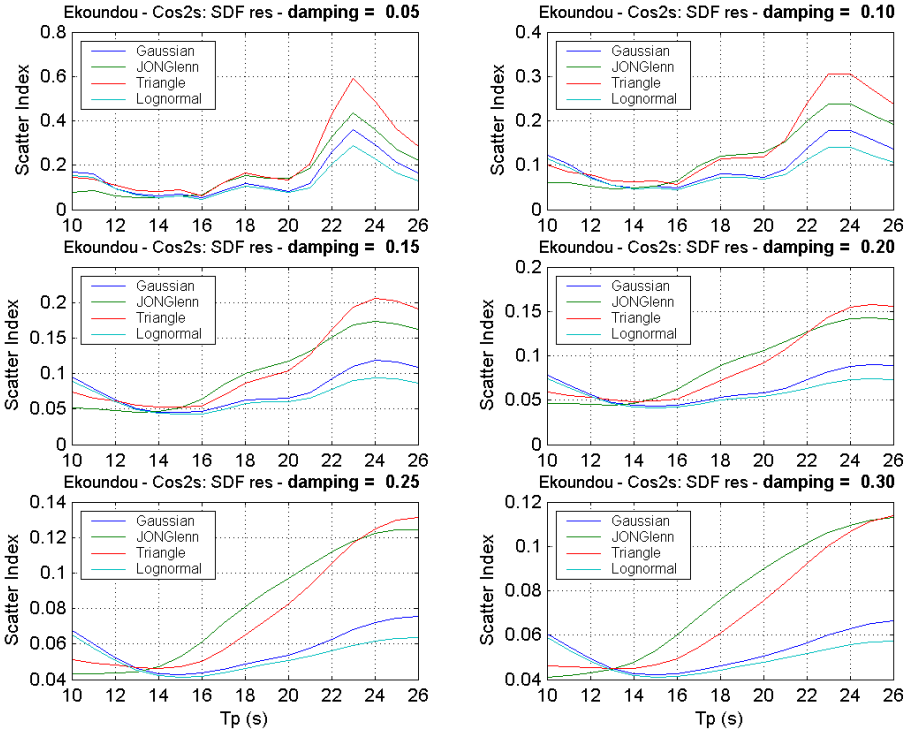

FIGURE 6.36 : Scatter index of the SDF response to the measured and modelled spectra, for the Bonga Chevron 8m Cos2s data set. Each plot corresponds to a different value of ξ .

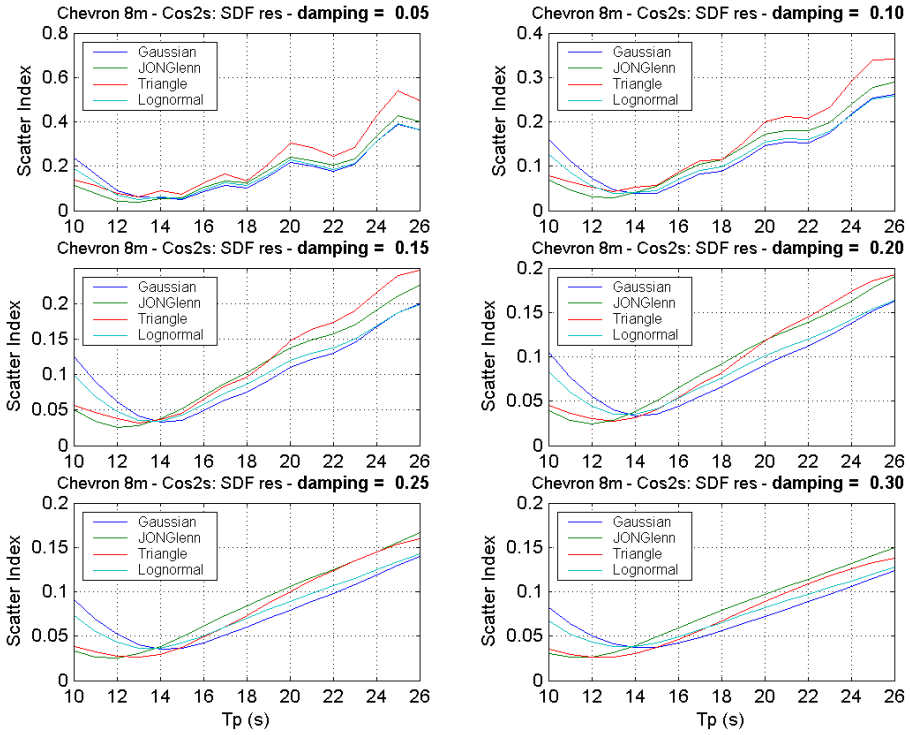

FIGURE 6.37 : Scatter index of the SDF response to the measured and modelled spectra, for the Bonga Chevron 85m Cos2s data set. Each plot corresponds to a different value of ξ .

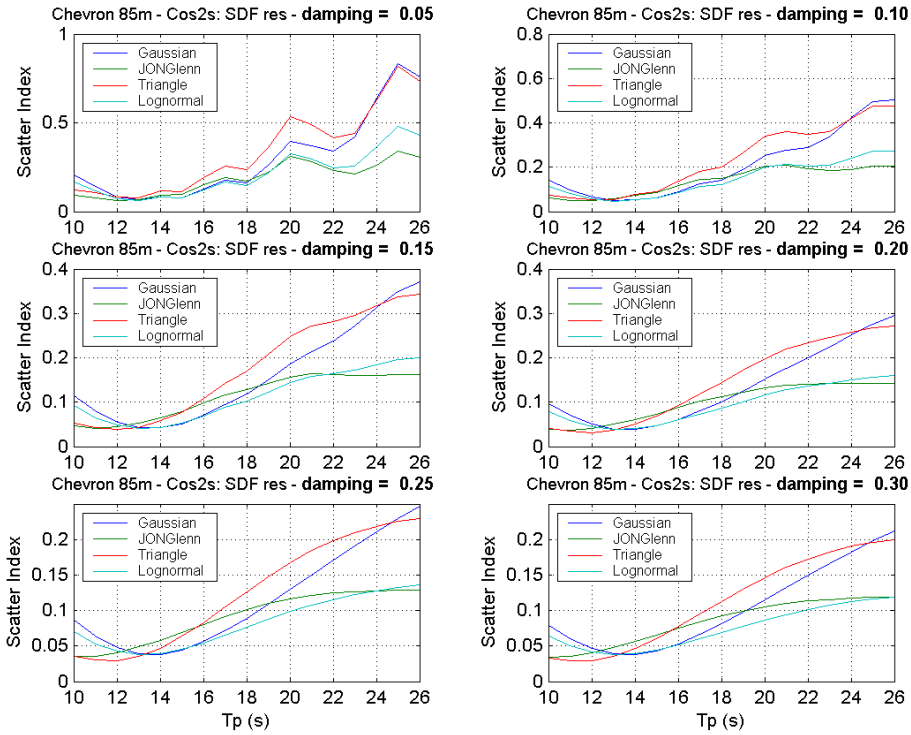

FIGURE 6.38 : Scatter index of the SDF response to the measured and modelled spectra, for the Bonga Kudu MEM data set. Each plot corresponds to a different value of ξ.

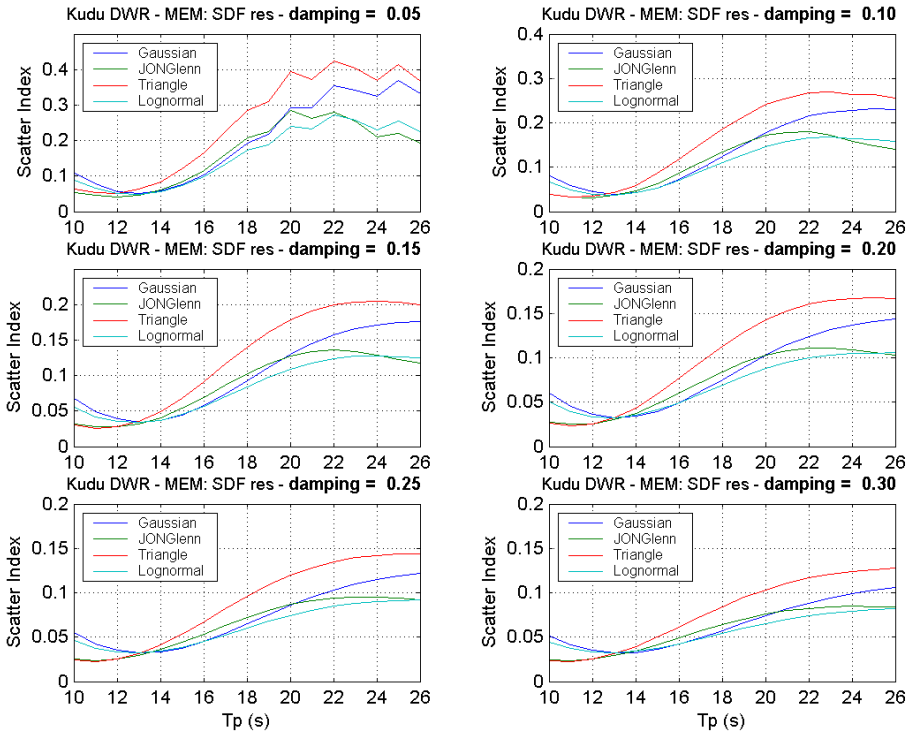

References

[6.1] Hanson, J. L. and O.M. Phillips, 2001: Automated analysis of ocean surface directional wave spectra. *J. Atmos. Oceanic Technol.,* **18,** 277-293.

[6.2] Longuet-Higgins, M.S, Cartwright, D.E., and N.D. Smith, 1963: Observations of the directional spectrum of sea waves using the motions of a floating buoy. *In: Ocean Wave Spectra: Proceedings of a conference*, 111-131, Prentice-Hall, Englewood Cliffs, New Jersey.

[6.3] Hwang and Wang, 2001: An operational method for separating wind sea and swell from ocean wave spectra. J. Atm. & Ocean. Tech., **18**, December, 2001, 2052-2062.

Appendix 6.1: Wave Systems Parameters

The following parameters are used to describe the wave systems that are extracted from observed or computed wave spectra. Table 6.1 summarizes the list of the parameters with their physical units and the format used in the output files of systems extraction.

- **Hm0**: Significant wave height

Def. $4\sqrt{m_0}$ **(EQ 6.6)**

$$m_i = \int_{f_{\min}}^{f_{\max}} S(f) f^i \mathrm{d}f \qquad \textbf{(EQ 6.7)}$$

- **Tp**: Spectral peak period

Def. $f_i = arg_{max}(S(f))$ **(EQ 6.8)**

$$f_p = \frac{f_{i-1}S(f_{i-1}) + f_i S(f_i) + f_{i+1}S(f_{i+1})}{S(f_{i-1}) + S(f_i) + S(f_{i+1})} \qquad \textbf{(EQ 6.9)}$$

$$T_p = \frac{1}{f_p} \qquad \textbf{(EQ 6.10)}$$

Note 1. Directional spectra should be summed into non-directional ones before identifying the peak.
Note 2. The weighted average over 3 points aims at avoiding some of the effects of poor discretizations.

- **T01**: Average spectral period

Def. $T_{01} = \frac{m_0}{m_1}$ **(EQ 6.11)**

$$m_i = \int_{f_{\min}}^{f_{\max}} S(f) f^i \mathrm{d}f \qquad \textbf{(EQ 6.12)}$$

- **T02**: Zero-crossing period

Def. $T_{02} = \sqrt{\frac{m_0}{m_2}}$ **(EQ 6.13)**

$$m_i = \int_{f_{\min}}^{f_{\max}} S(f) f^i \mathrm{d}f \qquad \textbf{(EQ 6.14)}$$

- **Alpha**: Wave direction.

  This is the commonly used wave direction parameter, expressing where the waves are coming from. Approved by PIANC as the angle between true north and the direction from where the waves are coming. Clockwise is positive to this definition.

- **Alphap**: Peak wave direction.

Def. $\alpha_j = arg_{max}(S(\alpha))$ **(EQ 6.15)**

$$\alpha_p = \arg\left(\sum_{j-1}^{j+1} S(\alpha_j)\cos(\alpha_j) + i \sum_{j-1}^{j+1} S(\alpha_j)\sin(\alpha_j) \right) \qquad \textbf{(EQ 6.16)}$$

Note. Directional spectra should be summed over frequencies to identify the peak of energy. The definition is thus different from that of mean direction at the peak frequency α_{mp}, and was chosen for the sake of consistency with the definition for peak period.

- **Alpham**: Mean Wave direction at a given frequency.

$$\textit{Def 1.}\ \alpha_m(f) = \arg\left(\int_0^{2\pi} S(\alpha)\cos(\alpha)d\alpha + i\int_0^{2\pi} S(\alpha)\sin(\alpha)d\alpha\right) \quad \textbf{(EQ 6.17)}$$

$$\textit{Def 2.}\ \alpha_m(f) = arg(a_1+ib_1) \quad \textbf{(EQ 6.18)}$$

$$\textbf{Alphap} = \alpha_m(\boldsymbol{f_p}) \quad \textbf{(EQ 6.19)}$$

- **Alpham0**: Overall Mean Wave direction

$$\textit{Def 1.}\ \alpha_0 = arg\left(\int_{f_{\min}}^{f_{max}}\int_0^{2\pi} S(f,\alpha)\cos(\alpha)d\alpha df + i\int_{f_{\min}}^{f_{max}}\int_0^{2\pi} S(f,\alpha)\sin(\alpha)d\alpha df\right) \quad \textbf{(EQ 6.20)}$$

$$\textit{Def 2.}\ arg\left(\frac{1}{m_0}\int_{f_{\min}}^{f_{max}} S(f)e^{i\alpha_m(f)}\mathrm{df}\right) \quad \textbf{(EQ 6.21)}$$

- ***Lambda01***: Average wave length

$$\textit{Def.}\ \Lambda_{01} = \frac{gT_{01}^2}{2\pi}tanh\left(\frac{2\pi d}{\Lambda_{01}}\right) \quad \textbf{(EQ 6.22)}$$

Systems code: Three digits abc
a = nbr. of "North Atlantic" originating swells in that sea-state
b = nbr. of "South Atlantic" originating swells in that sea-state
c = nbr. of wind seas in that sea-state

- **Qp**: Peakedness factor (sometimes also called Goda parameter)

$$\textit{Def.}\ Q_p = \frac{2}{m_0^2}\int_{f_{\min}}^{f_{\max}} fS^2(f)\mathrm{df} \quad \textbf{(EQ 6.23)}$$

- **Stdev**: Bandwidth standard deviation

$$\textit{Def.}\ \sigma_f = \frac{1}{m_0}\sqrt{m_0m_2 - m_1^2} \quad \textbf{(EQ 6.24)}$$

$$\sigma_f = \frac{\varepsilon_2}{T_{01}} \quad \textbf{(EQ 6.25)}$$

- **Sigma**: Directional spreading width

$$\textit{Def.}\ \sigma(f) = \sqrt{\int_{\alpha_0-\pi}^{\alpha_0+\pi} D(f,\alpha)(\alpha-\alpha_0)^2 d\alpha} \quad \textbf{(EQ 6.26)}$$

- **Phi**: Directional spreading ratio from second order coefficients

$$\textit{Def.}\ \phi(f) = \sqrt{\frac{(1+|a_2+ib_2|)}{2}} \quad \textbf{(EQ 6.27)}$$

- **Sigma3**: Directional spreading width from first order coefficients

$$\textbf{\textit{Def.}}\ \sigma_3(f) = \sqrt{2(1-md_1)} \qquad \textbf{(EQ 6.28)}$$

$$md_1 = \int_{-\pi}^{+\pi} D(f,\alpha)\cos(\alpha-\alpha_0)d\alpha \qquad \textbf{(EQ 6.29)}$$

$$\text{or } md_1 = a_1 cos(\alpha_0)+b_1 sin(\alpha_0) \qquad \textbf{(EQ 6.30)}$$

$$\text{or } md_1 = |a_1+ib_1| \qquad \textbf{(EQ 6.31)}$$

Sigma should be prefered to **Sigma3** when $D(f,\alpha)$ is known with more details than its first 5 Fourier coefficients.

- **Sigmadt**: Total Directional spreading width

$$\textbf{\textit{Def.}}\ \sigma_t = \sqrt{\frac{1}{m_0}\int_{\alpha_0-\pi}^{\alpha_0+\pi}\int_{f_{min}}^{f_{max}} S(f,\alpha)(\alpha-\alpha_0)^2 d\alpha df} \qquad \textbf{(EQ 6.32)}$$

- **Phit**: Total Directional spreading ratio from 2nd order coeff.

$$\textbf{\textit{Def.}}\ \phi_t = \sqrt{\frac{1}{m_0}\int_{f_{min}}^{f_{max}} S(f)\phi^2 df} \qquad \textbf{(EQ 6.33)}$$

- **Sigma3t**: Total Directional spreading width from 1st order coeff.

$$\textbf{\textit{Def.}}\ \sigma_{3t} = \sqrt{\frac{1}{m_0}\int_{f_{min}}^{f_{max}} S(f)\sigma_3^2 df} \qquad \textbf{(EQ 6.34)}$$

- **Skewd**: Skewness of Directional spreading

$$\textbf{\textit{Def.}}\ \gamma(f) = -nd_2((1-md_2)/2)^{-3/2} \qquad \textbf{(EQ 6.35)}$$

$$md_2 = \int_{-\pi}^{+\pi} D(f,\alpha)\cos(2(\alpha-\alpha_0))d\alpha \qquad \textbf{(EQ 6.36)}$$

$$\text{or } md_2 = a_2 cos(2\alpha_0)+b_2 sin(2\alpha_0) \qquad \textbf{(EQ 6.37)}$$

$$nd_2 = \int_{-\pi}^{+\pi} D(f,\alpha)\sin(2(\alpha-\alpha_0))d\alpha \qquad \textbf{(EQ 6.38)}$$

$$\text{or } nd_2 = b_2 cos(2\alpha_0)-a_2 sin(2\alpha_0) \qquad \textbf{(EQ 6.39)}$$

- **Skewdt**: Total Skewness of Directional spreading

$$\textbf{\textit{Def.}}\ \gamma_t = -\frac{Nd_2}{((1-Md_2)/2)^{3/2}} \qquad \textbf{(EQ 6.40)}$$

$$Md_2 = \frac{1}{m_0}\int_{-\pi}^{+\pi}\int_{f_{\min}}^{f_{\max}} S(f,\alpha)\cos(2(\alpha-\alpha_0))d\alpha\mathrm{d}f \quad \textbf{(EQ 6.41)}$$

$$Nd_2 = \frac{1}{m_0}\int_{-\pi}^{+\pi}\int_{f_{\min}}^{f_{\max}} S(f,\alpha)\sin(2(\alpha-\alpha_0))d\alpha\mathrm{d}f \quad \textbf{(EQ 6.42)}$$

- **Kurtd**: Kurtosis of Directional spreading

Def. $\delta(f) = \frac{6-8md_1+2md_2}{4(1-md_1)^2}$ **(EQ 6.43)**

$$md_1 = \int_{-\pi}^{+\pi} D(f,\alpha)\cos(\alpha-\alpha_0)d\alpha \quad \textbf{(EQ 6.44)}$$

or $md_1 = a_1 cos(\alpha_0)+b_1 sin(\alpha_0)$ **(EQ 6.45)**

or $md_1 = |a_1+ib_1|$ **(EQ 6.46)**

$$md_2 = \int_{-\pi}^{+\pi} D(f,\alpha)\cos(2(\alpha-\alpha_0))d\alpha \quad \textbf{(EQ 6.47)}$$

or $md_2 = a_2 cos(2\alpha_0)+b_2 sin(2\alpha_0)$ **(EQ 6.48)**

- **Kurtdt**: Total Kurtosis of Directional spreading

Def. $\delta_t = \frac{6-8Md_1+2Md_2}{4(1-Md_1)^2}$ **(EQ 6.49)**

$$Md_1 = \frac{1}{m_0}\int_{-\pi}^{+\pi}\int_{f_{\min}}^{f_{\max}} S(f,\alpha)\cos(\alpha-\alpha_0)d\alpha\mathrm{d}f \quad \textbf{(EQ 6.50)}$$

$$Md_2 = \frac{1}{m_0}\int_{-\pi}^{+\pi}\int_{f_{\min}}^{f_{\max}} S(f,\alpha)\cos(2(\alpha-\alpha_0))d\alpha\mathrm{d}f \quad \textbf{(EQ 6.51)}$$

- **Gamma**: Overshooting factor of the Jonswap formula

Def 1. $Gamma = f(Q_p)$ **(EQ 6.52)**

Def 2. Least-square fit of Jonswap spectrum **(EQ 6.53)**

- **m**: Triangular shape parameter.

Def. Spectrum is a triangle from $\frac{m-1}{m}f_p$ to $\frac{m}{m-1}f_p$ **(EQ 6.54)**

Note that $m = \frac{3Q_p+2}{4}$ **(EQ 6.55)**

TABLE 6.1 : Wave systems parameters

Parameter	Format	(as real)	Units	Notes
Latitude	f7.2	f7.2	Deg.	
Lontitude	f7.2	f7.2	Deg.	
Date	i13	f13.0	ccyymmjjhhmm	
Hm0	f6.2	f6.2	m	
Tp	f5.1	f5.1	s	
T01	f5.1	f5.1	s	
T02	f5.1	f5.1	s	
Alphap	i4	f4.0	Deg.	
Alpham0	i4	f4.0	Deg.	
Lambda01	i5	f5.0	m	
Systems code	i4	f4.0		
$Speed_{Wind}$	f6.1	f6.1	m/s	
$Alpha_{Wind}$	i4	f4.0	Deg.	
Hm0(i)	f6.2	f6.2	m	
Tp(i)	f5.1	f5.1	s	
T01(i)	f5.1	f5.1	s	
T02(i)	f5.1	f5.1	s	
Alphap(i)	i4	f4.0	Deg.	
Alpham0(i)	i4	f4.0	Deg.	
Lambda01(i)	i5	f5.0	m	
Qp(i)	f6.2	f6.2		
Stdev(i)	f7.4	f7.4	10^{-2}Hz	
Sigmadt(i)	f5.1	f5.1	Deg.	
Phit(i)	f6.3	f6.3		
Sigma3t(i)	f5.1	f5.1		
Skewdt(i)	f6.2	f6.2		
Kurtdt(i)	f6.2	f6.2		
$Hm0_t$(i)	f6.2	f6.2	m	From LS triangle fit
Tp_t(i)	f5.1	f5.1	s	
m_t(i)	f6.2	f6.2		
$Hm0_n$(i)	f6.2	f6.2	m	From LS normal fit
Tp_n(i)	f5.1	f5.1	s	
$Sigma_n$(i)	f7.4	f7.4	10^{-2}Hz	
$Hm0_{ln}$(i)	f6.2	f6.2	m	From LS Log-normal fit
Tp_{ln}(i)	f5.1	f5.1	s	
$Sigma_{ln}$(i)	f7.4	f7.4	10^{-2}Hz	
$Hm0_j$(i)	f6.2	f6.2	m	From LS Jonswap fit
Tp_j(i)	f5.1	f5.1	s	
$Gamma_j$(i)	f5.1	f5.1		

Missing values set to -9, -99, -999, ..., as to comply with format.

Appendix 6.2: QSCAT Swell Tracks

FIGURE 6.39 : QSCAT Swell Tracks

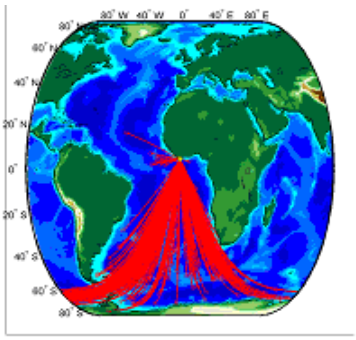

GP 28678 – Côte d'Ivoire

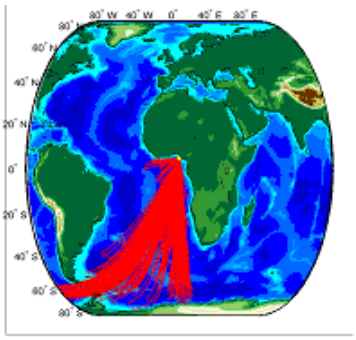

GP 28793 – Bonga

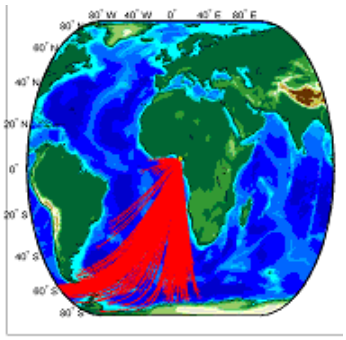

GP 28701 – Ekoundou

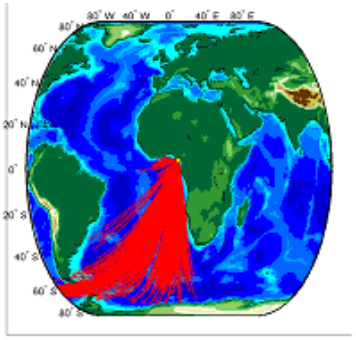

GP 28606 – Marathon

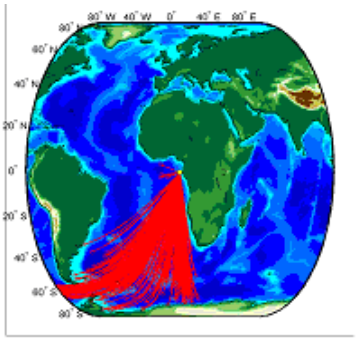

GP 27088 – Gabon

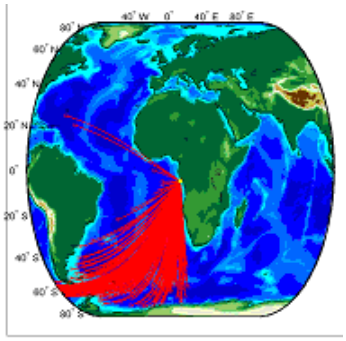

GP 26099 – Nemba

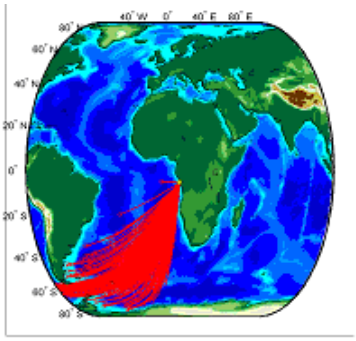

GP 25947 – Exxon

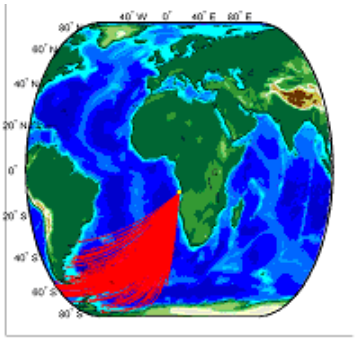

GP 24873 – Central Angola

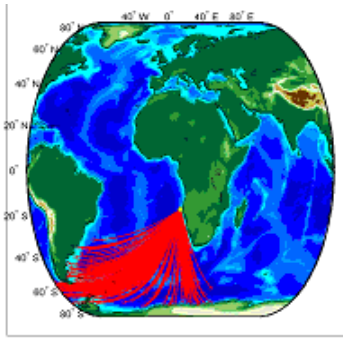

GP 22917 – Namibia

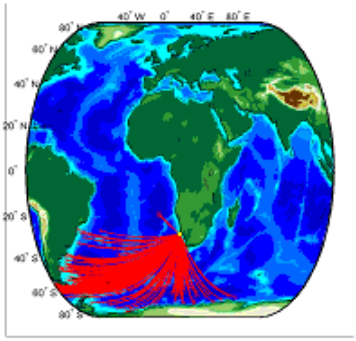

GP 19573 – Kudu

CHAPTER 7

Response spectra

George Z. Forristall

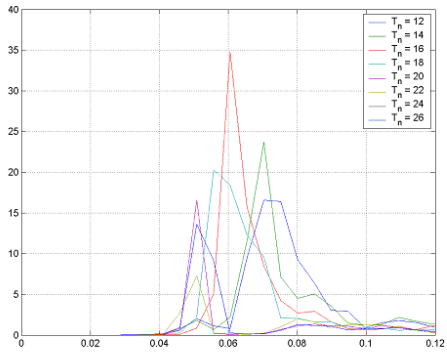

The idea of characterizing wave spectra through response spectra has been borrowed from the field of earthquake engineering. The basic concept is illustrated in Figure 7.1. A measured time series of earthquake ground motions or accelerations is applied to a series of single degree of freedom (SDF) oscillators. An SDF system can be thought of as a spring and dashpot. The characteristics of the system can be described as a natural period T_n and a damping ratio ξ. This type of system is linear, so that the response scales with the amplitude of the input.

FIGURE 7.1 : Response spectra in the bottom graph are calculated by running an input time series through a set of single degree of freedom oscillators with different natural periods and damping ratios.

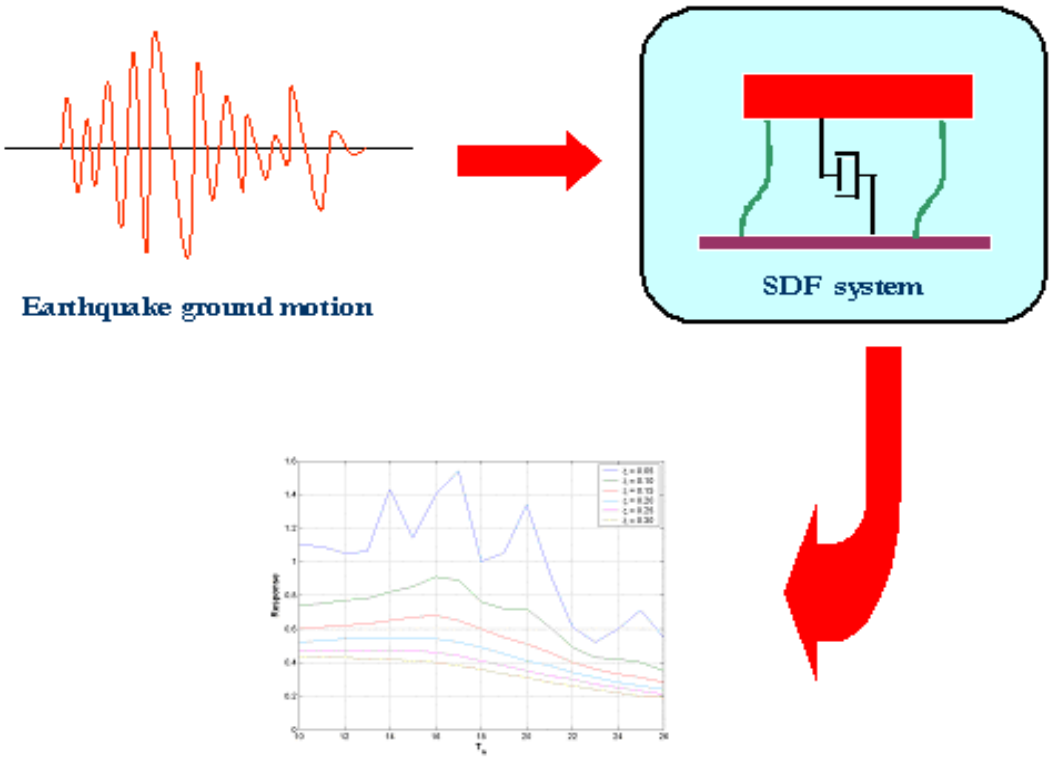

The ground motion is applied to each combination of T_n and ξ, and the maximum response of the system is found. The graph at the bottom of Figure 7.1 shows this maximum response as a function of T_n, with each curve for a different value of ξ. From such response spectra diagrams, it is easy to see how changing the characteristics of the systems will affect its response to an earthquake. The same technique can be applied using an ocean wave time series as input.

In concept, the calculation of the response of the system is made in the time domain, using the convolution integral

$$v(t) = \frac{1}{\omega_D}\int_0^t w(\tau)\sin\omega_D(t-\tau)\exp[-\xi\omega(t-\tau)]d\tau \qquad \textbf{(EQ 7.1)}$$

where $w(t)$ is the input, $v(t)$ is the response, and $\omega_D = 2\pi/T_n$.

In practice, since an SDF is a linear system, it is quicker to take the Fourier transforms of the input and output and express the convolution as a transfer function so that

$$V(\omega) = W(\omega)H(\omega) \qquad \textbf{(EQ 7.2)}$$

where

$$H(\omega) = \frac{\omega_D^2}{\omega_D^2 - \omega^2 + 2i\xi\omega_D\omega} \qquad \textbf{(EQ 7.3)}$$

FIGURE 7.2 : SDF Response functions for a fixed damping ratio, ξ=0.15.

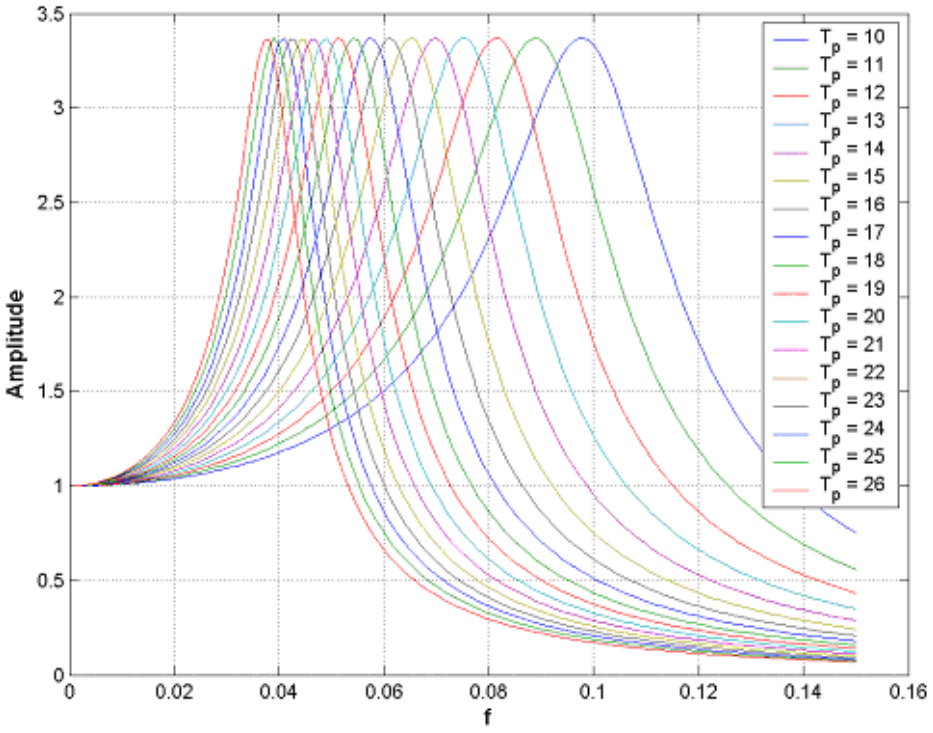

Figure 7.2 shows the absolute value of the transfer function $H(\omega)$ for various values of T_n and a fixed value of ξ and Figure 7.3 shows it as a function of damping ratio and a fixed natural period of 15 seconds. The peak of the transfer function is at the natural frequency and the peak becomes sharper as the damping ratio decreases.

FIGURE 7.3 : SDF response functions for a fixed natural frequency, T_p=15s, and various damping ratios.

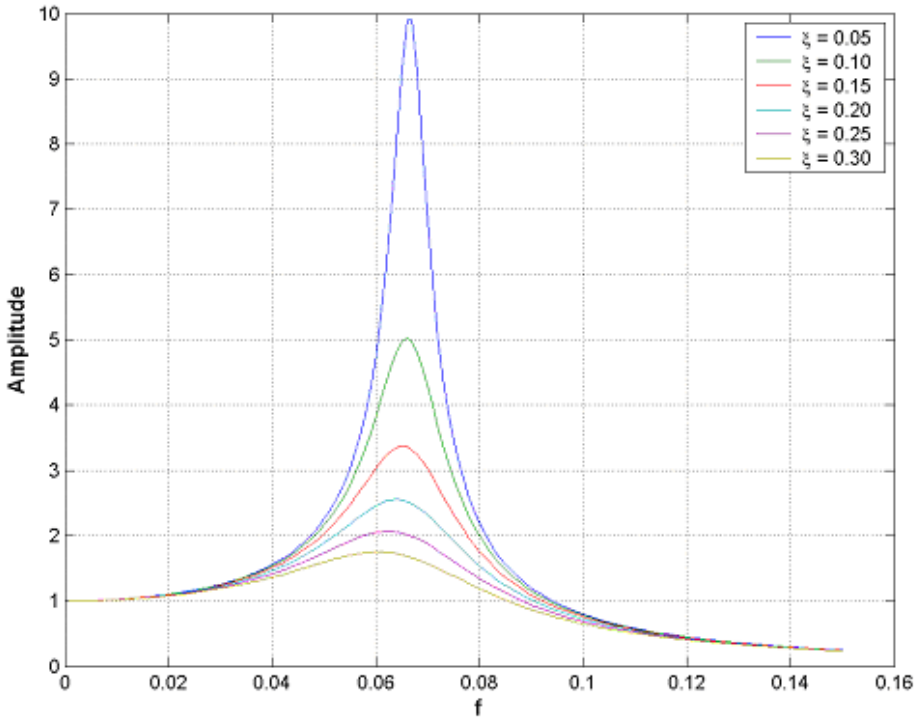

To illustrate the method, we calculated the responses to the a single time series of wave elevations measured by the Wavescan buoy at Bonga at 2100 on 24 March 2002. The calculations were made using equation 7.3 applied to the Fourier transform of the wave time series, and then taking the inverse Fourier transform to find the time series of the response. The maximum value of the response in the time series was then found for each combination of natural period and damping ratio. The results are plotted in Figure 7.4.

The maximum responses to this particular time series are for natural periods near 19 seconds, which corresponds to the peak of the input wave spectrum. The maximum response naturally increases with decreasing damping ratio. For larger damping ratios, the peak is less pronounced since the transfer function for the response integrates over a wider range of the input wave spectrum.

Response spectra showing the maximum response to a time series are appropriate for the non-stationary time series common in earthquake engineering. Wave records are however stationary over reasonable time intervals, so average values of response may be more informative. Figure 7.5 shows the probability distribution of the response to the wave record used to derive Figure 7.4. The red dashed line is a normal distribution with the same standard deviation as the data points. The sample distribution is apparently close to normal. The response of this oscillator can thus be characterized by its standard deviation.

FIGURE 7.4 : Response spectra showing the maximum response to SDF oscillators with a single wave time series as input (Bonga Wavescan, 24 Mar 2002 21:00).

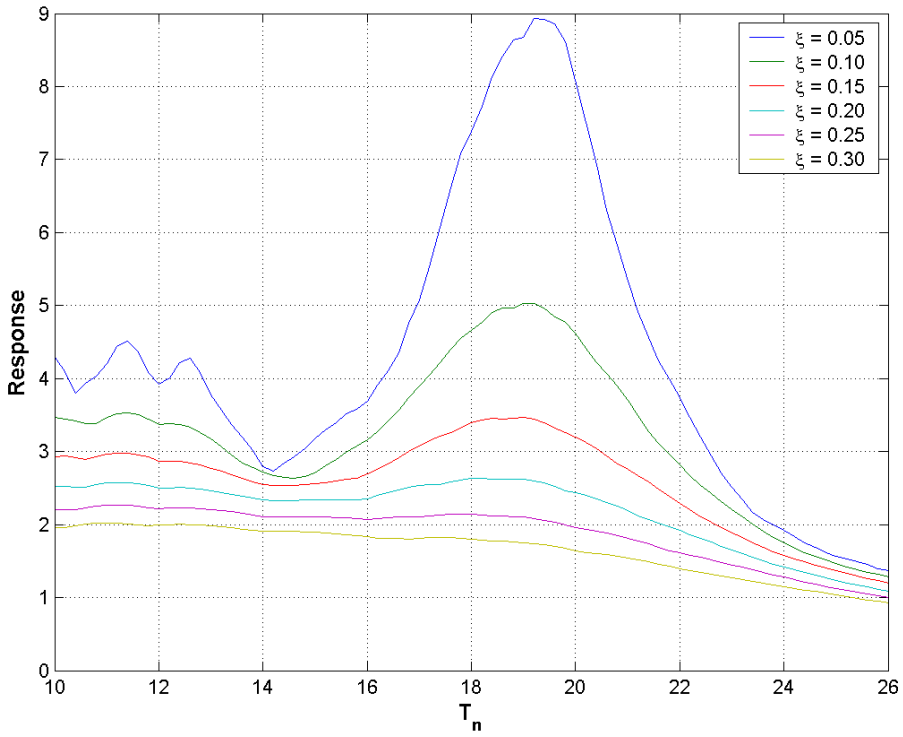

FIGURE 7.5 : Probability distribution of response to Wavescan spectrum measured at 2100 on 24 March 2000 using a transfer function with a natural period of 20 seconds and a damping factor of 0.05.

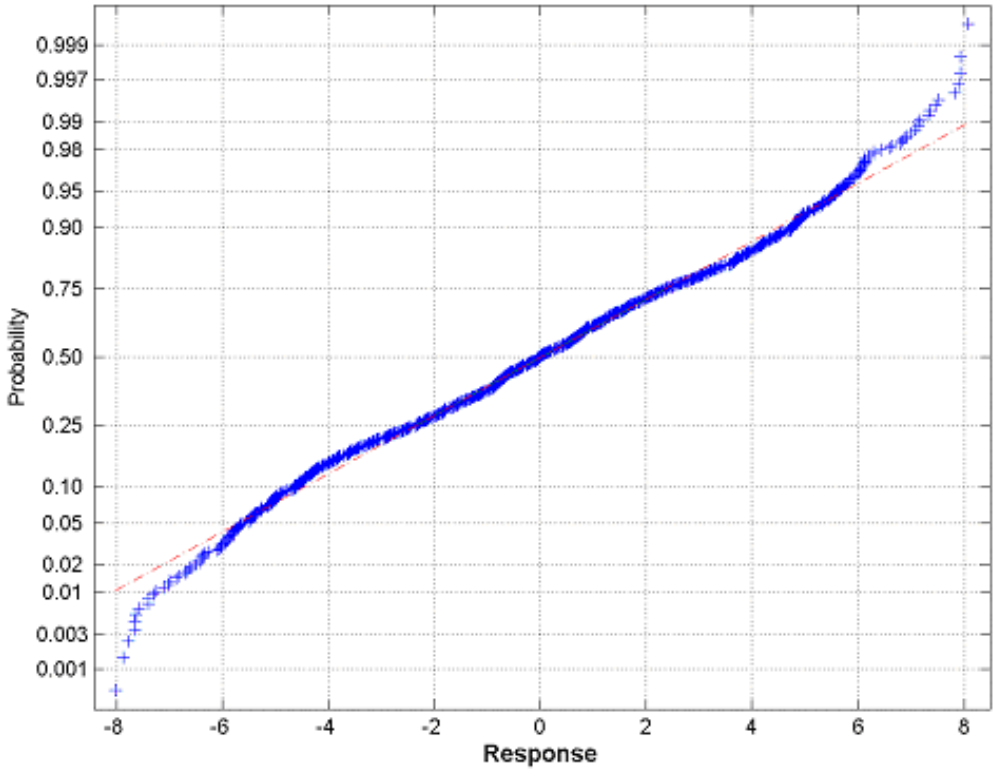

The normality of the response distribution was checked by using the Kolmogorov Smirnov test on 45 other response time series with large wave heights. Only 5 of the samples failed the test at the 95% level, so it is reasonable to assume that the response distribution is close to normal. The rms of the response thus captures all of the information from the response calculations. The great benefit of working with the rms response is that it can be calculated given only the spectrum of the waves instead of the time series of individual waves. Many of our data sets, in particular the hindcast data, include only the wave spectra.

The rms response for each set of oscillator parameters can be calculated for each wave spectrum. Figure 7.6 shows the maximum value of the rms responses over the entire set of measurements made by the Bonga Wavescan buoy. We can see that oscillators with natural periods in the range of 14-16 seconds have the largest response. Diagrams such as Figure 7.6 can be used to quickly see the benefit of changing the natural period of a floating system exposed to the measured environment.

FIGURE 7.6 : The maximum rms response for the entire set of Bonga Wavescan measurements.

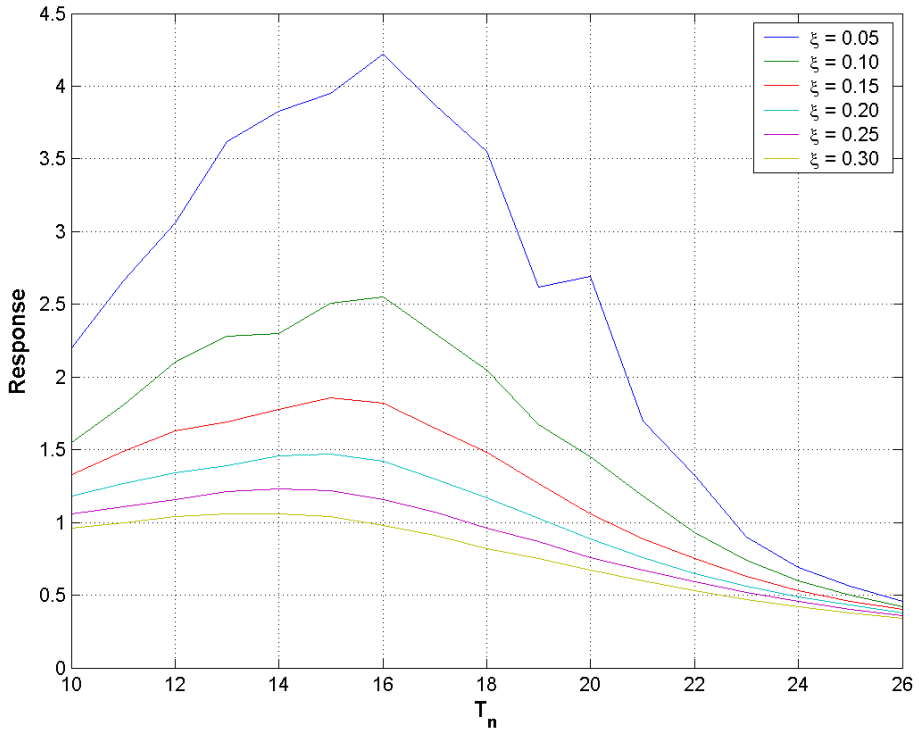

For each natural period and damping factor, we can find the wave spectrum which caused the maximum response in Figure 7.6. The spectra for a damping factor of 0.05 are shown in Figure 7.7. For this small damping factor, the oscillator generally selects for spectra which are sharply peaked at the natural frequency of the system. For the very long natural periods, no such spectra exist in this data set, so the largest responses are where the overlap of the flanks of the spectra and the response function have the greatest overlap.

FIGURE 7.7 : The wave spectra which caused the maximum rms responses in Figure 7.6 for a damping factor of 0.05 and the natural periods shown in the legend.

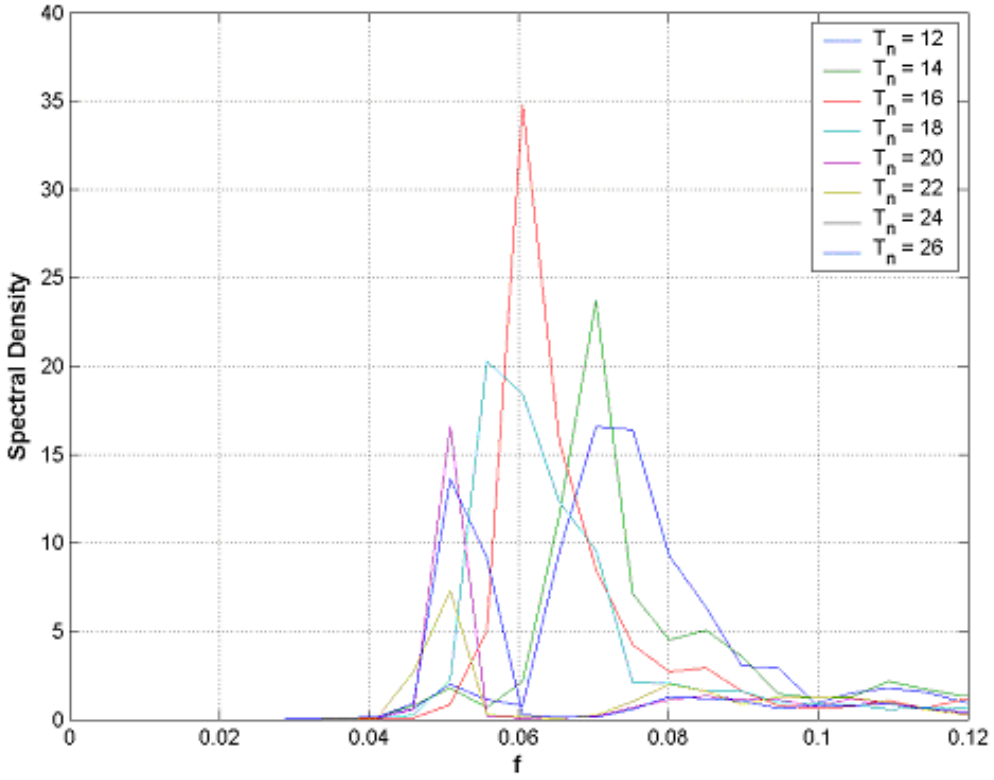

Given the rms response for each spectrum in a long data set, it is possible to fit them with an extreme value distribution and extrapolate to the expected maximum rms response at a long return interval. It is also possible to produce a design spectrum for a given system. The measured or hindcast spectrum which produces the maximum response is found. Then it is inflated as illustrated in equation 7.4 for the 100 year response to give a spectrum of the same shape which produces the design level response.

$$S_{100}(f) = \left\{ \frac{rms(100)}{rms(\text{data})} \right\}^2 S_{\text{data}}(f) \qquad \textbf{(EQ 7.4)}$$

Figure 7.8 shows the maximum rms response for the data sets near Bonga and Figure 7.9 shows the spectra which produced these responses. Similar sets of plots for the other locations are given in the Appendices 7.1-7.5. The shapes of the response spectra curves for the measurements and hindcasts are reasonably similar. The measurement responses are generally lower than the hindcast responses, which is as expected since the measurements cover a shorter time period. The exceptions are the responses from the Bonga directional Waverider spectra for natural periods of 24 –26 seconds. These responses are caused by the spectrum with a peak at 0.04 Hz shown in Figure 7.9.

Surprisingly, the responses from the operational hindcasts are larger than those from the storm hindcasts (note that the scales are different). The storm hindcasts cover more years, and are intended to include all of the strongest storms, so the maximum responses from the storms would be expected to be larger than those from the operational hindcasts, but this is not the case. The reason turns out to be

that the storm data set does not include some of the storms which produce the highest responses. In particular, many of the operational hindcast spectra shown in Figure 7.9 are from a swell event on August 20-21, 1999, which gave the highest responses for natural periods of 21 seconds or longer.

The maximum responses from the operational hindcasts are at somewhat lower natural periods than those from the storms hindcasts. This is presumably because the operational hindcasts include some storms that were not severe enough to produce very low frequency swell but were close enough to send relatively high waves to the site.

The spectrum from the operational hindcasts in Figure 7.9 which produced the highest response for a natural period of 16 seconds is also very interesting. Its peak is at a frequency of 0.039 Hz, which is the lowest frequency in the hindcast model. It is conceivable that the storm which produced this spectrum could have produced some waves at even lower frequencies.

List of appendices: Maximum rms Responses and Associated Spectra

Appendix 7.1: WANE Operational Data

Appendix 7.2: WANE QSCAT Data

Appendix 7.3: WANE Storm Data

Appendix 7.4: Measured Data

Appendix 7.5: Comparisons of WANE and Measured Data

FIGURE 7.8 : Maximum rms response for data sets at Bonga

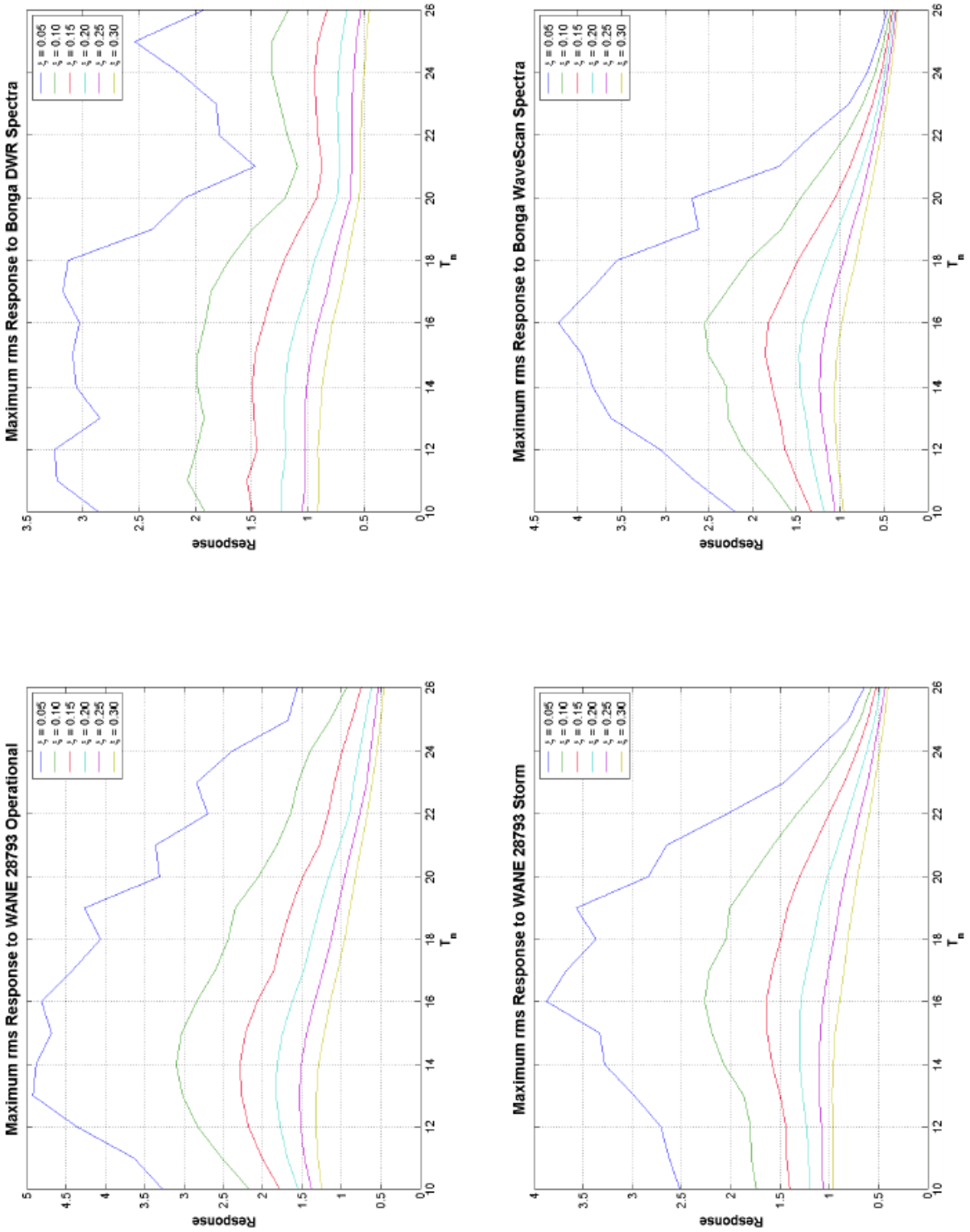

FIGURE 7.9 : Spectra which produce the maximum rms response at Bonga (Wavescan)

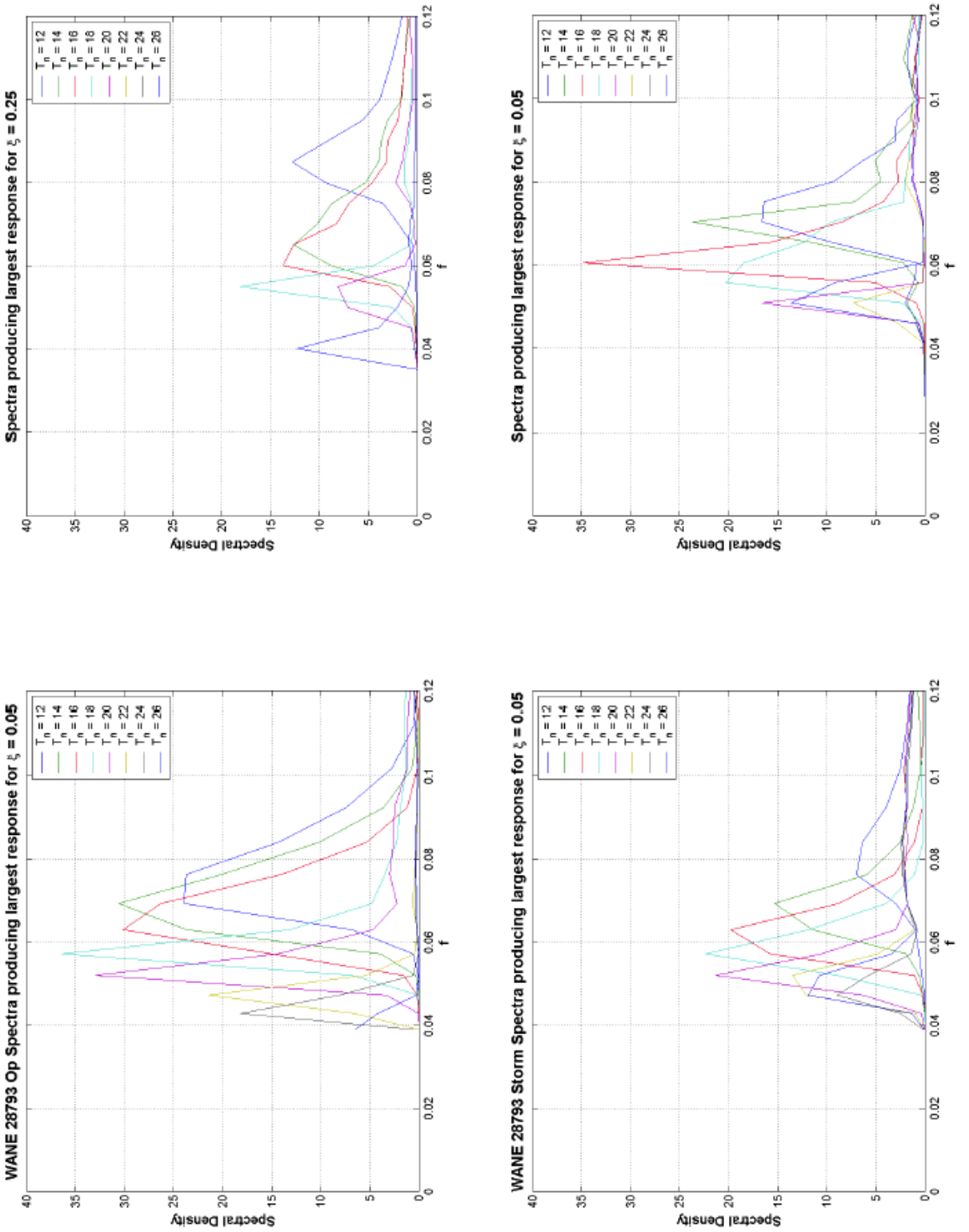

CHAPTER 8

Scatter plots and environmental contours

George Z. Forristall
Marc Prevosto

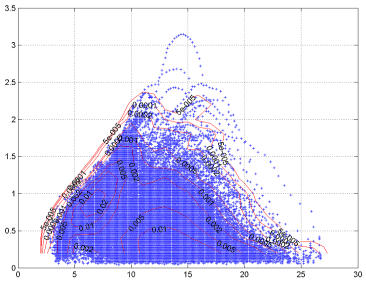

Scatter plots of significant wave height against peak period have been constructed for all of the data sets, and are shown in Appendix 8.1. Examples for the Kudu location (WANE grid point 19573) are copied in Figures 8.1-8.3. Each of these diagrams includes all of the wave systems identified by the partitioning algorithm. For example, in Figure 8.1 from the WANE operational hindcast, there are 43,824 sea-states, but 108,853 wave systems. This means there are an average of about 2.5 wave systems identified per sea-state. In contrast, the measurements at Kudu shown in Figure 8.3 were split into almost 4 wave systems per sea-state. The larger number of partitions in the measurements is apparently due to more irregularity in the measured spectra, but it is not clear whether this irregularity is due to the hindcasts missing wave systems or the sampling variability and instrumental noise in the measurements.

Both the hindcast and measured wave period distributions are generally bimodal. The modes of the hindcast distributions however appear to be at slightly longer periods than in the measurements. For example, the hindcast modes for waves between 2 and 3 m in height are between 8-9 seconds and 14-15 seconds while those in the measurements are between 7-8 and 12-14 seconds. The lower period modes are generally labelled wind sea by the partitioning algorithm.

Environmental contours give curves of equal probability for wave height and period. They may be developed by fitting models of bivariate probability density to the data. Such parametric estimates can be very useful, for example in extrapolating to long return periods. We chose, however, to make nonparametric estimates of the joint probability density as a more direct description of the data.

Nonparametric probability density estimates require that the data be smoothed in some fashion. There is a large body of literature on this subject. Given cheap computer power, kernel density estimators are a very useful technique. A kernel density estimate is formed by replacing each sample data point with a probability density function and then summing over all of the resulting distributions. In one dimension the kernel estimator $\hat{f}$ is given by

$$\hat{f}(x) = \frac{1}{nh}\sum_{i=1}^{n} K\left(\frac{x - x_i}{h}\right) \qquad \textbf{(EQ 8.1)}$$

where K represents a density function with location x_i and width h. For large n the results are rather insensitive to the form of K, and we have used a normal density function for simplicity.

The choice of the width of the density function is important, but there is theoretical guidance for its optimum value. Scott (1992, [8.1]) shows that the error of the estimate is minimized for

$$h = (4/3)^{1/5}\hat{\sigma}n^{-1/5} \quad \textbf{(EQ 8.2)}$$

where $\hat{\sigma}$ is the estimated standard deviation of the observations and n is the number of observations.

For two dimensions, a bivariate normal distribution is used with separate estimates of width of the density function for H_s and T_p made from equation 8.2. Once the distribution is smoothed, it is contoured using the standard contour function in MATLAB.

Figure 8.4 shows a sample of the results of these calculations for the data from Grid Point 28793 of the WANE hindcasts. All 121,588 swell peaks identified by the partitioning algorithm are included. The plotted data points show the peak period and significant wave height for the energy in each partition separately.

Figure 8.5 shows the difference in environmental contours when all swell peaks, the highest swell peak, the longest swell peak, or the second longest swell peak are included. The data set in this example is Grid Point 19573 from the WANE hindcasts. When only the highest swell peak in the spectrum is included, most of the data points with very long wave periods are eliminated, which is also reflected in the contours. If only the longest swell peaks are included, then the data points with low periods disappear, but the contours for long periods show very little change. The contours for the highest wave heights also show little change. Choosing the second longest swell peaks again eliminates the partitions with the longest periods. If a system sensitive to long periods is being designed, it may be sufficient to consider the contours for only the longest swell peaks.

Figure 8.6 shows environmental contours from different data sources for the Bonga location. In each case only the partitions with the longest periods are considered. The contours for the long and high swell are reasonably similar despite the fact that the measured and Quikscat data sets are much shorter than the operational data set. The highest long waves in the Quikscat data contour differently from the operational data set because this data set is shorter. Thus these points from one severe storm have a higher sample probability.

Environmental contours for all of the data sets are shown in the Appendices. Appendix 8.2 contains plots from the WANE operational data, Appendix 8.3 contains plots from the WANE Quikscat data, Appendix 8.4 contains data from the measured data sets and Appendix 8.5 compares data sets from co-located data sets.

List of appendices: Scatter diagrams and environmental contours

Appendix 8.1: Scatter Diagrams

Appendix 8.2: Environmental contours from the WANE operational data

Appendix 8.3: Environmental contours from the WANE Quikscat data

Appendix 8.4: Environmental contours from the measured data sets

Appendix 8.5: Comparison of WANE and measured Data

References

[8.1] Scott, D.W. (1992), *Multivariate Density Estimation: Theory, Practice and Visualization*, Wiley-Interscience, New York, 317 pp.

FIGURE 8.1 : Scatter plot of all wave systems from the WANE operational hindcast at grid point 19573.

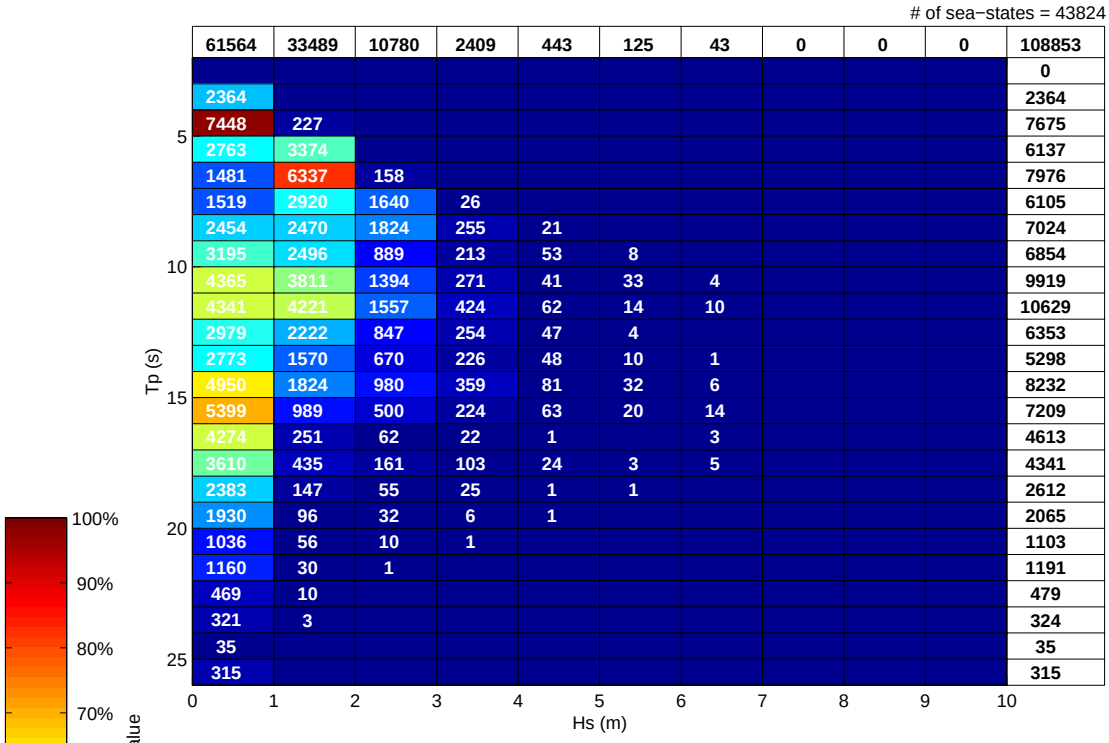

61564	33489	10780	2409	443	125	43	0	0	0	108853
										0
2364										2364
7448	227									7675
2763	3374									6137
1481	6337	158								7976
1519	2920	1640	26							6105
2454	2470	1824	255	21						7024
3195	2496	889	213	53	8					6854
4365	3811	1394	271	41	33	4				9919
4341	4221	1557	424	62	14	10				10629
2979	2222	847	254	47	4					6353
2773	1570	670	226	48	10	1				5298
4950	1824	980	359	81	32	6				8232
5399	989	500	224	63	20	14				7209
4274	251	62	22	1		3				4613
3610	435	161	103	24	3	5				4341
2383	147	55	25	1	1					2612
1930	96	32	6	1						2065
1036	56	10	1							1103
1160	30	1								1191
469	10									479
321	3									324
35										35
315										315

FIGURE 8.2 : Scatter plot of all wave systems from 270 – 360 degrees from the WANE operational hindcast at grid point 19573.

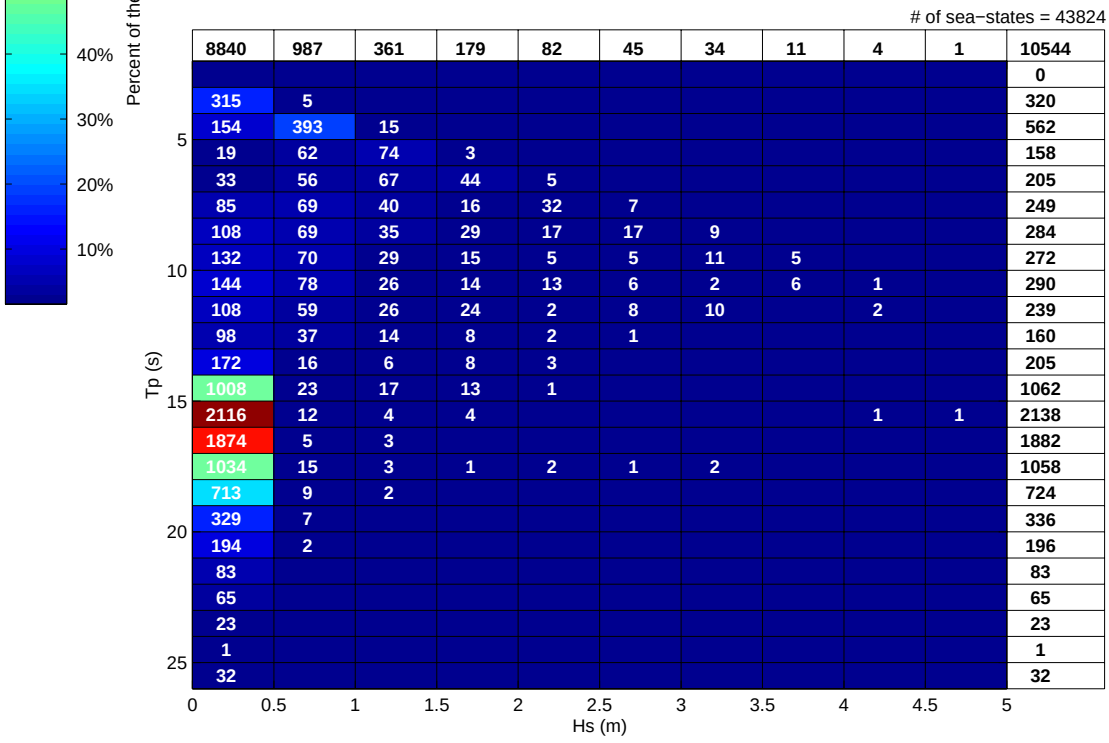

8840	987	361	179	82	45	34	11	4	1	10544
										0
315	5									320
154	393	15								562
19	62	74	3							158
33	56	67	44	5						205
85	69	40	16	32	7					249
108	69	35	29	17	17	9				284
132	70	29	15	5	5	11	5			272
144	78	26	14	13	6	2	6	1		290
108	59	26	24	2	8	10		2		239
98	37	14	8	2	1					160
172	16	6	8	3						205
1008	23	17	13	1						1062
2116	12	4	4					1	1	2138
1874	5	3								1882
1034	15	3	1	2	1	2				1058
713	9	2								724
329	7									336
194	2									196
83										83
65										65
23										23
1										1
32										32

FIGURE 8.3 : Scatter plot for all wave systems in the directional Waverider measurements at Kudu.

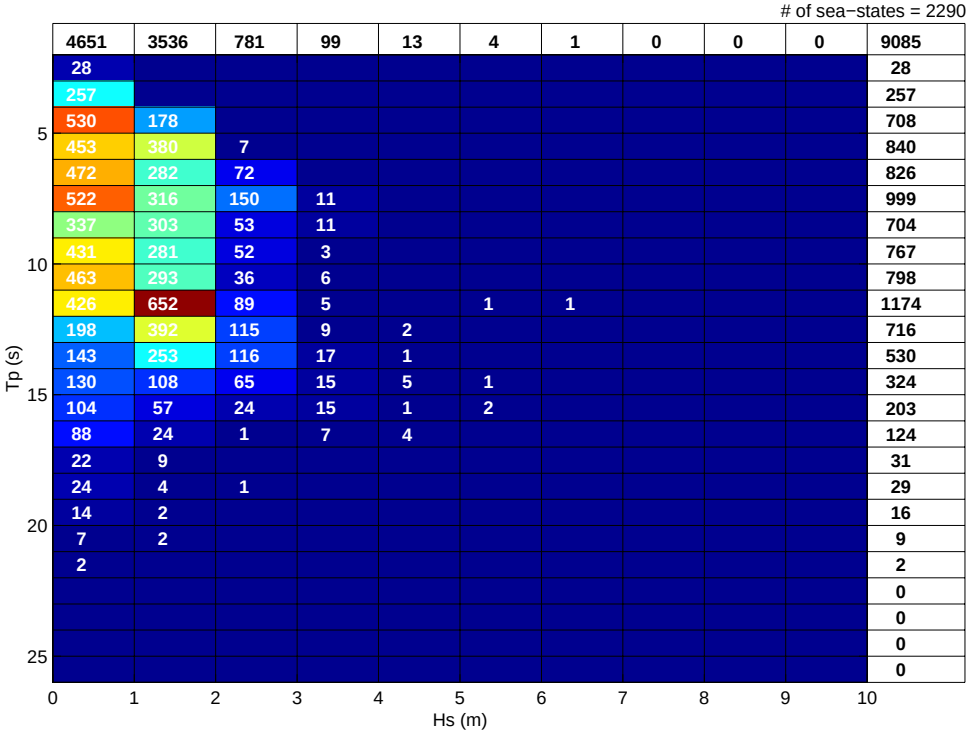

FIGURE 8.4 : Kernel density estimate of environmental contours for all swell peaks identified from the WANE hindcast at GP 28793.

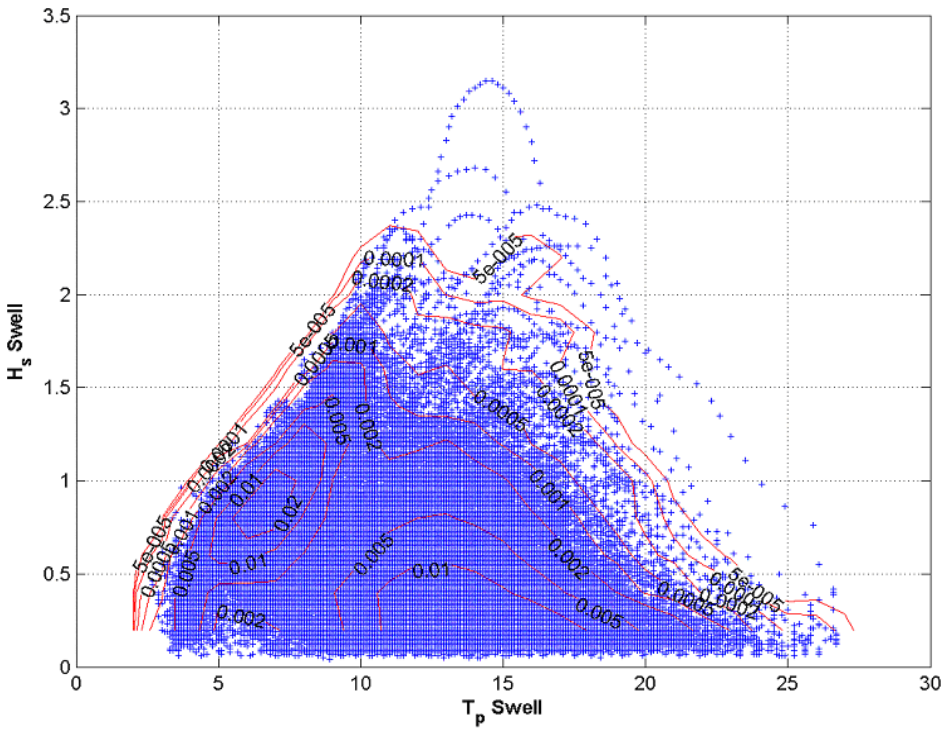

FIGURE 8.5 : Environmental contours based on different subsets of the identified swell peaks at GP 19573.

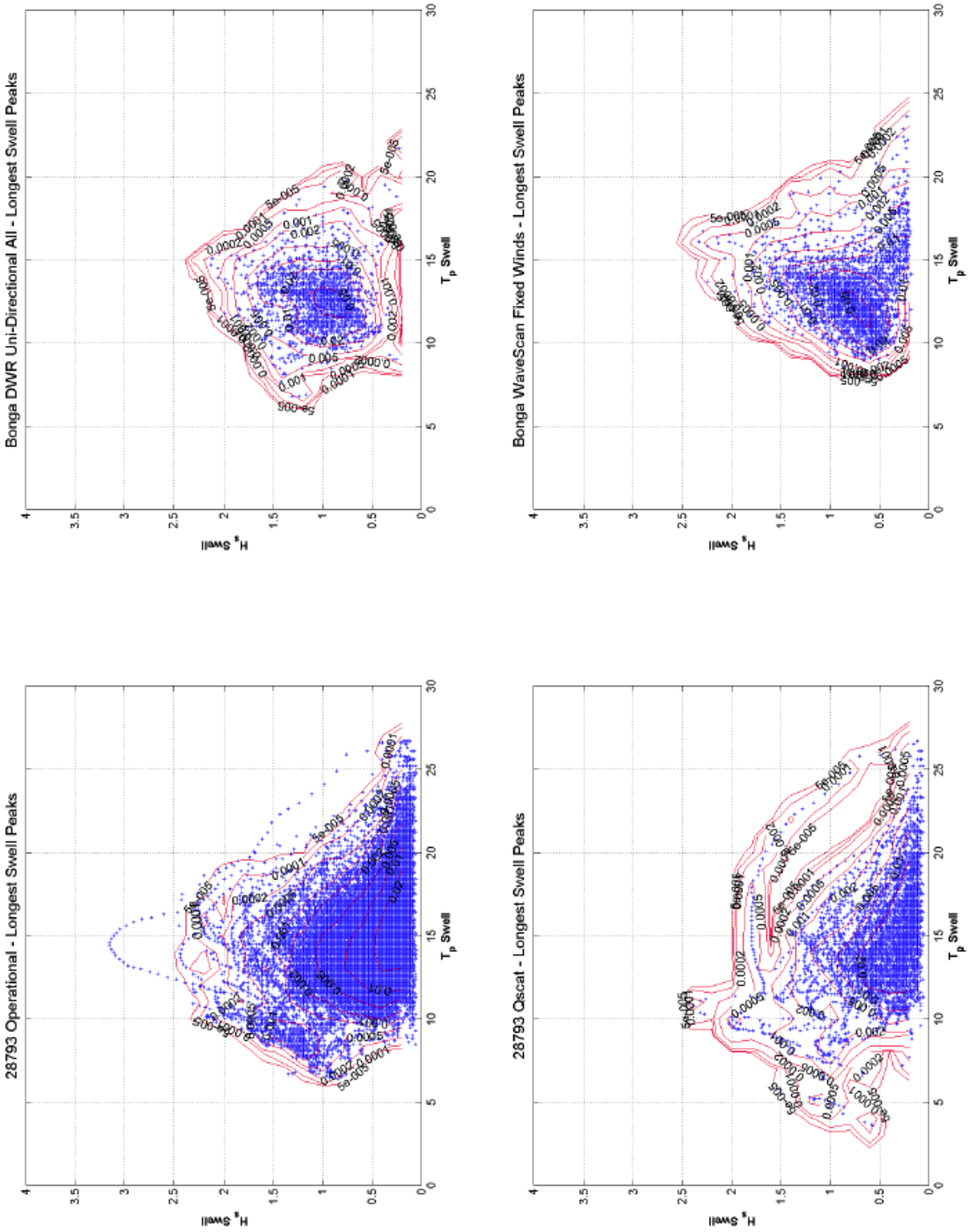

FIGURE 8.6 : Environmental contours for Bonga from different data sources.

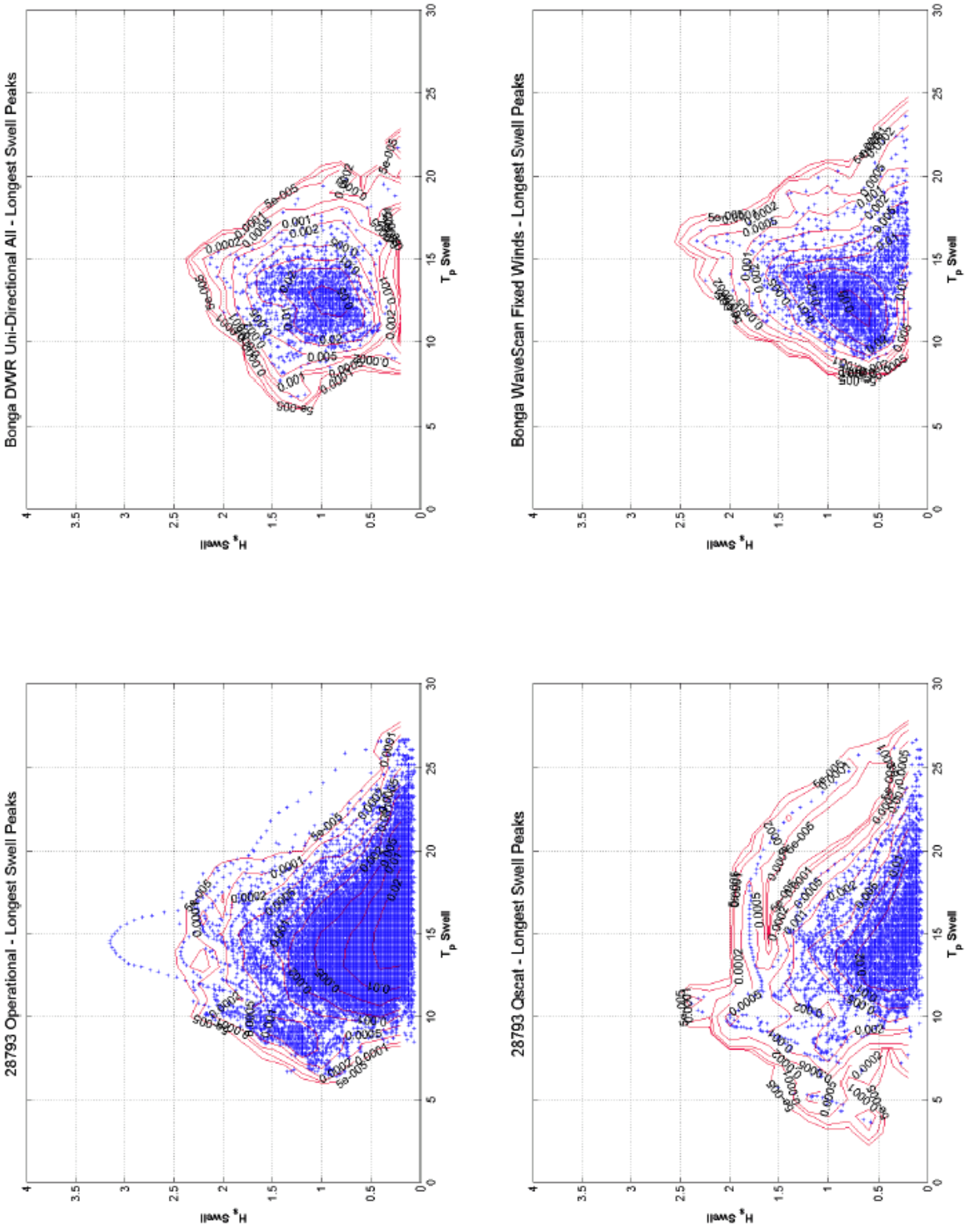

CHAPTER 9

Measurements vs hindcast

Marc Prevosto

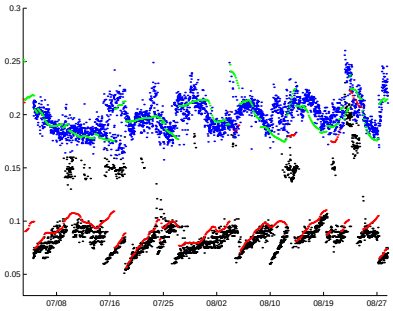

Comparisons between *in situ* measurements and hindcast models are not always very easy, and this for two reasons. First the periods of time of the in situ measurements (often relatively short) do not coincide with the period of time of the hindcast data bases; secondly the short durations of the in situ measurements do not permit to accurately proceed to a statistical comparison. The choice, in this study, has been made to compare qualitatively and simultaneously the sea-states parameters extracted from the measurements and the hindcast data to establish some features of the differences. However, statistical information in term of quantile/quantile plots are given for the global sea-state Hs. The aim would be, to validate the swell information given by the hindcast models, in order to give confidence in the statistics that could be calculated from large time duration data bases.
Statistical comparisons are also available with the scatter plots calculated in Chapter 8.

Three sites have been used for this study, Bonga (directional Waverider and Wavescan, 1018m water depth), Kudu (directional Waverider, 180m water depth) and Cabinda (hereafter called Chevron, 2 wavestaffs, 8m and 85m water depth). The overlaps of hindcast periods and measurement periods are given in Table 9.1.

TABLE 9.1 : Hindcast and Measurement Periods

1985	1986	1987	1988	1989	1990	1991	1992	1993	1994	1995	1996	1997	1998	1999	2000	2001	2002
WANE OPR																	
													WANE QUIKSCAT				
												NOAA					
														BONGA Waverider 1st			
													BONGA Waverider 2nd				
														BONGA Wavescan			
Chevron Wavestaff 8m & 85m																	
													Kudu Waverider				
1985	1986	1987	1988	1989	1990	1991	1992	1993	1994	1995	1996	1997	1998	1999	2000	2001	2002

So, Bonga Waverider 1st and 2nd period and Kudu can be compared to WANE OPR and NOAA hindcasts, Chevron only with WANE OPR and Bonga Wavescan only with NOAA. No measurement intersects with WANE QUIKSCAT.

Hindcast-Measurements comparisons

Hs of the sea-states

Bonga. In looking at the frequency of the spectral peak (Fig. 9.2), some differences can be observed between the hindcasts and the measurements. First, WANE OPR and QSCAT hindcast gives a denser region between 0.1Hz and 0.15 Hz compared to measurements and NOAA hindcast. At the opposite, the range of high frequencies, higher than 0.16Hz is poor, specifically for WANE OPR. This is certainly due to an underestimation of local wind in WANE, partially corrected in QSCAT.

FIGURE 9.1 : BONGA - Significant Wave Height.

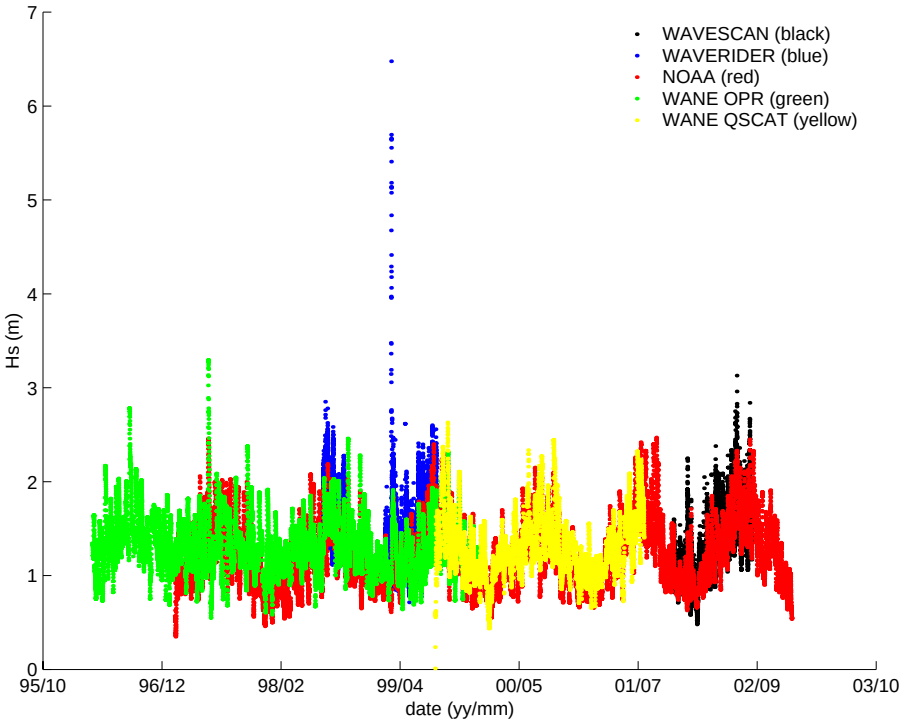

In Figs 9.4 and 9.8, the time evolutions of sea-state Hs for WANE and the Waverider measurements during the two periods are compared. If, more or less, the "storm" events observed by the buoys are present in the WANE hindcast, the hindcast gives "storms" of lower severity, with increasing and decreasing phases less steep. The scatter and quantile/quantile plots[1] (Figs 9.5 and 9.9) are not very good and show large difference between the two samples (hindcast and buoy).

NOAA hindcast (Figs 9.6 and 9.10), gives results more in agreement with the Waverider buoy measurements in amplitude and in shape (see for example from

1. The scatter and quantile/quantile plots are presented in the same figures, scatter plot on the left and qqplot on the right. On the qqplot, the red line indicates the best linear least square fit based on first, third (median) and last quartiles. The black line indicates equal distributions.

1999/06/24 to 1999/07/31). But, it misses again some events (swell or wind sea?). The scatter plots (Figs 9.7 and 9.11) are much better but the quantile plots (Figs 9.7 and 9.11) seems to indicate an offset (10-20 cm) on the distributions. This offset does not exist in the comparisons (Fig 9.13) between the Wavescan buoy and NOAA hindcast (WANE is not available for this period). The same comments stays for the time history (Fig 9.12) and the scatter plot with NOAA hindcast is again good (Fig 9.13).

Chevron. The Chevron site, more south, compared to WANE hindcast shows the same spreading in the scatter plot as for Bonga (Fig 9.15), but no offset (Wavestaff measurements). Only a slight gain effect is visible on the quantile plot (Fig 9.15). NOAA hindcast is not available for this period. For information, the same comparisons are given for the wavestaff, 8m water depth (Fig 9.15). The effect of the bottom is clear and can be modelled by a linear transfer on the Hs.

Kudu. On this site, very south (30°S Lat), the conditions are much more severe, up to 7 meters. Here again the NOAA hindcast shows a better agreement with the measurements, but the extreme events are underestimated by the hindcast. This underestimation is lower for the WANE hindcast, but it shows an offset of underestimation (~40cm) on all the distribution.

FIGURE 9.2 : BONGA - Peak frequency.

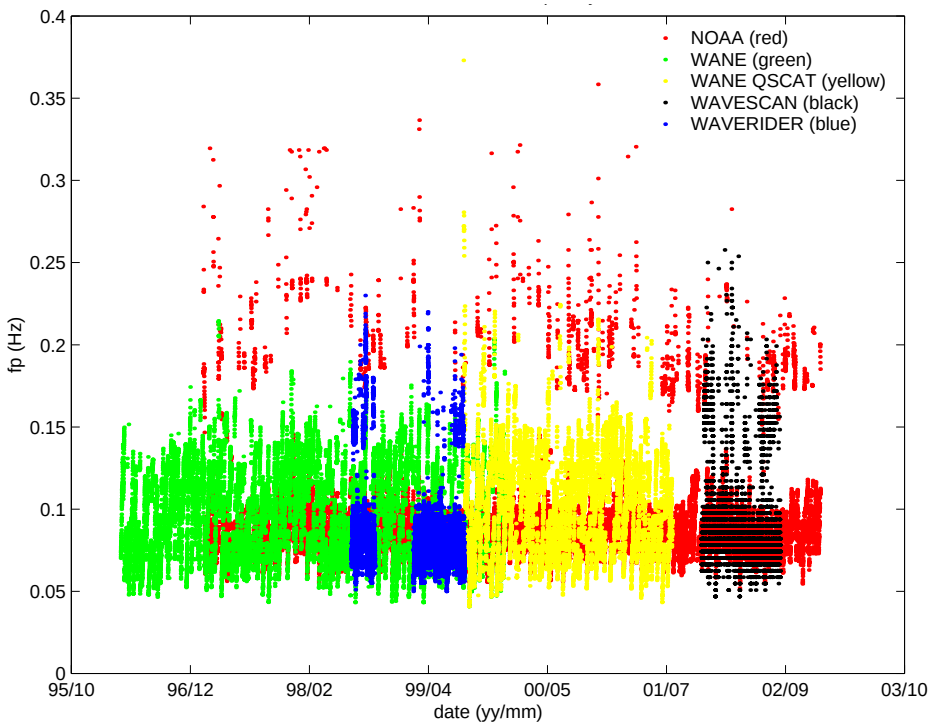

Spectral maximum peak frequency and direction

Bonga. As it has been observed on the sea-state Hs, the time history of the frequency of the spectral maximum, shows that hindcast models simulate well the swell event (Figs 9.22 to 9.26). However the frequency seems to be slightly higher with the hindcast models. The direction of the main peak is in agreement with the direction given by the Waverider during the 1st period (Fig 9.23). Unfortunately, for the other periods of time (Fig 9.24 and 9.26), the direction given by the buoys are so spread that it is not possible to conclude.

Peak frequency of the wave systems

The time history of the peak frequency of the wave systems obtained after partitioning are plotted for the three sites in Figs 9.27 to 9.30. The conclusions are the same for all. Compared to the partitioning in wave systems obtained from buoy measurements, the hindcast gives a more complete information on the superposition and evolution of swell systems (up to three, see for example from 1998/07/26 to 1998/08/03 in Fig 9.27). In most of these situations the energy in the satellite swell systems (one young, the other old) are much lower than the energy in the main swell system. And so the quality of the spectrum estimator from the buoy measurements does not permit to extract the satellite swell systems. On the other hand, the wind sea wave systems are practically absent in the hindcast. This is not there due to a problem of partitioning, but to an underestimation of the local wind field.

FIGURE 9.3 : BONGA - Peak direction.

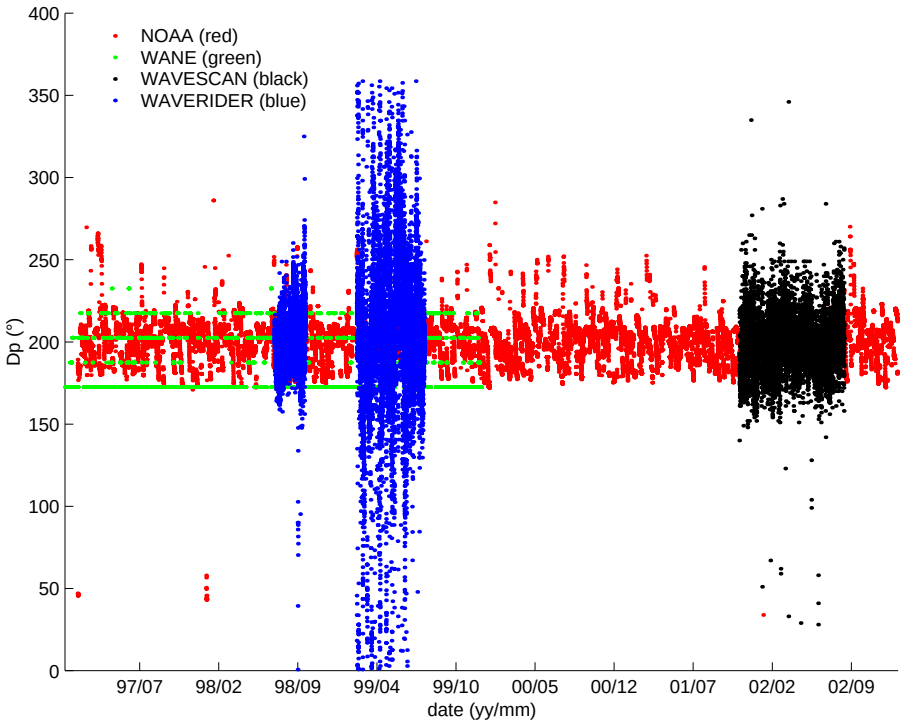

Hindcast-Hindcast comparisons

To help for a more complete analysis of the hindcast-measurements comparisons, the hindcast WANE OPR (1997/02/01 to 1999/12/31, ~3years), WANE QSCAT (1999/08/02 to 2001/07/31, ~2years) have been compared to hindcast NOAA in term of sea-state Hs. Scatter and quantile/quantile plots have been computed on the three sites on the maximum period of time of intersection of the hindcast data bases.

Hs of the sea-states

Bonga. Figs 9.31 and 9.32, the spreading of the scatter plot is lower with QSCAT. The probability distribution are quite similar, the difference in the tail being due to

one or two "storms".

Chevron. Here again (Figs 9.33 and 9.34) we observe a lower spreading of the scatter plot with QSCAT. The distributions NOAA vs WANE are quite similar, but there exists, for this location, an offset between the two distributions, for OPR and QSCAT.

Kudu. Figs 9.35 and 9.36, the same comments as for Chevron stay. For the three locations, the comparison of the upper tail of the distribution between NOAA and WANE OPR is pertubated by one "storm", dated 1997/05/27.

FIGURE 9.4 : BONGA - Waverider 1st period/WANE - Sea-state Hs.

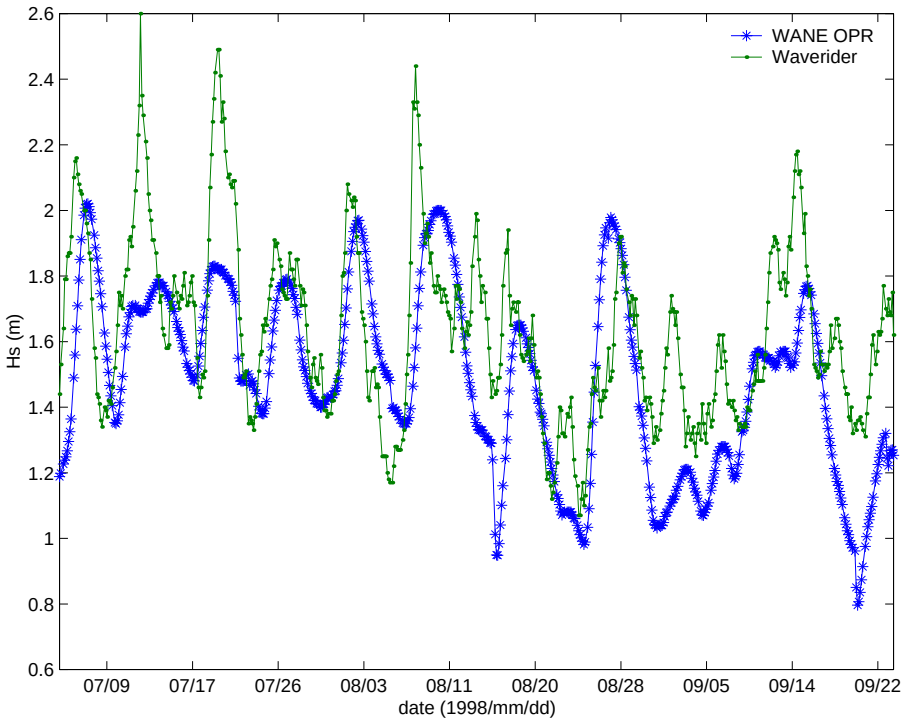

FIGURE 9.5 : BONGA - Waverider 1st period/WANE - Sea-state Hs. Scatter and quantile/quantile plots

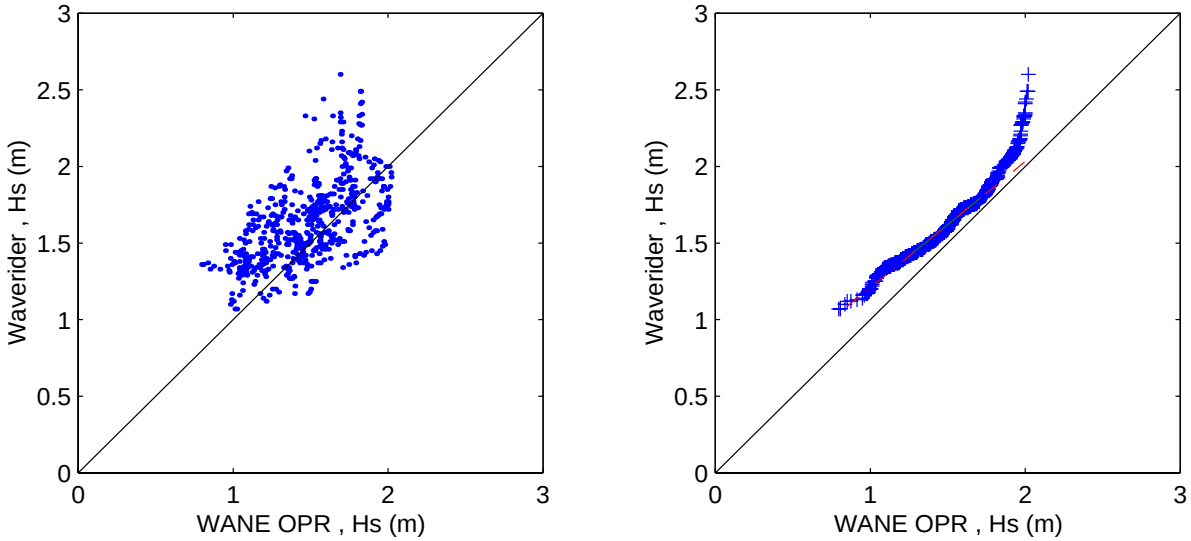

FIGURE 9.6 : BONGA - Waverider 1st period/NOAA - Sea-state Hs.

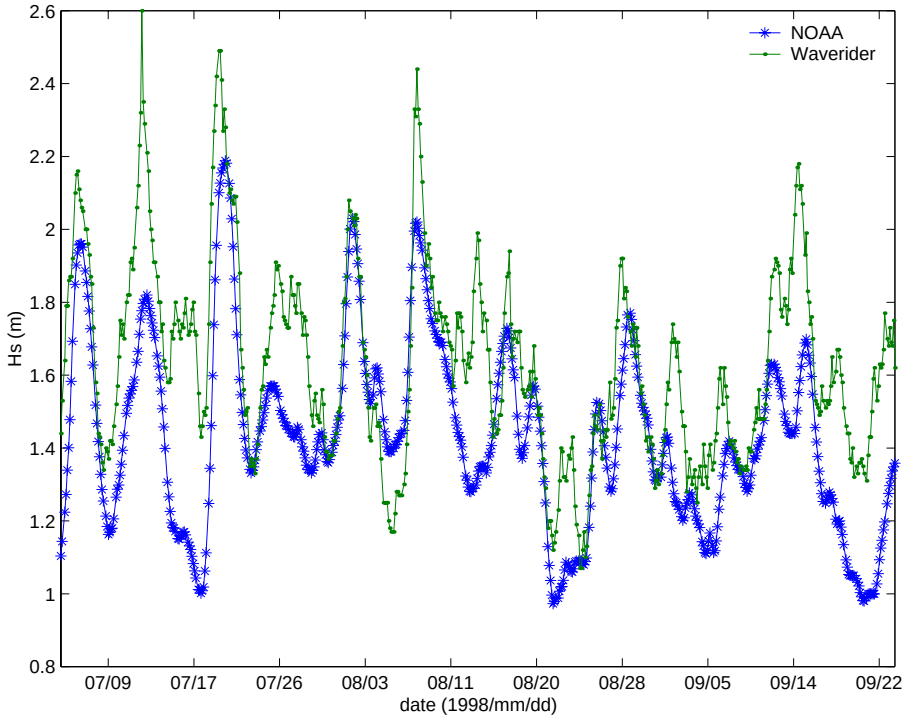

FIGURE 9.7 : BONGA - Waverider 1st period/NOAA - Sea-state Hs. Scatter and quantile/quantile plots

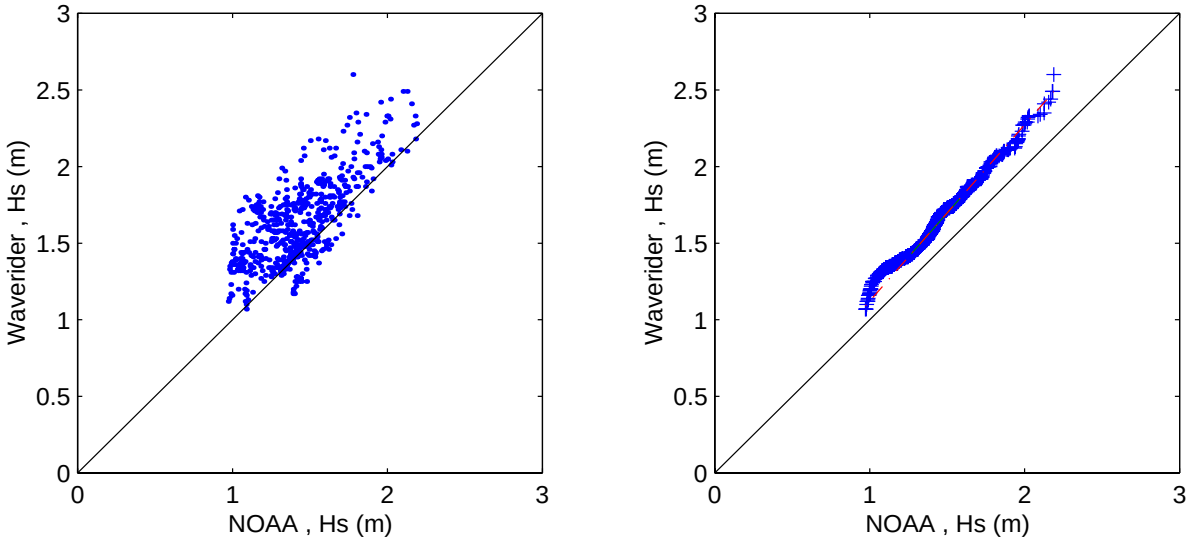

FIGURE 9.8 : BONGA - Waverider 2nd period/WANE - Sea-state Hs.

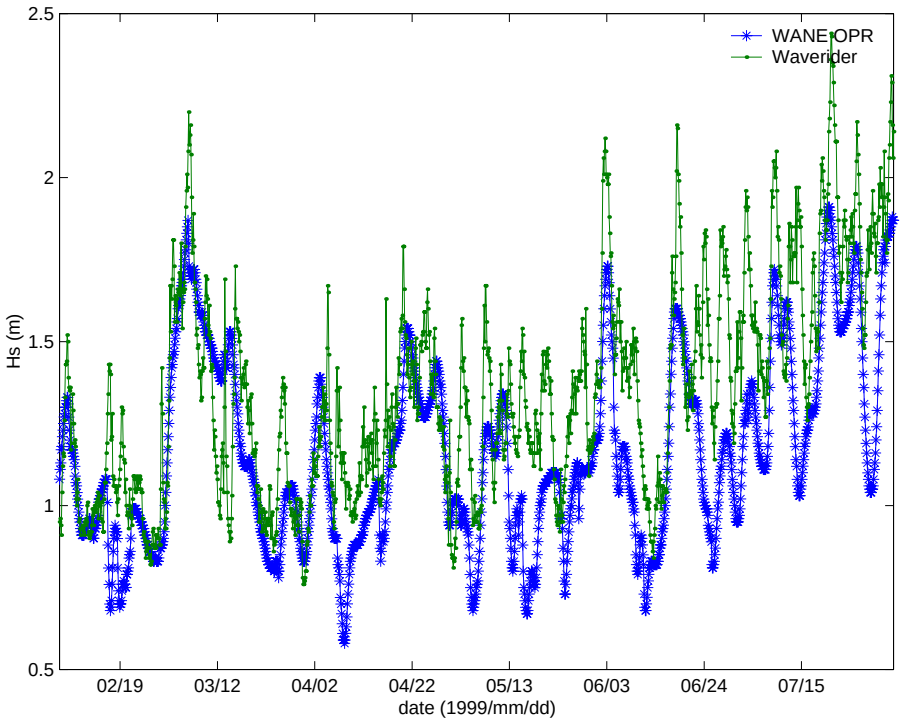

FIGURE 9.9 : BONGA - Waverider 2nd period/WANE - Sea-state Hs. Scatter and quantile/quantile plots

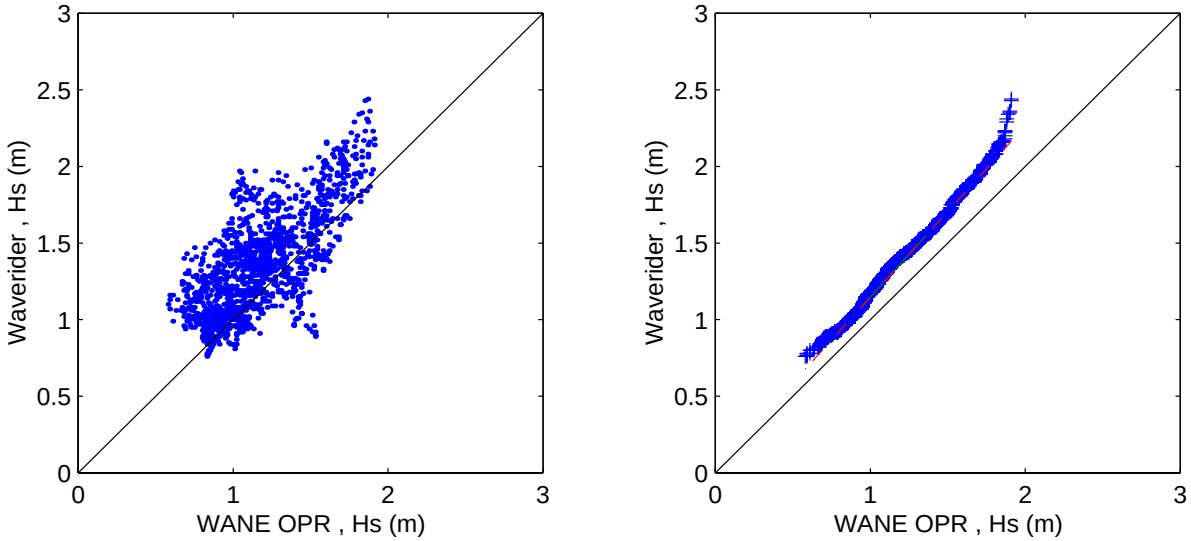

FIGURE 9.10 : BONGA - Waverider 2nd period/NOAA - Sea-state Hs.

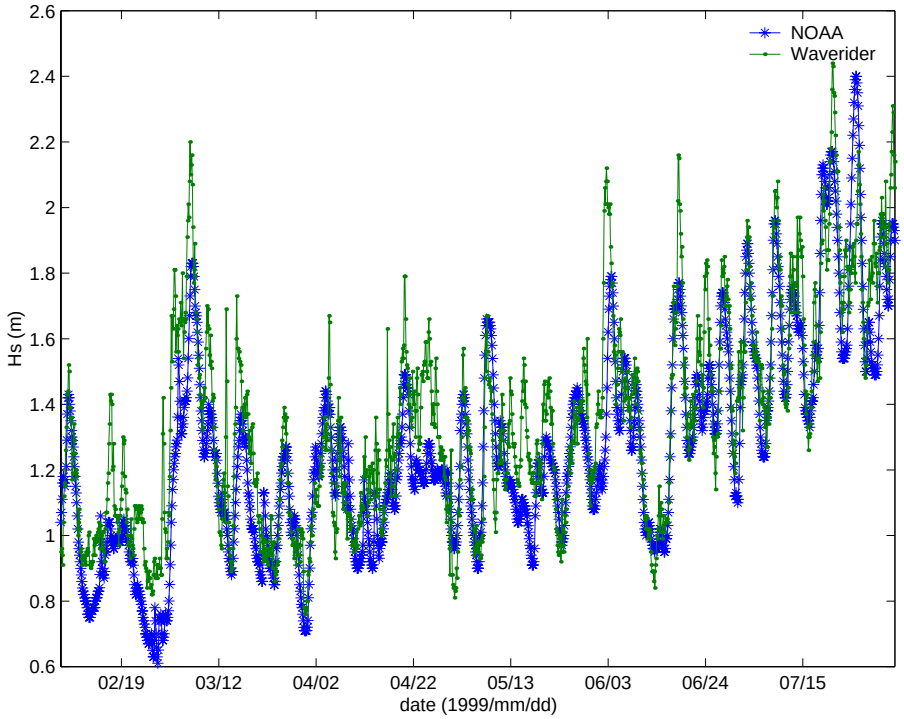

FIGURE 9.11 : BONGA - Waverider 2nd period/NOAA - Sea-state Hs. Scatter and quantile/quantile plots

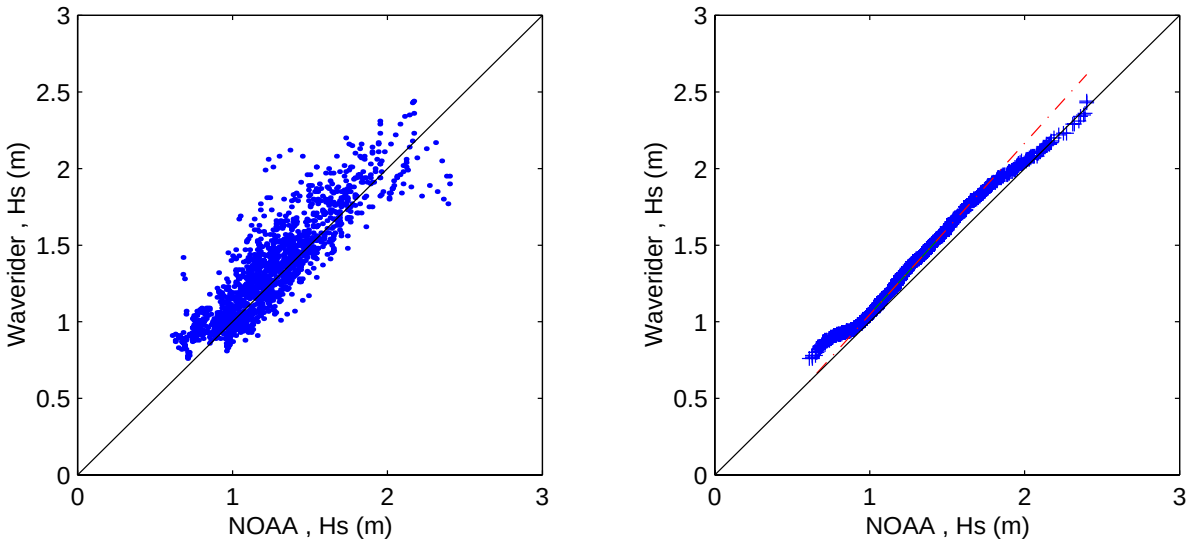

FIGURE 9.12 : BONGA - Wavescan/NOAA - Sea-state Hs.

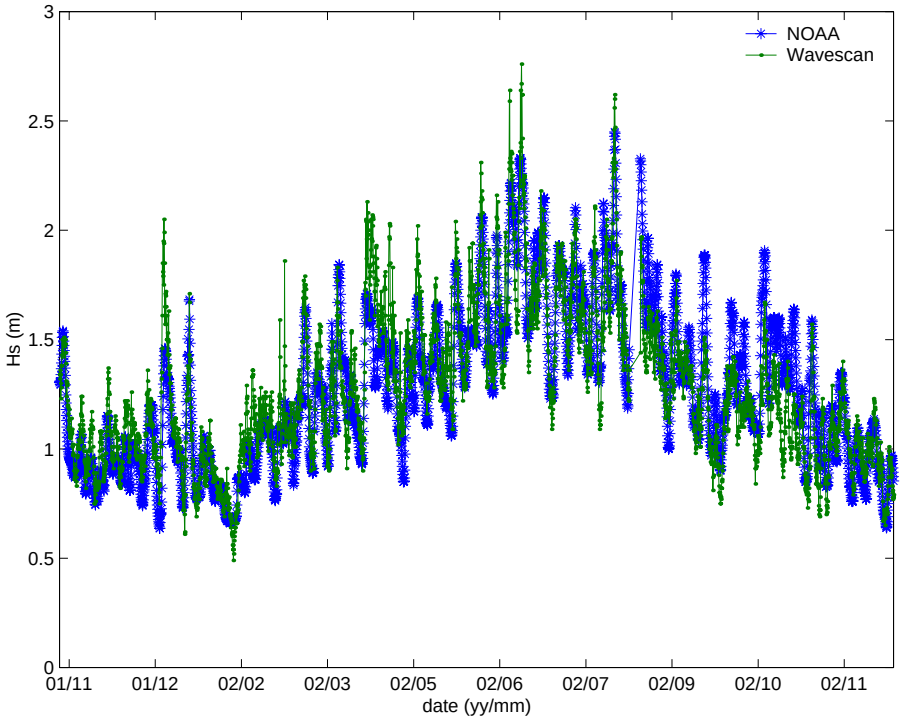

FIGURE 9.13 : BONGA - Wavescan/NOAA - Sea-state Hs. Scatter and quantile/quantile plots

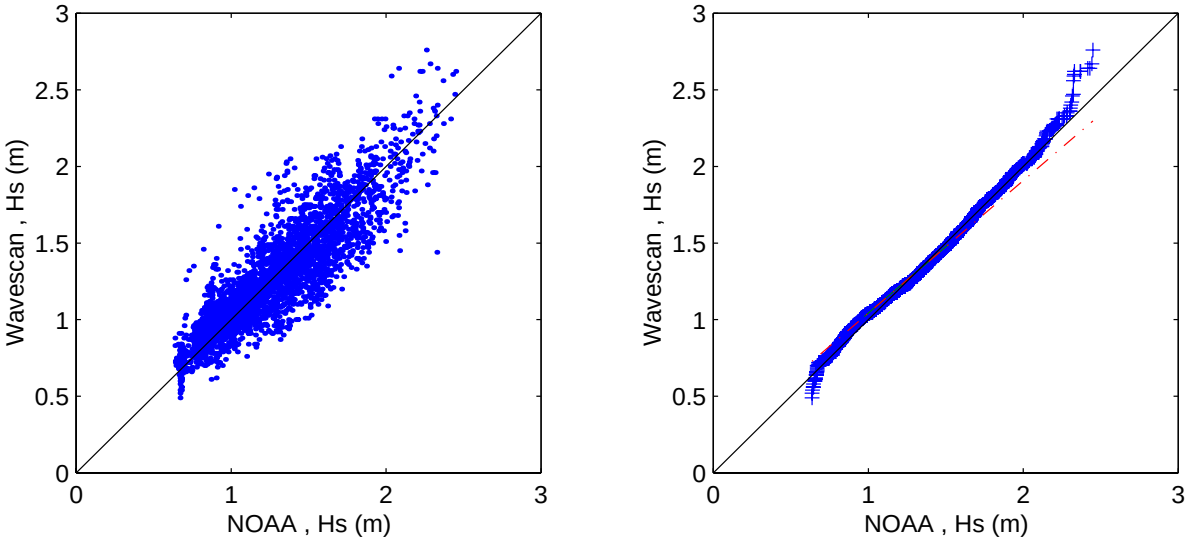

FIGURE 9.14 : Chevron - Wavestaff 85m/WANE - Sea-state Hs.

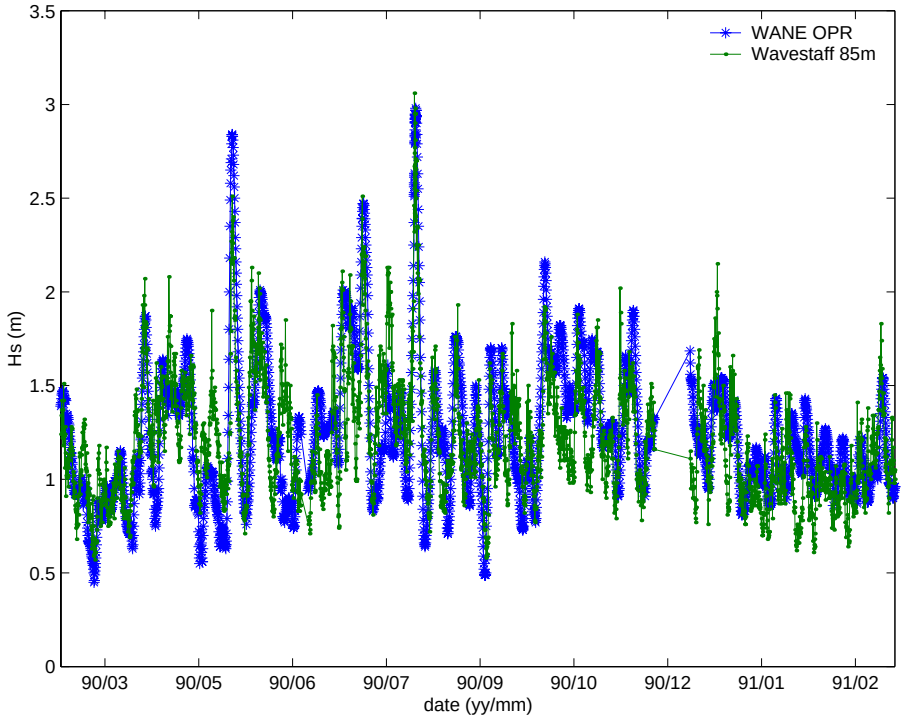

FIGURE 9.15 : Chevron - Wavestaff 85m/WANE - Sea-state Hs. Scatter and quantile/quantile plots

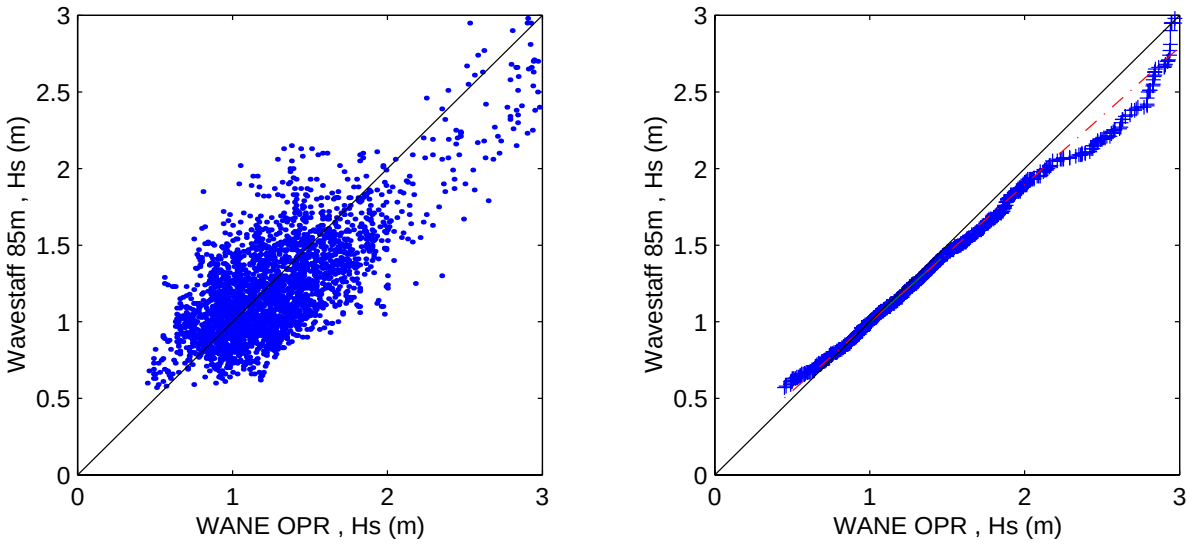

FIGURE 9.16 : Chevron - Wavestaff 8m/WANE - Sea-state Hs.

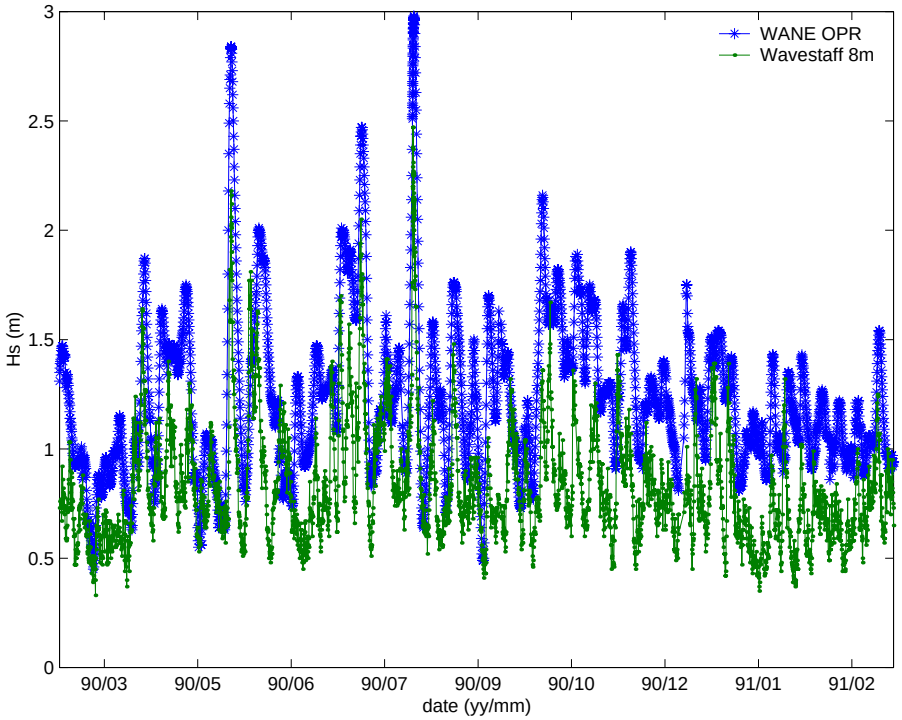

FIGURE 9.17 : Chevron - Wavestaff 8m/WANE - Sea-state Hs. Scatter and quantile/quantile plots

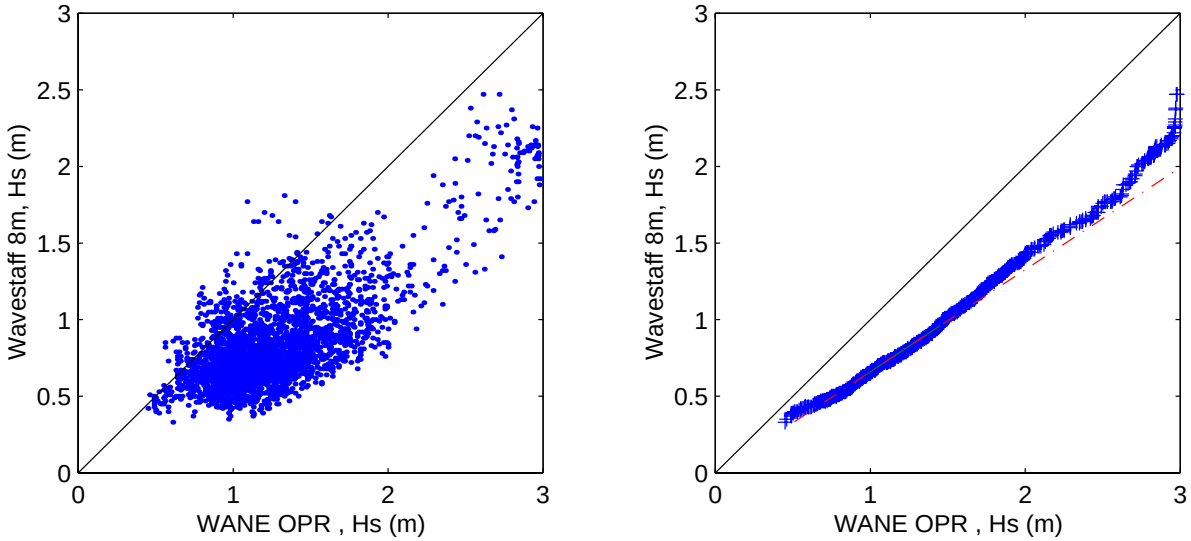

FIGURE 9.18 : KUDU - Waverider/WANE - Sea-state Hs.

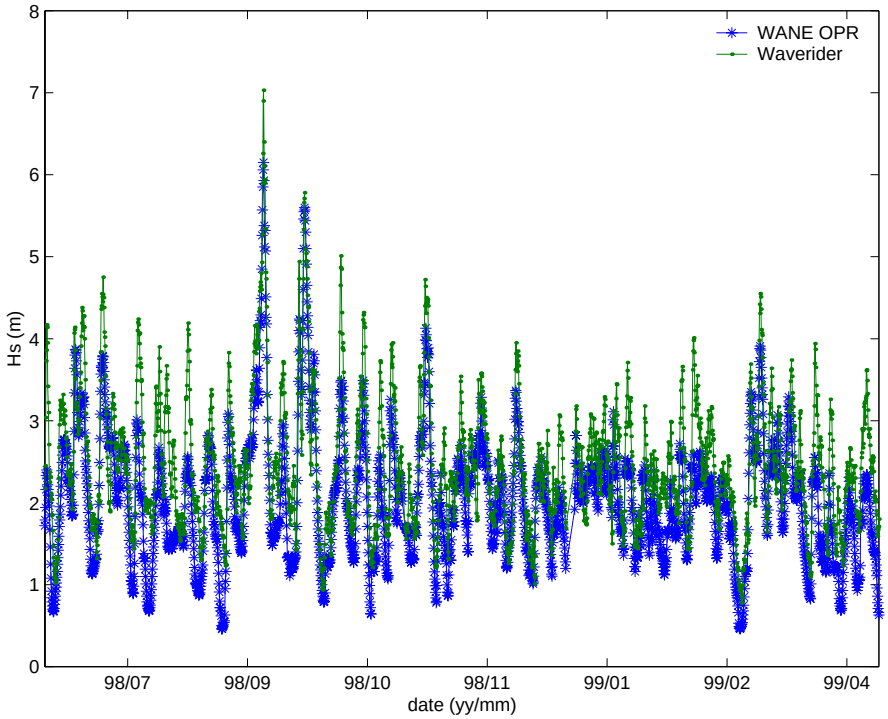

FIGURE 9.19 : KUDU - Waverider/WANE - Sea-state Hs. Scatter and quantile/quantile plots

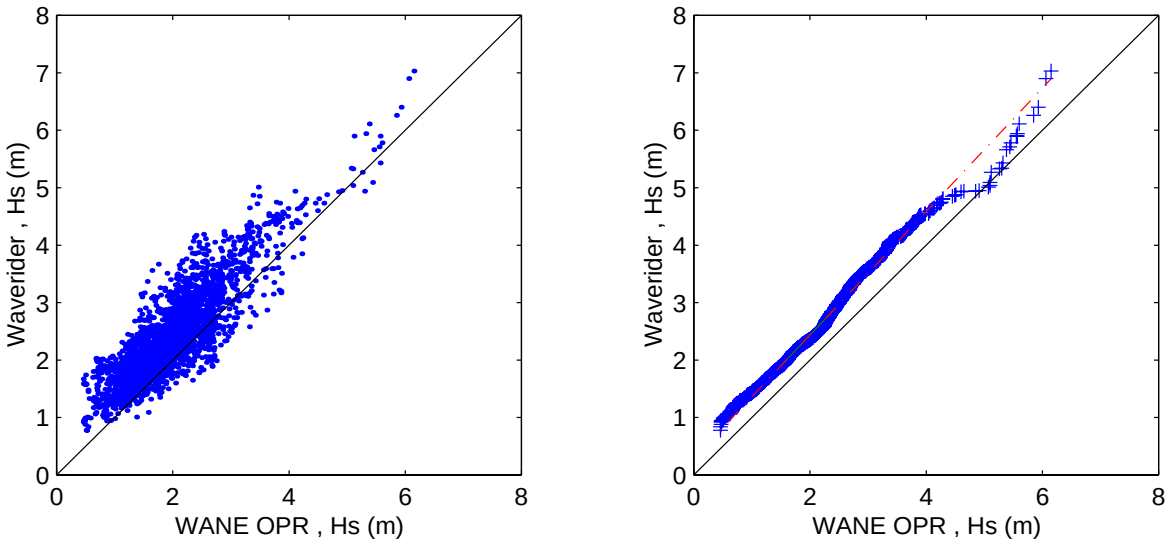

FIGURE 9.20 : KUDU - Waverider/NOAA - Sea-state Hs.

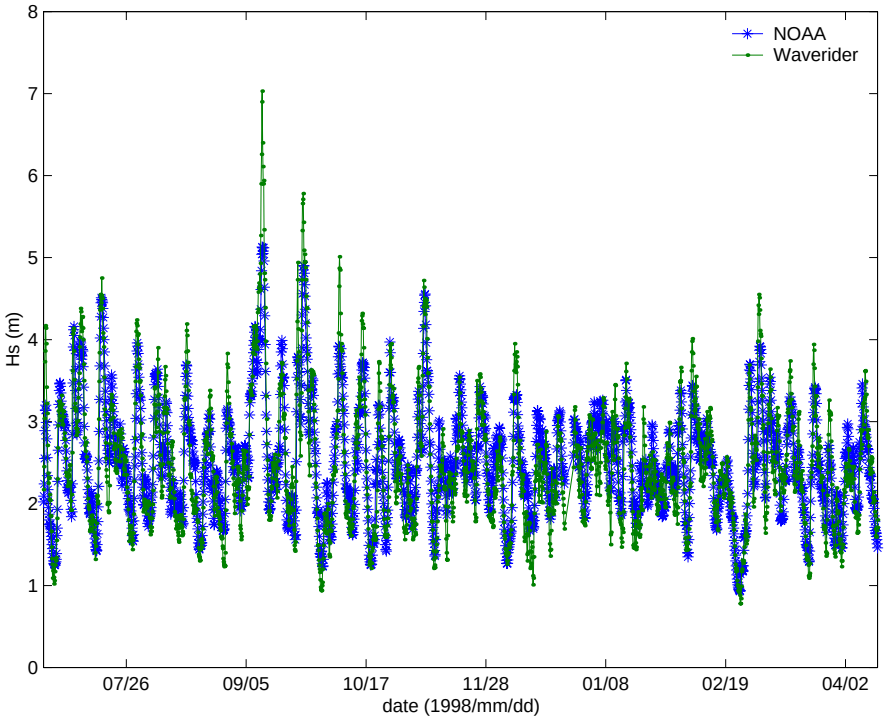

FIGURE 9.21 : KUDU - Waverider/NOAA - Sea-state Hs. Scatter and quantile/quantile plots

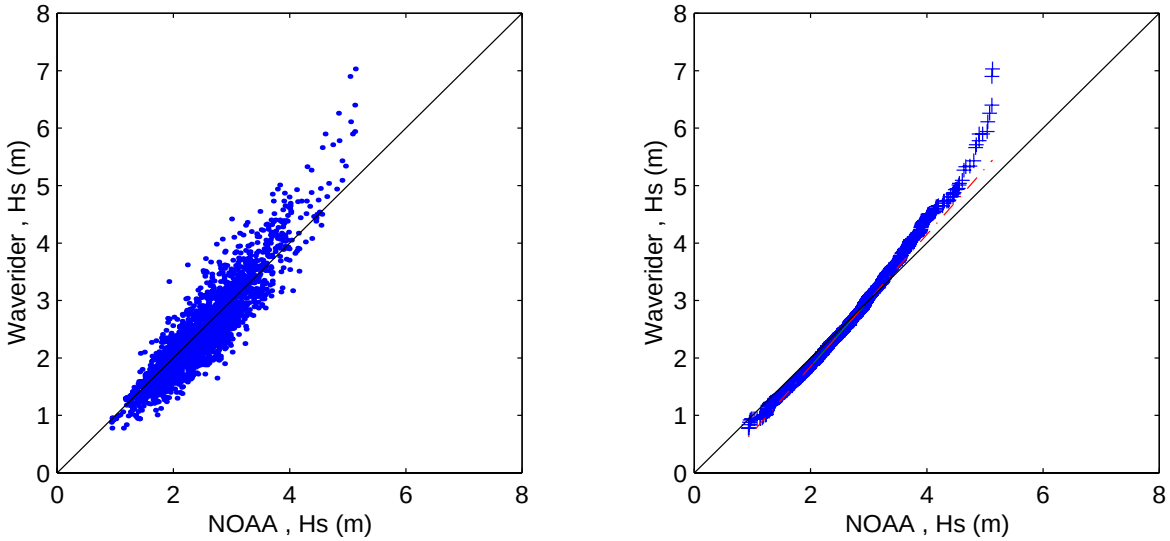

FIGURE 9.22 : BONGA - Waverider/NOAA/WANE - Peak frequency.

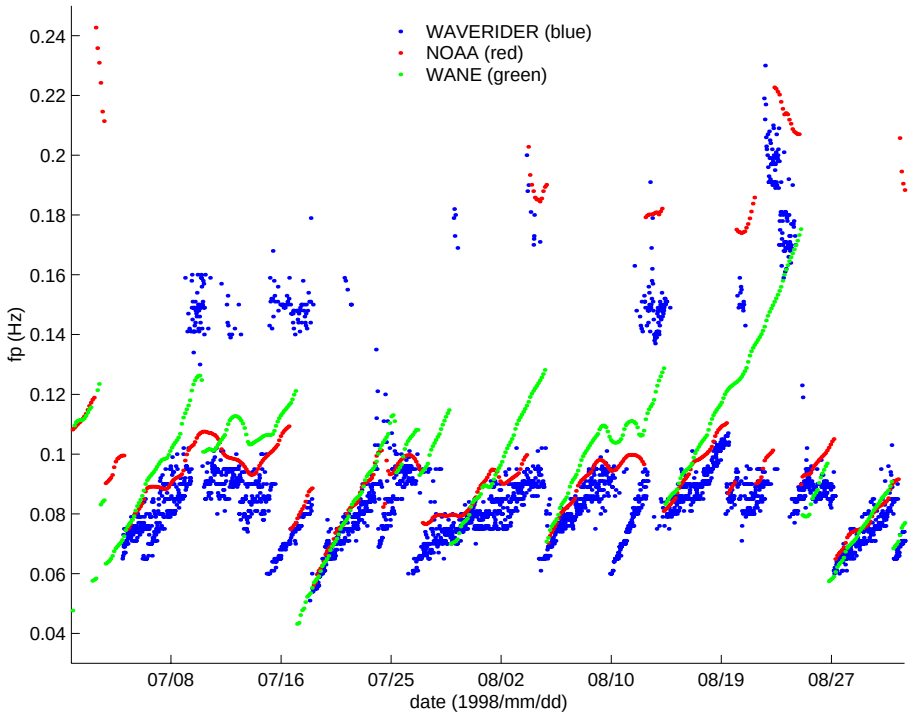

FIGURE 9.23 : BONGA - Waverider 1st period/NOAA - Peak frequency and peak direction ($x10^{-3}$).

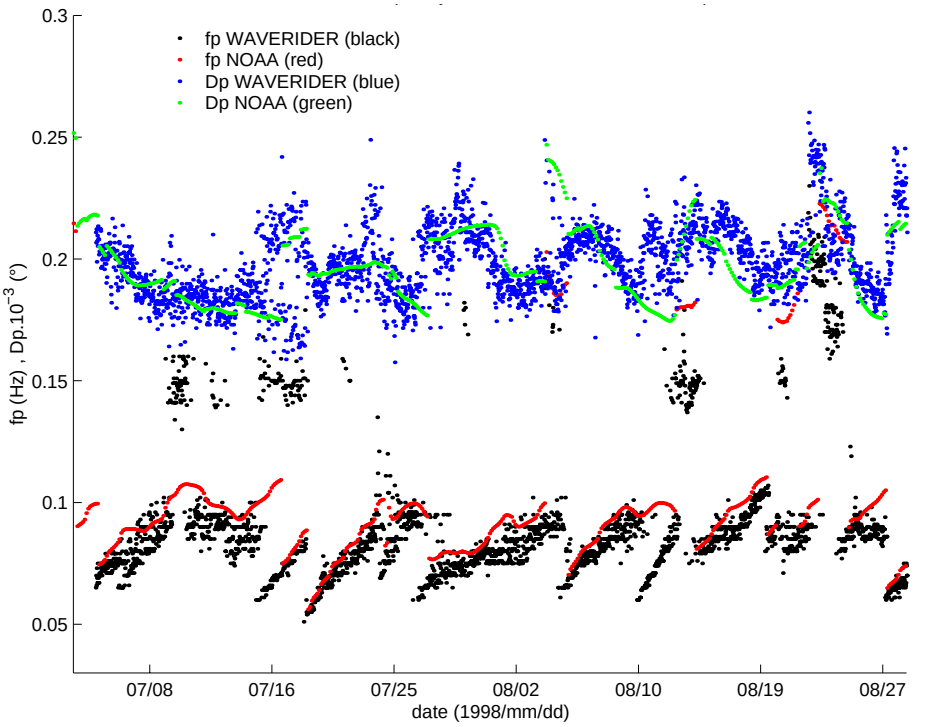

FIGURE 9.24 : BONGA - Waverider 2nd period/NOAA - Peak frequency and peak direction (x10^{-3}).

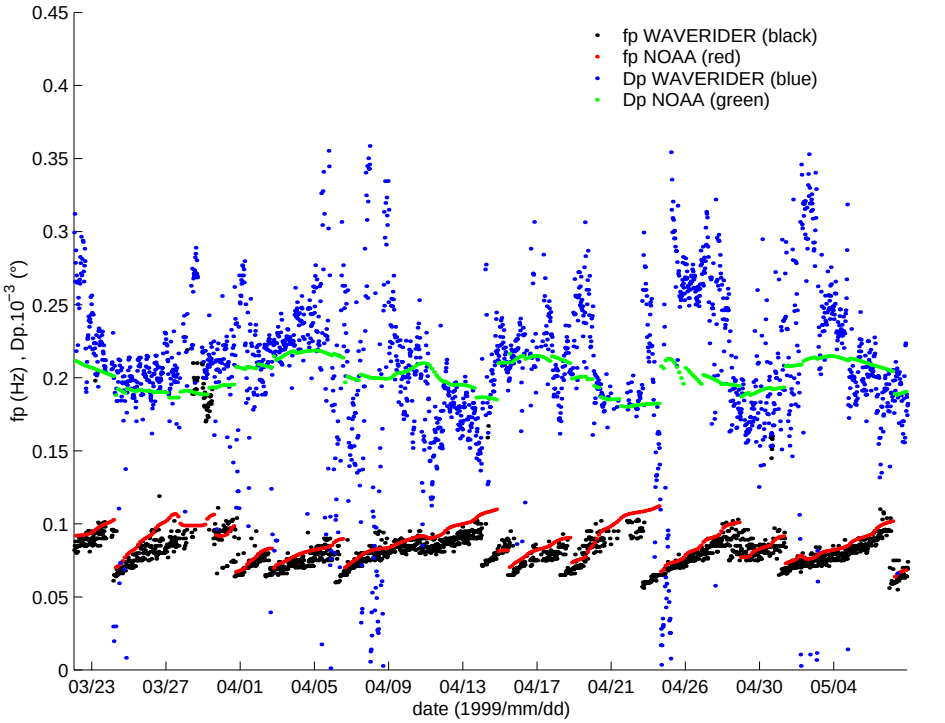

FIGURE 9.25 : BONGA - Wavescan/NOAA - Peak frequency.

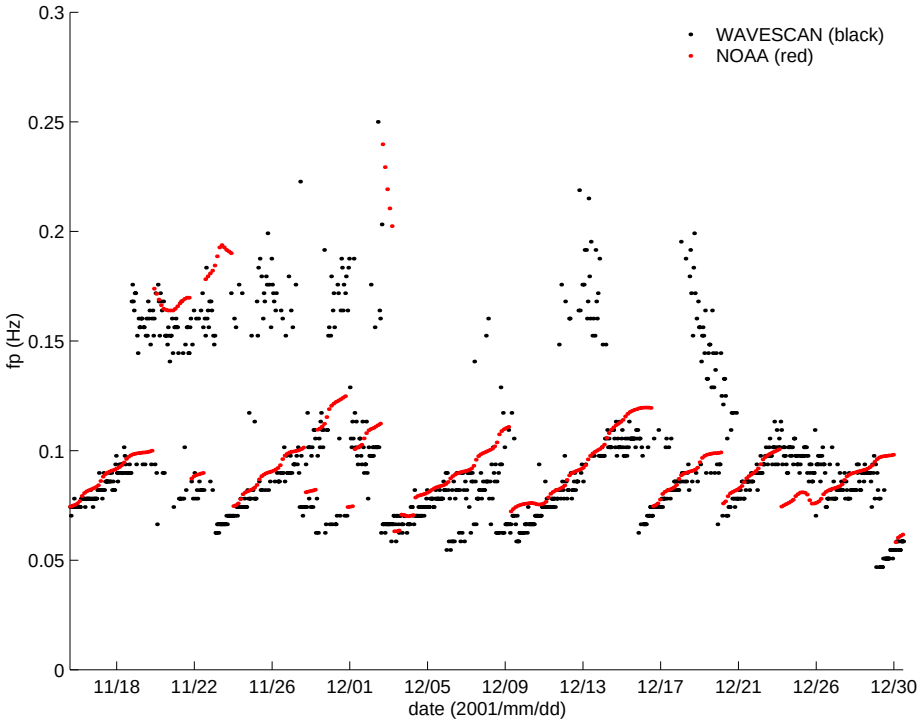

FIGURE 9.26 : BONGA - Wavescan/NOAA - Peak frequency and peak direction (x10^{-3}).

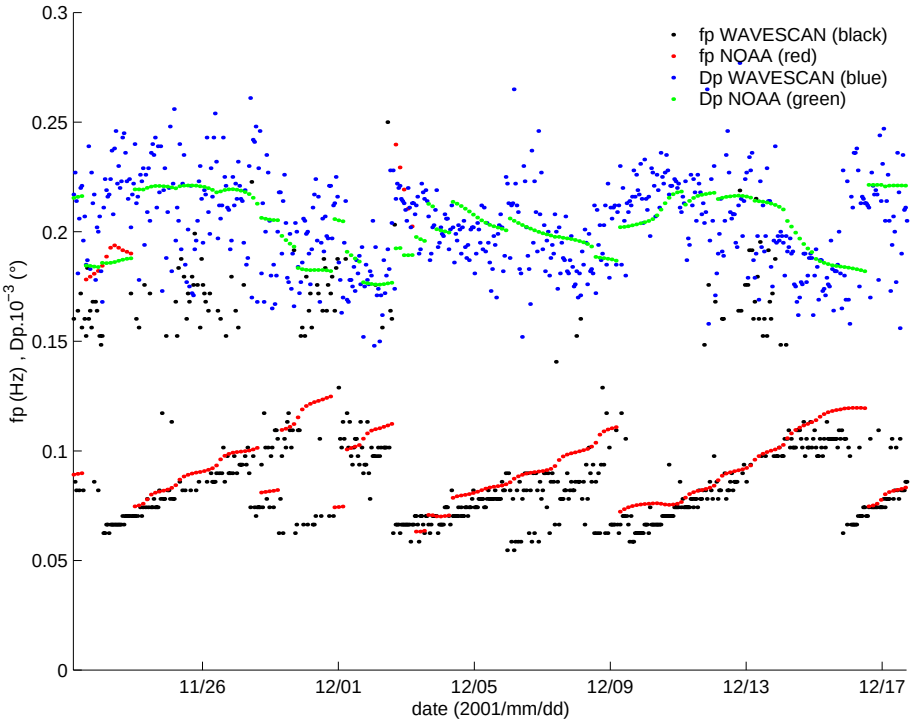

FIGURE 9.27 : Hindcast WANE 28793 (green) vs Bonga 1st period measurements (black) - Wave systems - Peak frequency.

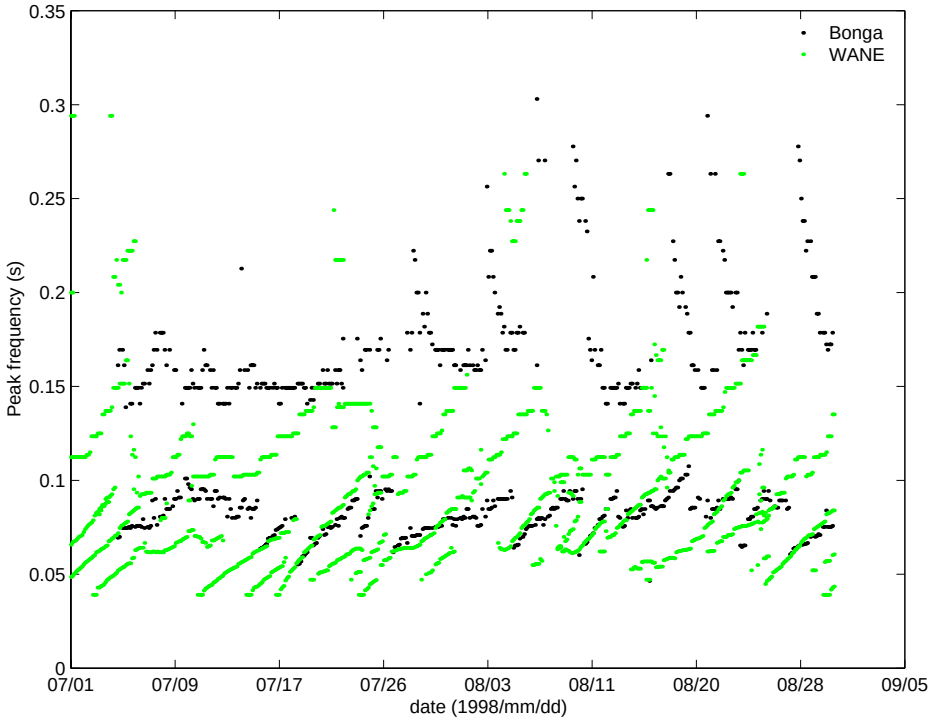

FIGURE 9.28 : Hindcast WANE 28793 (green) vs Bonga (black) 2nd period measurements - Wave systems - Peak frequency.

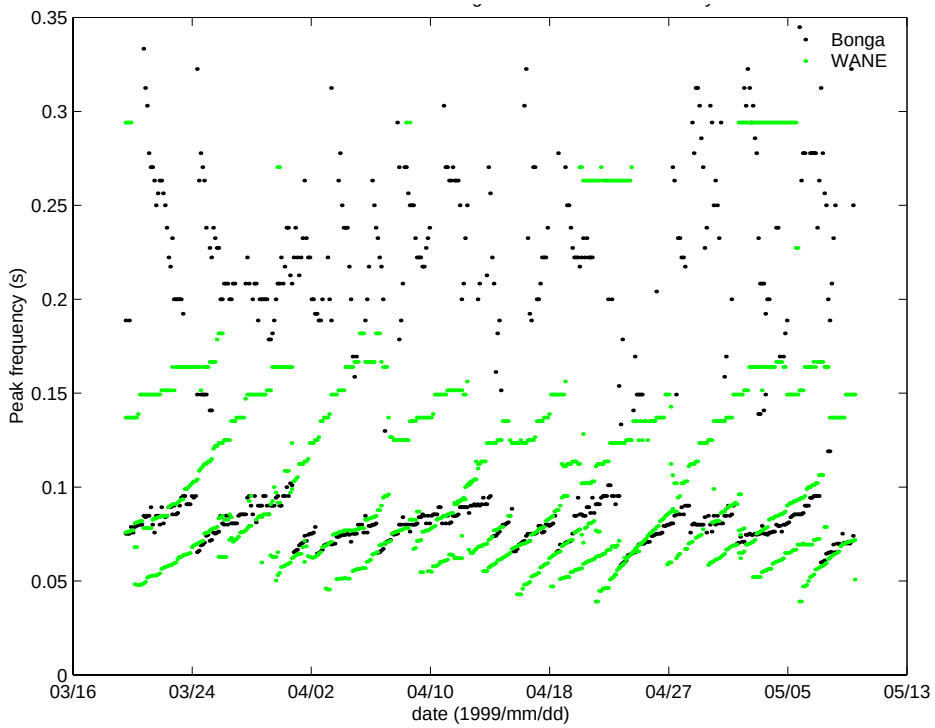

FIGURE 9.29 : Hindcast WANE 26099 (green) vs Chevron measurements (blue) - Wave systems - Peak frequency.

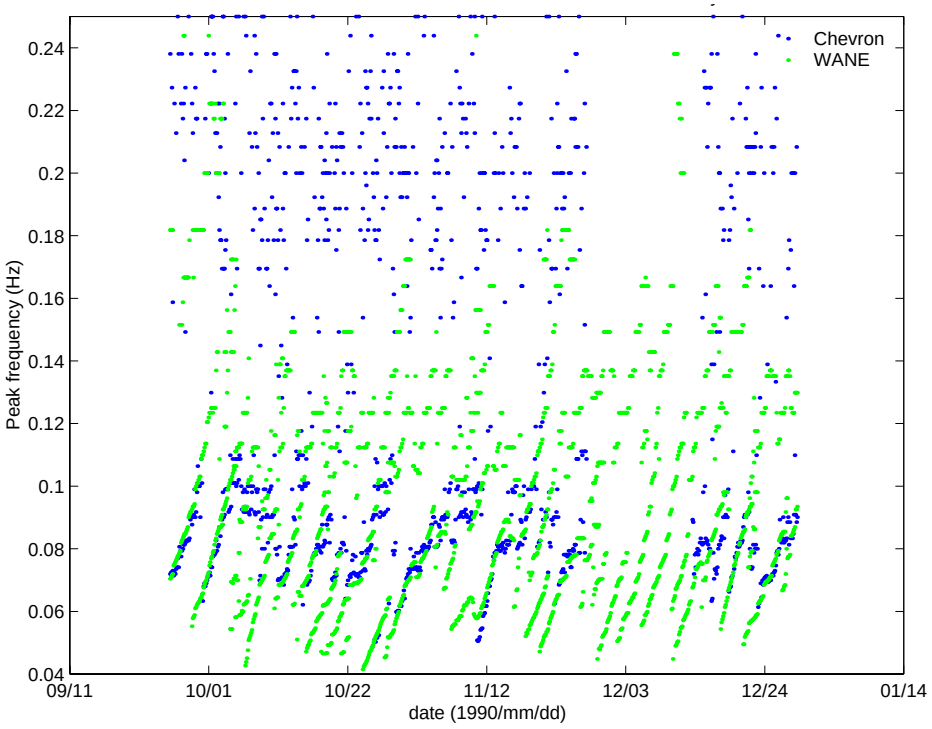

FIGURE 9.30 : Hindcast WANE 19573 (green) vs Kudu measurements (blue) - Wave systems - Peak frequency.

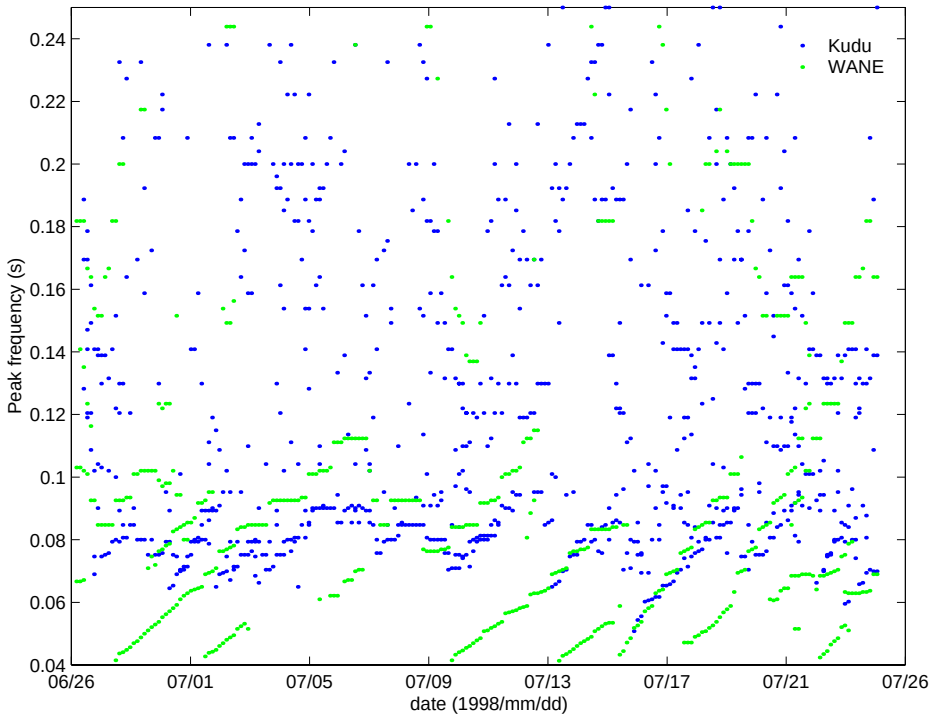

FIGURE 9.31 : BONGA - WANE OPR/NOAA - Sea-state Hs. Scatter and quantile/quantile plots

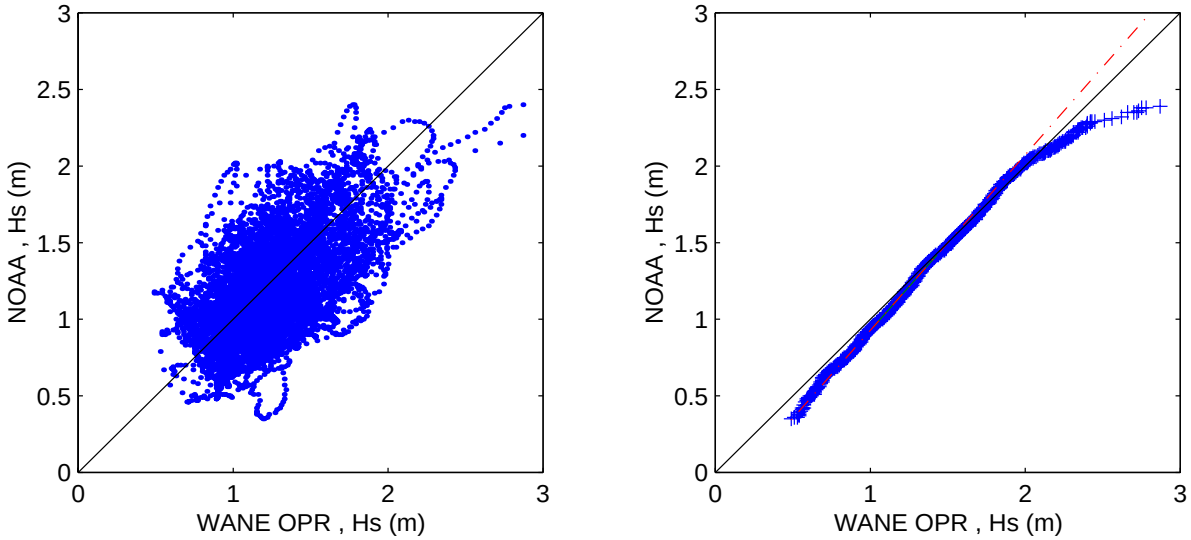

FIGURE 9.32 : BONGA - WANE QSCAT/NOAA - Sea-state Hs.

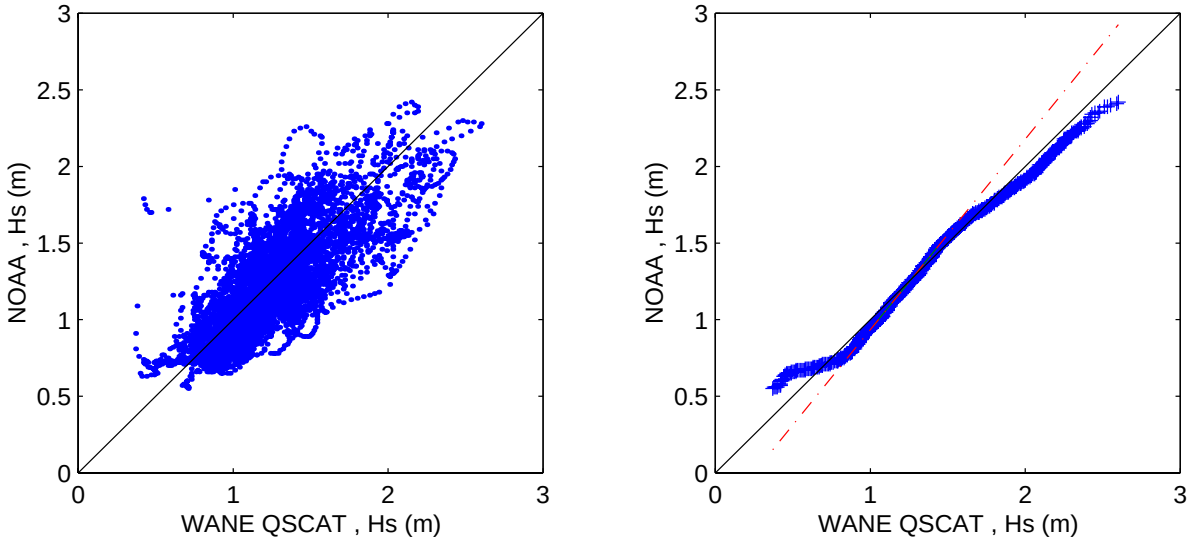

FIGURE 9.33 : CHEVRON - WANE OPR/NOAA - Sea-state Hs.

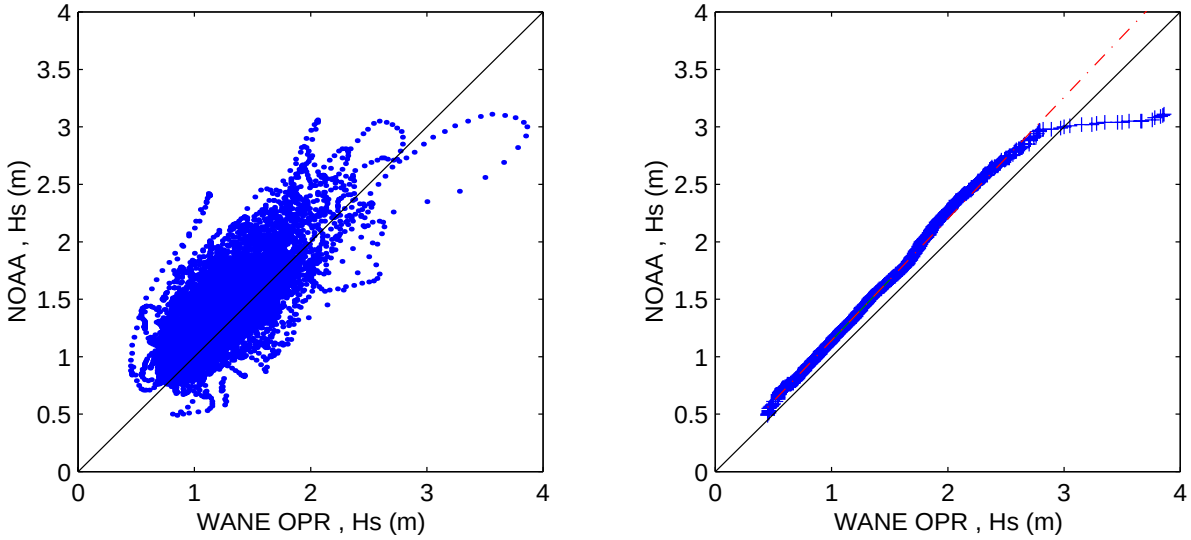

FIGURE 9.34 : CHEVRON - WANE QSCAT/NOAA - Sea-state Hs. Scatter and quantile/quantile plots

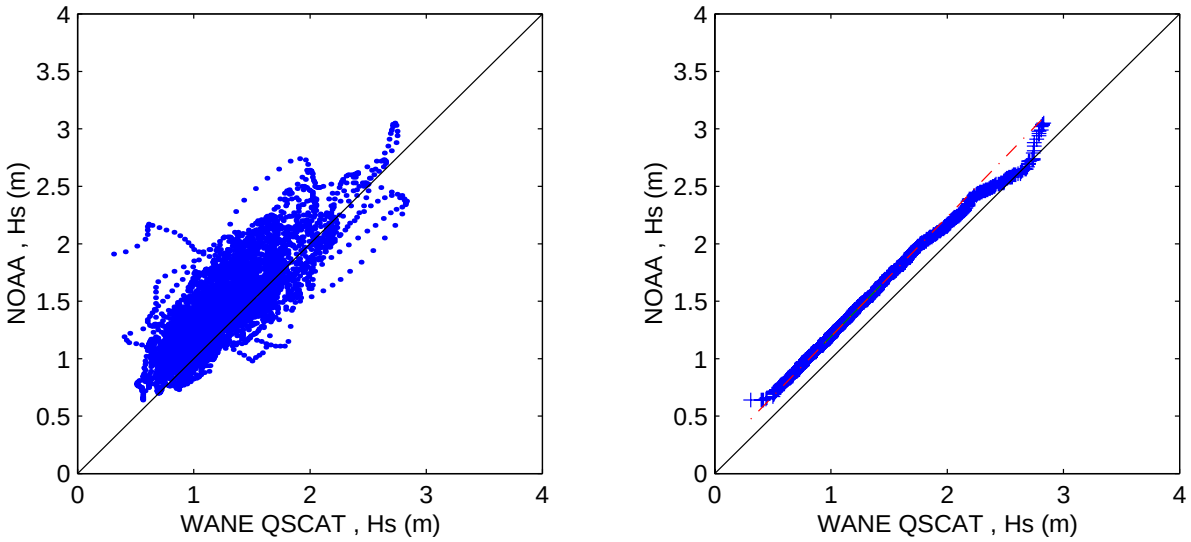

FIGURE 9.35 : KUDU - WANE OPR/NOAA - Sea-state Hs.

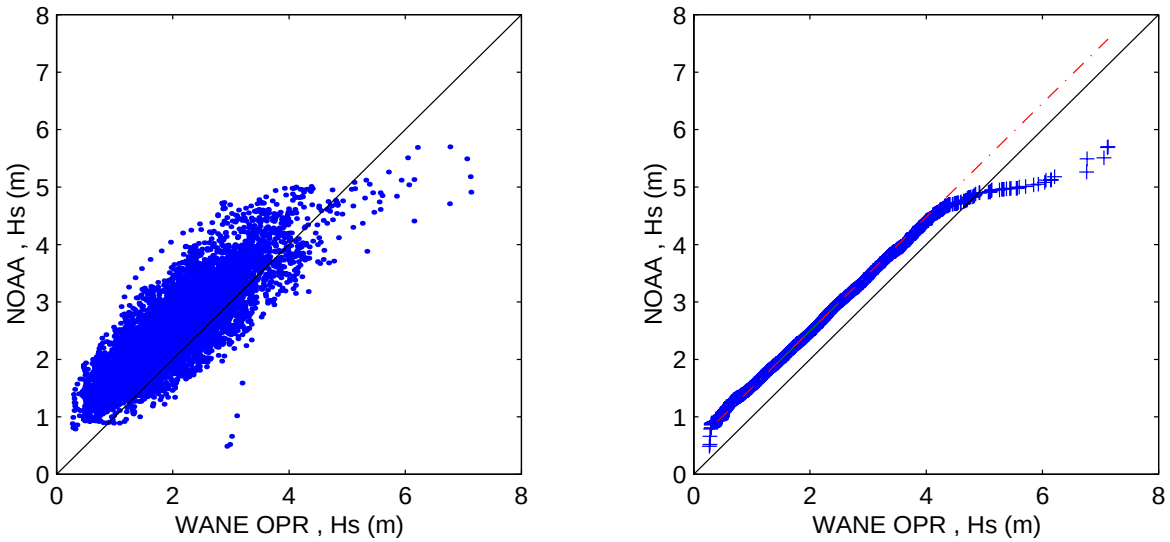

FIGURE 9.36 : KUDU - WANE QSCAT/NOAA - Sea-state Hs.

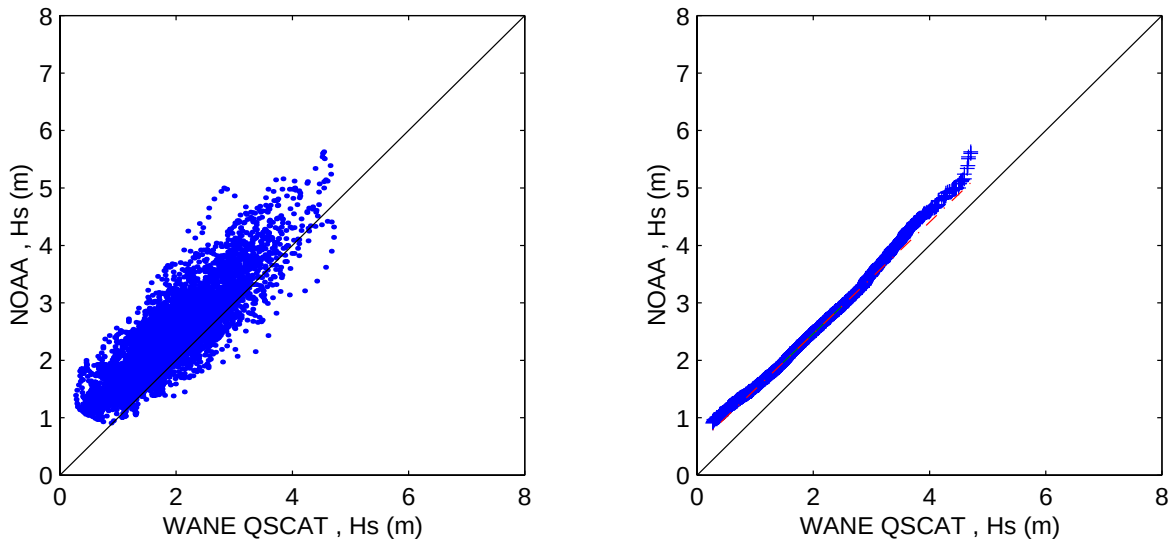

CHAPTER 10

West Africa swell gustiness A stationarity study

Michel Olagnon

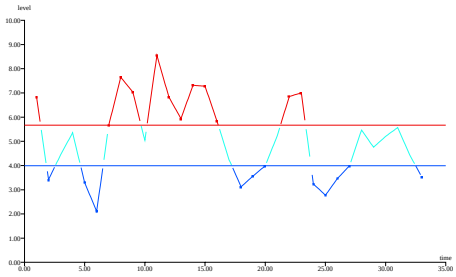

This chapter deals with item 6. of the WASP scope of work: *Stationarity of the sea-state*. The idea is to test the hypothesis that swell would come in gusts, with more energy at some times and less at some others than would be statistically expected from the linear spectral model.

Methodology

Swell spectrum “no switching” test

The assumption that a sea-state derives from a spectrum both implies that a sea-state is a stationary segment in the global history of the water surface elevation, and that the water surface elevation is the superimposition of an infinite number of independent (i.e. random phase) sine wave components.

FIGURE 10.1 : Consecutive windows for Welch’s averaging

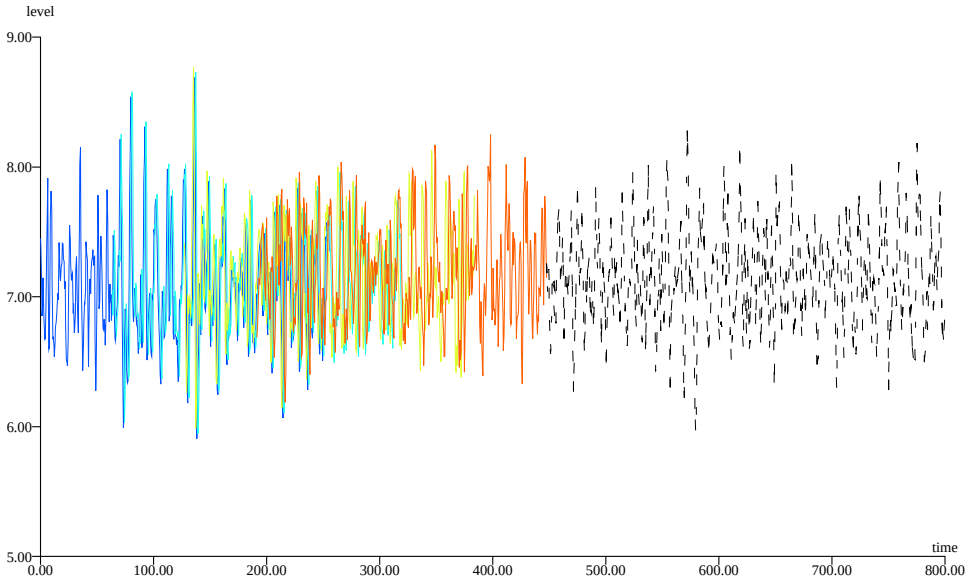

A kind of non-stationarity that we will test for would be that the swell would not derive from a single spectrum, but would be switching between two spectra of differing intensities. The test will thus consist in assuming that two spectra of differing intensities are alternating in the time-history, then estimate the intensities of those two spectra, and finally check the statistical significance of the ratio of those intensities.

FIGURE 10.2 : Consecutive spectral estimates

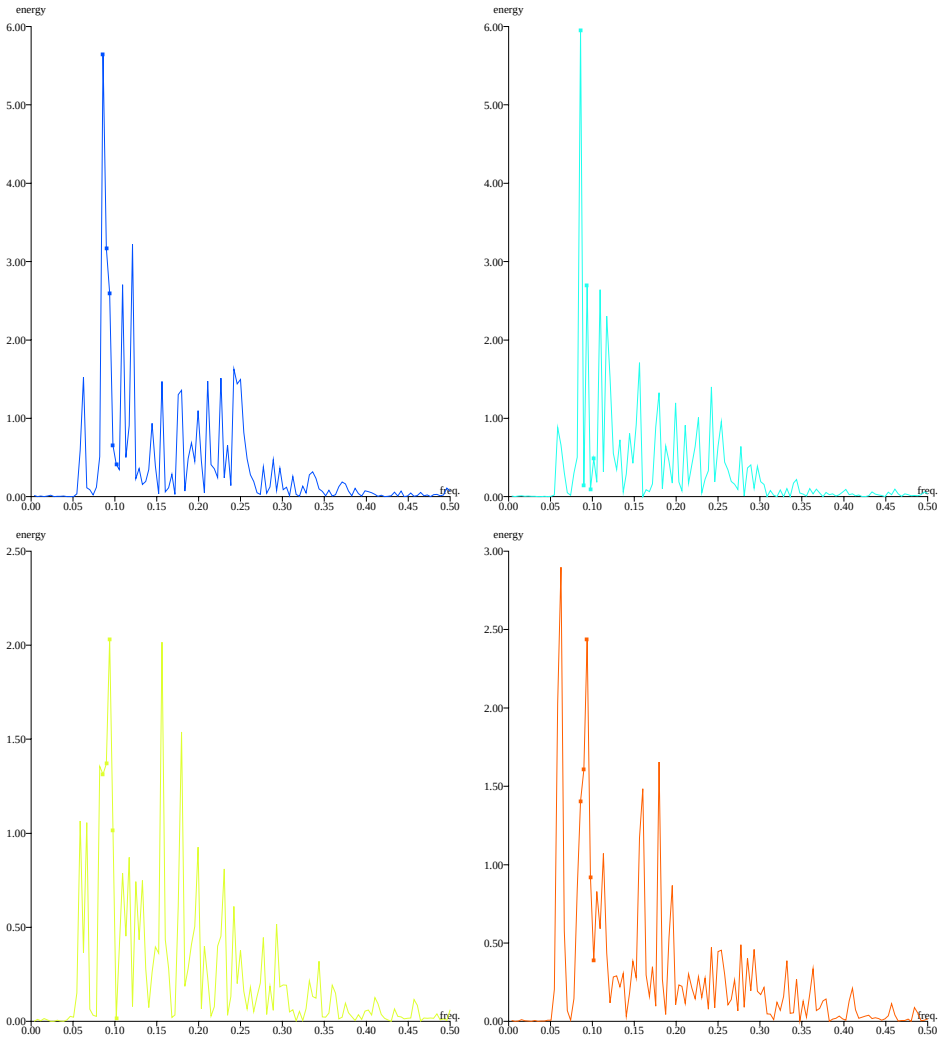

When estimating the spectrum from the Fourier transform of a stationary sampled signal, i.e. an instance of a temporal process with that spectrum, each spectral value estimate is a random variable equal to the sum of the squares of the real and imaginary parts of the Fourier transform complex coefficient at the frequency of interest. A Fourier transform complex coefficient is calculated as the weighted sum of the time series samples, with weights equal to the N-roots of -1, of unit modulus. Since all samples belong to the same statistical distribution and their number is large, the real and imaginary parts of the Fourier transform complex coefficient belong to normal distributions as a consequence of the central limit theorem, and the spectral estimate at a given frequency belongs to a χ^2 distribution with 2 degrees of freedom. It should be noted that for a χ^2 distribution with 2 degrees of freedom, the variance is equal to the mean.

Standard techniques use smoothing or averaging to reduce irregularity and to improve the estimation. One of the averaging techniques, ``Welch's averaging", can be suited to our needs. In that technique, the time history is split into N shorter segments as shown on figure 10.1 and the spectral estimates corresponding to each of these segments are then averaged. The quality of the estimation may be improved by making segments overlap.

FIGURE 10.3 : Spectral estimates history

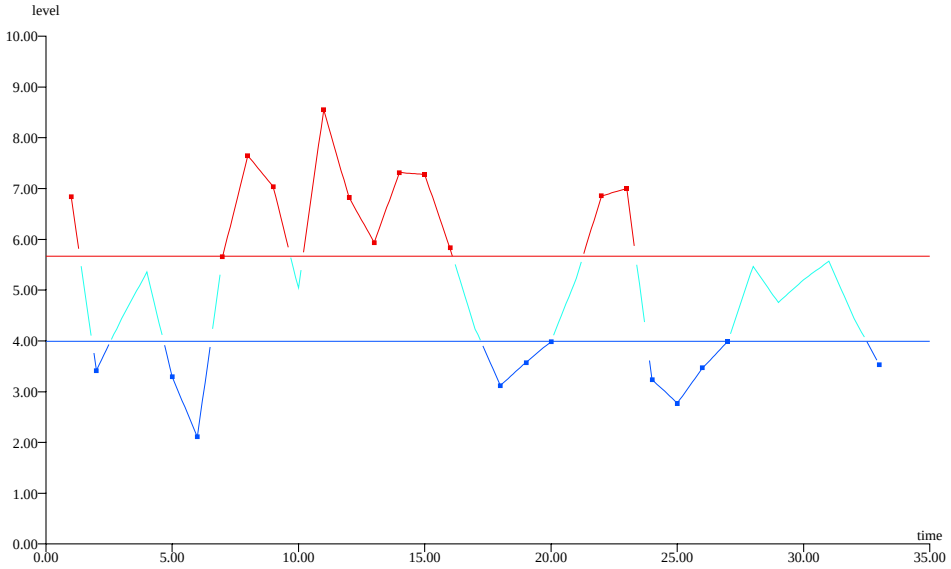

When we want to check for two differing switching spectra, instead of averaging all N segments periodograms of figure 10.2, one may estimate the spectrum in two different ways by correcting for each frequency band by the corresponding ratio to the distribution parameter in a χ^2 distribution, on one hand the average over the N/3 segments where energy at the frequency of interest is lowest, and on the other hand over the N/3 segments where is is highest. On Figure 10.3, this means that separate estimates are made by averaging only the red and only the blue values, and corrected through the use of their theoretical ratios to the overall mean, and the ratio of the two estimates is then studied.

The same ratio is computed for a large number of simulated instances deriving from a single spectrum, and the position in the distribution of the simulated ratios is then taken as a measure of the likelihood of the switching between two differing spectra.

Gust lengths distribution test

Even if the swell would not come from switching spectra, but from a single one, there might be more coherent low and high energy periods than given by the standard superimposition model.

Taking the history of the segments energies at the frequency of interest, the distributions of run-lengths vs threshold defining a run is computed for the measured data and for simulated data with the same spectrum. Comparison of the two provides the likelihood that some additional phenomenon would pack swell in bursts of energy.

Processing

Reference with synthetic data

Series of random instances were computed for a number of synthetic spectra. First, the 4 shapes defined in chapter 5 and shown on figure 10.4 were used isolated, for a 12.2 second swell. Then, a combination of 3 swell systems and wind sea was used, and the swell peaks were modelled with the 4 shapes. Combination of the various shapes in the same spectrum was however not tried.

FIGURE 10.4 : Spectral shapes used to reconstruct reference data

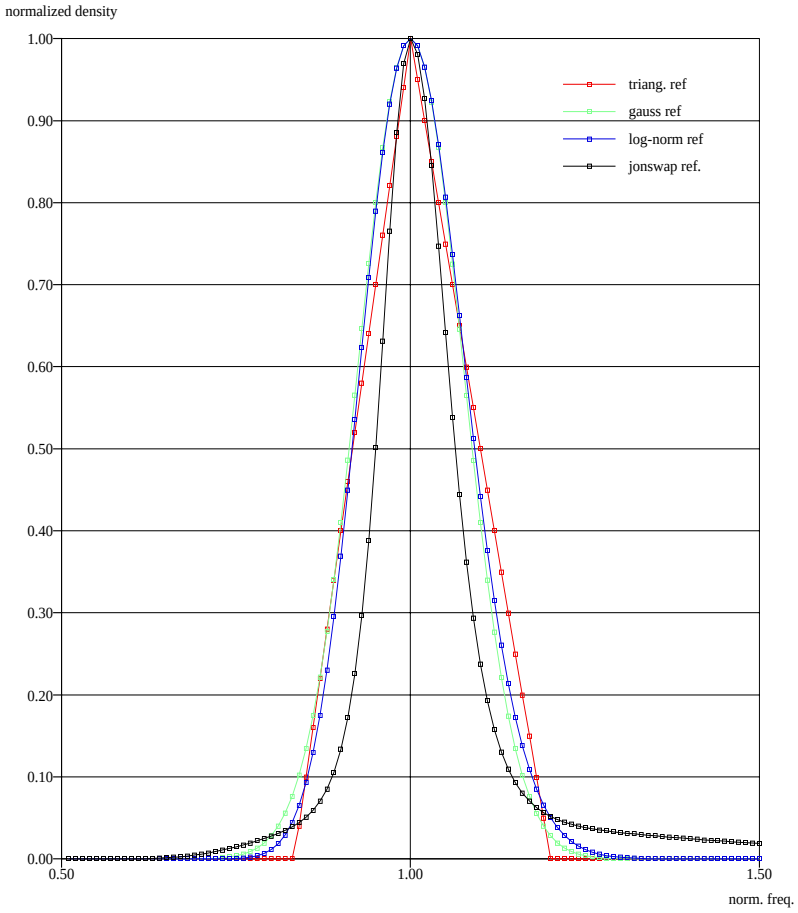

The reference cases for each of which 10000 simulations were made are as follows:

- Single peak, H_S=0.636, T_p=12.2, triangular shape, m=6
- Single peak, H_S=0.636, T_p=12.2, Gaussian shape, σ_f=0.075f_p
- Single peak, H_S=0.636, T_p=12.2, log-normal shape, σ_f=0.075f_p
- Single peak, H_S=0.636, T_p=12.2, Jonswap shape, γ=20.3
- Multiple peak with wave systems of table 10.1, triangular shape for swell, m=6
- Multiple peak with wave systems of table 10.1, Gaussian shape for swell, σ_f=0.075f_p
- Multiple peak with wave systems of table 10.1, log-normal shape for swell, σ_f=0.075f_p
- Multiple peak with wave systems of table 10.1, Jonswap shape for swell, γ=20.3

TABLE 10.1 : Composite spectrum

System	H_S	T_p
Swell 1	0.636	15.800
Swell 2	0.529	12.204
Swell 3	0.464	8.273
Wind sea	0.792	5.674

In each simulation, 2388 seconds were randomly selected and analysed as 33 consecutive windows of 256 seconds each, with 75 points of overlapping. For each window, a periodogram is computed, and provides a spectral estimate. For each simulation, we thus have a time-history of 33 spectral estimates, following a χ^2 distribution with 2 degrees of freedom at each frequency bin, that we analyse for stationarity.

The parameters that are investigated are named as follows:

- $R_{.l}$: ratio of average of lowest one third of the estimates to overall average, normalized by theoretical value for a χ^2 distribution.
- $R_{.h}$: ratio of average of highest one third of the estimates to overall average, normalized by theoretical value for a χ^2 distribution.
- $L_{.l}$: length of runs below empirical one third (lowest) quantile.
- $L_{.h}$: length of runs above empirical two thirds (highest one third) quantile.
- $_{.w.}$: the estimates are computed over interval $[f_p–0.075f_p,f_p+0.075f_p]$.
- $_{.p.}$: the estimates are computed at the peak frequency f_p.
- $_{.n.}$: the estimates are computed at the peak frequency f_p and normalized by the theoretical χ^2 corresponding to their empirical quantile position.

Processing of the Ekoundou data

The Ekoundou data consists of records of 2388 seconds duration, that are processed in the same way as the synthetic data. For the definition of peak frequencies f_p, the 3 (or less when fewer were found) swell peaks with the highest H_s that were identified in the partitioning are numbered 1, 2 and 3 in the order of decreasing periods (increasing frequencies). The number of swell systems numbered 1 is 128, numbered 2 is 74, and numbered 3 is 18.

The numbering is thus consistent with that of table 10.1 for the simulations.

Comparisons

In the following tables the different cases are indicated by **(Sn/m)**. **S** indicates the spectral shape (**T**riangle, **G**aussian, **L**og-normal, **J**onswap), **n** the number of the peak which is considered, **m** the number of peaks in the sea-state.

"Wideband" ratios.

Ratios R_{wh} and R_{wl} are computed over interval $[f_p-0.075f_p, f_p+0.075f_p]$, *i.e.* a significant part of the identified wave system. They exhibit the following characteristics for synthetic data:

TABLE 10.2 : R_{wl}

Case	average	std. dev.	skewness	kurtosis
(T1/1)	1.07	0.155	-0.06	2.8
(G1/1)	1.06	0.158	-0.07	2.9
(L1/1)	1.06	0.156	-0.06	2.9
(J1/1)	1.01	0.160	-0.03	2.8
(T1/3)	0.88	0.165	+0.05	2.8
(G1/3)	0.88	0.168	+0.05	2.9
(L1/3)	0.88	0.167	+0.05	2.8
(J1/3)	0.84	0.170	+0.10	2.8
Ekoundou 1	0.93	0.196	+0.09	2.7
(T2/3)	1.10	0.148	-0.08	2.8
(G2/3)	1.08	0.150	-0.05	2.9
(L2/3)	1.09	0.150	-0.09	2.9
(J2/3)	1.05	0.156	-0.08	2.9
Ekoundou 2	1.06	0.150	+0.04	3.0
(T3/3)	1.09	0.149	-0.06	2.9
(G3/3)	1.09	0.152	-0.06	2.8
(L3/3)	1.09	0.152	-0.11	2.9
(J3/3)	1.07	0.153	-0.06	2.8
Ekoundou 3	1.11	0.151	-0.35	1.9

TABLE 10.3 : R_{wh}

Case	average	std. dev.	skewness	kurtosis
(T1/1)	1.00	0.073	+0.38	3.1
(G1/1)	1.00	0.076	+0.41	3.1
(L1/1)	1.00	0.075	+0.36	3.1
(J1/1)	1.03	0.081	+0.37	3.1
(T1/3)	1.08	0.087	+0.29	3.0
(G1/3)	1.09	0.090	+0.34	3.0
(L1/3)	1.09	0.090	+0.36	3.1
(J1/3)	1.11	0.094	+0.32	3.0
Ekoundou 1	1.07	0.104	+0.36	2.9
(T2/3)	0.99	0.070	+0.40	3.1
(G2/3)	1.00	0.072	+0.39	3.2
(L2/3)	0.99	0.071	+0.41	3.2
(J2/3)	1.01	0.077	+0.42	3.3
Ekoundou 2	1.01	0.066	-0.23	3.0
(T3/3)	0.99	0.070	+0.40	3.2
(G3/3)	0.99	0.071	+0.38	3.1
(L3/3)	0.99	0.070	+0.38	3.2
(J3/3)	1.00	0.074	+0.41	3.1
Ekoundou 3	0.99	0.073	+0.06	1.8

Peak ratios

Ratios R_{ph} and R_{pl} are computed at the only frequency bin f_p, *i.e.* a small part of the identified wave system. They exhibit the following characteristics::

TABLE 10.4 : R_{pl}

Case	average	std. dev.	skewness	kurtosis
(T1/1)	0.45	0.136	+0.45	3.1
(G1/1)	0.44	0.137	+0.46	3.2
(L1/1)	0.44	0.138	+0.49	3.1
(J1/1)	0.45	0.141	+0.46	3.1
(T1/3)	0.45	0.139	+0.47	3.2
(G1/3)	0.44	0.137	+0.49	3.2
(L1/3)	0.44	0.139	+0.50	3.2
(J1/3)	0.45	0.144	+0.48	3.2
Ekoundou 1	0.44	0.142	+0.40	2.9
(T2/3)	0.44	0.135	+0.47	3.3
(G2/3)	0.44	0.137	+0.49	3.2
(L2/3)	0.44	0.136	+0.46	3.2
(J2/3)	0.44	0.141	+0.49	3.2
Ekoundou 2	0.43	0.129	+0.31	3.6
(T3/3)	0.44	0.134	+0.45	3.1
(G3/3)	0.44	0.134	+0.46	3.2
(L3/3)	0.44	0.135	+0.49	3.2
(J3/3)	0.44	0.135	+0.44	3.1
Ekoundou 3	0.44	0.154	+1.01	4.7

TABLE 10.5 : R_{ph}

Case	average	std. dev.	skewness	kurtosis
(T1/1)	1.30	0.102	+0.11	2.9
(G1/1)	1.30	0.102	+0.15	2.9
(L1/1)	1.30	0.103	+0.12	2.9
(J1/1)	1.30	0.106	+0.11	2.8
(T1/3)	1.30	0.103	+0.11	2.9
(G1/3)	1.31	0.103	+0.10	2.8
(L1/3)	1.31	0.104	+0.12	2.8
(J1/3)	1.30	0.108	+0.15	2.8
Ekoundou 1	1.31	0.104	+0.40	2.9
(T2/3)	1.31	0.101	+0.13	2.9
(G2/3)	1.31	0.102	+0.14	2.9
(L2/3)	1.31	0.102	+0.12	2.9
(J2/3)	1.31	0.105	+0.13	2.9
Ekoundou 2	1.31	0.101	+0.05	2.8
(T3/3)	1.31	0.101	+0.17	2.9
(G3/3)	1.31	0.101	+0.12	2.9
(L3/3)	1.31	0.100	+0.11	2.9
(J3/3)	1.31	0.102	+0.11	2.9
Ekoundou 3	1.32	0.093	-0.44	3.3

Normalized ratios

Ratios R_{nh} and R_{nl} are computed at the only frequency bin f_p, *i.e.* a small part of the identified wave system, but from estimates that are corrected from the theoretical χ^2 factor corresponding to their quantile. They exhibit the following characteristics:

TABLE 10.6 : R_{nl}

Case	average	std. dev.	skewness	kurtosis
(T1/1)	0.95	0.312	+0.58	3.4
(G1/1)	0.95	0.313	+0.60	3.5
(L1/1)	0.95	0.317	+0.62	3.4
(J1/1)	0.95	0.321	+0.58	3.4
(T1/3)	0.95	0.317	+0.63	3.6
(G1/3)	0.94	0.313	+0.63	3.5
(L1/3)	0.94	0.318	+0.64	3.5
(J1/3)	0.96	0.329	+0.63	3.6
Ekoundou 1	0.93	0.321	+0.45	3.0
(T2/3)	0.94	0.308	+0.61	3.5
(G2/3)	0.94	0.312	+0.61	3.4
(L2/3)	0.94	0.310	+0.60	3.5
(J2/3)	0.94	0.321	+0.64	3.6
Ekoundou 2	0.92	0.289	+0.50	4.0
(T3/3)	0.94	0.306	+0.58	3.4
(G3/3)	0.94	0.304	+0.59	3.5
(L3/3)	0.94	0.308	+0.62	3.5
(J3/3)	0.94	0.307	+0.57	3.3
Ekoundou 3	0.94	0.367	+1.30	5.5

TABLE 10.7 : R_{nh}

Case	average	std. dev.	skewness	kurtosis
(T1/1)	0.92	0.063	+0.04	2.9
(G1/1)	0.92	0.063	+0.10	2.9
(L1/1)	0.92	0.063	+0.05	2.8
(J1/1)	0.92	0.065	+0.06	2.9
(T1/3)	0.92	0.063	+0.03	2.9
(G1/3)	0.92	0.063	+0.03	2.8
(L1/3)	0.92	0.064	+0.06	2.9
(J1/3)	0.92	0.066	+0.08	2.8
Ekoundou 1	0.92	0.062	+0.24	2.9
(T2/3)	0.92	0.062	+0.05	3.0
(G2/3)	0.92	0.063	+0.06	2.9
(L2/3)	0.92	0.063	+0.06	2.9
(J2/3)	0.92	0.065	+0.06	2.9
Ekoundou 2	0.92	0.059	-0.02	2.8
(T3/3)	0.92	0.062	+0.10	2.9
(G3/3)	0.92	0.062	+0.05	2.9
(L3/3)	0.92	0.062	+0.05	2.9
(J3/3)	0.92	0.062	+0.03	2.9
Ekoundou 3	0.93	0.062	-0.19	3.4

"Wideband" run-lengths

Run-lengths L_{wh} and L_{wl} are computed over interval $[f_p-0.075f_p, f_p+0.075f_p]$, *i.e.* a significant part of the identified wave system. They exhibit the following characteristics:

TABLE 10.8 : L_{wl}

Case	average	std. dev.	skewness	kurtosis
(T1/1)	2.68	0.788	+1.95	12.5
(G1/1)	2.69	0.790	+1.84	11.2
(L1/1)	2.70	0.785	+1.92	12.6
(J1/1)	2.78	0.834	+2.07	13.5
(T1/3)	2.64	0.759	+1.81	11.2
(G1/3)	2.68	0.776	+1.79	10.7
(L1/3)	2.68	0.774	+1.98	12.8
(J1/3)	2.80	0.824	+2.10	14.0
Ekoundou 1	2.63	0.768	+1.66	9.2
(T2/3)	2.55	0.756	+1.86	11.7
(G2/3)	2.61	0.773	+1.79	11.2
(L2/3)	2.58	0.755	+1.90	12.9
(J2/3)	2.70	0.799	+1.86	11.7
Ekoundou 2	2.51	0.673	+1.30	6.1
(T3/3)	2.61	0.766	+2.03	13.9
(G3/3)	2.61	0.751	+1.89	12.4
(L3/3)	2.63	0.758	+1.89	12.6
(J3/3)	2.68	0.789	+1.95	12.2
Ekoundou 3	2.28	0.844	+1.72	6.8

TABLE 10.9 : L_{wh}

Case	average	std. dev.	skewness	kurtosis
(T1/1)	2.50	0.795	+2.24	16.2
(G1/1)	2.54	0.793	+1.86	12.0
(L1/1)	2.52	0.782	+1.98	13.5
(J1/1)	2.59	0.835	+2.02	13.2
(T1/3)	2.45	0.769	+2.06	14.6
(G1/3)	2.47	0.765	+2.08	14.7
(L1/3)	2.48	0.776	+2.00	13.5
(J1/3)	2.57	0.808	+1.94	12.9
Ekoundou 1	2.50	0.738	+1.65	9.8
(T2/3)	2.40	0.734	+1.94	13.0
(G2/3)	2.45	0.765	+1.96	13.3
(L2/3)	2.43	0.748	+1.88	12.2
(J2/3)	2.50	0.775	+1.96	13.4
Ekoundou 2	2.37	0.739	+1.26	7.7
(T3/3)	2.44	0.748	+1.86	12.2
(G3/3)	2.45	0.761	+1.83	11.9
(L3/3)	2.46	0.776	+1.99	13.5
(J3/3)	2.51	0.783	+2.05	14.4
Ekoundou 3	2.49	0.504	+1.14	3.2

"Peak" run-lengths

Run-lengths L_{wh} and L_{wl} are computed at the only frequency bin f_p, *i.e.* a small part of the identified wave system. They exhibit the following characteristics:

TABLE 10.10 : L_{pl}

Case	average	std. dev.	skewness	kurtosis
(T1/1)	2.26	0.639	+1.68	9.7
(G1/1)	2.24	0.622	+1.68	9.9
(L1/1)	2.23	0.606	+1.51	7.8
(J1/1)	2.38	0.670	+1.91	13.9
(T1/3)	2.30	0.637	+1.78	11.5
(G1/3)	2.32	0.641	+1.87	13.2
(L1/3)	2.32	0.649	+1.86	11.9
(J1/3)	2.49	0.725	+1.99	13.6
Ekoundou 1	2.19	0.678	+2.01	9.2
(T2/3)	2.23	0.623	+1.78	11.6
(G2/3)	2.23	0.608	+1.72	10.4
(L2/3)	2.22	0.620	+1.94	13.6
(J2/3)	2.35	0.657	+1.85	11.9
Ekoundou 2	2.11	0.548	+0.55	3.1
(T3/3)	2.19	0.611	+1.82	12.8
(G3/3)	2.17	0.600	+1.67	9.7
(L3/3)	2.18	0.594	+1.63	9.0
(J3/3)	2.25	0.632	+1.94	13.9
Ekoundou 3	2.20	0.666	+1.21	5.1

TABLE 10.11 : L_{ph}

Case	average	std. dev.	skewness	kurtosis
(T1/1)	1.97	0.524	+1.75	9.9
(G1/1)	1.96	0.522	+1.77	11.6
(L1/1)	1.96	0.500	+1.59	9.5
(J1/1)	2.06	0.569	+1.96	14.2
(T1/3)	2.00	0.536	+1.78	11.0
(G1/3)	2.01	0.531	+1.73	10.8
(L1/3)	2.02	0.540	+1.64	9.3
(J1/3)	2.15	0.597	+1.78	12.0
Ekoundou 1	1.96	0.538	+2.29	13.9
(T2/3)	1.95	0.518	+1.84	12.3
(G2/3)	1.95	0.511	+1.93	14.6
(L2/3)	1.95	0.505	+1.84	13.7
(J2/3)	2.05	0.549	+1.74	11.5
Ekoundou 2	1.89	0.416	+1.17	4.6
(T3/3)	1.92	0.498	+1.76	12.5
(G3/3)	1.91	0.496	+1.80	12.2
(L3/3)	1.90	0.488	+1.77	12.9
(J3/3)	1.97	0.522	+1.81	12.5
Ekoundou 3	1.90	0.556	+0.91	4.4

Discussion

From the examination of the ratios, it is clear that the most energetic and the least energetic windows all belong to the same spectrum, and that the switching model hypothesis is invalidated.

From the study of the run lengths, one sees that measured lengths exhibit as many or less high values than the simulated ones. There is thus no need for concern about excitation by longer runs of energetic swell than would be obtained from the conventional spectral model.

CHAPTER 11

Parametric description of swell spectra

Kevin Ewans

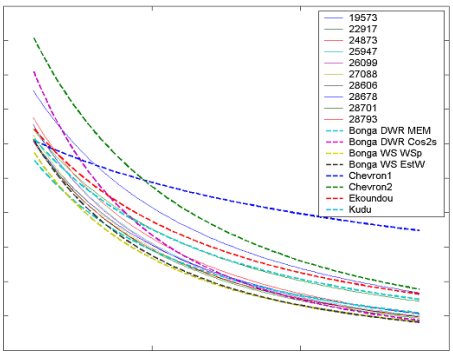

The objective is to provide a parametric description of the swell spectra off West Africa, based on the assessment of the goodness-of-fits of the model spectral comparisons with the spectra, both in terms of the direct spectral comparisons and also in terms of the response amplitude comparisons.

The spectral forms have the general form

$$G(f) = G(f\,;\, H_s, T_p, p) \qquad \textbf{(EQ 11.1)}$$

where p is a parameter relating to the spectral width

Thus, the spectral description is a function of three parameters, two - H_s and T_p - relating to the sea-state, and the third possibly related to location. It is the specification of the third parameter that is of interest here.

Since the results presented in Chapter 6 suggest the lognormal spectral description is best for the majority of measured swell spectra off West Africa, a parameterisation for p for this spectrum has been established.

Theoretical Considerations

Suppose the observation point, O, is a distance, D, from a point source, S. Assume for simplicity that the spectrum at S has a simple triangle shape with bandwidth f_l to f_u, with peak frequency, f_p as given in figure 11.1.

What we would like to know is the bandwidth Δf at the observation point, as a function of distance and time from the storm source, as this will provide insight into a possible parameterisation of the parameter, p in the equation above.

Now, ocean waves are dispersive with a group velocity, c_g, given by

$$c_g = \frac{gT}{4\pi} \qquad \textbf{(EQ 11.2)}$$

which gives

$$f = \frac{g}{4\pi D}(t - t_0) \qquad \textbf{(EQ 11.3)}$$

where t_0 is the start time of the storm.

FIGURE 11.1 : Spectral shape of wind-sea at source.

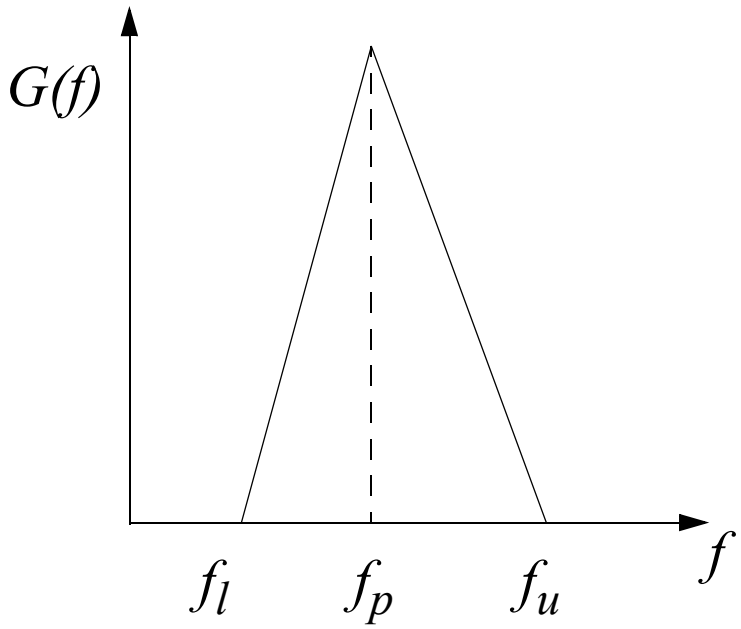

This equation expresses the frequency at the observation point, which is a distance, D, from the storm, in terms of the time required for the component to travel the distance, D. This function is plotted in figure 11.2 together with an equivalent (time shifted) function for the end time, t_e of the storm.

The bandwidth, Δf, of the spectrum at the observation point is given by

$$\begin{aligned} \Delta f &= \frac{1}{T_p} - f_l \qquad t_1 < t < t_2 \\ \Delta f &= \frac{g\tau}{4\pi D} \qquad t_2 < t < t_3 \\ \Delta f &= f_u - \frac{1}{T_p} \qquad t_3 < t < t_4 \end{aligned} \qquad \textbf{(EQ 11.4)}$$

where $\tau = t_e - t_0$ is the storm duration.

During the first period, t_1 to t_2, the spectral peak is shifting to higher frequency, and the spectral bandwidth is increasing. After this time the bandwidth is either constant or the spectral amplitude is decreasing. This suggests a suitable parameterisation for the spectral bandwidth might take the form

$$\Delta f = \frac{a}{T_p} + b \qquad \textbf{(EQ 11.5)}$$

where a and b are constants to be determined.

FIGURE 11.2 : Frequency dispersion lines for a storm starting at t_0 and ending a t_e.

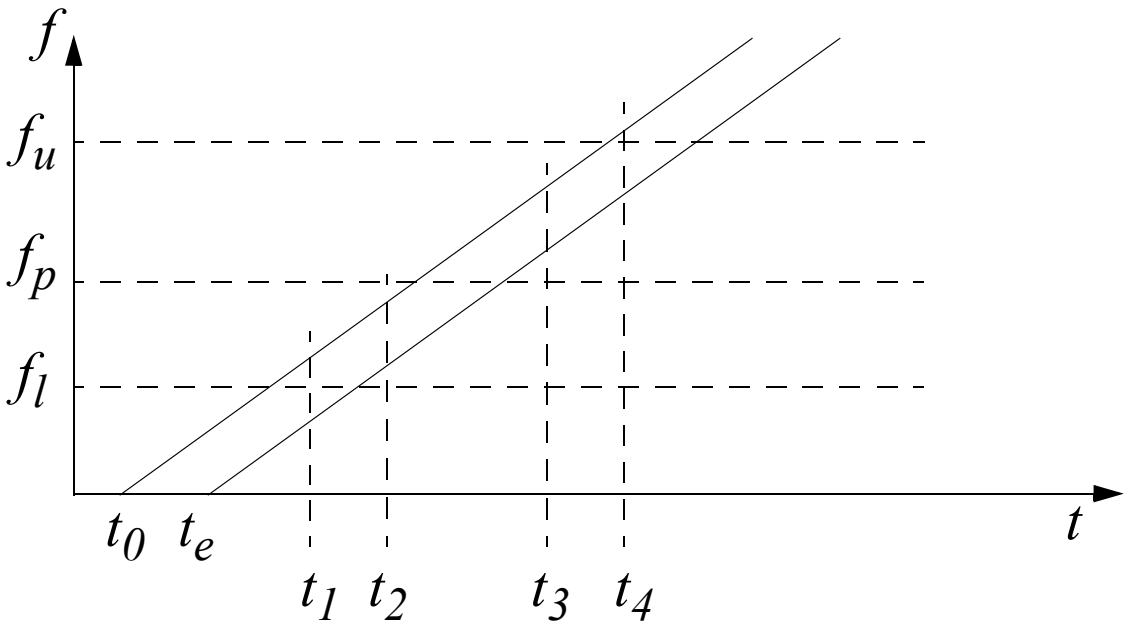

Lognormal Parameterisation

figure 11.3 gives a scatter plot of the lognormal standard deviation parameter versus the peak period. The red points are those for which $T_p > 10\text{s}$ and $H_s > 1.0\text{m}$. The green line is the best fit line of $sd = a/T_p + b$ to the red points, for the QSCAT 28793 (Bonga) data set. figure 11.4 is the comparative plot for the QSCAT 19573 (Kudu) data set.

Both plots shows that the lognormal standard deviation is reasonably well described by the proposed bandwidth function, even for peak periods less than 10s, whose points were excluded from the curve-fit. However, best-fit curve clearly under estimates the very long period points.

A better fit of the lognormal standard deviation parameter to the data is given by the function

$$sd = a/T_p^b \qquad \textbf{(EQ 11.6)}$$

as demonstrated in figure 11.5, figure 11.6, and figure 11.7. This function now provides a good fit to the long-period data points. Figure 11.8 to figure 11.13 show that the function also provides a good fit to the measured data sets.

The curves resulting from the best fit of this function to all the QSCAT and measured data are given in figure 11.14 for comparison. The figure shows that with the exception of the Chevron, 8m water depth curve, which is likely showing shallow-water effects, the lines corresponding to the measured data are consistent with those from the QSCAT data sets. In addition, the plot shows a general trend for the

standard deviation of the lognormal to increase with increasing latitude, although this effect doesn't become significant until latitudes south of 10 degrees South - the Central Angola grid point. The trend is more clearly seen in figure 11.15, which gives the same curves plotted only for periods greater than 10 s.

The parameters of the QSCAT best-fit curves are given in table 11.1.

FIGURE 11.3 : Scatter diagram of the lognormal standard deviation parameter versus the peak period. The red points are those for which $T_p > 10\text{s}$ and $H_s > 1.0\text{m}$. The green line is the best-fit line of $sd = a/T_p + b$ to the red points, for the QSCAT 28793 (Bonga) data set.

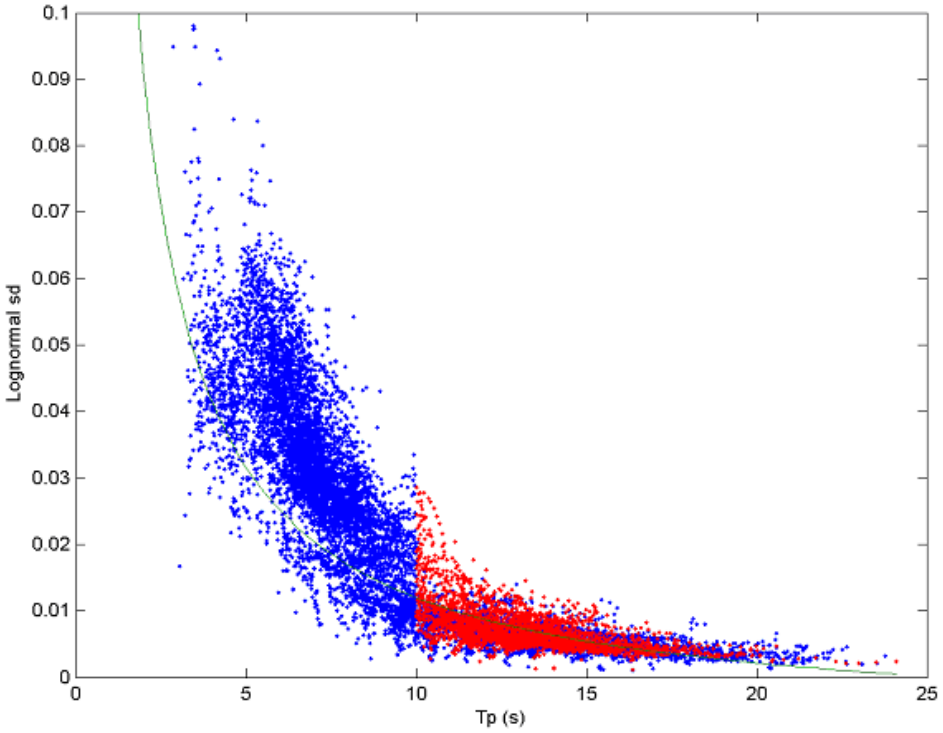

FIGURE 11.4 : Scatter diagram of the lognormal standard deviation parameter versus the peak period. The red points are those for which $T_p > 10\text{s}$ and $H_s > 1.0\text{m}$. The green line is the best-fit line of $sd = a/T_p + b$ to the red points, for the QSCAT 19573 (Kudu) data set.

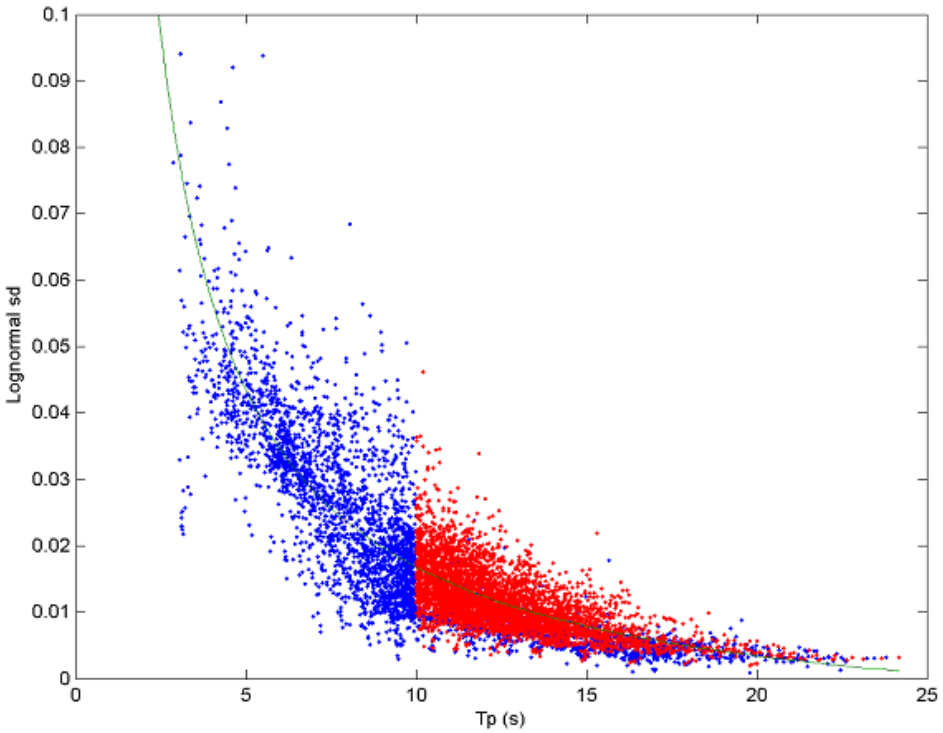

FIGURE 11.5 : Scatter diagram of the lognormal standard deviation parameter versus the peak period. The red points are those for which $T_p > 10\text{s}$ and $H_s > 1.5\text{m}$. The green line is the best fit line of $sd = a / T_p^b$ to the red points, for the QSCAT 28793 (Bonga) data set.

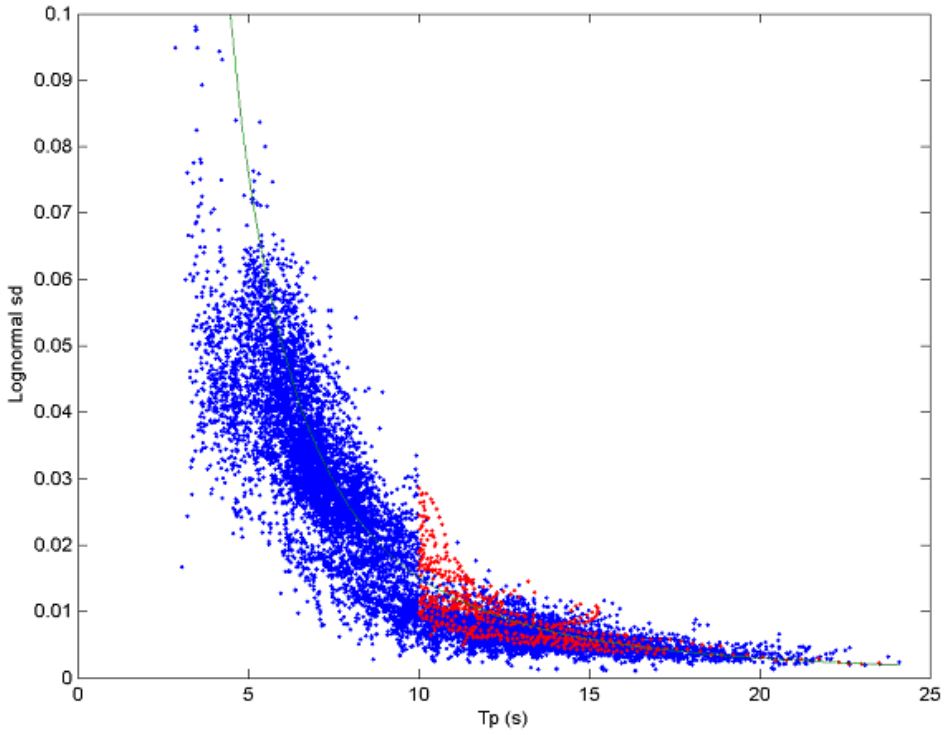

FIGURE 11.6 : Scatter diagram as for figure 11.5, but for the QSCAT 24873 (Central Angola) data set.

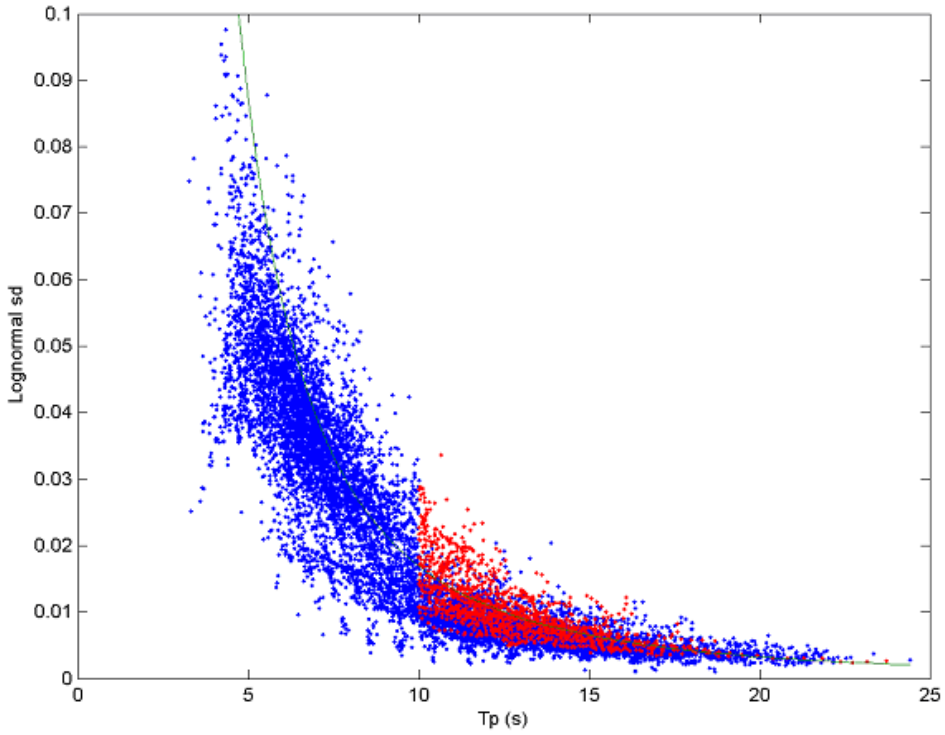

FIGURE 11.7 : Scatter diagram as for figure 11.5, but for the QSCAT 19573 (Kudu) data set.

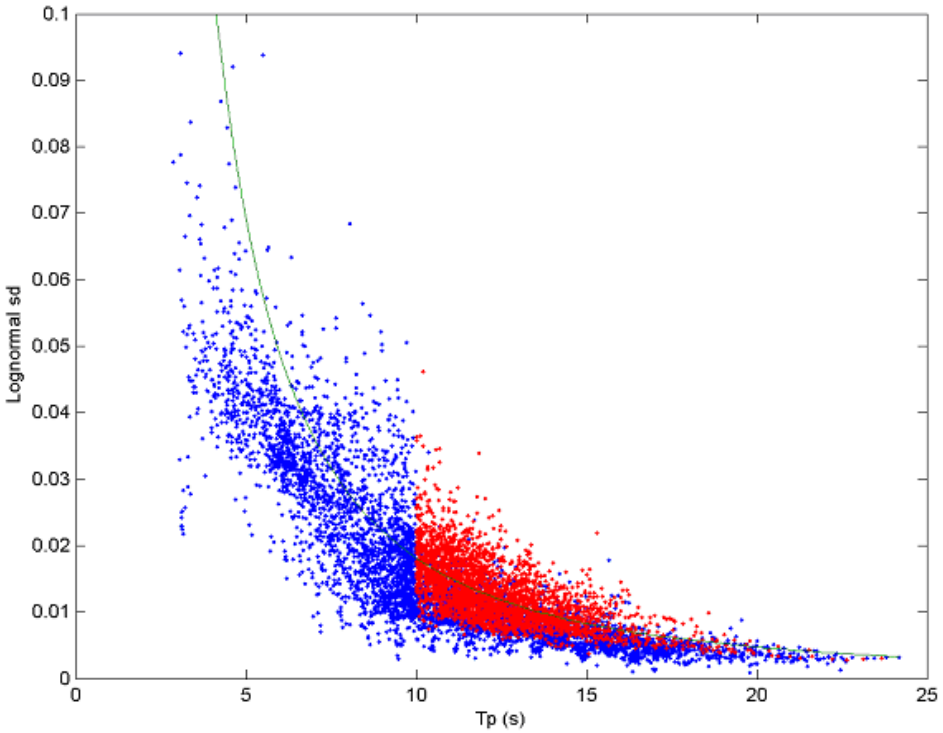

FIGURE 11.8 : Scatter diagram as for figure 11.5, but for the Bonga DWR, MEM measured data set.

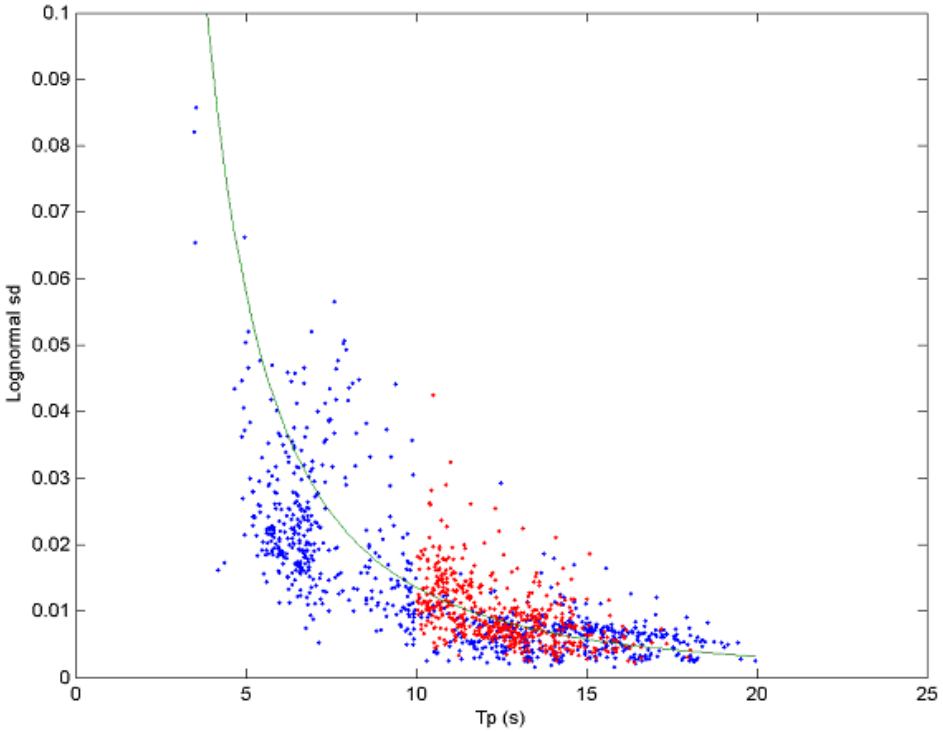

FIGURE 11.9 : Scatter diagram as for figure 11.5, but for the Bonga Wavescan, Cos2s measured data set.

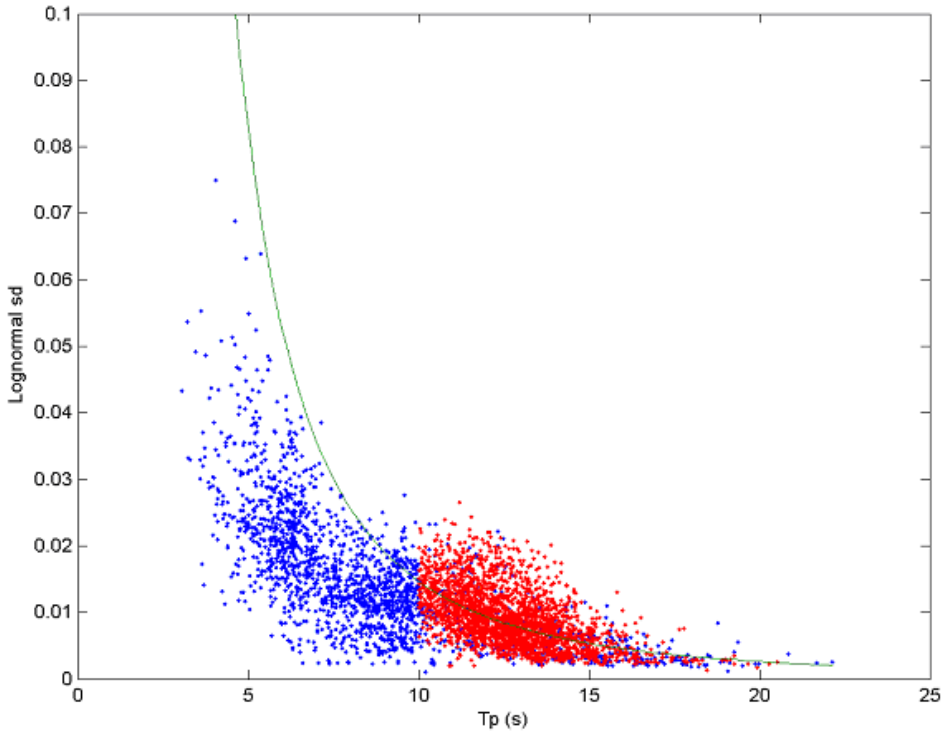

FIGURE 11.10 : Scatter diagram as for figure 11.5, but for the Ekoundou, Cos2s measured data set.

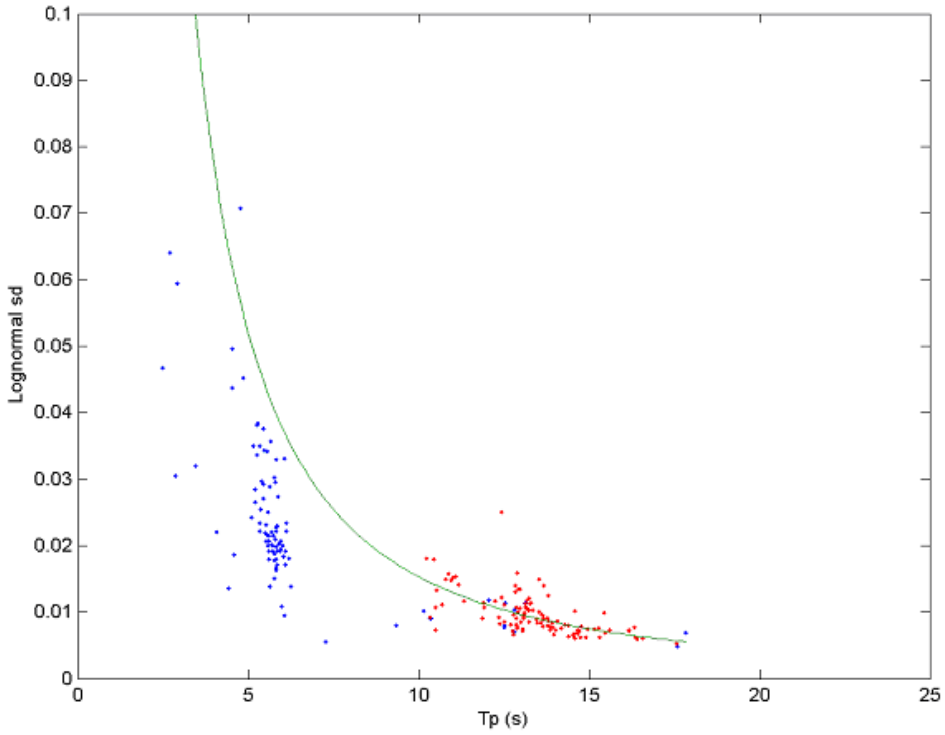

FIGURE 11.11 : Scatter diagram as for figure 11.5, but for the Chevron, Cos2s, 8m water depth measured data set.

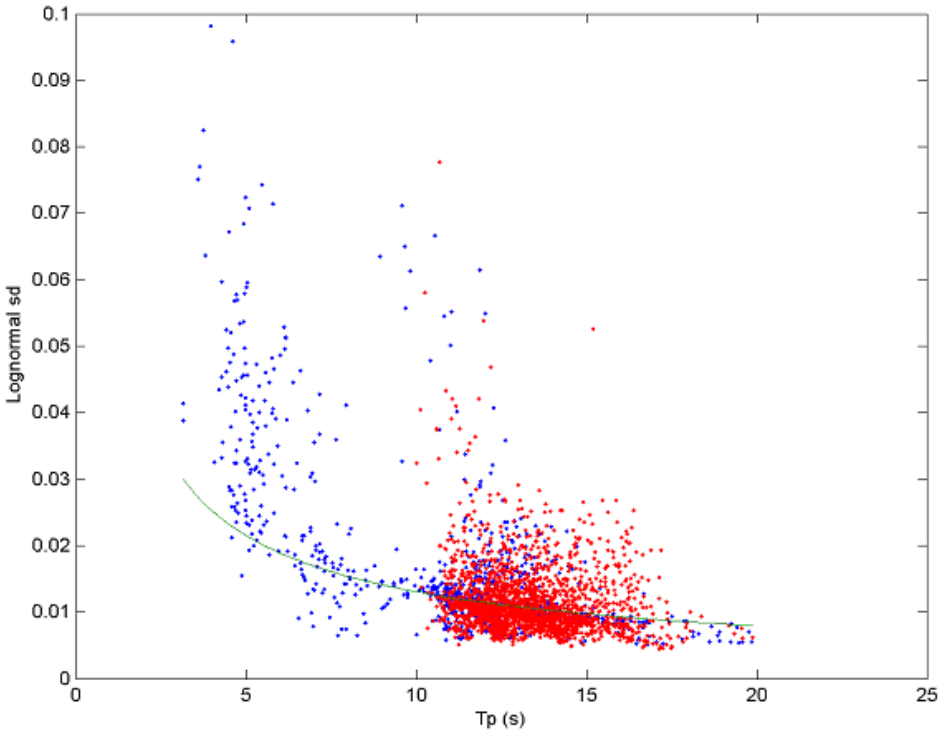

FIGURE 11.12 : Scatter diagram as for figure 11.5, but for the Chevron, Cos2s, 85m water depth measured data set.

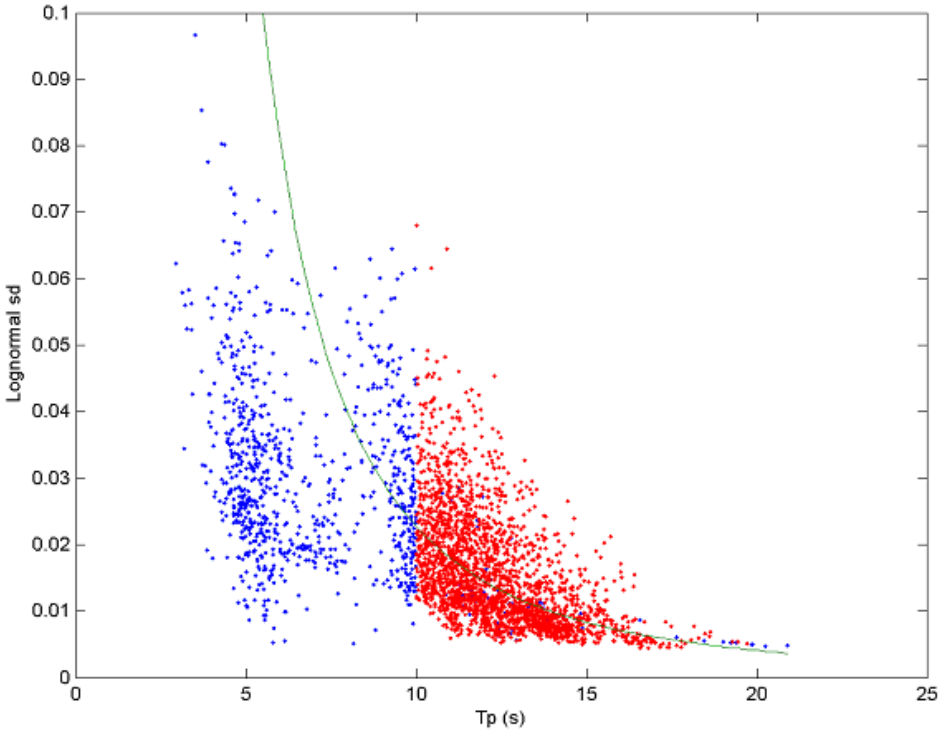

FIGURE 11.13 : Scatter diagram as for figure 11.5, but for the Kudu, MEM measured data set.

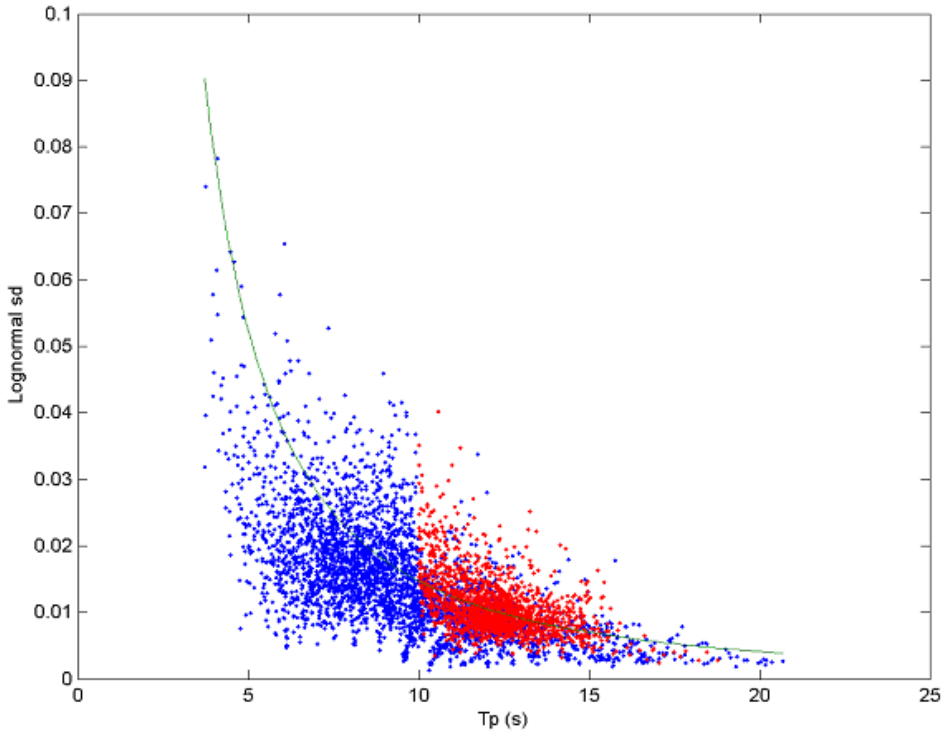

FIGURE 11.14 : The curves corresponding to the best fit of the function $sd = a / T_p^b$ to the QSCAT and measured data sets.

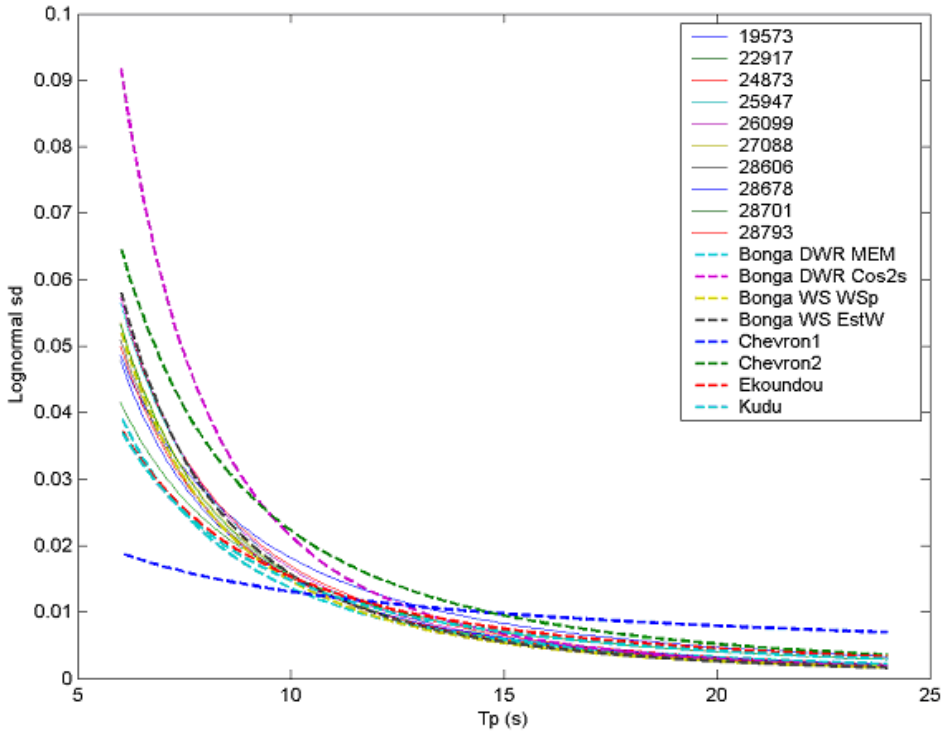

FIGURE 11.15 : The same plot as for figure 11.14 except plotted only for periods greater than 10s.

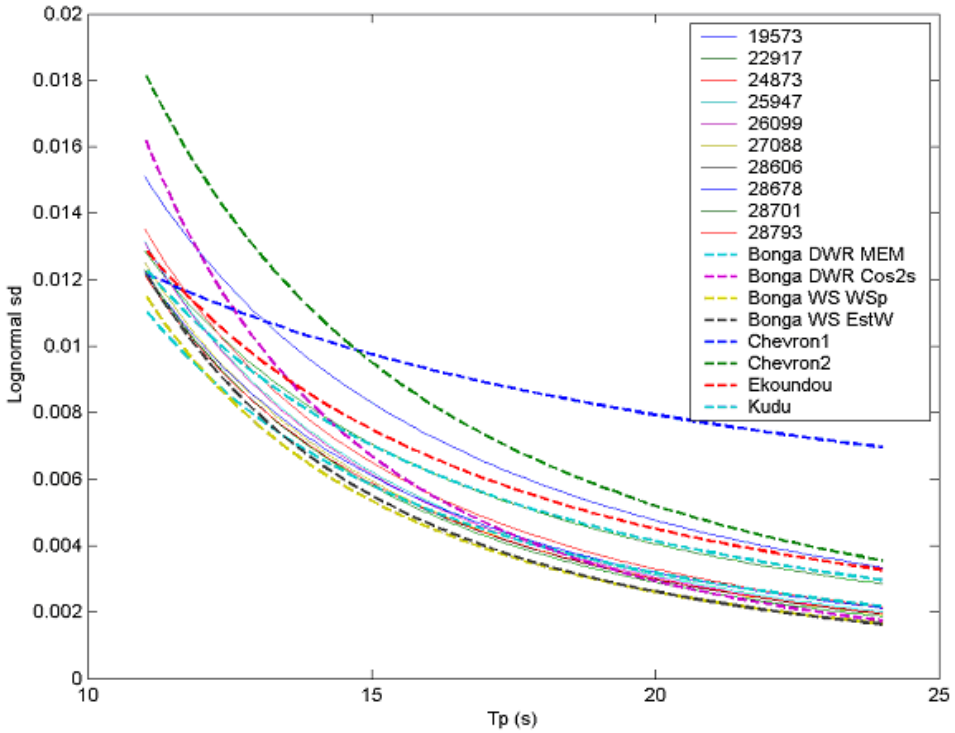

.

TABLE 11.1 : Frequency bandwidth: Values of the parameters *a* and *b* of the best fit of the function $sd = a / T_p^b$ to the QSCAT and data.

Grid point	Name	Latitude (°)	Longitude (°)	a	b
19573	Kudu	-28.7500	15.000	1.55	1.93
22917	Namibia	-17.5000	10.625	1.33	1.93
24873	Central Angola	-10.0000	11.875	3.88	2.36
25947	Exxon	-5.6250	11.875	4.23	2.41
26099	Nemba	-5.0000	10.625	4.52	2.44
27088	Gabon	-1.2500	7.500	3.92	2.40
28606	Marathon	3.7500	8.125	3.48	2.36
28678	Côte d'Ivoire	4.0625	-6.875	2.67	2.25
28701	Ekoundou	4.0625	7.500	4.07	2.42
28793	Bonga	4.3700	5.000	3.28	2.34

Wrapped-Normal Directional Distribution

The directional distribution, $D(\theta)$, is defined by (see Chapter 4):

$$D(\theta) = \int_0^{\infty} S(f, \theta) df \qquad \textbf{(EQ 11.7)}$$

This quantity has been computed for all individual swell components, and based on experience with earlier evaluations of the directional distribution of swell (Ewans, 2001), a wrapped-Normal distribution (Chapter 4) was fit to each distribution.

Figure 11.16, figure 11.17, and figure 11.18 give scatter diagrams of the wrapped-Normal distribution standard deviation versus the spectral peak period, for the partitioned swell components of the QSCAT 28793 (Bonga), QSCAT 24873 (Central Angola), and QSCAT 19573 (Kudu) data sets. Components with $H_s > 0.5$m and $T_p > 10$s are plotted in red. The best-fit of the function $sd = a/T_p^b$ to the red points is the green line. The plots are representative of the 10 QSCAT data sets and show that the function $sd = a/T_p^b$ provides a good description of the variation of the standard deviation as a function of peak period.

The best-fit lines for all 10 QSCAT data sets are given in figure 11.19. As was observed with the frequency spectrum, increasing directional spread with increasing southern latitude is apparent from this figure.

The values of the parameters, a and b are given in table 11.2.

FIGURE 11.16 : Scatter diagram of the wrapped-Normal distribution standard deviation versus the spectral peak period, for the partitioned swell components of the QSCAT 28793 (Bonga) data set. Components with $H_s > 0.5$m and $T_p > 10$s are plotted in red. The best-fit of the function $sd = a/T_p^b$ to the red points is the green line.

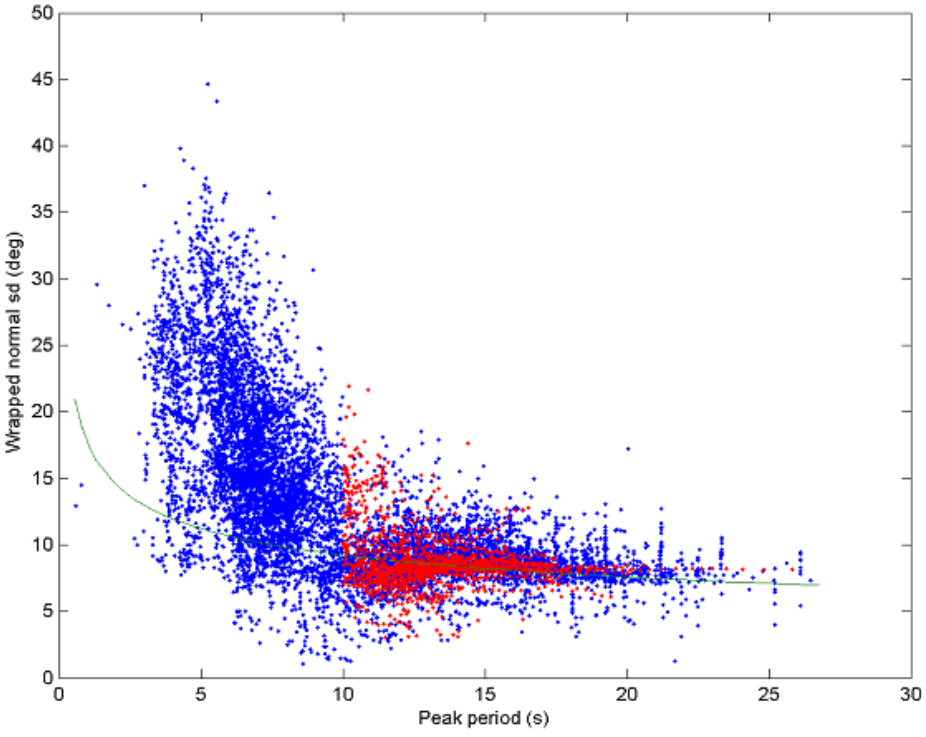

FIGURE 11.17 : Scatter diagram as for figure 11.16 for the QSCAT 24873 (Central Angola) data set.

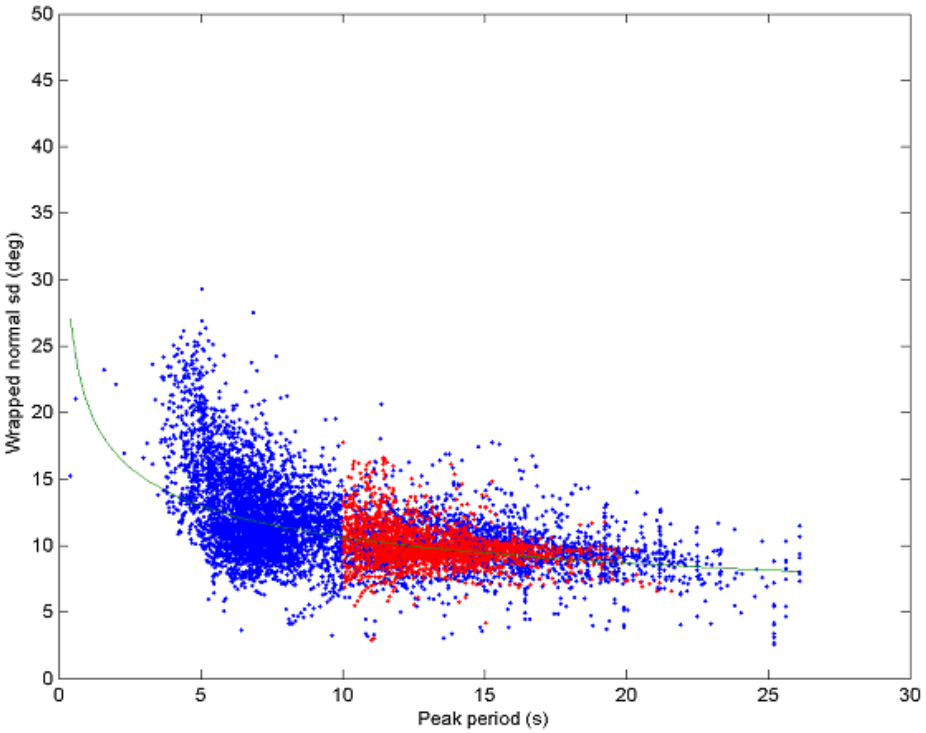

FIGURE 11.18 : Scatter diagram as for figure 11.16 for the QSCAT 19573 (Kudu) data set.

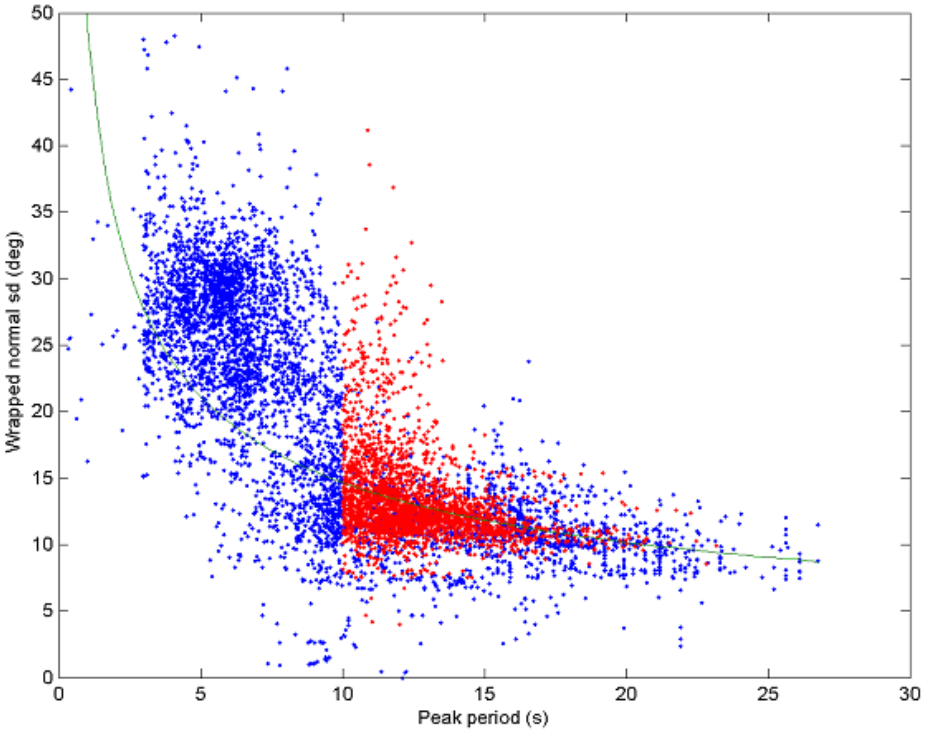

FIGURE 11.19 : The curves corresponding to the best fit of the function $sd = a / T_p^b$ to the QSCAT data sets.

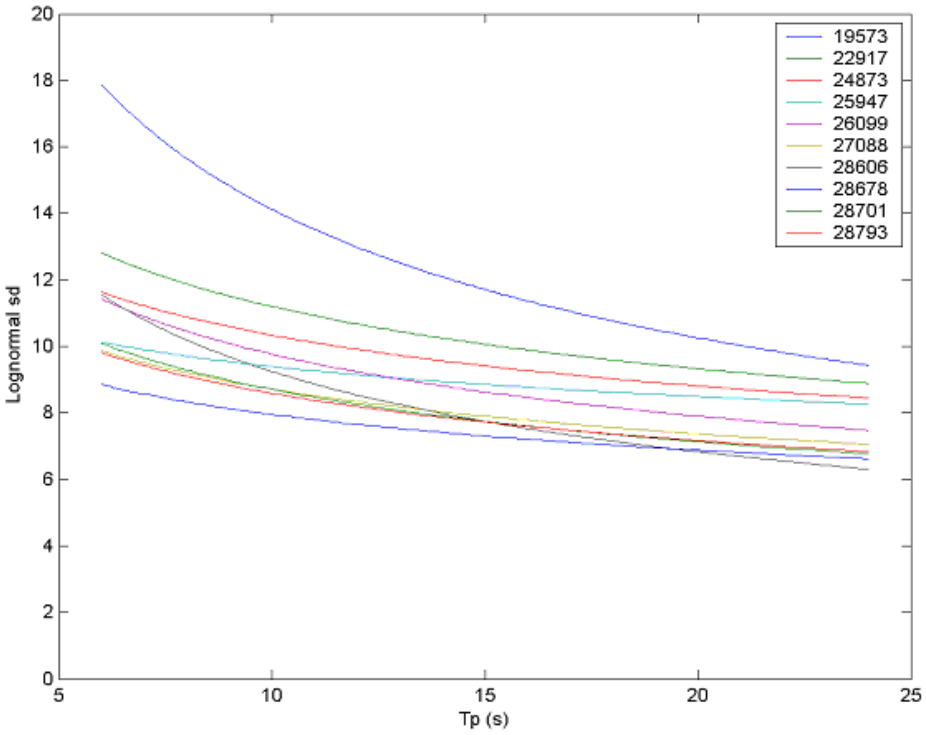

TABLE 11.2 : Directional bandwidth: Values of the parameters a and b of the best fit of the wrapped-Normal function standard deviation $sd = a / T_p^b$ to the QSCAT and data.

Grid point	Name	Latitude (°)	Longitude (°)	a	b
19573	Kudu	-28.7500	15.000	40.8	0.451
22917	Namibia	-17.5000	10.625	20.5	0.263
24873	Central Angola	-10.0000	11.875	17.6	0.230
25947	Exxon	-5.6250	11.875	13.1	0.146
26099	Nemba	-5.0000	10.625	19.7	0.306
27088	Gabon	-1.2500	7.500	15.2	0.242
28606	Marathon	3.7500	8.125	25.3	0.437
28678	Cote d'Ivoire	4.0625	-6.875	12.9	0.209
28701	Ekoundou	4.0625	7.500	16.9	0.288
28793	Bonga	4.3700	5.000	15.7	0.261

References

[11.1]Ewans, K. C., 2001, "Directional spreading in ocean swell", *The Fourth International Symposium on Ocean Wave Measurement and Analysis*, ASCE, San Francisco.

CHAPTER 12

Infra-gravity waves

Marc Prevosto

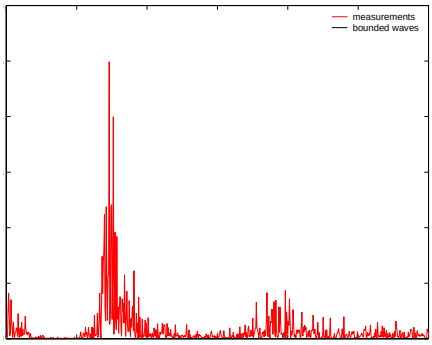

The knowledge and prediction of the infragravity waves, by models or from measurements, has not been yet extensively explored. The aim of this work has been to first produce an annotated bibliography, as large as possible, to make a point on the state of the works on the subject, and secondly, to extract from the measurements available in the WASP project some conclusions on the energy present in the low frequency bands, which could be related to this phenomenon.

General

Infragravity waves are a possible source of low-frequency energy. These waves are not directly generated by the wind, but instead are generated in shallow water through nonlinear mechanisms from "short-period" waves (>0.04Hz) as they impinge on the coast. As a matter of fact, second order, difference frequency effects in the wind-wave field produce long-period waves (<0.04Hz) that are bound to the wave group and produce wave set-down. When the wave field impinges on the coast, the short-period energy is lost in wave breaking at the shore, while the long-period waves are reflected.

In most cases, offshore, the wave spectrum (hindcast models or buoy measurements) do not contain energy in the very low frequency band. In that case, for structural responses, the estimates of the low-frequency spectrum is based only on 2nd order calculations from the "short-period" frequency band of the wave spectrum and the energy calculated in this way will account only for the component that is bound to the wave group and not the freely propagating (infragravity) part that is reflected from the coastlines of the entire ocean.

Anyway, it is a very difficult problem and most of studies have been based on measurements. Unfortunately it is climatology and site (bathymetry) dependent. Most of infragravity waves generated in surf zone are trapped in shallow waters and their intensity offshore is very difficult to evaluate as most of measurements available come from buoy which filter the infragravity frequencies.

In shallow water (water depth 13 m) the studies of Herbers et al [12.5,12.6,12.7] show that, (IGW stands for InfragGravity Waves, BW stands for Bound Waves):

FIGURE 12.1 : Ekoundou. Spectrum, measurements vs second order

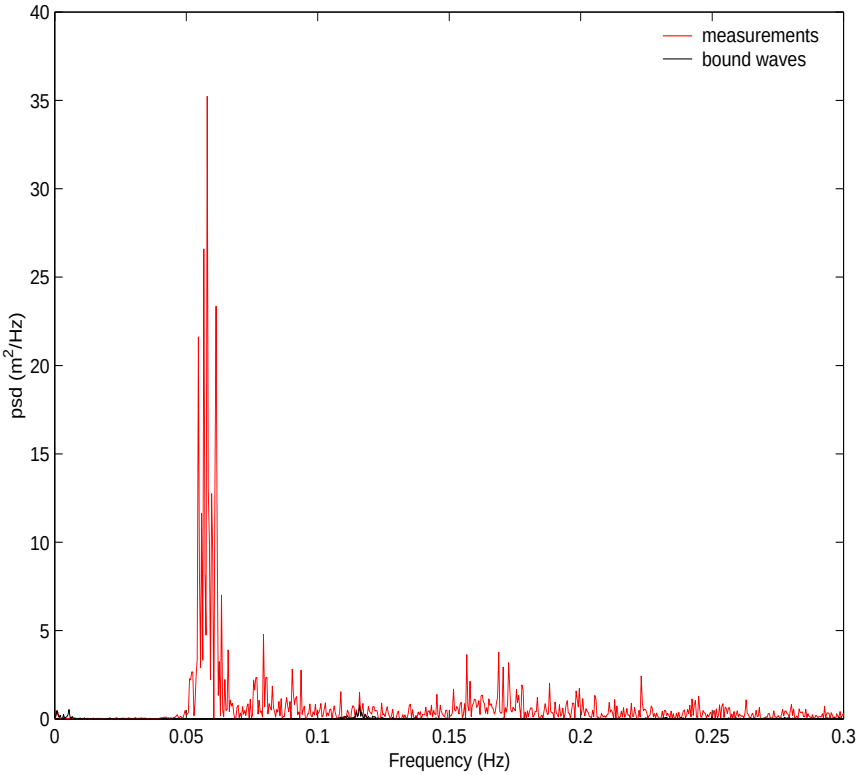

FIGURE 12.2 : Ekoundou. Spectrum, low frequency measurements vs second order

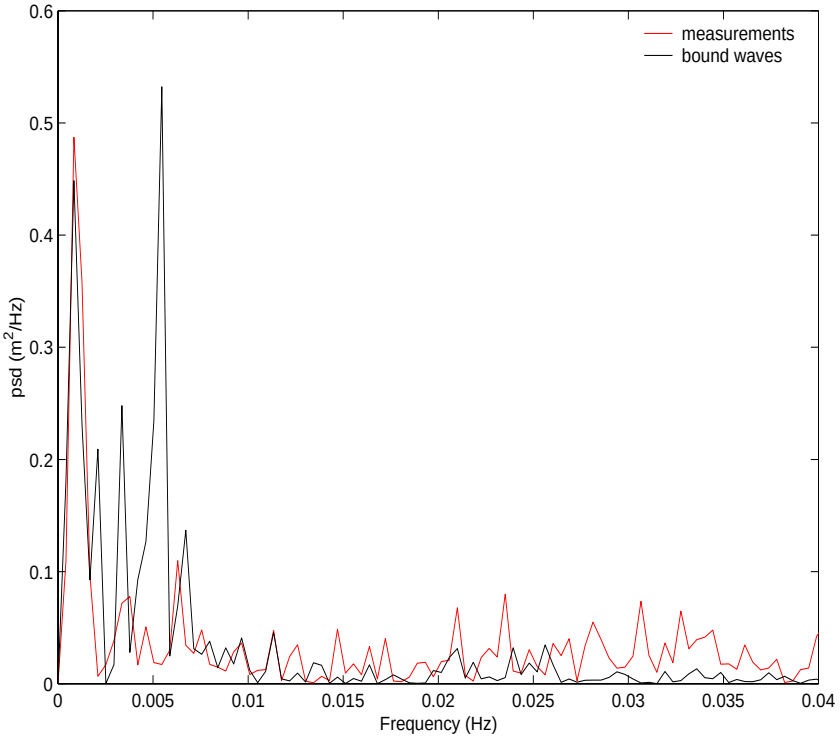

- the energy ratio IGW/BW goes from 3 to 1500;
- when the swell energy is increasing, IGW/BW is decreasing;
- the energy of IGW are measured between $0.5*10^{-4}m^2$ and $6*10^{-3}m^2$.

Low frequency energy and second order bound waves.

Measurements at Ekoundou (Wavestaff) and Malabo (Pressure probe) have been used to compare second order bound waves energy calculated from the free short waves and low frequency energy estimated from the measured spectra.

Ekoundou

At Ekoundou, the surface elevation is measured with a wavestaff. The water depth is 18 m. The type of instrument indicates that the low frequency waves (free or bound) will be measured.

To calculate the energy of the second order bound waves, the spectra have been filtered to keep only the "short-waves", [0.04Hz-2Hz], and then the second order bound waves have been calculated in using the classical second order transfer functions (see for example [12.16,12.17]). Figures 12.1 and 12.2 show a first example of comparison. In black is plotted only the second order part. When we compare in Fig 12.2 the low frequency part, [0Hz-0.04Hz], we observe very comparable energy. No additional energy coming from free propagating long waves is visible. A second example (Figs 12.3 and 12.4) corresponds to a less steep sea-state, and so weaker second order effect. On the other hand, here (Fig 12.4), the second order low frequency energy is much lower than the total energy measured by the wavestaff. This could indicate low frequency free waves.

The same processing is applied to the complete data base of Ekoundou.
Figure 12.5, shows the energy calculated in the band [0Hz-0.04Hz], bound and total waves. The total low frequency energy values are included in the range $[0.5*10^{-4}m^2-6*10^{-3}m^2]$ indicated by Herbers et al [12.5,12.7], and the comparison with second order bound waves confirms his comment that forced (bound) infragravity waves are consistently much less energetic than free infragravity waves.

Malabo

The processing of the Malabo measurements is a little bit more complicated. The pressure probe is located on the sea bottom in a water depth of 25 m, but sheltered from offshore by an island. So it does not measure the swell which could generate free infragravity waves.

So, to obtain the spectral information on the offshore sea-state we have used the Wavescan measurements at Bonga, which we expect is close to offshore Malabo sea conditions.

The pressure IGW energy from Wavescan is obtained in several steps:

- The Wavescan spectra are filtered to keep only the "short-waves", [0.04Hz-2Hz];
- The second order part of the wave elevation is calculated with 25 m water depth;
- The total wave elevation is transfer linearly to bottom pressure.

The comparison with the IGW energy measured at Malabo is given Fig 12.6. Again, the energy of the IGW measured is much higher than the energy of the second order bound waves.

FIGURE 12.3 : Ekoundou. Spectrum, measurements vs second order

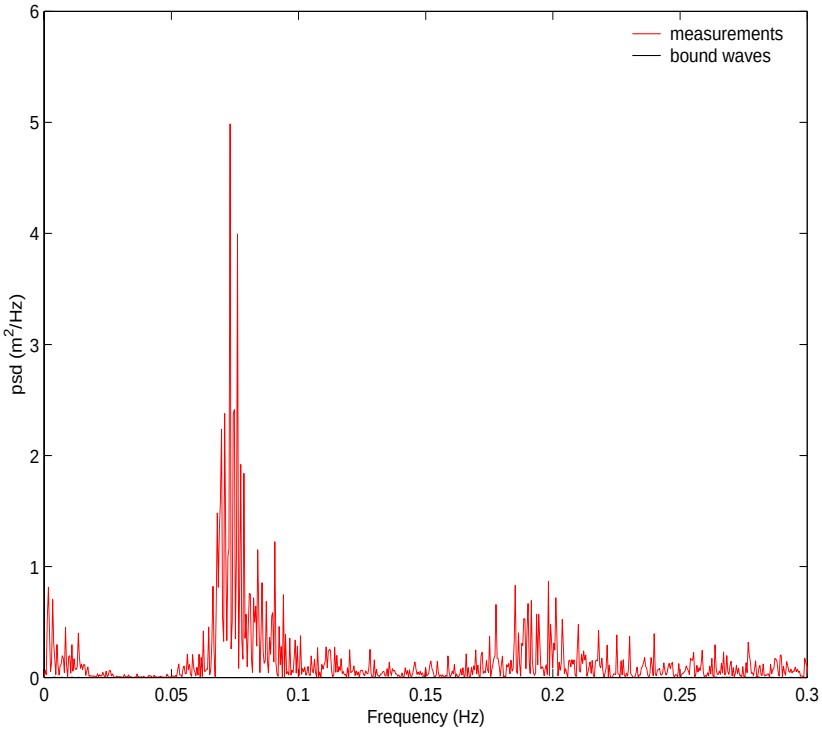

FIGURE 12.4 : Ekoundou. Spectrum, low frequency measurements vs second order

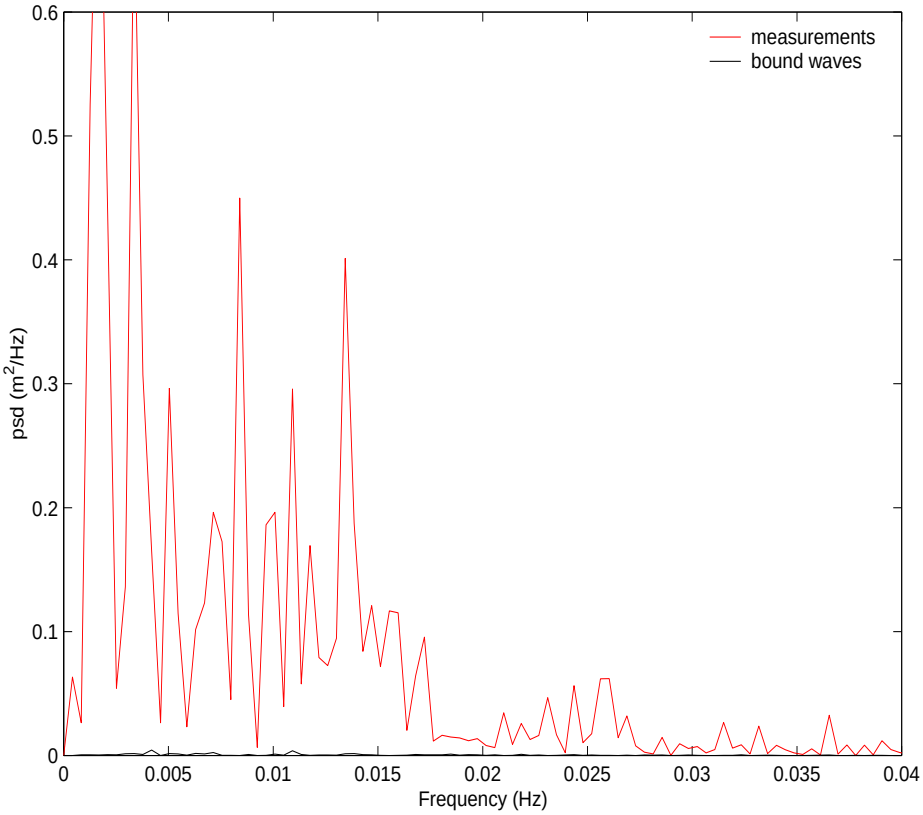

FIGURE 12.5 : Ekoundou. Energy, measurements vs second order

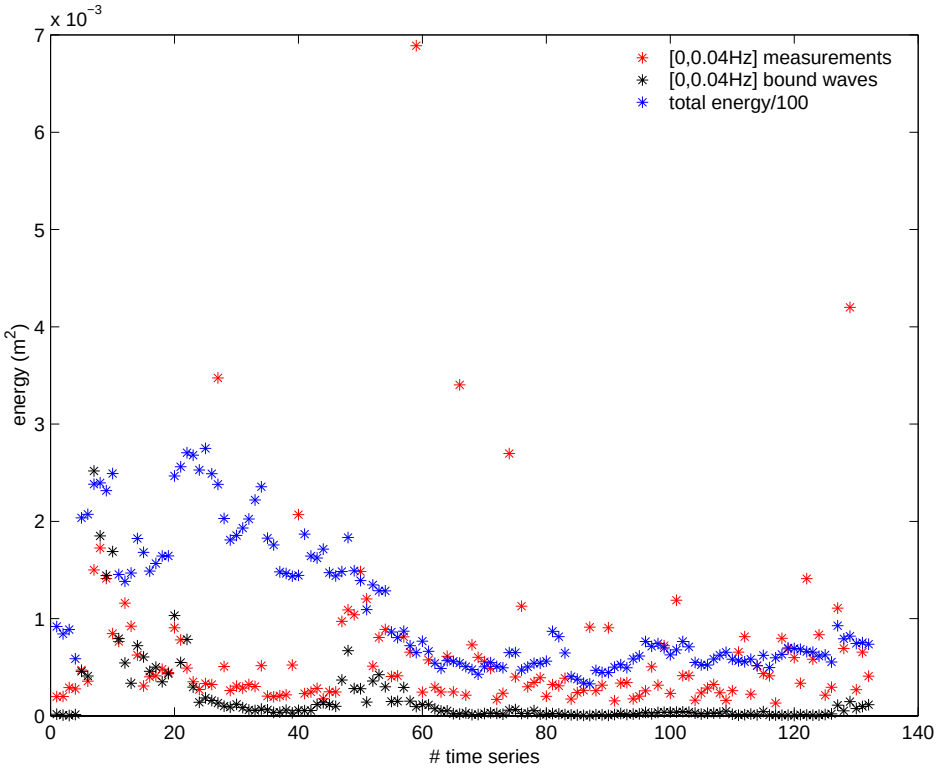

FIGURE 12.6 : Malabo. Energy, measurements vs second order

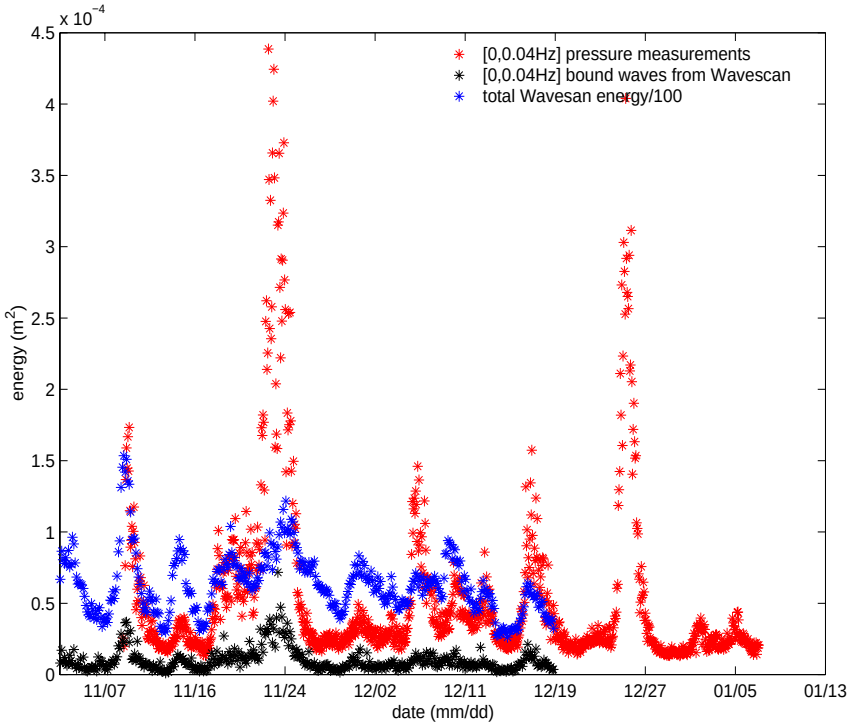

Annotated references

[12.1]Aagaard, T., Bryan, K., 2003, "Observations of infragravity wave frequency selection", *Continental Shelf Research*, vol. 23, no. 10, pp. 1019-1034.

Field measurements of sea-surface elevation, cross-shore and longshore velocities were obtained during a storm event on the north coast of Zealand, Denmark from a cross-shore array of co-located pressure sensors and current meters. During the major part of this storm, statistically significant spectral peaks at a frequency of *f*~0.025 Hz were identified at several cross-shore locations. Based on examinations of cross-shore coherence and phase relationships, it appeared that these motions were due to cross-shore standing wave structures rather than caused by shear wave activity. Comparisons with synthetic edge wave spectra, which were computed assuming a white shoreline surface elevation spectrum, suggested that the identified spectral peaks were not artifacts of a cross-shore standing wave nodal structure but an indication that those frequencies where the peaks occurred were preferentially forced. Analyses of local and spatial phase relationships of velocity and sea-surface elevation, as well as comparisons with numerically calculated theoretical cross-shore wave structures suggested that these waves were standing edge waves with mode number (n)>=3. The selected frequency of f~0.025 Hz corresponds to one of the cut-off frequencies that can theoretically occur on this bathymetric geometry which asymptotes to a constant depth offshore.

[12.2]Elgar, S., Herbers, T.H.C., Okihiro, M., Oltman-Shay, J., Guza, R.T., 1992, "Observations of infragravity waves", *J. of Geophysical Research*, vol. 97, no. C10, pp. 15,573-15,577.

Infragravity-wave (periods of one-half to a few minutes) energy levels observed for about one year in 8-m water depth in the Pacific and in 8- and 13-m depths in the Atlantic are highly correlated with energy in the swell-frequency band (7- to 20-s periods), suggesting the infragravity waves were generated locally by the swell. The amplification of infragravity-wave energy between 13- and 8-m depth (separated by 1 km in the cross shore) is about 2, indicating that the observed infragravity motions are dominated by free waves, not by group-forced bound waves, which in theory are amplified by an order of magnitude in energy between the two locations. However, bound waves are more important for the relatively few cases with very energetic swell, when the observed amplification between 13- and 8-m depth of infragravity-wave energy was sometimes three times greater than expected for free waves. Bispectra are consistent with increased coupling between infragravity waves and groups of swell and sea for high-energy incident waves.

[12.3]Elgar, S., Herbers, T.H.C., Guza, R.T., 1994, "Reflection of ocean surface gravity waves from a natural beach", *J. of Physical Oceanography*, vol. 24, no. 7, pp. 1503-1511.

The energy of seaward and shoreward propagating ocean surface gravity waves on a natural beach was estimated with data from an array of 24 bottom-mounted pressure sensors in 13-m water depth, 2 km from the North Carolina coast. The ratio of seaward to shoreward propagating energy in the swell-sea frequency band (0.044-0.20 Hz) decreased with increasing wave frequency and increasing wave height, and increased with increasing beach-face slope. Although most incident swell-sea energy dissipated in the surf zone, reflection was sometimes significant when the beach face was steep (at high tide) and the wave field was dominated by low-energy, low-frequency swell. Frequency-directional spectra show that reflection of swell

and sea was approximately specular. The ratio of seaward to shoreward propagating energy in the infragravity frequency band (0.010-0.044 Hz) varied between about 0.5 and 3 and increased with increasing swell energy.

[12.4]Henderson, S.M., Bowen, A.J., 2003, "Simulations of dissipative, shore-oblique infragravity waves", *Journal of Physical Oceanography*, vol. 33, no. 8, pp. 1722-1732.

A model of forced, dissipative shore-oblique shallow water waves predicts net cross-shore infragravity wave propagation, in qualitative agreement with field observations. Forcing applied near the shore generates edge waves, whose energy is mostly trapped shoreward of the edge wave turning point. Forcing applied sufficiently far seaward of the turning point generates only evanescent waves, whose energy decays almost exponentially with distance from regions of forcing. Weakly dissipative edge waves are nearly cross-shore standing, whereas strongly dissipative edge waves propagate obliquely across-shore. Groups of directionally spread incident waves can nonlinearly force evanescent bound waves, which propagate shoreward, lowering the sea level under large incident waves. Unlike the bound waves described by previous researchers, evanescent bound waves are not released when incident waves break and do not radiate far from the breakpoint. Regions of evanescent waves between the shoreface and shore-parallel sandbars are barriers to energy transport, which can decouple bar- and shore-trapped waves even when dissipation is weak.

[12.5]Herbers, T.H.C., Elgar, S., Guza, R.T., 1995, "Generation and propagation of infragravity waves", *J. of Geophysical Research*, vol. 100, no. C12, pp. 24,863-24,872.

The generation and propagation of infragravity waves (frequencies nominally 0.004-0.04 Hz) are investigated with data from a 24-element, coherent array of pressure sensors deployed for 9 months in 13-m depth, 2 km from shore. The high correlation between observed ratios of upcoast to downcoast energy fluxes in the infragravity ($F_{up}^{IG}/F_{down}^{IG}$) and swell ($F_{up}^{swell}/F_{down}^{swell}$) frequency bands indicates that the directional properties of infragravity waves are strongly dependent on incident swell propagation directions. However, $F_{up}^{IG}/F_{down}^{IG}$ is usually much closer to 1 (i.e., comparable upcoast and downcoast fluxes) than is $F_{up}^{swell}/F_{down}^{swell}$, suggesting that upcoast propagating swell drives both upcoast and downcoast propagating infragravity waves.

[12.6]Herbers, T.H.C., Elgar, S., Guza, R.T., 1994, "Infragravity-frequency (0.005-0.05 Hz) motions on the shelf. Part I: forced waves", *J. of Physical Oceanography*, vol. 24, no. 5, pp. 917-927.

Data from a large aperture (250 m × 250 m) array of 24 bottom-mounted pressure transducers deployed in 13 m depth is used to investigate the local forcing of infragravity motions by nonlinear difference-frequency interactions of surface gravity waves. Second-order nonlinear theory (Hasselmann) and observed swell-sea frequency-directional spectra are used to predict the energy levels of forced infragravity waves.

[12.7]Herbers, T.H.C., Elgar, S., Guza, R.T., O'Reilly, W.C., 1995, "Infragravity-Frequency (0.005–0.05 Hz) Motions on the Shelf. Part II: Free Waves", *J. Physical Oceanography*, vol. 25, no. 6, pages 1063–1080.

In Part I, the energy levels of ocean surface waves at infragravity frequencies (nominally 0.005–0.05 Hz) locally forced by swell in 13-m water depth were shown to be predicted accurately by second-order nonlinear wave theory. However, forced infragravity waves were consistently much less energetic than free infragravity waves. Here, in Part II, observations in depths

between 8 and 204 m, on Atlantic and Pacific shelves, are used to investigate the sources and variability of free infragravity wave energy. Both free and forced infragravity energy levels generally increase with increasing swell energy and decreasing water depth, but their dependencies are markedly different. Although free waves usually dominate the infragravity frequency band, forced waves contribute a significant fraction of the total infragravity energy with high energy swell and/or in very shallow water. The observed h^{-1} variation of free infragravity energy with increasing water depth h is stronger than the $h^{-1/2}$ dependence predicted for leaky surface gravity waves propagating approximately perpendicular to local depth contours, but is consistent with a heuristic, geometrical optics-based (WKB) model of the refractive trapping of a directionally broad wave field generated close to shore. Preliminary analysis shows that free infragravity waves are indeed directionally broad and that the propagation directions of infragravity waves and incident swell are related. Free infragravity energy levels also depend on the general geographic surroundings. Comparisons of observations from the same depth and with similar swell conditions, but on different shelves, suggest that more free infragravity wave energy is radiated from wide, sandy beaches than from rocky, cliffed coasts and that less energy is trapped on a narrow shelf than on a wide shelf.

[12.8]Munk, W., Snodgrass, F., Gilbert, F., 1964, "Long waves on the continental shelf: an experiment to separate trapped and leaky modes", *J. Fluid Mech.*, vol. 20, no. 4, pp. 529-554.

Random fluctuation in sea level, ξ, in the frequency range 0.1-60 cycles per hour were measured along the coast near Oceanside, California, where the coastline and bottom contours are fairly straight and parallel for 30 km. The two-dimensional covariance

$$R(\eta,\tau) = <\xi(y,t)x(y+\eta,t+\tau)>$$

was computed for points separated by various distances η along the coast. The Fourier transform

$$S(f,n) = \iint R(\eta,\tau)\exp[2\pi i(n\eta+f\tau)]d\eta d\tau$$

gives the contribution towards the "energy" $<\xi^2>$ per unit temporal frequency f per unit special frequency (long-shore component) n. It is found that most of the energy is confined to a few narrow bands in (f,n) space, and these observed bands correspond very closely to the gravest trapped modes (or edge waves) computed for the actual depth profile. The bands are 0.02 cycles per km wide, which equal the theoretical resolution of the 30 km array. Very roughly $S(f,n)\approx S(f,-n)$, corresponding to equal partition of energy between waves travelling up and down the coast. Theory predicts "Coriolis splitting" between the lines $f^{\pm}(n)$ corresponding to these oppositely travelling waves, but this effect is below the limit of detection. The principal conclusion is that most of the low-frequency wave energy is trapped.

[12.9]Okihiro, M., Guza, R.T., Seymour, R.J., 1992, "Bound infragravity waves", *J. of Geophysical Research*, vol. 97, no. C7, pp. 11,453-11,469.

Model predictions of bound (i.e., nonlinearly forced by and coupled to wave groups) infragravity wave energy are compared with about two years of observations in 8- to 13-m depths at Imperial Beach, California, and Barbers Point, Hawaii. Frequency-directional spectra of free waves at sea and swell frequencies, estimated with a small array of four pressure sensors, are used to predict the bound wave spectra below 0.04 Hz. The predicted total bound wave energy is always less than the observed infragravity energy, and

the underprediction increases with increasing water depth and especially with decreasing swell energy. At most half, and usually much less, of the observed infragravity energy is bound. Bound wave spectra are also predicted with data from a single wave gage in 183-m depth at Point Conception, California, and the assumption of unidirectional sea and swell.

[12.10]Reniers, A.J.H.M., van Dongeren, A.R., Battjes, J.A., Thornton, E.B., 2003, "Linear modeling of infragravity waves during Delilah", *Journal of Geophysical Research C: Oceans*, vol. 107, no. 10, pp. 1-1 - 1-18.

The generation of infragravity waves by directionally spread shortwaves incident on an alongshore uniform beach is investigated. Two mechanisms responsible for the generation of infragravity waves are considered: the release of the bound infragravity waves associated with changes in the spatial variation of the incident shortwave energy and the forcing of trapped waves by obliquely incident directionally spread shortwaves. The infragravity wave response is examined using linear shallow water equations, taking into account the presence of bottom friction, setup of the mean water level, rollers, and longshore current. Summing all infragravity contributions due to difference interactions between pairs of shortwave spectral components with the same frequency difference results in infragravity energy density spectra. Calculated spectra are compared with measured spectra obtained during the Delilah field experiment for 11 consecutive days, including calm, mild, and storm conditions. In the comparison, attention is focused on the frequency distribution of the infragravity energy density throughout the surf zone and the transformation of the root mean square infragravity wave height. The measured infragravity response in the frequency range from 0.01 to 0.06 Hz is reproduced by the computations, with relatively broad spectra offshore and a clear nodal structure closer to shore. Typically 80% of the infragravity wave height variability is explained by the model of which 30% or less is due to bound infragravity waves. Differences occur mainly during storm events in which the infragravity energy is underpredicted in the outer surf zone and overpredicted in the inner surf zone.

[12.11]Sheremet, A., Guza, R.T., Elgar, S., Herbers, T.H.C., 2002, "Observations of nearshore infragravity waves: Seaward and shoreward propagating components", *Journal of Geophysical Research C: Oceans*, vol. 107, no. 8, pp. 10-1 - 10-10.

The variation of seaward and shoreward infragravity energy fluxes across the shoaling and surf zones of a gently sloping sandy beach is estimated from field observations and related to forcing by groups of sea and swell, dissipation, and shoreline reflection. Data from collocated pressure and velocity sensors deployed between 1 and 6 m water depth are combined, using the assumption of cross-shore propagation, to decompose the infragravity wave field into shoreward and seaward propagating components. Seaward of the surf zone, shoreward propagating infragravity waves are amplified by nonlinear interactions with groups of sea and swell, and the shoreward infragravity energy flux increases in the onshore direction. In the surf zone, nonlinear phase coupling between infragravity waves and groups of sea and swell decreases, as does the shoreward infragravity energy flux, consistent with the cessation of nonlinear forcing and the increased importance of infragravity wave dissipation. Seaward propagating infragravity waves are not phase coupled to incident wave groups, and their energy levels suggest strong infragravity wave reflection near the shoreline. The cross-shore variation of the seaward energy flux is weaker than that of the shoreward flux, resulting in cross-shore variation of the squared infragravity reflection coefficient (ratio of seaward to shoreward energy flux) between about 0.4 and 1.5.

[12.12]Van Dongeren, A., Reniers, A., Battjes, J., Svendsen, I., 2003, "Numerical modeling of infragravity wave response during DELILAH", *Journal of Geophysical Research C: Oceans*, vol. 108, no. 9, pp. 4-1 - 4-19.

The nearshore circulation model SHORECIRC is applied to simulate the infragravity wave conditions at two intervals during the 1990 DELILAH campaign at Duck, N.C. The model has been extended to solve the energy equation for random short waves (on the timescale of the wave groups) which acts as a wave driver for the long-wave model. To simulate the wave conditions an algorithm has been derived which synthesizes a directional offshore wavefield from measured data including the bound, directional low-frequency components. The model-data comparison shows that the mean short wave transformation and mean longshore current are predicted well. The structure of the infragravity spectrum as measured in the nearshore array is correctly represented, albeit that the energy levels are underpredicted in most locations. The 2-D frequency longshore-wavenumber spectra show that the infragravity wave energy consists mostly of edge waves, and that the computations qualitatively resemble the measurements. It is shown that for 1 day, bar-trapped edge waves are present. The model is also used to show that the influence of the longshore variability is small for this particular beach and that the directional spreading in the offshore wave field is critical in predicting the nearshore infragravity wave conditions correctly. Edge waves which propagate against the current are generated by the directionally broad short-wave forcing and to a lesser extent by back-scattering. The nonlinear terms are relatively unimportant for the prediction of the infragravity wave climate. The cross-shore gradient of the onshore-directed radiation stress is the most important of the forcing terms.

[12.13]Van Dongeren, A.R., Svendsen, I.A., 2000, "Nonlinear and 3D effects in leaky infragravity waves", *Coastal Engineering*, vol. 41, no. 4, pp. 467-496.

In this paper, infragravity (IG) waves, forced by normally and obliquely incident wave groups, are studied using the quasi-3D (Q3D) nearshore circulation model SHORECIRC [Van Dongeren, A.R., I.A. Svendsen, 1997b. Quasi 3-D modeling of nearshore hydrodynamics. Research report CACR-97-04. Center for Applied Coastal Research, University of Delaware, Newark, 243 pp.], which includes the Q3D effects. The governing equations that form the basis of the model, as well as the numerical model and the boundary conditions, are described. The model is applied to the case of leaky IG waves. It is shown that the Q3D terms have a significant effect on the cross-shore variation of the surface elevation envelope, especially around the breakpoint and in the inner surf zone. The effect of wave groupiness on the temporal and spatial variation of all Q3D terms is shown after which their contribution to the momentum equations is analyzed. This reveals that only those Q3D coefficients, which appear in combination with the largest horizontal velocity shears make a significant contribution to the momentum equations. As a result of the calculation of the Q3D coefficients, the IG wave velocity profiles can be determined. This shows that in the surf zone, the velocity profiles exhibit a large curvature and time variation in the cross-shore direction, and a small - but essential - depth variation in the longshore direction.

[12.14]Webb, S.C., Zhang, X., Crawford, W., 1991, "Infragravity waves in the deep ocean", *JGR*, vol. 96, no. C2, pp. 2723-2736.

Energetic pressure fluctuations at periods longer than 30 s are a ubiquitous feature of pressure spectra from instrUments sited on the deep seafloor in both the Atlantic and the Pacific oceans. We show these pressure fluctuations are caused by freely propagating ocean surface waves. The waves are

generated in the near shore region along the entire coastline of an ocean basin through nonlinear transfer of energy from short-period waves. This view contrasts with some earlier work, which described these long-period pressure fluctuations as trapped waves tied to groups of short waves. We have constructed a model based on the average energy in tile short (wind driven and swell) wave band along the North Atlantic coast to predict the energy in tile long wave band at a site in the Atlantic. Maximum likelihood wave number-frequency spectra calculated on data from an 11 element array in the North Pacific confirm that the long wave energy is confined to wave numbers corresponding to the surface gravity wave dispersion relation. We have used the wave number spectra to isolate particular regions of the Pacific Ocean which are sources of long wave energy. Energetic short-period waves are incident on tile coastline in these regions. Long waves are detected at the array which originate in the Gulf of Alaska, the northwestern Pacific, and at the southern tip of South America.

[12.15]Webb, S.C., Crawford, W., 1999, "Long-period seafloor seismology and deformation under ocean waves", *Bull. Seis. Soc. Am.*, vol. 89, no. 6, pp. 1535-1542.

The deformation of the seafloor under loading by long-period ocean waves raises vertical component noise levels at the deep seafloor by 20 to 30 dB above noise levels at good continental sites in the band from 0.001 to 0.04 Hz. This noise substantially limits the detection threshold and signal-to-noise ratio for long-period phases of earth quakes observed by seafloor seismometers. Borehole installation significantly improves the signal-to-noise ratio only if the sensor is installed at more than 1 km below the seafloor because the deformation signal decays slowly with depth. However, the vertical-component deformation signal can be predicted and suppressed using seafloor measurements of pressure fluctuations observed by differential pressure gauges. The pressure observations of ocean waves are combined with measurements of the transfer function between vertical acceleration and pressure to predict the vertical component deformation signal. Subtracting the predicted deformation signal from pressure observations can reduce vertical component noise levels near 0.01 Hz by more than 25 dB, significantly improving signal-to-noise ratios for long-period phases. There is also a horizontal-component deformation signal but it is smaller than the vertical-component signal and only significant in shallow water (<1-km deep). The amplitude of the deformation signal depends both on the long-period ocean-wave spectrum and the elastic-wave velocities in the oceanic crust. It is largest at sedimented sites and in shallow water.

References

[12.16]Prevosto, M., 2000, "Statistics of wave crests from second order irregular wave 3D models", *Proc. Rogue Waves 2000*, pp. 59-72.

[12.17]Sharma, J. N., Dean R. G., 1979, "Development and evaluation of a procedure for simulating a random directional second order sea surface and associated wave forces", *Ocean Engineering, Report*, no. 20, University of Delaware, Newark.

CHAPTER 13

Conclusions

WASP analyzed a large quantity of existing wave data with the goal of producing an improved description of the characteristics of swell off West Africa. The data base included both measured and hindcast wave data from several locations from Côte d'Ivoire to Namibia. The main focus of the project was to test various descriptions of the shape of the spectrum of swell, but many other features of the swell environment were also studied.

General

Several spectral forms described in Chapter 4 were fitted to the hindcast and measured spectra. The goodness of the fits were quantified by both their rms error and through the response of simple systems in Chapter 6. Considerations of sampling variability in Chapter 5 show that it is difficult to distinguish between these forms for real data. For the most part however, the lognormal provides a better fit to the swell components than the other three spectral functions we tested. The JONGlenn ("JONSWAP") spectral shape was only marginally bettered by the lognormal and on occasions gave a better fit than the lognormal. The choice of the "best" spectral shape for swell depends on the application. The "JONSWAP" allows a larger high frequency tail, which is sometimes seen in swell spectra, but in these cases the swell component may be "contaminated" with some high frequency energy from another source or processing effects. The "JONSWAP" low-frequency tail falls off much faster than measured swell spectral levels, and here the lognormal normal distribution provides a better description in almost every case. The low frequency description is likely to be more important than the high frequency description for the response of floating systems. For these reasons we recommend using the lognormal function to describe the swell peaks in wave spectra off West Africa. Parameters of the other spectra forms for all of the data have been calculated, however, and are available for use if the participants find those forms more convenient.

Simple theoretical arguments given in Chapters 3 and 11 show that the standard deviation of the lognormal function should vary inversely with the peak period. In addition, the standard deviation should decrease as the distance from the source of the swell increases. Both of these hypotheses are borne out by the detailed calculations in Chapter 11. Table 11.1 gives the parameters which allow the calculation of

the standard deviation of the lognormal function for each of the WANE grid points. We recommend that these functions be used for the calculation of the shape of the swell spectrum for any site off West Africa at a similar latitude to those grid points.

The directional spreading of the swell components can be described by a wrapped normal function. Calculations show that the standard deviation of the spreading is inversely proportional to the peak period, and that the directional spreading becomes narrower as the distance from the source of the swell increases. Parameters of the spreading function for each of the WANE grid points are given in Table 11.2. We recommend that these functions be used along with the lognormal form of the frequency spectrum.

The partitioning of the spectra using the Johns Hopkins software, as described in Chapter 6, often led to more than one swell partition in addition to a wind sea partition. One way of dealing with this complexity is to consider the response of simple systems to the spectra. Response spectra can be found by calculating the response of single degree of freedom systems to all of the wave spectra. The calculations given in Chapter 7 show that the largest responses are given by spectra which are nearly uni-modal. This observation means that it should be possible to use fairly simple spectra for design of floating systems. The design spectrum for a system with a given natural period and damping factor can be found through an extreme value analysis of the responses. One surprise from the response spectra calculations was that the maximum responses from the WANE operational hindcasts were larger than those from the storm hindcasts. The reason is that the storm hindcasts did not include some of the storms which produced the highest responses.

Scatter plots and environmental contours of swell height and period for all of the data sets are given in Chapter 8 and its Appendix. The environmental contours were calculated using kernel density estimators, which provide a rational means of producing smooth contours. The contours for the measured and hindcast data sets are in reasonable agreement.
Additional comparisons of the measured and hindcast data in Chapter 9 show good agreement between the dates of "storm" events. The NOAA hindcast of total significant wave height agrees better with some of the measured data than the WANE hindcasts. This better agreement is possibly because stronger (and therefore better) local winds increase the wind wave component of the sea state off Nigeria. On the other hand, the peak frequency and direction of the main swell system given by the hindcast model is in good agreement with the measurements. A finer description of the superposition of the swell systems is available with the hindcast models. More investigations would be necessary to conclude precisely on the use of statistics from hindcast models.

Test of the gustiness of the swell spectrum are given in Chapter 10. The tests described there demonstrate that the swell spectrum is in fact stationary. The swell does not come in gusts with more energy at one time and less at others.

Investigations of the infragravity portion of the wave spectrum are described in Chapter 12. The measurements at Ekoundou and Malabo, both in shallow water, were suitable for these investigations. High levels of infragravity energy were generally associated with higher values of swell energy. Calculations of the second order low frequency energy due to the swell spectrum showed energy levels much less than those measured, however.

Recommendations for additional work

The execution of the WASP scope of work naturally led to additional questions about the swell environment off West Africa, and about how to apply the oceanographic data to design. Discussions at the project meetings led to the development of plans for two additional studies, Plan A and B. These studies are outlined below. Plan B is now being executed using late participation fees.

Plan A – Comparison of new hindcasts and measurements

Utilize recent wave measurements acquired in truly deep water offshore Nigeria and Angola to further enhance understanding of error structure of the WANE hindcast data base and lay the foundation for a future WANE update and enhancement.

Data Sources.
Nigeria Bonga Wavescan, Dec 2001 – Dec 2002, includes winds
Angola Block 14 Directional Waverider, Feb 2000 – Feb 2001, includes winds
Angola Block 17 Directional Waverider, Mar 2001 – Nov 2002, includes winds

The project will require release of the Angola data to WASP by ExxonMobil and Total and their partners. The release will be under a confidentiality clause according to which only derivative products will be released to the WASP participants.

Hindcasts. Oceanweather will develop "best windfields" by assimilating QuikScat winds kinematically into the background and checking against the *in-situ* Bonga, AB14 and AB17 winds. These windfields could also be quite useful to drive current models in the future).

Wave hindcasts will be made with the ODGPR and OWI3G52 models used in WANE. We also need to make runs with the wave models using winds that do not include QuickScat. This will give us a better handle on the value of WANE results. It will also give us a handle on the model error should we proceed with a WANE 2 that covers the entire 35-odd years.

Comparisons of Hindcasts and Measurements.

- Standard difference statistics of WS, WD, HS, TP, and VMD
- QQ comparisons
- Annual and seasonal distributions of WS and HS
- Frequency by frequency comparisons of hindcasts and measurements
- Run spectra through SDF oscillators and calculate scatter of responses
- Compare response spectra for hindcasts and measurements
- Partition spectra using JHU program
- Parameterize partitions
- Compare HS, TP and spectra width of sea and swell partitions
- Compare environmental contours of partitioned spectra
- Time series comparisons of WS, WD, HS, TP, and VMD during major storm events.

Test Improvements to Hindcast Technology. Possible changes to the hindcasts which may be tried to minimize systematic effects revealed by the comparisons include

- Addition of lower frequency bins and testing a few extreme events drawn from the three years of new hindcasts, or if necessary earlier
- Refinement of the ODGP2R PM scaling
- Refinement of OWI2G52

Plan B – Use of Multi-Peaked Spectra

The spectral partitioning and parameterization done in WASP showed that the majority of the spectra measured and hindcast off West Africa contained multiple swell peaks as well as a wind sea. The intention of Plan B is to investigate methods of specifying and utilizing such spectra in design.

Floating Systems. Response operators for floating systems will be used to test the methods of describing the spectra and their joint statistics. A generic FPSO can be described easily using its linear RAO. An important response variable would be the motion of a riser head. It should be possible to also produce a look-up table for a typical CALM buoy. In both cases, the directional characteristics of the floating systems and the directional wave spectra will be used.

Description of Spectra.

- The sensitivity of the responses to the number of peaks allowed in the spectral description will be tested.
- Joint statistics of the swell peaks will be calculated.
- The spectra which produce the highest responses will be identified and extrapolated to give design spectra for a 100 year return period.
- The probability density function of responses will be calculated, and representative spectra for each range of response will be identified for fatigue analyses.
- The results using the RAO and lookup tables will be compared to appropriate SDF models.

References

[2.1] **Haring, R.E., Heideman, J.C.**, 1978, "Gulf of Mexico rare wave return periods", *Proc. 10th Offshore Tech. Conf.*, OTC 3230, pp. 1537-1550.

[2.2] **Tolman, H.L.**, 1999, "User manual and system documentation of WAVEWATCH-III version 1.18", *NOAA/NWS/NCEP/OMB Technical Note 166*, p. 110.

[2.3] **Gumbel, E.G., Greenwood, J.A., Durand, D.**, 1953, "The circular normal distribution: Theory and tables", *American Statistical Society Journal*, vol. 48, pp. 131-152.

[2.4] **Pearson, E.S., Hartley, H.O.**, "Biometrika Tables for Statisticians", Cambridge University Press.

[3.1] **Carter, D.J.T.**, 1982, "Prediction of wave height and period for a constant wind velocity using the Jonswap results", *Ocean Engineering*, vol. 9, pp. 17-33.

[4.1] **Borgman, L.**, "A technique for computer simulation of ocean waves.", Probabilistic Mechanics and Structural Reliability Specialty Conference, ASCE, Jan. 1979.

[4.2] **Gonella, J.**, "A rotary component method for analysing meteorological and oceanographic vector time series.", Deep Sea Research, Vol.19, 1972.

[4.3] **Guedes Soares, C.**, "Representation of double peak spectra.", Ocean Engineering, Vol.11, 1984, pp. 185–207.

[4.4] **Guedes Soares, C.**, "Spectral Modeling of Sea States With Multiple Wave Systems", Journal of Offshore Mechanics and Arctics Engineering, vol.114 1992.

[4.5] **Hasselmann, K., Ross, D.B., Müller, P. & Sell, W.** "A parametric wave prediction model", J. Phys. Oceanogr., vol. 6, no. 2, pp. 200–228.

[4.6] **Hasselmann, K, et al.** "Measurements of wind-wave growth and swell decay during the Joint North Sea Wave Project", Deutsche Hydrographische Zeitschrift, Reihe A 8 (12), 1973, 95 pp.

[4.7] **International Association for Hydraulic Research**, 1986, "List of Sea State Parameters" Supplement to bulletin No 52.
[4.8] **Massel, S.R.** Ocean Surface Waves, their Physics and Prediction, World Scientific 1996.
[4.9] **Mooers, C.N.K.**, "A technique for cross-spectrum analysis of complex valued time series.", Deep Sea Research, Vol.20, 1973.
[4.10] **Ochi, M.K. & Hubble, E.N.**, "Six-parameter wave spectra.", Coastal Engineering, 1976.
[4.11] **Olagnon, M. & Krogstad, H.E.** "Observed short- and long-term distributions of wave steepness", Proc. Int. Offshore and Polar Engineering Conf., Vol. 3, Montréal (1998), pp. 63–70.
[4.12] **Olagnon, M.** "Representativity of some standard spectral models for waves", Proc. Int. Offshore and Polar Engineering Conf., ISOPE Vol. 3, Stavanger (2001), pp. 92-99.
[4.13] **Pierson, W.J. & Moskowitz, L.** "A proposed spectral form for fully developed wind seas based on the similarity of S.A. Kitaigorodskii", J. Geophys. Res., vol. 69, no. 24, pp. 5181–5190.
[4.14] **Quiniou-Ramus, V., Hoche, M.-A., François, M., Nerzic, R., Ledoux, A., Orsero, M.** (2003) "Recent Breakthroughs in the Analysis of Total E&P Angola Block 17 wind/wave/current records and their impact on floating structures design" Proc. XVth Deep Offshore Technology Conf., DOT, Marseilles, Nov. 19-21 2003.
[4.15] **Rychlik, I.**, 1996, "A note on significant wave height" J. Ocean Engineering vol 23 No.6, pp. 447-454.
[4.16] **Torsethaugen, K.** "A two Peak wave spectrum model" Proc. Int. OMAE Conf., Vol.2, (1993), pp. 175–180.
[4.17] **Torsethaugen, K.** "Model for a double peak wave spectrum" Report SINTEF SFT22 A96204, (1996).
[4.18] **van Iseghem, S., Deleuil, G. & Guérin, P.** "Improved characterizations for design waves" Proc. Int. Offshore and Polar Engineering Conf., ISOPE Vol.3, Stavanger (2001).
[5.1] **Brillinger, D.R.**, 2001, "Time Series: Data Analysis & Theory", *Soc. for Industrial & Applied Math*, p. 540.
[5.2] **Harris, F.J.**, 1978, "On the Use of Windows for Harmonic Analysis with the Discrete Fourier Transform", *Proc. IEEE*, vol. 66, no. 1, pp. 51-84.
[6.1] **Hanson, J. L. and O.M. Phillips**, 2001: Automated analysis of ocean surface directional wave spectra. J. Atmos. Oceanic Technol., 18, 277-293.
[6.2] **Longuet-Higgins, M.S, Cartwright, D.E., and N.D. Smith**, 1963: Observations of the directional spectrum of sea waves using the motions of a floating buoy. In: Ocean Wave Spectra: Proceedings of a conference, 111-131, Prentice-Hall, Englewood Cliffs, New Jersey.
[6.3] **Hwang and Wang**, 2001: An operational method for separating wind sea and swell from ocean wave spectra. J. Atm. & Ocean. Tech., 18, December, 2001, 2052-2062.
[8.1] **Scott, D.W.** (1992), Multivariate Density Estimation: Theory, Practice and Visualization, Wiley-Interscience, New York, 317 pp.

[11.1] **Ewans, K. C.**, 2001, "Directional spreading in ocean swell", *The Fourth International Symposium on Ocean Wave Measurement and Analysis*, ASCE, San Francisco.
[12.1] **Aagaard, T., Bryan, K.**, 2003, "Observations of infragravity wave frequency selection", *Continental Shelf Research*, vol. 23, no. 10, pp. 1019-1034.
[12.2] **Elgar, S., Herbers, T.H.C., Okihiro, M., Oltman-Shay, J., Guza, R.T.**, 1992, "Observations of infragravity waves", *J. of Geophysical Research*, vol. 97, no. C10, pp. 15,573-15,577.
[12.3] **Elgar, S., Herbers, T.H.C., Guza, R.T.**, 1994, "Reflection of ocean surface gravity waves from a natural beach", *J. of Physical Oceanography*, vol. 24, no. 7, pp. 1503-1511.
[12.4] **Henderson, S.M., Bowen, A.J.**, 2003, "Simulations of dissipative, shore-oblique infragravity waves", *Journal of Physical Oceanography*, vol. 33, no. 8, pp. 1722-1732.
[12.5] **Herbers, T.H.C., Elgar, S., Guza, R.T.**, 1995, "Generation and propagation of infragravity waves", *J. of Geophysical Research*, vol. 100, no. C12, pp. 24,863-24,872.
[12.6] **Herbers, T.H.C., Elgar, S., Guza, R.T.**, 1994, "Infragravity-frequency (0.005-0.05 Hz) motions on the shelf. Part I: forced waves", *J. of Physical Oceanography*, vol. 24, no. 5, pp. 917-927.
[12.7] **Herbers, T.H.C., Elgar, S., Guza, R.T., O'Reilly, W.C.**, 1995, "Infragravity-Frequency (0.005–0.05 Hz) Motions on the Shelf. Part II: Free Waves", *J. Physical Oceanography*, vol. 25, no. 6, pages 1063–1080.
[12.8] **Munk, W., Snodgrass, F., Gilbert, F.**, 1964, "Long waves on the continental shelf: an experiment to separate trapped and leaky modes", *J. Fluid Mech.*, vol. 20, no. 4, pp. 529-554.
[12.9] **Okihiro, M., Guza, R.T., Seymour, R.J.**, 1992, "Bound infragravity waves", *J. of Geophysical Research*, vol. 97, no. C7, pp. 11,453-11,469.
[12.10] **Reniers, A.J.H.M., van Dongeren, A.R., Battjes, J.A., Thornton, E.B.**, 2003, "Linear modeling of infragravity waves during Delilah", *Journal of Geophysical Research C: Oceans*, vol. 107, no. 10, pp. 1-1 - 1-18.
[12.11] **Sheremet, A., Guza, R.T., Elgar, S., Herbers, T.H.C.**, 2002, "Observations of nearshore infragravity waves: Seaward and shoreward propagating components", *Journal of Geophysical Research C: Oceans*, vol. 107, no. 8, pp. 10-1 - 10-10.
[12.12] **Van Dongeren, A., Reniers, A., Battjes, J., Svendsen, I.**, 2003, "Numerical modeling of infragravity wave response during DELILAH", *Journal of Geophysical Research C: Oceans*, vol. 108, no. 9, pp. 4-1 - 4-19.
[12.13] **Van Dongeren, A.R., Svendsen, I.A.**, 2000, "Nonlinear and 3D effects in leaky infragravity waves", *Coastal Engineering*, vol. 41, no. 4, pp. 467-496.
[12.14] **Webb, S.C., Zhang, X., Crawford, W.**, 1991, "Infragravity waves in the deep ocean", *JGR*, vol. 96, no. C2, pp. 2723-2736.

[12.15] **Webb, S.C., Crawford, W.**, 1999, "Long-period seafloor seismology and deformation under ocean waves", *Bull. Seis. Soc. Am.*, vol. 89, no. 6, pp. 1535-1542.
[12.16] **Prevosto, M.,** 2000, "Statistics of wave crests from second order irregular wave 3D models", Proc. Rogue Waves 2000, pp. 59-72.
[12.17] **Sharma, J. N., Dean R. G.,** 1979, "Development and evaluation of a procedure for simulating a random directional second order sea surface and associated wave forces", Ocean Engineering, Report, no. 20, University of Delaware, Newark.